Geophysical Image to Root Function

Guillaume Blanchy

This PhD thesis is submitted for the degree of Doctor of Philosophy

July 2020

Lancaster Environment Center

Supervisors:
Prof. Andrew Binley (Lancaster University)
Dr. Richard Whalley (Rothamsted Research)
Dr. Malcolm Hawkesford (Rothamsted Research)

Declaration

This thesis has not been submitted in support of an application for another degree at this or any other university. Except when stated otherwise, it is the result of my own work. Collaborations with other researchers and publications are properly acknowledged.

Guillaume Blanchy

Authorship statement

Excerpts of this thesis have been published/accepted in the following academic publications:

- Blanchy, Guillaume, Sina Saneiyan, Jimmy Boyd, Paul McLachlan, and Andrew Binley. 2020. 'ResIPy, an Intuitive Open Source Software for Complex Geoelectrical Inversion/Modeling'. *Computers & Geosciences* 137 (April): 104423. https://doi.org/10.1016/j.cageo.2020.104423.

- Blanchy, Guillaume, Christopher W. Watts, Rhys W. Ashton, Colin P. Webster, Malcolm J. Hawkesford, William R. Whalley, and Andrew Binley. 2020. 'Accounting for Heterogeneity in the ϑ–σ Relationship: Application to Wheat Phenotyping Using EMI'. *Vadose Zone Journal* 19 (1). https://doi.org/10.1002/vzj2.20037.

- Blanchy, Guillaume, Nicolas Virlet, Pouria Sadeghi-Tehran, Christopher W. Watts, Malcolm J. Hawkesford, William R. Whalley, and Andrew Binley. 2020. 'Time-Intensive Geoelectrical Monitoring under Winter Wheat'. *Near Surface Geophysics* n/a (n/a). https://doi.org/10.1002/nsg.12107.

- McLachlan, Paul, Guillaume Blanchy and Andrew Binley. Accepted. 'EMagPy: open-source standalone software for processing, forward modeling and inversion of quasi-2D/3D electromagnetic induction data'. *Computer & Geosciences* n/a (n/a).

- Blanchy, Guillaume, C. W. Watts, J. Richards, J. Bessel, K. Hunterburg, D. Sparks, M. J. Hawkesford, W. R. Whalley and A. Binley. Accepted. 'Time-lapse geophysical assessment of agricultural practices on soil moisture dynamics'. Accepted in a special issue of the *Vadose Zone Journal*

The statements below highlight the contribution of the PhD author. Detailed statements of authorship for all co-authors are available in the published work.

For manuscript "Time-lapse geophysical assessment of agricultural practices on soil moisture dynamics", the PhD author collected the geophysical data on potatoes and cover crops experiments. The PhD author and Chris Watts collected the geophysical data on the Pastures experiment. The PhD author processed the data for all experiments and wrote the manuscript.

Other co-authors provided additional (non-geophysical) data and feedback on the manuscript. Andrew Binley and Richard Whalley provided additional ideas for the paper and edits on the manuscript.

For manuscript "Accounting for Heterogeneity in the ϑ–σ Relationship: Application to Wheat Phenotyping Using EMI", the PhD author collected geophysical data on the experiment, processed the data and wrote the manuscript. Other authors provided additional (non-geophysical) data and feedback on the manuscript. Andrew Binley and Richard Whalley provided additional ideas for the paper and edits on the manuscript.

For manuscript "Time-Intensive Geoelectrical Monitoring under Winter Wheat", the PhD author set up the geophysical acquisition system, processed the data and wrote the manuscript. Other co-authors provided additional (non-geophysical) data and feedback on the manuscript. Andrew Binley provided additional ideas for the paper and edits on the manuscript.

For manuscript "ResIPy, an Intuitive Open Source Software for Complex Geoelectrical Inversion/Modeling", the PhD author along with Sina Saneiyan, Jimmy Boyd and Paul McLachlan wrote the code and the manuscript (equal contribution). Andrew Binley provided feedback on the manuscript.

For manuscript "EMagPy: open-source standalone software for processing, forward modeling and inversion of quasi-2D/3D electromagnetic induction data", the PhD author and Paul McLachlan wrote the code, the Jupyter notebook for the cases and the manuscript (equal contribution). Andrew Binley contributed to writing the manuscript and supervised work on the field case studies.

I hereby agree with the above statements,
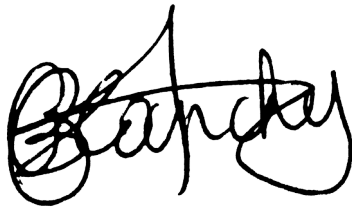
Guillaume Blanchy

Andrew Binley

Abstract

Our agroecosystems are challenged by climate-induced stresses and the need to increase food production for a growing global population. Improving their resilience and sustainability are key challenges for tomorrow's agriculture. Alternative agricultural practices (e.g. reduced tillage, cover crops, etc.) and selection of more robust crop varieties have the potential to help meet these challenges. To fully assess the effectiveness of such practices, an improved understanding of the soil-plant-water interactions is needed, however, such improvement is constrained by existing field-based measurement methods. In this work, we used a combination of time-lapse electrical resistivity tomography (ERT) and electromagnetic induction (EMI) to study soil moisture dynamics for a range of agricultural settings.

In a study of cover crops, it was found that tap-rooted cover crops had larger impact on the soil drying than shallow-rooted ones. Additionally, the effect on soil drying of long-term cover crops (grown over two seasons) was larger than that over one season. However, in both cases the effect of the cover crops on the soil drying quickly vanished after their destruction. Soil compaction is another issue that might impact crop water availability. In this work, time-lapse ERT measurements enabled the imaging of the restricted drying depth of traffic-induced compacted plots compared to non-compacted ones under potatoes. The impact of tillage and nitrogen levels was also investigated using time-lapse EMI surveys under winter wheat. It was found that nitrogen levels only had an ephemeral effect on the change in electrical conductivity (EC) measured independently of the tillage treatment. Also direct drilled plots showed a smaller drying compared to mouldboard ploughed plots over the season.

Aside from different agricultural practices, efforts have also been undergoing to breed varieties of crops more resilient to water stresses. Part of this resilience lies with the root system of the crop and its capacity to extract soil moisture. However, acquiring information on the variety traits (phenotypes) in a field-scale setup is one of the major bottlenecks of crop breeding, especially for below-ground traits. Time-lapse geophysical methods have been successfully used to discriminate soil drying between different winter wheat varieties in large field-scale trials. However, the results here show that the discriminating power of this approach can, under some conditions, be hindered by local variation of the pedophysical relationship used to convert change in EC to change in soil moisture. This study shows that this can have important impacts on the ranking of the varieties; alternative models and experimental procedure are proposed to further account for this heterogeneity.

Finally, the emergence of automated field phenotyping platforms offers a unique means for crop breeders to screen large number of varieties in a controlled field environment. These platforms can provide a wealth of above-ground measurements, but they usually lack below-ground data. In this work, time intensive geoelectrical monitoring was performed on four plots of winter

wheat with two different nitrogen levels in a field phenotyping platform. The measured seasonal dynamics of the soil EC appears to be related to the evolution of above-ground variables but are also impacted by the different nitrogen levels applied. Large decreases in the soil EC observed after large rainfall events are associated with both crop nitrogen and soil moisture uptake. At the hourly scale, time series analysis enables the identification of diurnal patterns that could be linked to root water uptake.

Overall, time-lapse geophysical monitoring has proven to be a useful tool to monitor root zone processes with minimal invasiveness. The work, however, also demonstrates the limitations of the approach; a range of perspectives for future improvement are discussed. While not sufficient on their own, geophysical methods remain a useful tool for the emerging field of agrogeophysics and can provide valuable insights for shaping future agricultural practices.

Acknowledgements

I am grateful to all collaborators who helped me on the experiments: Chris, Rhys, Colin, Nicolas, Pouria from Rothamsted Research; Jake, Jennifer, Will and Debbie from the University of Nottingham; Katharina (Lancaster University) and Mark (NIAB CUF). A special thanks to Chris Watts who supported a number of field experiments at Rothamsted Research and for its enthusiasm about geophysical methods in agriculture.

I would like to thank my friendly colleagues with who I had fostering discussions, namely in no particular order, Paul, Michael, Tuvia, Malika, Fatima, Jimmy, Martina and Carmen.

I would like to thank the Hydrogeophysical Knowledge Exchange group, that offered a friendly environment for exchanging on geophysical methods through a series of monthly webinars. A special thanks to Sina and Jimmy for their involvement into the ResIPy project.

I am also very grateful to my three supervisors: Andrew Binley (Lancaster University), Richard Whalley (Rothamsted Research) and Malcolm Hawkesford (Rothamsted Research) for their involvement and support all along my PhD adventure.

Special thank goes to my supervisor, Andrew Binley, for his guidance and continuous support throughout the PhD process. His involvement and advices helped me to develop research projects and transform their outputs into publishable manuscripts.

Special thanks goes to Paul McLachlan with who I spent long hours talking about EMI, for his collaboration into EMagPy and his generous friendship.

Finally, I would also like to thank my family and friends and especially my partner Marie-Eve for their support all along this adventure.

List of Tables

List of Figures

9

11

Contents

List of abbreviations

ERT : Electrical Resistivity Tomography
EMI : Electromagnetic Induction (in this context: frequency domain)
GPR: Ground Penetrating Radar
IP : Induced Polarisation
SIP : Spectral Induced Polarisation
TDIP : Time-Domain Induced Polarisation
NMR : Nuclear Magnetic Resonance
VCP : Vertical CoPlanar
HCP : Horizontal CoPlanar
PRP : PeRPendicular
EC : Electrical Conductivity
ECa : Apparent Electrical Conductivity
CS : Cumulative Sensitivity
LIN : Low Induction Number approximation
FS : Full Solution, refers to the full solution of Maxwell's equation
Q : Quadrature component (expressed as parts per thousand, ppt)

Chapter 1

Introduction

Authorship statement

1.1   Drivers

Tomorrow's agriculture will have to be more sustainable for our land but also more resilient to environmental stresses, in particular those induced by climate change. An example of such stresses are the more frequent and longer drought periods that might jeopardise crop production. To better prepare our agroecosystems to such scenarios, we need a better understanding of the complex soil-plant-water interactions taking place in the subsurface. Soil and water are essential resources for agriculture. However, intensive practices have endangered them in some cases, potentially impacting our food security (Amundson *et al.*, 2015). Development of more sustainable agricultural practices such as those from conservation agriculture (FAO http://www.fao.org/conservation-agriculture/en/) aims at addressing these issues. However, assessing their effectiveness on the soil moisture dynamics at the field-scale remains challenging. Indeed, soil moisture can often be measured at very large-scale by remote sensing approaches such as satellite imagery or using cosmic ray sensors (https://cosmos.ceh.ac.uk). However, these approaches lacks resolution for field-scale studies. Moreover, these two approaches also do not provide depth-specific soil moisture estimate but rather an integrated measurement, often mainly controlled by soil moisture at shallow depths. Other soil moisture measurement methods, such as time domain reflectometry (TDR), operate at the "point-scale" but are very useful for monitoring depth-specific soil moisture. In contrast, geophysical methods provide measurements more adapted to field-scale studies, easily spanning scales of several orders of magnitude (Figure 1.1). In addition, they often can provide depth-related information and are less invasive than auger-based techniques. When using contact-less sensors, they enable collection of large amount of information rapidly. However, these methods do not directly measure soil properties or states but rather a geophysical property that is influenced by them. Hence, geophysical methods often require site-specific relationships to convert the geophysical variable to the soil state or property of interest. An example of successful agricultural application of geophysical tools is the use of electromagnetic induction (EMI) for mapping soil properties or state of interest. Such approach usually rely on a single survey done when the field is vegetation-free. It does allow the creation of detailed maps of soil texture or salinity (Corwin, 2008) and the delineation of management zones for agriculture (Hedley *et al.*, 2004). However, to better understand the impact of agricultural practices on the soil-water-plant interactions, the time dimension is crucial. Time-lapse geophysical approach has been widely used in controlled setups to monitor infiltration and fluid movements, however fewer experiments have attempted to user the approach for field-scale vegetated study focused on agricultural practices. In this project, we explore the use of time-lapse geophysical measurements at assessing the impact of different agricultural practices on the soil-water-plant interactions in field-scale setup (Chapter 4).

Another important aspect of tomorrow's agriculture is the crop itself: varieties have been
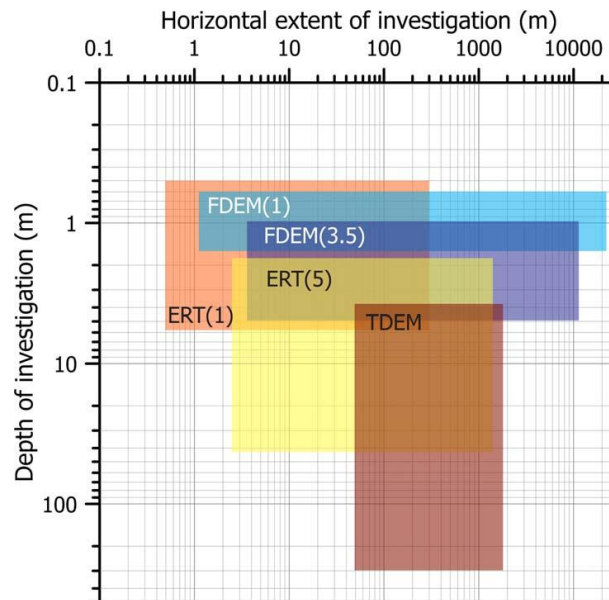
Figure 1.1 – Horizontal and vertical investigation range of several geophysical methods: electrical resistivity tomography (ERT) for 1 and 5 m electrode spacing, frequency domain electromagnetic (FDEM) for 1 and 3.5 m and time-domain electromagnetism (Binley *et al.*, 2015).

selected for years based on various above-ground traits such as yield or straw; but very little selection has been carried out on "hidden" traits such as the root system (Fradgley *et al.*, 2020). As highlighted by Godfray *et al.* (2010), the genetic improvement of crops for desirable traits is needed to ensure global food security. To select more robust varieties, deeper knowledge about their below-ground traits (root system architecture and function) is needed (Wasson *et al.*, 2012). Root water uptake and resistance to water stress is now part of targeted wheat traits to be improved as shown by simulation of Senapati *et al.* (2020). Recently, Carminati & Javaux (2020) also emphasis that the stomatal drought response is more controlled by the soil than by xylem vulnerabilities, further highlighting the need to study both above- and below-ground hydraulics. While below-ground traits can easily be measured in pot-scale experiments, sometimes using automated setup, field-scale study remains challenging but needed. Indeed, the phenotype of the crop (i.e. the combination of its traits) is the result of complex interactions between its genetics and its environment. Hence, to fully assess the potential of a variety, it has to be tested in its environment: the field. This often results in experimental field trials where numerous varieties are tested. High-throughput phenotyping of such experiments is challenging and remains a major bottleneck of crop breeding (Furbank & Tester, 2011). While several methods are being developed to relieve this bottleneck (Araus & Cairns, 2014; Atkinson *et al.*, 2019) they mainly focus on the above-ground part of the crop despite the clear need to develop field-scale high-throughput methods to acquire below-ground information (Atkinson *et al.*, 2019). The 'core-break' method for wheat (Wasson *et al.*, 2014; White *et al.*, 2015) and the "shovelomics" method for maize (Trachsel *et al.*, 2011) are two sampling approach that provides information on the

root system of the crop. The methods are labour-intensive but also destructive and hence are limited for monitoring of the crop during the growth season. In contrast, less invasive approaches based on measuring the soil drying induced by crop uptake have been developed. While this approach does not directly measure root architecture, it nevertheless provides useful information on the root function as demonstrated by Ober *et al.* (2014); Lopes & Reynolds (2010) who found that deeper soil moisture extraction were associated with higher yield. Whalley *et al.* (2017) reviewed several methods to monitor soil drying under different winter wheat varieties. Among them, electrical resistivity tomography (ERT) and EMI have shown potential at imaging soil moisture change between varieties. Shanahan *et al.* (2015) also showed that time-lapse EMI was able to differentiate soil moisture change between different wheat varieties on a sandy clay loam. These two studies demonstrated that time-lapse geophysical monitoring has potential to help relieve the phenotyping bottleneck described earlier. However, one major challenge remains in quantifying the effect of the field heterogeneity on geophysically-derived soil moisture estimate. Indeed, pedophysical relationships (e.g. Waxman & Smits, 1968) are site-specific and can vary substantially with soil texture. Given the spatial extent of field phenotyping trials, the effect of field heterogeneity is potentially important. While such effects might be negligible when comparing crops of different species, when small differences between different varieties are being considered, this can potentially hinder the discriminative power of the approach, and needs to be investigated. This project aims at exploring the impact of field heterogeneity on geophysically-based soil moisture estimates that can potentially have important impact on variety selection (Chapter 5). On a smaller and more controlled scale, high-throughput field phenotyping platforms (Prasanna *et al.*, 2013; Virlet *et al.*, 2017) have evolved to enable automated monitoring of a large number of varieties and hence contribute to relieve the phenotyping bottleneck. While the plots of such facilities are usually larger than greenhouse-based experiments but smaller than conventional field-scale trials, they offer a unique setup to monitor above-ground traits at high temporal frequency, capturing the seasonal evolution of the crop. In this setup, the use of high-throughput geophysical monitoring could be useful to acquire below-ground information on the crop root function. Coupling above-ground information with below-ground geophysical variable, could allow a unique look into the evolution of the entire plant phenotype and its evolution along the season. In this work, we assess the capabilities of time-intensive geoelectrical monitoring to retrieve below-ground information that can be coupled with above-ground variables provided by a field high-throughput phenotyping platform (Chapter 6).

1.2   Research questions and thesis structure

This thesis addressed three research questions.

1. What is the potential of time-lapse geophysical methods for agriculture?

While single geophysical surveys have been widely used for diverse applications, time-lapse surveys are less common. Chapter 4 demonstrates through a series of case studies how time-lapse geophysical survey can help to assess different agricultural practices and retrieve information on soil-plant-water interactions.

2. How can time-lapse geophysical surveys be used in field phenotyping trials and what are the limitations?

   This question is addressed in Chapter 5 that focuses on the main challenge of the approach at the field-scale: the variation in the relationship between a specific geophysical variable, electrical conductivity (EC), and the soil state of interest (soil moisture).

3. How can below-ground information from time-intensive geophysical monitoring be coupled with above-ground data from a controlled field phenotyping platform? Chapter 6 illustrates the use of hourly ERT monitoring of different wheat varieties and nitrogen treatment under the Field Scanalyzer platform at Rothamsted Research.

In the following chapter we review the use of geophysics applied to agricultural problems: agrogeophysics. Chapter 3 then describes the field sites used for the experimental work in the thesis. Chapters 4 to 6 address the research questions, as listed above. Finally, Chapter 7 provides a discussion and synthesis of results, discusses limitations and offers recommendations for further research.

Chapter 2

Agrogeophysics

Authorship statement

Chapter written by the PhD author, comments and edits provided by Andrew Binley.

2.1   Geophysical properties

At the field-scale, collecting soil samples is the traditional method for acquiring information on soil properties or states. While this method is invasive and labour-intensive, especially over large areas, it offers direct measurements of the soil properties or states of interest which is invaluable. However, its destructive nature prevents repeated measurements and hence monitoring over the season. In contrast, geophysical properties can often be measured in-situ without much disturbance to the soil or the crop, which is a significant advantage in a monitoring study. In most cases, geophysical methods do not directly measure soil properties or states but are rather used as proxies (Table 2.1). Indeed, geophysical properties measured by geophysical methods are usually a complex combination of different soil or rock characteristics. A good example is the electrical conductivity (EC) which is controlled by solid constituents (particle size, distribution and mineralogy), arrangements of voids (pore size, distribution and connectivity), water saturation, EC of the fluid (solute concentration) and temperature (Samouëlian et al., 2005). The fact that geophysical properties are sensitive to multiple soil characteristics can also be viewed as an advantage. Hence, under specific circumstances, a same geophysical variable can be used to infer different soil characteristics. For instance, EC can be used to map soil texture (Abdu et al., 2008), soil moisture content (Robinson et al., 2012b) or soil salinity (Corwin & Lesch, 2005); as each of these soil characteristics contribute to the soil EC. Permeability, which depends on pores sizes and shapes but also their connectivity, has also been a target property of several geophysical methods (initially driven by the oil industry in exploration of new reservoirs). Soil moisture, or more generally water content (if rocks are considered), also influences several geophysical properties. Wet soils will be more electrically conductive than dry soil and hence EC can be used to estimate soil moisture content. Another example of method based on geophysical property, while usually not cited as a geophysical method, is given by time-domain reflectometry (TDR). TDR is a well-established method that sends electromagnetic pulses along metallic rods and assesses travel time of such a pulse (similar to ground penetrating radar). TDR measures the electrical permittivity (dielectric constant) of a material that can be translated to soil moisture (e.g. Topp et al., 1980). Direct estimation of soil moisture content can also be given using nuclear magnetic resonance (NMR) which is directly sensitive to proton density. NMR is an emerging method. Ground-based measurements are typically applied to study soil moisture to depths of several tens of metres, although very recent instrument advances has led to shallower depths of investigation.

Table 2.1 – Geophysical methods, their properties measured and examples of derived properties and states (Binley *et al.*, 2015).

Geophysical Method	Geophysical Properties	Examples of Derived Properties and States
DC resistivity	Electrical conductivity	Water content, clay content, pore water conductivity
Induced polarisation	Electrical conductivity, chargeability	Water content, clay content, pore water conductivity, surface area, permeability
Spectral induced polarisation	As above but with frequency dependence	Water content, clay content, pore water conductivity, surface area, permeability, geochemical transformations
Self-potential	Electrical sources, electrical conductivity	Water flux, permeability
Electromagnetic induction	Electrical conductivity	Water content, clay content, salinity
Ground penetrating radar	Permittivity, electrical conductivity	Water content, porosity, stratigraphy
Seismic	Elastic moduli and bulk density	Lithology, ice content, cementation state, pore fluid substitution
Seismoelectrics	Electrical current density	Water content, permeability
Nuclear magnetic resonance	Proton density	Water content, permeability
Gravity	Bulk density	Water content, porosity

EC is a widely used geophysical property and, to better interpret it, several conduction models or "petrophysical" models were developed to identify the contribution of each constituent. In a porous media, such as rock or soil, most of the electrical conduction will be carried out by charged ions in the pore water solution. This explains while soil moisture content and pore water conductivity are two main contributing factors to soil EC. Less current goes through the solid phase compared to the fluid phase, however, surface conduction can play a significant role, notably if clay particles are present. The initial conduction models developed were mainly empirical but later models have been based on a more mechanistic approach that demonstrates the better understanding of the conduction phenomenon. Mineral exploration was one of the drivers of the expansion of geophysical methods. After the development of resistivity logging by Marcel and Conrad Schlumberger (Schlumberger, 1920), there has been increasing interest in linking geophysical variables to specific rock properties leading to the development of 'petrophysical' relationships. Based on empirical observations, Gustave Archie established one of the

first empirical model linking rock properties to resistivity (Archie, 1942):

$$EC(S_w) = EC_w \phi^m S_w^n, \tag{2.1}$$

where $EC(S_w)$ is the unsaturated rock conductivity, EC_w the pore fluid conductivity, ϕ the porosity with the m cementation exponent and S_w the saturation with n the saturation exponent. The so-called formation factor F can be calculated as $F = \phi^m$. This model did not take into account the contribution of clay minerals that was later added by Waxman & Smits (1968):

$$EC(S_w) = \frac{S_w^n}{F}(EC_w + \frac{BQ_v}{S_w}), \tag{2.2}$$

where B is the equivalence conductance of clay exchange cations and Q_v is the volume concentration of clay exchange cations. Revil *et al.* (1998) further developed Archie's law and proposed a physically based model to explain conduction in shaly sands. While these relationships mainly focus on rock, other models were specifically derived for soils. Rhoades *et al.* (1976) proposed a conceptual conduction model that contains two parallel conductors: one associated with the liquid phase and one associated with exchangeable ions at the liquid-solid interface.

$$EC(\theta) = T(\theta) \times \theta EC_w + EC_s, \tag{2.3}$$

where $T(\theta)$ is a transmission coefficient that aims to account for the complex geometry of the pore network and θ is the volumetric soil moisture content ($\theta = S_w \phi$). The transmission coefficient can be fitted for each soil using a simple linear equation: $T(\theta) = a\theta + b$ ($a = 2.1$ and $b = -2.5$ for clay soils). The model was later updated to distinguish between "mobile" (large pores) and "immobile" (fine pores) phases (Rhoades *et al.*, 1989). Mixing models can also be used, whereas the soil EC is determined from the sum of the EC of its constituents and their geometrical arrangements (e.g. Glover, 2015). Another approach consists in simulating the porous media using electrical circuits as Greenberg & Brace (1969) successfully showed by reproducing Archie's law that way. Focussing on saturated porous media, Cai *et al.* (2017) reviewed the different electrical conductivity models. Laloy *et al.* (2011) compared three of them for soil using a Bayesian framework and proposed the term 'pedo-physical' models to distinguish them from their rock-focused equivalent. Simplified version of the Waxman and Smith equations have also been applied to soils (Garré *et al.*, 2011). While, increasing knowledge have been acquired about the physical mechanisms affecting electrical conduction of a medium, simple linear relationships are still widely used to link EC to soil moisture for instance (Calamita *et al.*, 2015). This can be explained by the site-specific nature of these relationships but also by the difficulty of obtaining all variables needed for more complex conduction models. In this work, two geophysical methods: ERT and EMI are used to soil moisture dynamics in the portion of soil under the influence of

roots: the root-zone. Both methods are sensitive to the soil EC despite difference in how they physically measure it (see later). Figure 2.1 presents a range of EC of different soil types according to their wetness.
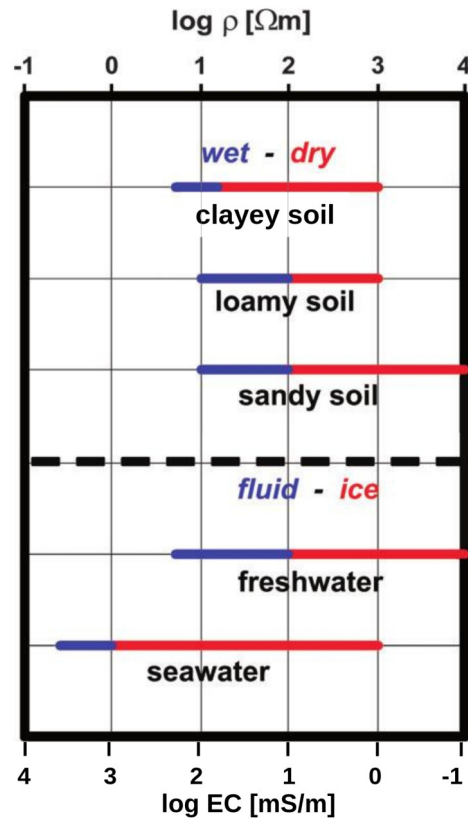
Figure 2.1 – Electrical resistivity (ρ) and corresponding electrical conductivity (EC) of different soils according to their wetness, and of freshwater and seawater according to their state presented on a log scale. Edited from Attia al Hagrey (2007) based on data from Keller & Frischknecht (1966).

As previously stated, different factors will influence the EC, such as the soil temperature, soil moisture content, soil porosity, pore water ionic content and the soil texture. The combined contribution of these factors to the soil EC makes it difficult to isolate a unique driver for the EC. For instance, one site can have a range of soil texture (from sandy to clay) and this can dominate the EC variations observed; while another site can have the same texture but large variation in soil moisture. To untangle these interactions, the dominant factor contributing to EC needs to be identified and the other factors accounted for. In this work, we used the following workflow to further relate the measured EC to soil moisture.

All studies presented in this work were carried out in rainfed agricultural fields in temperate climates where we can assume that the pore water EC stays relatively constant during the growth season. The same might not be true in more saline environments or with irrigation using higher EC water (e.g. from groundwater). However, even in temperate climates, sudden short-term

increase in the porer water EC can occur upon application of fertiliser for instance.

A time-lapse approach can be applied to enhance the soil moisture contribution to the EC. Taking differences in EC between two surveys enables the removal of the 'static' EC components of the system (Robinson *et al.*, 2012b), such as soil texture or porosity effects, that can be assumed constant during the study period. For time-lapse surveys taking place over the entire growth season, a unique reference survey is chosen to compare all surveys against it. This reference survey (or background) is usually chosen at the start of the growing season where minimal effects of the crops can be assumed.

Finally, to account for the temperature contribution to EC, which is essential for time-lapse surveys, the following correction equation has been applied that describes a 2% increase in EC per degree Celsius (Hayashi, 2004; Ma *et al.*, 2011):

$$EC_{25} = \frac{EC_T}{1 + 0.02(T - 25)} \tag{2.4}$$

where EC_{25} is the corrected EC at 25 degree Celsius, EC_T is the EC measured at temperature T (in degree Celsius).

2.2   Geophysical Methods

2.2.1   Overview

Several geophysical properties can be related to soil characteristics. While our work focuses on the use of EC measured by EMI and ERT, other geophysical methods have potential for agricultural studies and are worth developing.

Resistivity methods have been widely used in agricultural study (Allred *et al.*, 2008) and can be divided into two approaches: galvanic coupling and capacitive coupling. Galvanic methods use electrodes in direct contact with the soil. Electrical current is usually applied between two of them (current dipole) and potential difference is measured between two others (potential dipole). This provides a transfer resistance value that, given the geometry of the electrodes, can be used to estimate an effective or apparent soil resistivity. Such an approach has also been used in archaeology, where typically two electrodes are fixed and the other two are mobile, allowing mapping over an area. For higher-throughput mapping, vehicle-based acquisition systems have been developed, where the electrodes can be pulled on the ground (Sørensen, 1996) or mounted as discs on a towed system (Figure 2.2).

Figure 2.2 – Veris 3100 Soil EC Mapping instrument (Veris Technologies, USA). Picture taken from https://www.veristech.com/the-sensors/v3100 accessed on 2020-07-02.

The use of multiple electrodes increases the amount of information collected about the subsurface and led to the development of the electrical resistivity tomography (ERT) method which enables recovery of the distribution of subsurface resistivity. One main disadvantage of galvanic methods is the contact resistance between the electrode and the soil that can lead to bad measurement quality. In very resistive environments, galvanic coupling with the ground may not be possible. To address this, capacitive methods have been developed. They rely on the use of capacitive coupling between the electrodes and the soil to avoid contact resistance limitations. The OhmMapper TR1 (Geometrics, Inc.) is an example of such a commercial system. However, capacitive coupled methods are not well suited to low resistivity environment such as soils where the signal to noise ratio can be smaller than for galvanic coupled methods (Allred *et al.*, 2008).

The induced polarisation (IP) method can be viewed as an extension of resistivity methods. Initially developed for mineral exploration (e.g. Vinegar & Waxman, 1984), the IP methods measure the susceptibility of a material to polarise when subjected to an electrical field. Time-domain induced polarisation (TDIP) measures the voltage decay after current cut-off to infer the medium chargeability while frequency domain induced polarisation (FDIP) uses an alternating current at a specific frequency and measures a complex impedance. This is sometimes referred to as the complex resistivity method. FDIP can be applied at multiple current injection frequencies, allowing an assessment of the spectral properties of thecomplex electrical resistivity (spectral induced polarisation, SIP). Maurya *et al.* (2018) compared the TDIP and SIP methods in a field-scale setup and conclude that both methods provide similar quantitative IP information and TDIP presenting a shorter acquisition time compared to SIP. IP methods have been successfully used for imaging contamination (Cassiani *et al.*, 2009; Flores Orozco *et al.*, 2016) and hence could

be useful for monitoring soil remediation. At the lab-scale, Schwartz & Furman (2014) studied the SIP response to soil organic matter and proposed that future SIP electrical models should integrate this component as well. In agricultural studies, one of the attraction of IP methods has been imaging the polarisation originating from the root system of the crops (Kuzma & Schwartz, 2018). These methods have mainly been used at the lab-scale (Weigand & Kemna, 2017) with some recent applications to field studies (Mary *et al.*, 2017; Weigand & Kemna, 2018). However, interpretation of IP signal is often challenging, even more in complex porous system such as the soil where the IP response of the soil can dominate and mask the IP signal from the roots.

Electromagnetic induction methods have been widely used in agriculture (Corwin & Lesch, 2005) and rely on measuring electromagnetic fields resulting of induced eddy currents in the ground. It is sensitive to the soil EC and hence can be related to resistivity measurements from other geoelectrical methods. In addition, EMI methods often provide an 'inphase' component which related to the soil magnetic susceptibility but is rarely used in soil surveys. The method uses a contact-less sensor which makes is very attractive in field-scale studies to collect information on large areas. If original instrument had only a limited number of coil configuration, more recent instrument now often includes multiple coil configurations enabling the acquisition of depth-related ECa measurements. A detailed description of the method is provided hereafter.

Ground penetrating radar (GPR) is a popular shallow geophysics method that is based on energy scattering in the form of an electromagnetic wave in the subsurface. GPR instruments are composed of a transmitting and a receiving antenna. An electromagnetic pulse is sent towards the ground from the transmitter and, in the most common mode, the receiver records its "echos" as the pulse travels in the subsurface. The propagation speed of the electromagnetic wave through the subsurface is controlled by its electrical permittivity (when divided by the permittivity of vacuum it constitutes the dielectric constant). When the electromagnetic wave encounters a change in permittivity, part of the energy of the wave is reflected while the rest is transmitted or refracted. Recording this scattering provides information on the structure of the subsurface. For agricultural studies, the electrical permittivity is very useful as it can be linked to other soil characteristics such as soil moisture content (as in, e.g., TDR). GPR can also be used to map soil moisture by measuring the directed (not reflected) wave that travels along the ground surface (Algeo *et al.*, 2016) or using air-launched methods (Lambot *et al.*, 2006; Wu *et al.*, 2019). However, these methods usually only assess the soil moisture of the upper layer (few centimetres). Transmission GPR can also be used to measure wave speeds between boreholes (e.g. Binley *et al.*, 2001). Such a setup clearly relies on a more invasive configuration (e.g. Klotzsche *et al.*, 2018a,b). Huisman *et al.* (2003) provided a review of the use of GPR for soil moisture estimation. GPR can also be used to map drainage pipes buried in agricultural field (Allred *et al.*, 2008) or assess soil bulk density in geotechnical projects (Wang *et al.*, 2016).

Seismic method shares similarities with the GPR method but this time the scattering is

produced by a pressure wave caused by a shock, explosion or vibration. As this pressure wave propagates into the subsurface, it is partially scattered on materials with different elastic properties. The resulting reflected waves are recorded by sensors called geophones and can be used to reconstruct the distribution of subsurface properties. In agricultural studies, seismic methods have been used to assess soil compaction (Oelze *et al.*, 2002; Lu *et al.*, 2004) and also to measure wood decay in tree trunk (Attia al Hagrey, 2007). An acoustic source, two microphones and a laser Doppler vibrometer can also be used to create an acoustic-to-seismic coupled system that can be used to measure soil strength non-invasively while the crop is growing (Shin *et al.*, 2013, 2017).

Nuclear magnetic resonance (NMR) can also be used to obtain information on soil characteristics, mainly soil moisture. NMR measurement involve three steps: (1) a strong constant electromagnetic field is applied that orients (polarises) all the protons, (2) a weaker oscillating magnetic field is applied, (3) the weaker oscillating field is ceased and the protons realign on the stronger constant magnetic field of the start (relaxation). The electromagnetic signal emitted by the protons during phase (2) or (3) enables to discriminate between different nuclei but also, given the strength of the signal, to estimate the number of nuclei. This last output is a significant advantage of this method is that it offers a direct measurement of soil moisture content. One example of field-scale use of NMR for agricultural study is given by Paetzold *et al.* (1985), who successfully used NMR to map surface soil moisture content using a tractor-mounted system.

While the above methods can be used independently, there is often added value in combining the information of different geophysical methods in 'data-fusion' approaches (JafarGandomi & Binley, 2013; Castrignanò *et al.*, 2018) or through the mean of coupled framework (Skibbe *et al.*, 2020).

While various geophysical methods have potential application in agriculture, in this work, we focus on ERT and EMI. Two well-established methods that, when combined together, provide a powerful tool to study soil moisture processes at depth, in time and at the field-scale. The methods are detailed in the next sections.

2.2.2   Electrical resistivity tomography

Electrical resistivity tomography (ERT), also known as electrical resistivity imaging (ERI), is a technique that relies on an array of multiple electrodes to infer the electrical resistivity distribution of the subsurface. The method is now increasingly used in the field of hydrology, leading to the emergence of hydrogeophysics (Binley *et al.*, 2015).

The technique consists in injecting current between two electrodes (A and B) and measuring the potential difference between two others (M and N), hence forming a quadrupole (four electrodes) as show in Figure 2.3.
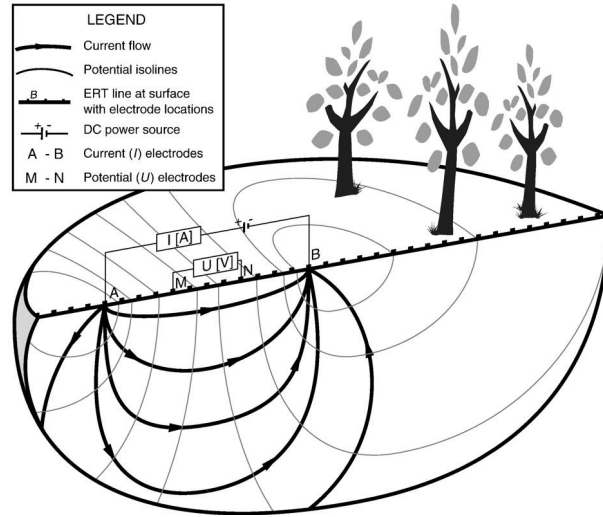
Figure 2.3 – Representation of a quadrupole with current injection between electrodes A and B and potential difference measured between M and N. The lines with arrows denote the current lines while the other lines show the equipotentials. Figure from Nijland *et al.* (2010).

The potential difference divided by the injected current, gives a 'transfer resistance':

$$R = \frac{\Delta U}{I}, \tag{2.5}$$

with R, the transfer resistance (ohm), ΔU the potential difference (also referred to voltage V) and I the injected current (A). The transfer resistance can be multiplied by a geometric factor, K, to obtain an 'apparent electrical resistivity' (ρa expressed in ohm.m) corresponding to the resistivity of a homogeneous half-space that leads to the same transfer resistance:

$$\rho_a = K \times R. \tag{2.6}$$

The value of the geometric factor (K) depends on the array geometry and can be computed for a collinear (2D) array on a flat ground surface as

$$K = \frac{1}{1/AM - 1/BM - 1/AN + 1/BN} \tag{2.7}$$

where AM, BM, AN and BN are the distance between the pair of electrodes.

Multiple combinations of quadrupoles along an electrode array enable the collection of overlapping information about the subsurface. ERT instruments have evolved to be able to measure simultaneously multiple quadrupoles sharing the same injection electrodes, considerably speeding up the survey for specific quadrupole geometries. For instance, the Syscal Pro instrument (Iris Instruments, Orléans, France) used in this project, is able to measure up to 10 contiguous potential difference pairs for the same injection electrodes. Different quadrupole configurations can be found in the literature. The common arrays are the dipole-dipole, Wenner and Schlum-

berger configurations (see Samouëlian *et al.* (2005) for more information). In this project only dipole-dipole sequences are used as they are highly optimised for our instrument. Figure 2.4 shows different resistivity instruments including the Syscal Pro used in this work.

Figure 2.4 – Resistivity meters through time. From left to right: bespoke instrument (1950s), ABEM SAS300 resistivity meter (1970s), Geoscan RM4 (1980s), Campus Instruments Geopulse (1990s), Iris Instruments Syscal Pro 96 (2000s).

Measurements from any instruments are likely to contain errors. They might originate from the instrument limited accuracy and the acquisition setup, or might just be random. In either case, assessing the quality of the measurements obtained is an important step. Errors for each quadrupole can be assessed by repeatability (stacking) or using the principle of reciprocity (e.g. Parasnis, 1988). The reciprocal method is usually more reliable than relying on stacking errors given by the instrument (Tso *et al.*, 2017) and hence is preferred in this work. For a given quadrupole AB-MN (qualified 'normal'), its reciprocal (MN-AB) is obtained by swapping the current and potential electrodes: the current is injected between M and N and potential measure at A and B. The absolute reciprocal error (R_{error}) is computed as:

$$R_{error} = |R_N - R_R|, \tag{2.8}$$

where R_N the transfer resistance for the normal configuration and R_R the transfer resistance for its reciprocal configuration. Using the reciprocal error and the mean of the normal and reciprocal transfer resistances (R_{avg}) grouped in bins (see Koestel *et al.*, 2008), an error model

can be fitted such as a power-law:

$$R_{error} = a \times R_{avg}^{n}.$$

(2.9)

Figure 2.5 shows an example of power-law error model. Other error models such as a linear model can also be used. Tso *et al.* (2017) suggested the use of a linear mixed-effect model to account for electrode-related errors. All previous error models account for both systematic and random errors. However, for time-lapse survey configuration, where multiple surveys are collected at different times over the same ERT array, it is common to interpret the data using differences between datasets. For instance, the values measured in the first survey are subtracted from all other survey. This has the effect of removing the systematic error component, just leaving the random part. Lesparre *et al.* (2019) designed an error model adapted for time-lapse configuration that removes the effect of systematic errors. Overall, one important advantage of an error model is that it provides a way to estimate the error for each quadrupole, even the ones without reciprocal. This will be essential when recovering the resistivity distribution of the subsurface, as explained below.
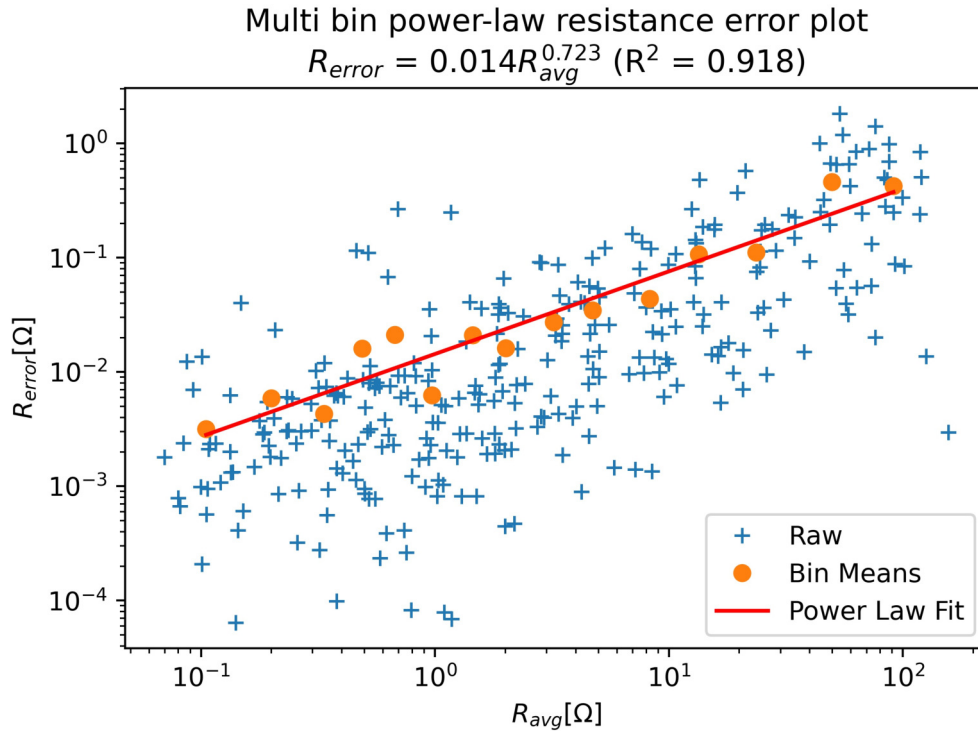
Figure 2.5 – Example of a power-law model fitted on reciprocal errors.

The apparent resistivities (or transfer resistances) collected are not depth-specific but rather a complex depth-integral of the true subsurface resistivities. In order to obtain a depth-specific resistivity distribution of the subsurface, a mathematical procedure needs to be applied: an inversion. The inversion aims at building a model of the resistivity distribution of the subsurface

that can explain the observed transfer resistances. The subsurface resistivity distribution is represented as a mesh (grid) in which each cell has a specific resistivity. The voltage $V(x, y, z)$ for a point source current I and an isotropic resistivity $\rho(x, y, z)$ inside this mesh can be modelled using:

$$\nabla[\frac{1}{\rho(x,y,z)}\nabla V(x,y,z)] = -I\delta(x,y,z), \tag{2.10}$$

with the following Neumann (no flux) boundary conditions:

$$\frac{1}{\rho}\frac{\partial V}{\partial n} = 0, \tag{2.11}$$

where δ is the Dirac function and n is the outward normal. Note that in this project, the inversion code used, R2 (Binley, 2015), uses a Neumann boundary for all boundaries, which means that the mesh needs to be extended far away from the zone of interest to correctly model the voltage field.

Subsequent application of the above equations for each measured quadrupole produces a voltage field which is used to model the potential difference measured at the M and N electrodes, hence reproducing a set of modelled transfer resistances. This procedure is called forward modelling. Each time the forward model is called, it produces a set of synthetic measurements based on the resistivity distribution of the mesh.

Given a set of parameters m (e.g. the resistivity of each cell of the model), the aim of an inversion is to fit the simulated measurements produced by the forward model ($F(m)$) with the observed data (d) (in this case, the observed transfer resistances). The inversion requires the definition of an objective function to minimise (or maximise). A weighted objective function Φ_d, quantifying the least squares difference between observations of forward model computed response and can be written as:

$$\Phi_d = ||W_d(d - F(m))||^2, \tag{2.12}$$

where W_d the diagonal matrix containing the errors for each quadrupole (estimated from an error model). However, as the number of parameter (resistivity for each cell element) is often larger than the number of measurements, the problem is under-determined. One common solution to solve this is to spatially regularise the solution by adding a model misfit term (Φ_m) that will penalise for departure from a smooth model (Constable et al., 1987):

$$\Phi_m = m^T R m, \tag{2.13}$$

where R, the roughness matrix representing the connectivity between contiguous elements and penalizing for departure from a smooth solution (Binley, 2015). The total misfit is then

given by:

$$\Phi = \Phi_d + \lambda\Phi_m, \tag{2.14}$$

where λ is the parameter controlling the regularization (smoothing factor). To minimise this misfit, a Gauss-Newton approach is usually used to linearise the problem into iterative steps. For each iteration, the update on the model parameter (Δm) is computed to decrease the total misfit.

$$(W_d J^T J W_d^T + \lambda I)\Delta m = J^T J(d - F(m_i)) - \lambda R m_i, \tag{2.15}$$

With J, the Jacobian matrix and m_i represents the model at iteration i. More details are provided in Binley (2015). Figure 2.6 illustrates this iteration process.
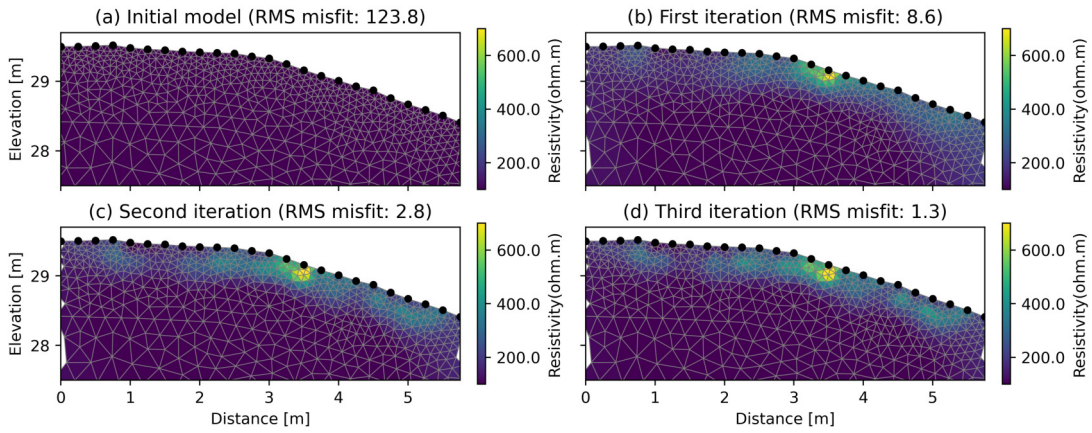
Figure 2.6 – (a) shows the initial model with 100 ohm.m as the starting value. (b), (c) and (d) show the inverted model after the first, second and third iteration respectively. The root mean square (RMS) which is defined by the misfit of the observed and modelled transfer resistances weighted by their respective errors, provides an indicator of how good the inverted model is at fitting the observations.

Further details on the data processing and inversion can be found in Appendix A. Inverted sections presented in this work have been produced using ResIPy (Blanchy et al., 2020b, ; appendix A) which is a Python wrapper around the well-established R2 inversion code (Binley, 2015).

The ERT method can be used in a 2D or 3D fashion (some authors also refer to 4D for 3D + time-lapse). 3D ERT surveys certainly provide more information on the 3D structures of the ground. However, in cases where lateral homogeneity can be assumed (such the plot-scale experiment in this work), 2D ERT surveys are sufficient. In addition, 2D surveys enable the allocation of a limited number of electrodes to increase the resolution of the survey by decreasing the electrode spacing. Also in this work, ERT was often used to provide robust measurements

to support the EMI method developed hereafter. For this purpose, 2D sections are well suited.

2.2.3 Frequency domain electromagnetic induction

This technique relies on the use of electromagnetic induction to infer the subsurface electrical conductivity. EMI instruments are composed of one transmitter coil (Tx) and at least one receiver coil (Rx). The transmitter coil emits a transient electromagnetic field (primary field, H_p) that induces eddy currents in the subsurface proportional to its EC. These eddy currents induce a secondary electromagnetic field (H_s). Both primary and secondary field are measured by the receiver coil (Figure 2.7).
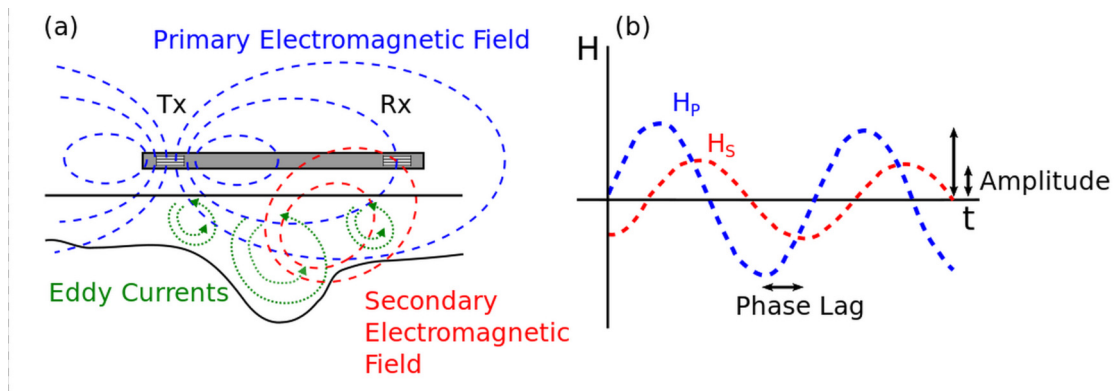
Figure 2.7 – Working of an electromagnetic instrument composed of one transmitter (Tx) and one receiver (Rx). The transmitter emits a primary electromagnetic field (H_p) which induces eddy currents in the subsurface. These eddy currents induce a secondary magnetic field (H_s). From both fields, the electrical conductivity of the subsurface can be inferred. Figure from (McLachlan et al., 2020b).

Figure 2.8 shows different EMI instruments including the CMD Mini-Explorer (GF Instruments, Brno, Czech Republic) used in project.

The imaginary part of the ratio of the primary and secondary field is called the quadrature (Q) and can be converted to an 'apparent' electrical conductivity (ECa) using the low induction number approximation (McNeill, 1980):

$$EC_a = \frac{4}{\omega \mu_0 s^2} Q, \tag{2.16}$$

where ω is the angular frequency (2π times the operating frequency), μ_0 is the permeability of free-space and s is the coil separation. Note that some manufacturer (e.g., GF Instruments) directly map the quadrature to an ECa using a linear relationship and hence do not use the low induction number approximation. Each EMI instrument has different coil configurations available to the operator. They are: (1) the coil orientation, (2) the coil separation, (3) the height of the device above the ground and (4) the operating frequency. The Tx and Rx coils can

Figure 2.8 – Electromagnetic induction instruments through time. From the background to the foreground: EM15 (Geonics), EM38 (Geonics), CMD Mini-Explorer (GF Instruments).

be horizontal co-planar (HCP), vertical co-planar (VCP) or perpendicular (PRP). In multi-coil instruments with multiple Rx coils, different coil separations between Rx and Tx are available. Large coil separations enable a larger sample volume and, hence, recovery of deeper information. Additionally, turning the instrument by 90 degrees transforms an HCP configuration into a VCP and vice-versa, hence providing additional coil configurations. In this work, the instrument was always placed on the ground and the frequency of the instrument was fixed at 30 kHz.

With multiple measurements from different coil configurations taken over the same surface, one has overlapping information and can perform a 1D inversion to recover a depth-specific EC. Similar to ERT, the inversion requires a forward model that will compute the response (ECa) of a given depth-specific EC model. Example of forward response can be a linear function derived from the cumulative sensitivity function (McNeill, 1980):

$$R_{VCP}(z) = \sqrt{4z^2 + 1} - 2z, \tag{2.17}$$

$$R_{HCP}(z) = \frac{1}{\sqrt{4z^2 + 1}}, \tag{2.18}$$

$$R_{PRP}(z) = 1 - \frac{2z}{\sqrt{4z^2 + 1}}, \tag{2.19}$$

where R_{VCP} the relative response at the relative depth z (z equals the depth divided by

coil spacing s). Alternatively a non-linear response can be computed using the Maxwell-based equations (Wait, 1955):

$$Q_{VCP} = \mathfrak{Im}\left(\frac{H_s}{H_p}\right)_{VCP} = \mathfrak{Im}\left(-s^2 \int_0^\infty R_0 J_1(s\lambda)\lambda d\lambda\right), \qquad (2.20)$$

$$Q_{HCP} = \mathfrak{Im}\left(\frac{H_s}{H_p}\right)_{HCP} = \mathfrak{Im}\left(-s^3 \int_0^\infty R_0 J_0(s\lambda)\lambda^2 d\lambda\right), \qquad (2.21)$$

$$Q_{PRP} = \mathfrak{Im}\left(\frac{H_s}{H_p}\right)_{PRP} = \mathfrak{Im}\left(-s^3 \int_0^\infty R_0 J_1(s\lambda)\lambda^2 d\lambda\right), \qquad (2.22)$$

where J is the Bessel function of zero of first order and λ is the integration variable. The reflection factor (R_n) is calculated at the interface of each layer, including between the air and the first layer. It can be obtained recursively from the infinite N^{th} layer, given that beyond N can be assumed homogeneous and therefore $R_{N+1} = 0$, and the following:

$$R_n = \frac{\frac{\Gamma_n - \Gamma_{n+1}}{\Gamma_n + \Gamma_{n+1}} + R_{n+1}e^{-2\Gamma_{n+1}h_{n+1}}}{1 + \frac{\Gamma_n - \Gamma_{n+1}}{\Gamma_n + \Gamma_{n+1}}e^{-2\Gamma_{n+1}h_{n+1}}}, \qquad (2.23)$$

where $\Gamma_n = \sqrt{\lambda^2 + i\omega\mu_0 EC_n}$, and h_n and EC_n are the thickness and the EC of the nth layer (increasing n with depth). R_0 is obtained by assuming the EC of layer 0 is 0 S/m to reflect the air. The integrals in the equations represent the Hankel transform and can be computed using linear filtering (Anderson, 1979; Guptasarma & Singh, 1997).

In low EC environments such as non-saline agricultural field ($40 - 80$ mS/m in this work), the CS function and the more accurate Maxwell-based approach produce similar sensitivity patterns, and hence are equally suited to model for forward response of EMI instruments. However, in environments with high EC values (> 100 mS/m), their sensitivity patterns can be very different. Figure 2.9 shows that effect using several synthetic models. Indeed, the high EC layer attenuates the electromagnetic wave (note the reflection coefficient of Equation 2.23) which, hence, does not penetrate deeper layers. The CS approach does not account for this effect and is hence not well suited in this case. Callegary et al. (2007) showed how the effective depth of investigation (depth above which 70% of the signal originates), decreases at higher EC values and how LIN-based approximation failed to account for that. This causes LIN-based instrument to underestimate the ECa in high EC environments. To prevent this, Hanssens et al. (2019) suggested the use of a 'robust ECa' approach. von Hebel et al. (2019) also proposed the use of an 'equivalent ECa' obtained through minimisation of the observed and simulated quadrature from an homogeneous EC (Van Der Kruk et al., 2000; Andrade et al., 2016). More details on these alternative approaches is provided in Appendix B.
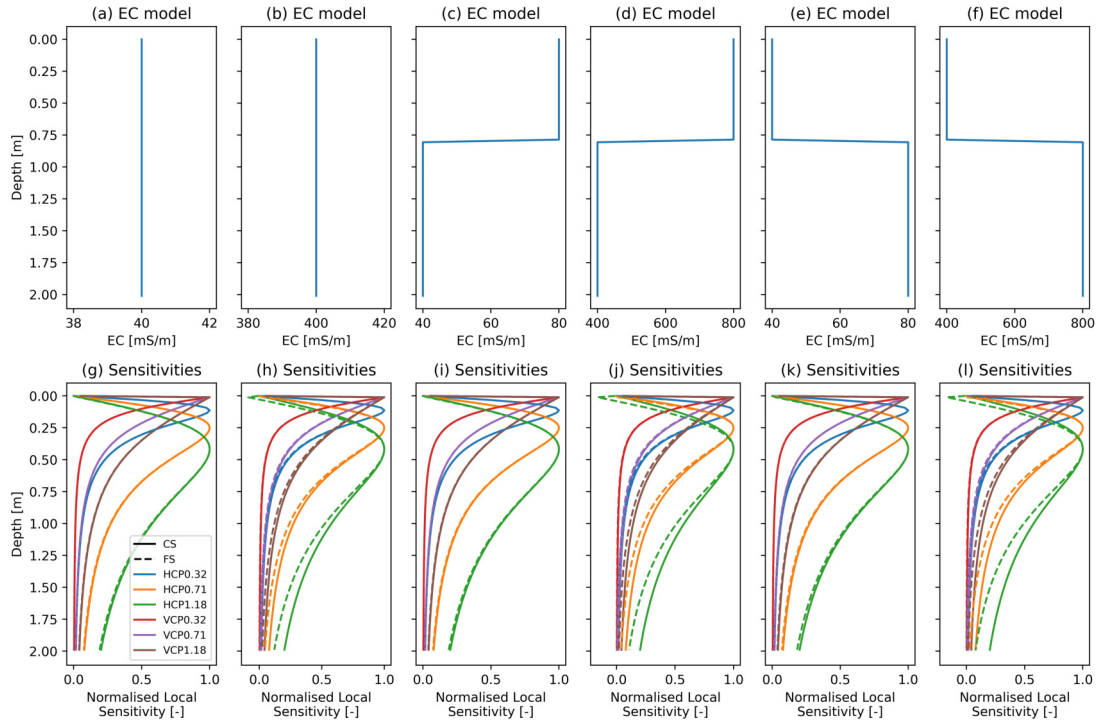
Figure 2.9 – (a-f) Several 1D EC models and (g-l) their respective computed normalised sensitivity from the cumulative sensitivity (solid line) and the Maxwell-based approach (dashed).

With the chosen forward model, different techniques can be used to invert the profile: Gauss-Newton (Whalley *et al.*, 2017), Markov chain Monte Carlo (JafarGandomi & Binley, 2013) or artificial neural network (Moghadas, 2020). Detailed descriptions of the different forward models and inversion approaches for EMI is provided in Appendix B.

EMI instruments are sensitive to drift and it is good practice to set up a drift station in the surveyed area to check the ECa value during the survey (Shanahan *et al.*, 2015; Whalley *et al.*, 2017). Additionally, raw ECa values provided by the EMI instruments are often qualitative. In order to make them quantitative, it is recommended that a calibration of the ECa values is made using a known EC structure. This EC structure can be obtained from an ERT transect, vertical electrical sounding or using multiple elevations methods (Lavoué *et al.*, 2010; Tan *et al.*, 2019; von Hebel *et al.*, 2019). While calibration of ECa value is less important for mapping applications, it is, however, essential for inversion.

The internal working of ERT and EMI has been developed. Both methods are sensitive to the subsurface EC even if they differ by the mean of measuring it. Due to the larger amount of information collected, the ERT method provides more robust distribution of the subsurface EC. However, the practicality of EMI and specially its high-throughput is a huge advantage for field-scale applications. The following section will review the applications of both methods in agricultural studies.

2.3   Applications

This section describes several applications of geophysical methods to agricultural studies with a focus on ERT and EMI methods. The applications have been divided in three categories. First, applications aiming at obtaining information on the soil characteristics independently of the crop are presented. Then, studies interested in the soil moisture dynamics of the root zone are described. Finally, methods proposing to directly assess the roots via their geophysical properties are developed.

2.3.1   Soil characteristics

While this work is more focussed on the dynamics of soil-plant-water interactions rather than on assessing static soil characteristics, it is important to present some of the applications of geophysical methods to infer soil characteristics for the following reasons. First because of their historical importance in developing the field of agrogeophysics but also because these applications are still currently relevant for agricultural studies. For further details, the reader is redirected to the review provided by Allred *et al.* (2008), in which the applications of several geophysical methods in agriculture are detailed.

Given their ability to cover large areas in short amount of time, geophysical methods have been extensively used for mapping soil characteristics. Viscarra Rossel *et al.* (2011) offered a review of proximal soil sensing methods in which several geophysical methods are described. In most studies, a single geophysical survey is carried out over the area investigated to collect geophysical information. Subsequent in situ or laboratory calibration is then needed to convert the geophysical variable into the soil characteristic of interest. This simple approach is widely used but requires a good understanding of the driving factors controlling the geophysical variable.

Soil texture is a major driver of soil EC, and early on, EMI was used to map soil textural properties such as clay content (Palacky, 1987; Triantafilis & Lesch, 2005; Reyes *et al.*, 2018). This sensitivity of ECa to soil texture makes it useful for defining soil management zones for precision agriculture (Hedley *et al.*, 2004; Moral & Serrano, 2019). At larger scales, multi-configuration EMI has also been used to map area "beyond the field-scale" (Brogi *et al.*, 2019a), providing multiple overlapping ECa maps that can be used to infer soil classes using image classification. These EMI-derived map of the subsoil heterogeneity have also been linked to leaf area index (LAI) pattern from remote sensing (Rudolph *et al.*, 2015; Brogi *et al.*, 2020). On a smaller scale, soil compaction or effect of tillage can also be assessed using 2D ERT as they impact the soil EC (Besson *et al.*, 2004, 2013). Furthermore, the potential of geophysical methods at assessing soil structure – defined by the authors as a "fragile product of soil biological activity" – has also been assessed by Romero-Ruiz *et al.* (2018). They found that several geophysical methods were suitable to obtain soil structure information at previously unexplored spatial and temporal

scales. EMI was also successfully used by Galambošová *et al.* (2020) to identify traffic-induced compacted area in shallow and subsoil. They found that compacted soils exhibit higher ECa compared to their direct surrounding but they also highlighted the significant spatial variability of ECa that needs to be accounted for. de Oliveira *et al.* (2020) also found that ECa correlates well with a pesticide (atrazine) movement parameters, making is a suitable tool to study mitigation strategies to prevent pesticide transport to groundwater.

One of the first use of EMI sensors in agriculture was to map soil salinity. Indeed, soil salinisation impacts crop productivity and ultimately lead to the soil being unsuitable for agriculture. Soil salinisation is not a new phenomenon but climate change could make some regions more susceptible to it (Corwin, 2020). Corwin & Lesch (2003) used ECa map to identify sampling area for soil salinity measurements. Jadoon *et al.* (2015) used an EMI device (CMD Mini-Explorer) to estimate soil salinity in a drip irrigation system. They successfully used a joint inversion approach to invert EMI measurements and calibrate them against the EC of saturated soil paste extracts which is a common measure of soil salinity. While it is well known that pedophysical relationship are known to be site-specific, Farzamian *et al.* (2019) investigated the use of local and regional relationship to convert EMI derived EC. They found that even if the local relationships provided slightly higher accuracy, the regional relationship was more practical and still provide useful information for soil salinity monitoring.

In study areas where the electrolyte concentration of the pore water is low, soil moisture is an important driver of soil ECa. Kachanoski *et al.* (1988) observed a strong correlation between ECa from EMI and soil moisture across a wide range of soil texture and anticipated that, using a proper calibration, EMI could be used for soil moisture mapping. In a precision agriculture approach, Brevik *et al.* (2006) monitored soil moisture and soil ECa of different sites at several occasions on two consecutive years. They observed that ECa was strongly correlated to soil moisture for all sites, with lower landscape positions exhibiting a higher increase in ECa for a given increase in soil moisture. They recommended that soil moisture should be recorded when using EMI for precise soil mapping. Several other applications of EMI to map soil moisture exist; Calamita *et al.* (2015) provided an extensive review of them. In addition to being site-specific, Altdorff *et al.* (2018) also noted that the relationship between ECa and soil moisture content was also function of the agronomical treatments, mainly because of higher pore water EC due to different type of fertiliser. Based on the effect of soil organic carbon on soil moisture (Rawls *et al.*, 2003), Huang *et al.* (2017a) also attempted to link depth specific organic matter with soil EC with some caveats mainly attributed to geomorphological features (erosion gully) and the small extent of the survey. Doolittle & Brevik (2014) reviewed the use of EMI for soil studies and highlighted the effectiveness of EMI to characterise diffuse soil boundaries. They also recognised the site-specific limitations of pedophysical relationships as well as the complex interactions of different factors that can make ECa interpretation difficult. Nevertheless, they conclude at the

usefulness of the technique for mapping soil characteristics at the field and landscape scales.

Most of the studies presented in this section aim at obtaining soil information based on a single geophysical survey, mainly for mapping applications. They also rely on ECa values and not inverted EC, in some cases because of the limited coil configurations available. In this sense, they constitute qualitative approaches where ECa measurements are used as proxy. However, the static view they provide might be limited when considering the dynamics of agroecosystems. Indeed, while soil texture is not likely to change during the course of a season, other soil characteristics such as soil moisture might be much more variable and linked to vegetation. Hence, measuring the dynamics of the soil moisture in relation to soil and vegetation using geophysical methods has the potential to provide more information on the internal working of an agricultural system.

2.3.2　Root zone soil moisture dynamics

Panissod *et al.* (2001) were one of the first to observe resistive anomalies under corn rows. But without independent soil moisture measurement they were unable to link it to soil moisture with certainty. Michot *et al.* (2001) repeated the experiment with TDR and 2D ERT and showed that the resistivity method was adapted at monitoring soil drying under rows of corn on an irrigated Calcisol. Using soil moisture measurements from TDR to relate to the soil electrical resistivity, they were able to follow the soil wetting front and identify preferential fluxes during two consecutive days. Michot *et al.* (2003) further developed their previous experiment, notably by adding soil temperature probes to correct resistivity values and extending the monitoring period to 10 days including an irrigation and a rainfall event. They derived a good linear relationship between electrical resistivity and soil moisture from TDR (with a root mean squared error of 3.65%).

In a pot experiment, Werban *et al.* (2008) used ERT to monitor soil moisture variations induced by a lupin plant in sand. They observed diurnal variation of soil moisture content that was attributed to evapotranspiration of the plant. Following this, Garré *et al.* (2011) monitored soil moisture variations due to root water uptake and evapotranspiration in an undisturbed soil column using 3D ERT and TDR. They showed that the soil moisture variation inferred correlates well with root development from mini-rhyzotron observations. They also noticed that horizon-specific pedophysical relationships are needed for better estimation of soil moisture.

In the field, Srayeddin & Doussan (2009) used time-lapse ERT to quantify the spatial variability of water uptake under corn and sorghum. They were able to quantitatively relate ERT measurements to soil moisture variations down to 60 cm but no deeper, mainly because of the lower sensitivity and resolution of their surface ERT setup. The also recognised the need for in situ calibration between soil moisture and electrical measurements and that the slope of this

calibration depends on the mean soil moisture content. This will be explored in more details in Chapter 5. Rather than relying on 2D sections, Beff *et al.* (2013) used 3D ERT and TDR to image soil moisture change under corn rows in the field. They also found very good relationship between soil moisture content and electrical resistivity (R^2=0.98) and highlight the higher resolution of ERT which leads to a better estimation of the water stock. In addition, 3D ERT revealed larger drying under corn rows and in the inter-rows. However, during rainfall, the area under the corn became wetter than the inter-rows, potentially revealing preferential infiltration pathways.

In an orchard, time-lapse ERT was also used to monitor root water uptake under different irrigation schemes (Vanella *et al.*, 2018). Their study indicated that root water uptake processes take place at the 0.1 m scale and that different irrigation schemes impacted them. In vineyards, Brillante *et al.* (2016b) used time-lapse ERT to study water stress on two different soils. They developed a statistical approach to visualise spatio-temporal plant soil water uptake and also highlighted the variability of soil contribution to plant water status in time and space. Recognizing the variability of pedophysical relationships, Brillante *et al.* (2016a) then successfully tested various machine learning algorithms to use ERT measurements to predict plant soil water availability. They found that the use of ERT coupled with these machine-learning approaches enables good quantification of plant soil water availability with minimal disturbance.

At a larger spatial scale, geoelectrical methods have also been used to investigate the impact of different agricultural practices on the soil moisture patterns. In effort to fill the gap between remotely-sensed and in-situ point-like measurements of soil moisture, Jayawickreme *et al.* (2008) used time-lapse ERT to image the change in soil moisture under a forest and a grassland. They found large difference in soil moisture and root depths for the two vegetation types and anticipated that land use change such as reforestation could have an impact on the ground water recharge. Building on this, Jayawickreme *et al.* (2010) repeated the experiment and found, among other things, that the intercept of the pedophysical relationship between soil resistivity and soil moisture derived from soil samples of the same transect can have a large impact on this same relationship. These observations highlighted already the effect of soil heterogeneity on pedophysical relationship (Chapter 5). Nijland *et al.* (2010) also used time-lapse ERT to monitor soil moisture extraction of vegetation on different soils. They showed that vegetation can extract water up to 6 m depth and below, right into the weathered bedrocks. They concluded that time-lapse ERT can provide crucial information to study soil moisture process that would not be available with other methods. Jayawickreme *et al.* (2014) reviewed the use of time-lapse ERT for ecological applications highlighting its usefulness of the method to study hydrological processes at relevant scales.

The impact of tillage and cover crops on the soil moisture was also studied by Celano *et al.* (2011) in an olive orchard. Using ERT, they observed a higher soil moisture content below

one meter depth for the cover crop treatments, a definite advantage for rainfed olive trees. Another agricultural practices to reduce soil erosion on sloping ground is the use of hedge-row intercropping. It consists in planting hedge-rows of (nitrogen-fixing crop) at regular interval with the main crop growing in between. However, such system can generate competition between the main crop and the hedge-row for water and nutrients. Garré et al. (2012) used synthetic modelling to estimate the usefulness of various ERT configurations in discerning soil moisture patterns under this system. They noticed that the sharp soil moisture contrasts were often smoothed by the ERT inversion. The authors recommended the use of geostatistics to estimate the ability of ERT to recover expected patterns in soil moisture and hence help survey design. Another alternative cropping system is the use of agroforestry in which crops are grown between rows of trees. In this system as well, it is suspected that water competition exists between the main crop and the trees. Coussement et al. (2018) used a tree-bordered field as a surrogate of an agroforestry system in which they performed time-lapse ERT. Using a reference ERT transect outside of the tree-bordered area, they were able to identify the zone of influence of the trees and hence demonstrate the potential of ERT to monitor tree-crop interactions.

Most of the agrogeophysics studies of soil moisture dynamics in the root zone concentrate on the use of ERT. Indeed, ERT is now a well-established method for studying root zone processes (Cimpoiaşu et al., 2020). However, other electrical methods such as EMI have also shown potential at monitoring root-zone soil moisture. For instance, Robinson et al. (2012a) used time-lapse EMI to map soil wetting patterns at the catchment scales. The use of time-lapse EMI allowed them to remove the 'static' contribution to the ECa due to mineralogy, and hence improve soil moisture prediction. The authors also acknowledged the limitation of the method as moisture dependent ECa contrasts might not occur in certain soils. Cassiani et al. (2012) highlighted the use of long-term time-lapse EMI and short-term ERT monitoring of soil moisture variations during vegetation growth. The techniques enabled them to image the positive feedback of the vegetation on rainfall infiltration and soil moisture recharge despite its rainfall interception from leaves. Similar to ERT, multi-configuration EMI data can be inverted to produce EC distribution. Huang et al. (2016) developed a spatio-temporal algorithm based on the CS function to inverted time-lapse EMI dataset. From its use, they were able to map the location of the wetting front in a transect under alfalfa (Medicago sativa). Huang et al. (2017c) further developed the pedophysical relationship between depth-specific EC and soil moisture for the same experiment. At the plot-scale, repeated EMI surveys have been used to compare soil drying of different wheat varieties. Shanahan et al. (2015) inverted time-lapse EMI using a Markov chain Monte Carlo (McMC) approach and computed change in depth-specific EC compared to baseline readings. Linking the difference in EC to difference in soil moisture from neutron probes, they were able to monitor soil moisture extraction by roots in depth and time. Building on this, Whalley et al. (2017) reviewed several field-based methods, including time-lapse ERT and EMI, to measured

soil moisture changes in a phenotyping context. Differences in the soil moisture pattern compared to a baseline were used to discriminate wheat varieties. The study also showed that dry conditions enable better discrimination. The authors also presented a non-linear pedophysical relationship between change in soil moisture and change in EC. This approach seems promising but the discrimination power of the approach as well as its susceptibility to other soil parameters is yet to be tested (Cimpoiaşu *et al.*, 2020). A similar, albeit less extensive, experiment was done by Huang *et al.* (2018) who used time-lapse inverted EMI to monitor soil moisture under different chickpea genotype at the plot-scale.

Cimpoiaşu *et al.* (2020) and Zhao *et al.* (2019) reviewed the use of electrical methods to investigate root zone processes. Being minimally invasive, cost-effective and sensitive to key root zone parameters (soil moisture content, salinity, roots themselves), they provide a unique opportunity to collect root-zone information in both space and time. Given the literature scrutinised, they concluded that electrical methods are very effective at monitoring root zone soil moisture dynamics and possibly at obtaining information on the root architecture as well. The authors also highlighted the necessity of robust pedophysical relationships and the potential of combined study using different geophysical methods. Zhao *et al.* (2019) further provided an exhaustive review of the different agrogeophysical studies and the processing methods used in the form of very informative tables. As summarised by both (Cimpoiaşu *et al.*, 2020) and Zhao *et al.* (2019), geophysical methods, can also provide, in some cases, direct measurement on the root system of the crops, as detailed in the next section.

2.3.3   Direct root detection

Some geophysical methods can be used to directly identify roots in the ground from their geophysical properties. For instance, Morelli *et al.* (2007) proposed the use of GPR in combination with ERT to identify coarse woody roots of trees. In this case, the coarse roots of the tree have contrasting electrical permittivity and appear as hyperbola in the GPR sections. Guo *et al.* (2013) offered a review of the applications of GPR for coarse root detection. They highlighted that relationships between GPR measurements and coarse roots were site-specific and that better detection could be achieved in low EC soil such as sand in dry conditions. Fine roots of herbaceous crop might be more difficult to detect given the smaller amount of electromagnetic signal that they reflect compared to coarse roots. However, they still have a contrasting electrical permittivity compared to the surrounding soil, further enhanced by their accumulation of nutrients and higher water content (Liu *et al.*, 2016). Given the fact that herbaceous crops, such as wheat, are often grown at high density, Liu *et al.* (2018) found that their root mass per unit of soil volume could be equivalent to the coarse roots of trees and hence should have a non-negligible impact on the overall soil electrical permittivity. Liu *et al.* (2018) further demonstrated the use

of different pixel-based metrics that, for some field-sites, made it possible to link root biomass to GPR (1600 MHz) signals for several varieties of wheat and energy cane. The relationships derived are highly soil specific and, in some cases, no significant relationship could be established. The authors also observed that wet soil provided stronger relationship compared to dry soil.

Computer X-ray tomography (CT) has been successfully used to image the root system of the different crops. Mooney *et al.* (2012) reviewed the use of CT for root detection and highlighted that despite the overlap between the attenuation density of root material and soil pore space, the method is promising to provide a direct measurement of the soil system. Similarly, MRI can also provide direct information on the root system (Metzner *et al.*, 2015). Nevertheless, we should note that both methods requires soil samples and hence are impossible to use *in situ*.

For herbaceous roots, Amato *et al.* (2009) found correlation between root biomass and electrical resistivity for alfalfa. However, they noted that the resistivity signal of roots is of the same order of magnitude as soil texture or soil moisture and hence can be difficult to differentiate in some cases. For woody roots, Rossi *et al.* (2011) successfully linked root biomass to electrical resistivity in an orchard study. Another method for woody roots detection is the use of mise-à-la-masse (MALM). In combination with ERT, it has proven useful to gain information on root location but also on soil moisture depletion from root water uptake (Mary *et al.*, 2018, 2020). The MALM method injects electrical current directly in the root system using an electrode in the trunk and uses an array of electrodes to measure the potential in the surrounding soil. This technique relies on the hypothesis that the root system (especially coarse woody roots) will act as preferential current paths until the tip of the roots, hence enabling to infer information on the root system (Mary *et al.*, 2018). However, this method is, so far, limited to woody roots as non-woody roots are not sufficiently electrically isolated to act as a point-source at the tip.

Fine roots in a soil are difficult to identify from their environment solely by a geophysical property such as resistivity. Early studies suggested that root systems might be distinguishable using other electrical properties, such as their capacitance (Chloupek, 1977). Dalton (1995) modelled roots as a resistor-capacitor circuit. However, Dietrich *et al.* (2012) and Ellis *et al.* (2013) found this representation inconsistent as they showed that most of the capacitance effect was due to the hydroponic solution and only a small amount to the roots themselves. More recently, induced polarisation and, more specifically, spectral induced polarisation (SIP) has proven useful for direct imaging of the root system at the lab scale. SIP has shown promising results in direct characterisation of roots in solution and soil at the lab-scale (Weigand *et al.*, 2017; Weigand & Kemna, 2017, 2018; Kuzma & Schwartz, 2018; Tsukanov & Schwartz, 2020; Wang *et al.*, 2019). Wang *et al.* (2019) related SIP parameters to soil moisture content and identify a frequency range (40-50 kHz) in which root biomass can be linked to the absolute phase difference. However, this method is still at an early stage of development: further studies are needed to better estimate the discrimination power of SIP between roots and soil. Direct

root detection using geophysical methods in the field has been mainly successful when applied on coarse woody roots. Applications to direct detection of fine roots are, for now, limited to controlled experiments. Detection of soil moisture variations due to crop uptake is much more established and while it does not provide direct information on the root system, it still provides useful agronomical information on soil-plant-water interactions. In this work, this last approach is developed through a series of experiments at facilities which are detailed in the next chapter.

Chapter 3

Field facilities

Authorship statement

Chapter written by the PhD author, comments and edits provided by Andrew Binley.

The experiments presented in this work are all field based and took place during the growing season of the crop. To study the impact of agricultural practices using time-lapse geophysical monitoring, several datasets of geophysical measurements were collected in parallel on multiple experiments, highlighting the need of multiple field-scale facilities. In contrast, the study of the impact on soil heterogeneity on the pedophysical relationship is tightly linked to one experimental setup. Similarly, the study of time-intensive geoelectrical surveys to couple below and above-ground information necessitated the very controlled environment of the Field Scanalyzer. It should be noted that the experiments in the facilities presented here have all a broader agronomical aims and were not solely designed for testing the capabilities of time-lapse geophysics. Nevertheless, the range of field-sites explored with different soils, crops and agricultural practices constitute a valuable source of diverse agricultural environments to study the capabilities of time-lapse geophysical monitoring. They also demonstrate the collaboration effort of various actors in maintaining and monitoring such a diverse range of field facilities.

Some facilities were focused on different agricultural practices such as the use of cover crops or different tillage treatments with multiple nitrogen fertiliser rates (Pastures experiment in 2019) that are susceptible to impact the root zone soil moisture dynamics. The impact of traffic-induced compaction, a common problem in agriculture due to the heavy machinery used, in particular at harvest time, was also investigated for potatoes (Cambridge experiment in 2018). To further explore the impact of field-heterogeneity on pedophysical relationships, a commercial wheat field trials was also used (Warren experiment in 2017). And to further investigate the link between below-ground and above-ground phenotyping traits, geophysical monitoring was conducted under the Field Scanalyzer field phenotyping platform (Scanalyzer experiment in 2019). Figure 3.1 shows the locations of the field-sites across the UK. Table 3.1 summarises the characteristics of the experiments. The following sections give an overview of the field facilities but more details on the experiments and the specific methods used are given in the following chapters.
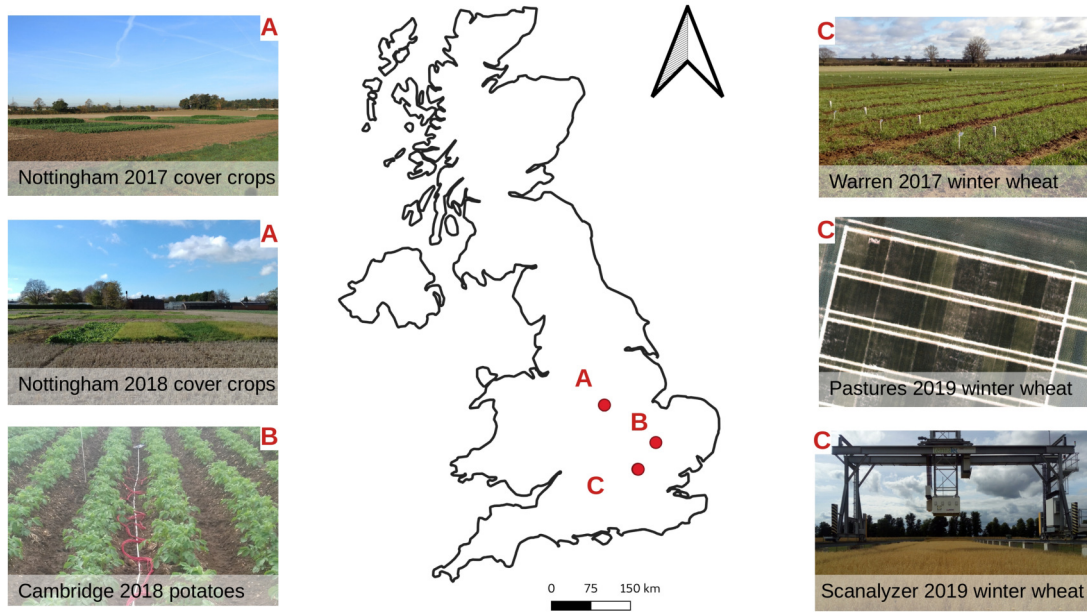
Figure 3.1 – Map of the different facilities used in this work.

Table 3.1 – Summary of the experiments.

Chapter	Experiment	Duration	Location	Crop	Soil	Treatment	Geophysical tools
4	Effect of short-term cover crops on water availability	Nov. 2016 – Jun. 2017	Nottingham, UK; 52°50'12.4"N 1°15'05.7"W	Cover crops	Cambisol (13.2% clay, 19.5% silt and 67.3% sand)	oil radish, tillage radish, forage rye, black oat, white mustard and Egyptian clover	Time-lapse EMI calibrated with ERT
4	Effect of long-term cover crops on water availability	Sep. 2017 – Sep. 2019	Nottingham, UK; 52°49'53.8"N 1°14'49.3"W	Cover crops	Cambisol	chicory, a mix of red clover and cocksfoot, lucerne (also called alfalfa) and cocksfoot; grown during one or two years	Time-lapse EMI calibrated with ERT
4	Effect of compaction and irrigation on potatoes	Jun. 2018 – Aug. 2018	Cambridge, UK; 52°14'13.4"N 0°05'57.9"E	Potato (Maris Piper)	Cambisol (sandy loam)	irrigation (full or deficit) and soil compaction (compacted or not)	Time-lapse ERT
4	Effect of tillage and nitrogen fertilisation on winter wheat	Dec. 2018 – Sep. 2019	Harpenden, UK; 51°48'28.6"N 0°22'23.6"W	Winter wheat	Luvisol (clayey loam)	0, 80, 140, 180, 220 kgN/ha; direct drill/ploughing	Time-lapse EMI calibrated with ERT
5	Heterogeneity of pedophysical relationship	Oct. 2016 – Jun. 2017	Woburn, UK; N, 52°01'06.5" 0°35'29.0"W	Winter wheat	Distric Cambisol (54% sand, 20% silt and 26% clay)	72 varieties	Time-lapse EMI calibrated with ERT
6	Time-intensive geophysical monitoring of winter wheat	Nov. 2017 – Aug. 2018	Harpenden, UK; 51°48'34.56"N, 0°21'22.68"W	Winter wheat	Luvisol (clayey layer with flints below the Ap (Batcombe))	4 varieties, no repetition	Time-lapse ERT
6	Time-intensive geophysical monitoring of winter wheat	Dec. 2018 – Sep. 2019	Harpenden, UK; 51°48'34.56"N, 0°21'22.68"W	Winter wheat	Luvisol (clayey layer with flints below the Ap (Batcombe))	2 varieties and 2 N levels (50 and 350 kgN/ha)	Time-lapse ERT

3.1   Warren 2017

This experiment aimed at comparing soil drying under different wheat varieties along the season. Regular soil moisture measurements (neutron probe), EMI and ERT data were collected away from rainfall events to ensure the soil drying measured was mainly driven by crop uptake. The experiment took place on a commercial field trials for wheat, as shown in Figure 3.2. It was composed of a 216 standard plots (9 m by 1.8 m) arranged in a random block design (3 blocks). The site was called Warren Field (Woburn, UK; 52°01'06.5"N, 0°35'29.0"W) and operated by Rothamsted Research. The soil at the site is classified as a sandy clay loam (Distric Cambisol with 54% sand, 20% silt and 26% clay (more details in Shanahan *et al.* (2015)). Each plot was equipped with a 1.5 m-long neutron probe access tube (for soil moisture measurement) situated at 1 m from the edge of each plot. A fallow plot was included in each block for reference. ERT arrays were installed in the middle of 12 specific plots (four wheat varieties, three replicates) at the beginning of the growth season and left in place until the harvest. EMI measurements were carried out using a CMD Mini-Explorer by taking three measurements down the middle of the plots, away from the access-tube. EMI measurements were averaged per plot. The data from an experiment on this facility are used in Chapter 5.

Figure 3.2 – Warren Field in March 2017 sown with winter wheat and managed by Rothamsted Research at Woburn UK. Access tubes for the neutron probe are visible at the nearer end of the plot.

3.2   Pastures 2018

Pastures experiment aimed to look at the impact of different tillage and nitrogen fertiliser treatments on wheat. Regular EMI measurements calibrated with ERT arrays aimed at providing an

overview of the below-ground processes taking place. Figure 3.3 shows the layout of the Pasture field (51°48'28.6"N 0°22'23.6"W) managed by Rothamsted Research (Harpenden, UK). The soil of the field is classified as a Luvisol (WRB) with a clayey loamy texture. Winter wheat (*Triticum aestivum* L.) was sown on 2018-10-03. The experimental setup is composed of five blocks of ten plots each (6 m by 9 m). Two tillage treatments (direct drill and conventional ploughing) and five different nitrogen fertiliser rates (0, 80, 140, 180, 220 kgN/ha) were applied. ERT arrays were installed in four selected plots and monitored during the entire season. EMI measurements were collected on all the plots (three stacks per plot) at regular interval throughout the season. The data from the facility are used in Chapter 4.
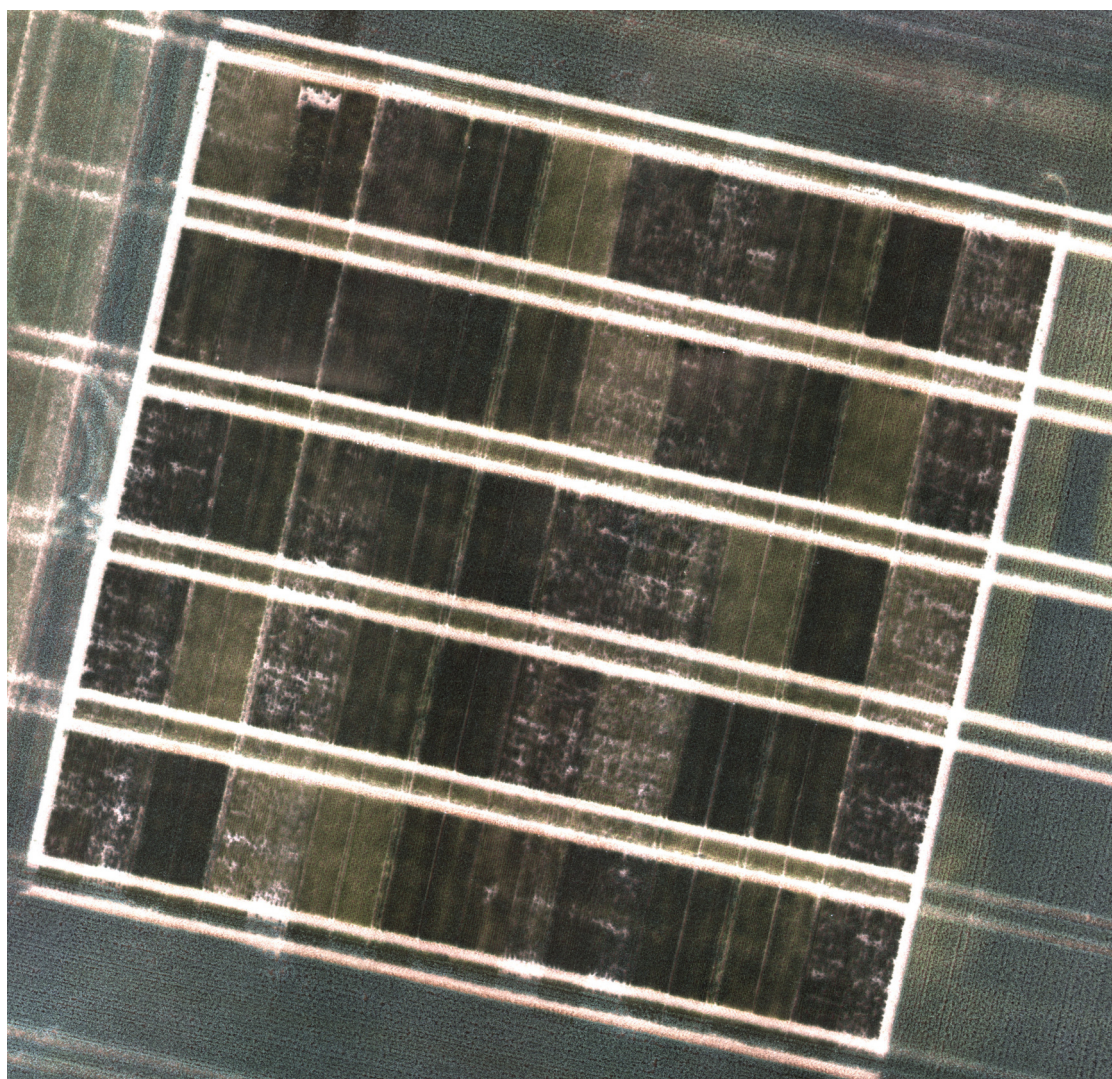
Figure 3.3 – Aerial view of Pasture field in summer 2019. Crop sown was winter wheat. More patchy plot usually belong to the direct drill treatment which has a lower germination rate. The different tones of green are related to the amount of nitrogen fertiliser applied.

3.3   Cambridge potatoes trial 2018

The experiment was managed by NIAB Agronomy Centre (52°14'13.4"N 0°05'57.9"E) in Cambridge UK in 2018 and aimed at looking at the effect of compaction and irrigation on the growth of potatoes. Time-lapse ERT measurements were performed to provide an image the soil moisture dynamics between two dates. The soil is defined as a sandy loam Cambisols (WRB). Two different treatments were applied: compaction/no compaction and abundant irrigation (wet) /deficit irrigation (dry). The experiment was composed of four blocks of sixteen plots (3 m by 4.5 m, 4.5 by 4.5 m with guard rows) planted with the potatoes (*Solanum tuberosum* L.) Maris Piper variety at a density of 180 tubers per plot on 4 rows (15 plants per row). There was two discard rows between the plots. ERT measurements were collected using 24 electrodes (0.5 m spacing) placed between the ridges (Figure 3.4) twice during the growth season. The data from this experiment are used in Chapter 4.

Figure 3.4 – Electrical resistivity array (24 electrodes, 0.5 m spacing) between the ridges of potatoes in June 2018.

3.4   Nottingham cover crop 2017

This experiment looked at the impact of cover crops on the water availability of sugar beets. Regular EMI measurements calibrated with ERT were collected during the season to get insights on the soil moisture dynamics. The experiment was sown in September 2016 at Nottingham Sutton Bonington campus (52°50'12.4"N 1°15'05.7"W) on a Cambisol (WRB) with a texture

of 13.2% clay, 19.5% silt and 67.3% sand. Eight different cover crops were tested: oil radish (*Raphanus sativus* L.), tillage radish (*Raphanus sativus* L.), forage rye (*Secale cereale* L.), black oat (*Avena strigosa* Schreb.), white mustard (*Sinapsis alba* L.) and Egyptian clover (*Trifolium alexandrinum* L.). An additional bare soil plot was added to the treatments for comparison. A random block design with 4 blocks and 8 plots (3 m by 7.5 m) per block was used. The cover crops were mown in December 2016 and sugar beet was sown in spring 2017 using direct drill. Figure 3.5 illustrates the state of the experiment autumn 2016. The experiment was monitored using EMI (three stacks per plot) and an ERT array was used for calibration of the EMI data. The data from this experiment are used in Chapter 4.

Figure 3.5 – Picture of the cover crops experiment in autumn 2016.

3.5 Nottingham long-term cover crop 2018

This experiment also looked at the impact of cover crops on soil moisture availability but in addition, the effect of long-term and short-term cover crops were also compared. The experiment took place at Nottingham Sutton Bonington (UK) campus (52°49'53.8"N 1°14'49.3"W), in a field close to the 2017 experiment, also classified as Cambisol. The experimental design was composed of four blocks with 10 plots per block (12 m by 3 m). Four different cover crops were grown: chicory (*Cichorium intybus* L.), a mix of red clover (*Trifolium repens* L.) and cocksfoot (*Dactylis spp* L.), lucerne (also called alfalfa) (*Medicago sativa* L.) and cocksfoot. An additional bare soil treatment is also added to the treatments for comparison. The five treatments were applied in half of the plots in September 2017 and left to grow during the entire season. In September 2018,

the treatments were applied to the remaining plots. In March 2019, the cover crops of all plots were destroyed and sugar beet were drilled directly (no tillage). Figure 3.6 shows the experiment in October 2018. The experiment was monitored using EMI (three stacks per plot). Time-lapse ERT was used for EMI calibration. The data from this experiment are used in Chapter 4.

Figure 3.6 – Picture of the long-term cover crop experiment in October 2018.

3.6   High Throughput Phenotyping Platform (HTPP) 2019

The experiment conducted in 2019 under the Field Scanalyzer platform aimed at observing the response of different winter wheat varieties to different nitrogen levels. In addition, to the wealth of above-ground measurements provided by the automated platform, time-intensive time-lapse ERT measurements were collected on a subset of plots to investigate how above- and below-ground information could be related. The outdoor facility is situated in Rothamsted Research, UK (51°48'34.56"N, 0°21'22.68"W) in Great Field. The platform covers an area of 0.12 ha and the soil underneath is classified as a Luvisol (WRB). It is composed of a loamy top layer (0.3 m) over a more clayey layer with flints (Batcombe). This second layer can impede the drainage, especially close to the railings, more subject to compaction during the platform construction. Two experiments were conducted with winter wheat (*Triticum aestivum* L.) during the growing season in 2017–2018 and 2018–2019 under rainfed conditions. Both experiment where monitored using ERT arrays running down each plot (more details in Chapter 6). Above-ground data were collected by the automated platform (Virlet *et al.*, 2017). Specifically, RGB pictures were

collected using a Prosilica GT3300 (Allied Vision 3296 x 2472 pixels) to estimate the canopy cover. Height information was capture from 3D cloud points measured using a laser scanner (Fraunhofer Institute). Figure 3.7 shows the Field Scanalyzer facility in July 2017 with a previous experiment. The data from this experiment are used in Chapter 6.

Figure 3.7 – The Field Scanalyzer platform at Rothamsted Research in July 2017. The Scanalyzer is composed of a remotely controlled moving gantry and a box containing a range of sensors (thermal camera, RGB camera, laser scanner, fluorescence camera) that allows automated hight-throughput collection of above-ground plant traits. The crop under the platform is oat.

Chapter 4

Time-lapse geophysical assessment of agricultural practices on soil moisture dynamics

G. Blanchy[1,2], C. W. Watts[2], J. Richards[3], J. Bussell[formerly3,4], K. Huntenburg[1], D. Sparks[3], M. Stalham[5], M. J. Hawkesford[2], W. R. Whalley[2], A. Binley[1]

[1] Lancaster University, Lancaster, Lancashire LA1 4YW, UK

[2] Rothamsted Research, Harpenden, Hertfordshire AL5 2JQ, UK

[3] University of Nottingham, Nottingham, Nottinghamshire NG7 2RD, UK

[4] The Game & Wildlife Conservation Trust, Allerton Project, Loddington, Leicestershire LE7 9XE, UK

[5] NIAB CUF, Cambridge, Cambridgeshire, CB3 0DL, UK

Authorship statement

The PhD author and Chris Watts collected the geophysical data on the Pastures experiment. The PhD author processed the data for all experiments and wrote the manuscript. Other co-authors provided additional (non-geophysical) data and feedback on the manuscript. Andrew Binley and Richard Whalley provided additional ideas for the paper and edits on the manuscript.

Abstract

Geophysical surveys are now commonly used in agriculture for mapping applications. High-throughput collection of geophysical properties such as electrical conductivity (inverse of resistivity), can be used as a proxy for soil properties of interest (e.g. moisture, texture, salinity). Most applications only rely on a single geophysical survey at a given time. However, time-lapse geophysical surveys have greater capabilities to characterize the dynamics of the system, which is the focus of this work. Assessing the impact of agricultural practices through the growth season can reveal important information for the crop production. In this work, we demonstrate the use of time-lapse electrical resistivity tomography (ERT) and electromagnetic induction (EMI) surveys through a series of three case studies illustrating common agricultural practices (cover crops, compaction with irrigation, tillage with nitrogen fertilization). In the first case study, time-lapse EMI reveals the initial effect of cover crops on soil drying and the absence of effect on the subsequent main crop. In the second case study, compaction, leading to a shallower drying depth for potatoes was imaged by time-lapse ERT. In the third case study, larger change in electrical conductivity over time were observed in conventional tillage compared to direct drill using time-lapse EMI. In addition, different nitrogen application rates had significant effect on the yield and leaf area index but only ephemeral effects on the dynamics of electrical conductivity mainly after the first application. Overall, time-lapse geophysical surveys show great potential for monitoring the impact of different agricultural practices that can influence crop yield.

4.1   Introduction

Geophysical methods such as electromagnetic induction (EMI) and electrical resistivity tomography (ERT) are increasingly being used for agricultural applications. ERT enables the generation of an image of the electrical resistivity of the subsurface from measurements made using electrodes in contact with the ground. In contrast, EMI senses the electrical conductivity (the inverse of resistivity) of the ground through inductive signals and thus does not require galvanic contact with the subsurface. Originating, in part, from the mineral and oil exploration industries (Schlumberger, 1920), ERT is now widely used for many shallow near-surface applications. EMI has proved effective for soil salinity mapping (Corwin & Lesch, 2005). It has since been widely used for mapping different soil properties (Doolittle & Brevik, 2014), defining management zone in agriculture (Hedley et al., 2004) or assessing soil structure (Romero-Ruiz et al., 2018). More recently the development of multi-coil EMI instruments has enabled simultaneous measurements at multiple depths, enabling the recovery of the distribution of electrical conductivity of the subsurface as in ERT.

Understanding the availability and movement of water in the ground has become a signif-

icant driver for many geophysical studies and has led to the field of hydrogeophysics (Binley et al., 2015). Geophysical methods have the capability to characterize properties of soil that influence the flow and storage of soil water making such methods relevant for plant-related application (Jayawickreme et al., 2014; Shanahan et al., 2015; Whalley et al., 2017; Zhao et al., 2019; Cimpoiaşu et al., 2020). For more information on other geophysical methods, we redirect the reader to the review of Allred et al. (2008) who illustrate a range of geophysical applications in agriculture, and the broader overview of geophysical methods for proximal soil sensing given by Viscarra Rossel et al. (2011). These reviews focus on static surveys for assessment of soil properties and states, however, there is much greater potential for geophysical methods for characterizing the dynamic state of the subsurface, which is the focus of this study.

Soil and water are essential resources for agriculture. However, these resources are endangered by intensive agricultural practices which can impact food security (Amundson et al., 2015). Loss of soil structure due to tillage or compaction can substantially affect the plant water availability and nutrients uptake and impact crop growth. Conservation agriculture practices aim at addressing some of these specific issues and improve and sustain crop production. The FAO (http://www.fao.org/conservation-agriculture/en/) define three axes for conservation agriculture: (1) minimum mechanical soil disturbance, (2) permanent soil organic cover and (3) species diversification. The case studies presented in this work concentrates on (1) and (2). More specifically, this paper focuses on the agricultural practices: compaction with irrigation, tillage with nitrogen fertilization and cover crops. This work does not aim at exhaustively detailing each practice but rather at assessing the potential of two popular geophysical methods (ERT and EMI) at monitoring the effects of these different management practices on soil properties and soil water status.

Traffic-induced soil compaction can be significant in certain (mainly loamy) soils as the compaction occurs in deeper layers. Over short time scales, compaction reduces the soil porosity making it more difficult for the roots to penetrate and access water stored in the soil (Keller et al., 2013), potentially impacting the effectiveness of irrigation practices. We redirect the reader to Hamza & Anderson (2005) and Batey (2009) who review the different agricultural impacts of soil compaction. Soil compaction can also have long-term effects (Keller et al., 2017).

Tillage, conventionally moldboard plowing increases the soil porosity but worsens the soil structure. Direct drilling (zero-tillage) offers an alternative to conventional tillage as it prevents major disruption of the soil structure. The structure of the soil plays a key role in making water and nutrients available to the crop and hence can affect crop productivity. While tillage has other major implications for the biological activity of the soil (Hobbs et al., 2008), the case study presented in this manuscript focuses on the comparison of plowing and direct drill treatments on the soil moisture dynamics and nitrogen uptake.

Cover crops, usually sown in a sequence with the main cash crop, have many benefits. They

can improve the soil structure, increase the availability of organic matter and also prevent the loss of nutrients to depth, among other advantages (Fageria *et al.*, 2005). Deep rooting cover crops can increase the porosity of the soil, hence potentially improving the water availability for the main crop.

The impact of these practices on the agricultural ecosystem is often assessed using small sampling volumes over a short time-window. Some methods, such as soil coring or installation of access tubes for soil moisture probes can be destructive for the crop and the soil. In contrast, geophysical methods such as ERT and EMI are minimally invasive and enable repeated measurements without disturbing the growth of the crop. The other significant advantages of geophysical methods are their large sampling volume and their high-throughput data collection making them well suited to study field-scale processes.

All these advantages make geophysical methods attractive for obtaining a quick single scan survey of the field. This single mapping approach is widely used today and even commercially available for obtaining a proxy textural map for precision agriculture. However, such an approach is not well suited to study highly dynamic soil-plant-water interactions. Instead of a single survey, we argue that geophysical time-lapse monitoring can bring more information about how the agricultural practices influence the soil-plant-water interactions and how this can impact crop productivity.

Through a series of case studies, this manuscript aims to demonstrate the potential of time-lapse geophysical investigation to better understand the impact of these practices on the soil moisture dynamics. Specifically, the manuscript aims to:

- highlight the potential of time-lapse geophysical surveys to assess conservation agricultural practices;

- detail the current limitations of the approach;

- provide recommendations on the use of time-lapse geophysical monitoring.

4.2   Materials and methods

4.2.1   Geophysical properties

Geophysical methods measure geophysical properties which are then linked to soil properties of interest using pedophysical relationships (Archie, 1942; Waxman & Smits, 1968; Rhoades *et al.*, 1976; Laloy *et al.*, 2011; Wunderlich *et al.*, 2013). ERT measures the soil electrical resistivity using galvanic coupling and EMI measures the soil electrical conductivity (EC) using inductive coupling. The soil EC (or resistivity) is influenced by many factors such as soil temperature, soil moisture, pore water EC, soil texture and porosity. This makes the interpretation of EC values

challenging as the user needs to identify the dominant factor influencing EC for a given site and account for effect of the other ones. This also emphasizes the need for site-specific relationships (e.g. Calamita *et al.*, 2015).

The time-lapse approach can help here as some factors are usually relatively constant during the survey time such as soil texture and porosity. Soil temperature can be corrected for (Ma *et al.*, 2011) and in a non-saline rainfed environment the EC of the pore water can often be assumed to remain constant except when fertilizers or other chemicals are applied. Thus, the soil moisture is often the main factor controlling the change in EC observed over the growing season of a crop.

4.2.2   Electrical resistivity tomography

Electrical resistivity tomography uses multiple electrodes to measure the distribution of the electrical resistivity of the subsurface. In the case studies of this manuscript, all electrodes are located on the surface, but other configuration might involve borehole electrodes, hence increasing the sensitivity of the measurements at depth. ERT measurements are made using four electrodes: a quadrupole. Current is injected between two electrodes and the difference in electrical potential is measured between the other two. Each measurement provides an apparent resistivity, i.e. the resistivity of an equivalent homogeneous subsurface. Given multiple combinations of current and potential electrodes along a transect, a 2D image of the true resistivity can be reconstructed using inverse modeling (Binley, 2015). For a more detailed review on ERT methods in soil science, the reader is directed to Samouëlian *et al.* (2005).

4.2.3   Electromagnetic induction

EMI instruments use electromagnetic induction principles to measure the apparent electrical conductivity (ECa) of the subsurface. By making measurements with different induction coil spacing and/or orientation, it is possible to sense different depths of the subsurface, and thus like ERT, inverse methods can used to convert the apparent conductivity measurements to a depth profile of electrical conductivity (McLachlan *et al.*, 2020b; von Hebel *et al.*, 2019). The instrument used in this study is the CMD Mini-Explorer (GF Instruments, Czech Republic), which is composed of one transmitter coil and three receiver coils and can be used in horizontal co-planar (HCP) or vertical co-planar (VCP) orientation. When measuring, the transmitter coil emits a primary time-varying electromagnetic field that induces eddy currents proportional to the ground EC. These eddy currents, in turn, induce a secondary electromagnetic field. Both primary and secondary electromagnetic fields are sensed by the receiver coils. From their ratio, a depth-weighted, "apparent", electrical conductivity (ECa) can be derived. The larger the separation between the transmitter and the receiver coil, the deeper the volume investigated.

The combination of HCP/VCP orientations and the three coils separations enables the collection of up to six data points per sampling location with the CMD Mini-Explorer. In the rest of the manuscript coil configuration will be presented as VCP0.32 with VCP the orientation and 0.32 the coil separation in meters. We redirect the reader to Callegary *et al.* (2007) for more information on the specific aspects of EMI measurements. The inverted change in EC profiles presented in this manuscript were obtained using a Gauss-Newton approach following Whalley *et al.* (2017), implemented in the open-source code EMagPy (McLachlan *et al.*, 2020a).

The ECa maps provided by the EMI instruments are often qualitative, showing areas of higher EC and lower EC. While this does not have any impact for mapping applications, its effect is significant for quantitative application. Different methods exist to calibrate apparent EMI values based on independently measured depth profiles of EC. Trenches and soil samples can be used to build an EC depth profile. In this study, EMI calibration was done using the inverted EC values from an ERT transect (Lavoué *et al.*, 2010; von Hebel *et al.*, 2014). Other methods such as using multi-elevation measurements have also been proposed to calibrate EMI data (Tan *et al.*, 2019). von Hebel *et al.* (2019) review the best practices for calibration, conversion and inversion of EMI data.

4.2.4 Time-lapse approach

A one-time geophysical survey is useful for assessing the static soil properties but when assessing dynamic states, such as soil moisture, the time-lapse approach is more appropriate. The time-lapse approach consists of multiple surveys taken at different times during the period of interest, e.g. the growing season of a crop. A reference survey, usually chosen as a 'wet' or 'dry' reference, is subtracted from the other surveys to obtain a change in EC. This way, static effects on soil EC (e.g. from texture) is accounted for and only the dynamic part of the EC is analyzed. In non-arid conditions, one of the major drivers of the change in EC observed through the season is the change in soil moisture. Since rainfall events can induce sudden increases in soil moisture, when surveys are focused on assessing changes due to evapotranspiration field measurements should be conducted following significant rainfall events to avoid sensing localized changes in soil moisture.

Note that the EC (and hence resistivity) is sensitive to temperature and hence a temperature correction is needed for proper interpretation of a time-lapse survey (Hayashi, 2004; Ma *et al.*, 2011). In this study, ECa values were corrected using:

$$EC_{25} = \frac{EC_T}{1 + 0.02 \times (T - 25)}, \tag{4.1}$$

where EC_{25} is the temperature corrected EC (at 25 degrees Celsius) and T is the soil temperature in degrees Celsius. When soil temperature profiles were available (all studies except the

compaction case), a depth-weighted temperature was computed using the cumulative sensitivity function of the EMI instrument (Blanchy *et al.*, 2020a). This 'apparent' temperature was then used in Equation 1 to correct the ECa values.

4.2.5   Experiments

To demonstrate the potential of time-lapse geophysics to study the impact of different agricultural practices, three case studies with different crops were selected (Figure 4.1). The first one focuses on the impact of cover crops on the soil moisture availability for the main crop (sugar beet). It also compares short-term and long-term cover crops (Figure 4.1a). The second case focuses on the impact of soil compaction with two different irrigation treatments on the water uptake of potatoes (Figure 4.1b). The third case explores the interactions between two types of tillage (moldboard plowing and direct drill) and different application rates of nitrogen fertilizer on winter wheat (Figure 4.1c).

Cover crops

Two experiments were carried out with cover crops aiming at assessing the impact on the cover crops on soil moisture availability for the main crop. Cover crops are usually sown in autumn after the harvest of the main crop. They are kept over the winter and, if needed, are destroyed in spring before sowing of the main crop. The hypothesis behind these experiments is that cover crops will improve the soil structure via its root system. The improved soil structure will then help the following cash crop (in this case: sugar beet, *Beta vulgaris* L.) to better access soil moisture. Time-lapse EMI was used to monitor the potential effect of the cover crops on the dynamics of soil moisture. The first experiment was sown with the different cover crops in September 2016 at Nottingham Sutton Bonington campus (52°50'12.4"N 1°15'05.7"W) on a Cambisol (WRB) with a texture of 13.2% clay, 19.5% silt and 67.3% sand. The cover crops were sown in a random block design of four blocks with eight plots (3 m by 7.5 m) per block. Seven different cover crops were tested: oil radish (*Raphanus sativus* L.), tillage radish (*Raphanus sativus* L.), forage rye (*Secale cereale* L.), black oat (*Avena strigosa* Schreb.), white mustard (*Sinapsis alba* L.) and Egyptian clover (*Trifolium alexandrinum* L.). An additional bare soil plot was also part of the treatments as a reference. The cover crops were destroyed in December 2016. Sugar beet was then established using direct drilling in spring of the following year and harvested in autumn. EMI data were collected using the CMD Mini-Explorer (GF Instruments, Czech Republic) on 2016-11-09, 2016-12-08 (a few days after the crop was destroyed), 2017-03-08, 2017-05-11 and 2017-06-22 (all dates expressed as ISO 8601).

The second experiment was sown with cover crops in September 2017 in a field near to the first experiment (52°49'53.8"N 1°14'49.3"W), also classified as Cambisol. Its aim was not
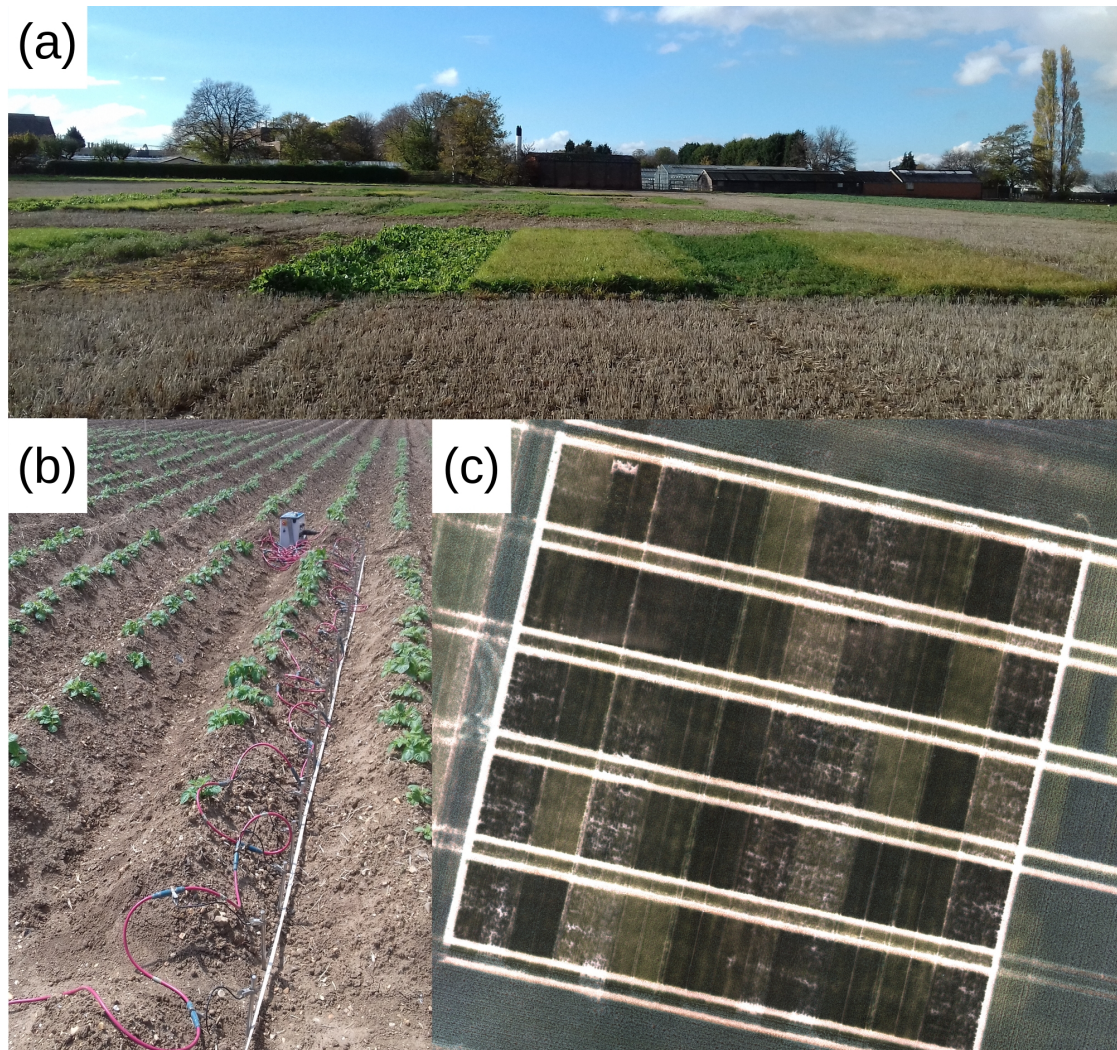
Figure 4.1 – (a) Long-term cover crop experiment (picture taken on 2018-10-29). (b) Compaction experiment on potatoes showing an ERT measurement taking place in a furrow. (c) Experiment on the effects of tillage and nitrogen treatment on winter wheat.

only to estimate the impact of cover crops on soil moisture availability but also to compare cover crops grown over the winter with cover crops in place for a full season. The experimental design was composed of four blocks with 10 plots per block (12 m by 3 m). Four different cover crops were tested: chicory (*Cichorium intybus* L.), a mix of red clover (*Trifolium repens* L.) and cocksfoot (*Dactylis* spp L.), lucerne (also called alfalfa) (*Medicago sativa* L.) and cocksfoot alone. An additional bare soil treatment was also added as a reference. In September 2017, the five cover crop treatments were applied to five plots inside each block. Wheat was grown on the unattributed plots. In September 2018, after the wheat had been harvested, the five treatments were applied on the remaining plots. As such, each block contained two plots with the same treatment, but one was in place since September 2017 and one since September 2018. Figure 4.1a shows the experiment in October 2018. At the beginning of March 2019, the cover crops were destroyed, and sugar beet was sown using direct drilling. Sugar beet was harvested in autumn 2019. EMI data were collected on 2017-10-25, 2017-12-08, 2018-03-26, 2018-06-19, 2018-08-01, 2018-10-29, 2019-03-11, 2019-05-14, 2019-06-04, 2019-07-03 and 2019-09-10. EMI data were calibrated using ERT lines collected in another experiment nearby following Lavoué *et al.* (2010).

Compaction and irrigation

A compacted soil can potentially impede root water extraction and hence lead to water stress for some crops. In this experiment, the impact of soil compaction and irrigation is explored on potatoes. The compaction experiment took place in a field managed by the NIAB Agronomy Centre (52°14'13.4"N 0°05'57.9"E) in Cambridge UK in 2018. Two different treatments were applied: compaction/no compaction and frequent irrigation (wet) /severe deficit irrigation (dry). The experiment was composed of four replicate blocks (16 plots; each 3 m by 4.5 m) planted with potatoes (*Solanum tuberosum* L.), cultivar Maris Piper, at a density of 180 tubers per plot in four rows (15 plants per row). Two extra rows were used as irrigation barriers between the plots. The soil was a sandy loam (67% sand, 27% silt, 13% clay, 2.9% organic matter) Cambisol (WRB). The compaction treatment was applied by successive passes of a tractor-drill-cultivator combination with high pressure, row-crop tyres on soil irrigated to field capacity before the formation of the ridges for tuber plantation. An ERT array of 24 electrodes (0.25 m electrode spacing) was used to collect resistivity transects on all plots of block 3 by putting the electrodes in the furrows between the ridges (Figure 4.1b). ERT data were collected on 2018-06-12 and 2018-08-03. ERT data were inverted with a background constrained approach using ResIPy (Blanchy *et al.*, 2020b) that makes use of the R2 inverse code (Binley, 2015).

Tillage and N treatments

The experiment aims at analyzing the impact of tillage and nitrogen fertilizer application on the growth of winter wheat and the associated soil moisture dynamics. It took place in a field, named "Pastures" (51°48'28.6"N 0°22'23.6"W) managed by Rothamsted Research (Harpenden, UK). The soil of the field is classified as a Luvisol (WRB) with a clayey loamy texture. On 2018-10-03, the experiment was sown with winter wheat (*Triticum aestivum* L.). The experimental setup is composed of five blocks of ten plots each (6 m by 9 m). Two tillage treatments (direct drilling and conventional plowing) and five different nitrogen fertilizer rates (0, 80, 140, 180, 220 kg N/ha) were applied by hand to each plot in two equal splits on 2019-03-04 and 2019-04-23. The tillage treatment was applied in bands across all the blocks while the nitrogen fertilizers were randomly applied to each plot within a block (Figure 4.1c). ERT arrays (24 pins, 0.25 m electrode spacing) were installed in four selected plots in the experiment to calibrate EMI measurements following (Lavoué *et al.*, 2010). ERT measurements were collected on 2019-02-05, 2019-04-05, 2019-05-07, 2019-05-24, 2019-06-06, 2019-06-18, 2019-07-09, 2019-07-22 and 2019-08-05. EMI measurements using the CMD Mini-Explorer were collected on 2018-12-07, 2019-02-05, 2019-03-01, 2019-03-04, 2019-03-05, 2019-03-07, 2019-03-11, 2019-03-13, 2019-03-21, 2019-04-05, 2019-04-15, 2019-04-30, 2019-05-07, 2019-05-20, 2019-06-06, 2019-06-18, 2019-07-09, 2019-07-22 and 2019-08-05. The field had a large variability with ECa values ranging from 20 to 45 mS/m. Analysis of variance (ANOVA) was used to detect significant differences ($p < 0.05$) between the treatments.

Table 4.1 summarizes the different experiments, instrument used and processing steps.

Table 4.1 – Summary of the experiments, devices used and processing steps performed.

Experiments	Devices	Processing steps
Impact of cover crops on soil moisture availability	EMI calibrated with ERT	1. inversion of ERT transects 2. calibration of EMI data with inverted ERT (Lavoué *et al.*, 2010) 3. temperature correction of calibrated ECa (Ma *et al.*, 2011) 4. computing ΔECa from reference 2017-07-22 5. inversion of ΔECa (Whalley *et al.*, 2017)
Impact of compaction and irrigation on potatoes water uptake	ERT	1. inversion of ERT transects 2. temperature correction of the inverted profiles (Ma *et al.*, 2011) 3. computing ΔECa from reference 2019-03-11
Impact of tillage and nitrogen fertilization on soil drying under winter wheat	EMI calibrated with ERT	1. inversion of ERT transects 2. calibration of EMI data with inverted ERT (Lavoué *et al.*, 2010) 3. temperature correction of calibrated ECa (Ma *et al.*, 2011) 4. computing of ΔECa from reference 2018-06-12

4.3 Results

4.3.1 Cover crops

Figure 4.2 shows the evolution of the soil ECa (both apparent Figure 4.2a and inverted Figure 4.2b, c and d) for three selected cover crops and the bare soil treatment in 2016-2017. There is clear difference in ECa in November 2016 with higher values implying greater soil moisture content. The plots with tillage radish and white mustard exhibit significantly lower apparent

conductivity than the bare soil or the vetch treatments. After the cover crops were destroyed (mowed) in December 2016, this difference is still visible, but starts to reduce. Finally, in March 2017, there is no difference between the bare soil and the cover crops treatments. Similar interpretation can be made using the profiles (Figure 4.2b, c and d) of inverted change in conductivity (changes are expressed from July 2017). There are differences between the bare soil and the cover crops in November 2016 which tend to reduce in December 2016 and vanish in March 2017.
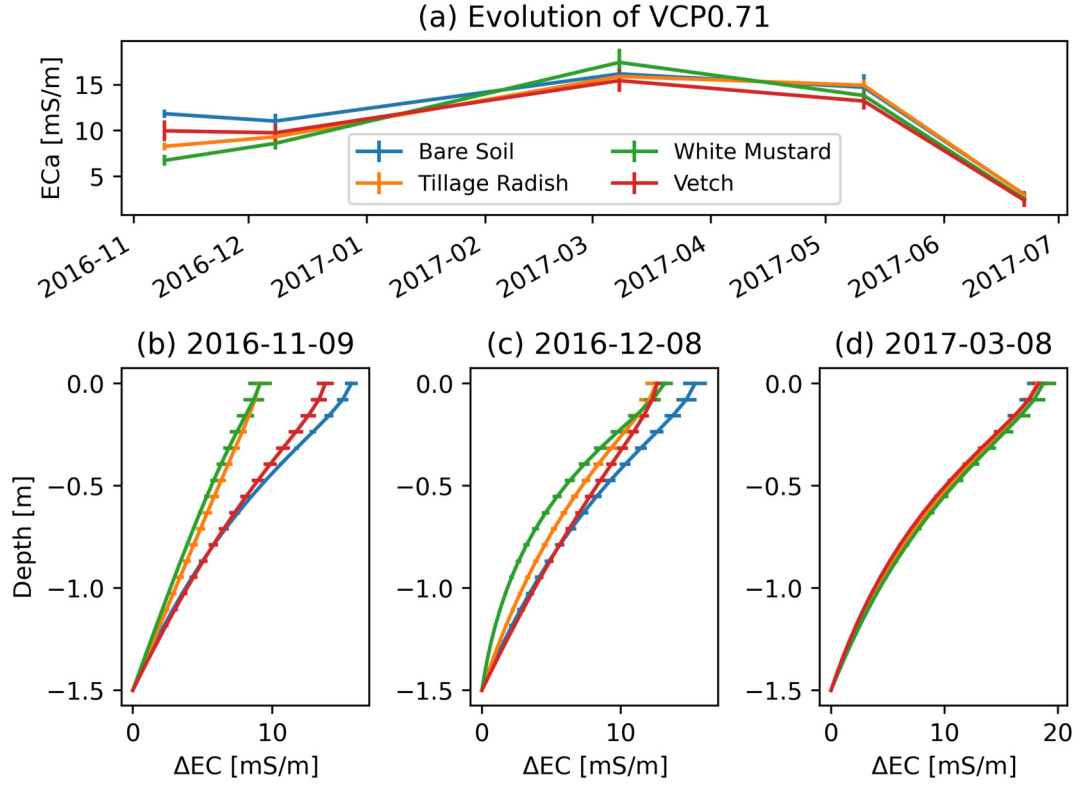
Figure 4.2 – (a) shows the evolution of the apparent electrical conductivity (ECa) for four selected treatments: bare soil, tillage radish, white mustard and vetch. (b), (c) and (d) shows the inverted change in electrical conductivity (ΔEC) for three different dates. The inverted changes are computed as differences with respect to 2017-07-22 (dry reference).

Figure 4.3b shows the evolution of the ECa for the long-term cover crop experiment expressed as differences relative to 2018-03-11. Given the amplitude of the signal in Figure 4.3b, for each survey date (t), we averaged all differences (ΔECa_t which are still differences from 2018-03-11) from all treatments to form the mean difference ($\Delta \bar{EC}a_t$). For each survey date, this mean was then subtracted from the difference for each treatment. This allows easier comparison between treatments (Figure 4.3c):

$$\Delta ECa_{i,t} - \Delta \bar{EC}a_t = \Delta ECa_{i,t} - \frac{1}{N}\sum_{i=0}^{N}\Delta ECa_{i,t}, \qquad (4.2)$$

where t is the index of the survey, i is the index of the treatment, N is the number of treat-

ments, $\Delta ECa_{i,t}$ represents the differences relative to 2018-03-11 for treatment i at survey date t, and $\Delta \bar{EC}a_i$ is the mean encompassing all treatments for the survey t. Thus, Figure 4.3c removes the seasonal trend of Figure 4.3b and enhances the difference between treatments inside the same survey. The date 2019-03-11 was chosen as a reference because it is the date with minimal effects of the treatments and most homogeneous ECa, all cover crops having been destroyed in the beginning of March. Figure 4.4 supports Figure 4.3 by showing subplots of differences in ECa for all varieties. Figure 4.3 and Figure 4.4 show data from VCP0.71 (the coil configuration that appears to be the most sensitive to the root zone). However, similar trends, albeit less strong for other coil configurations, can also be observed. Both short-term (sown in September 2018) and long-term (sown in September 2017) cover crops show a significant difference compared to the bare soil treatments (2018-06-19, 2018-08-01, 2018-10-29 in Figure 4.4). This can be seen over the summer of 2018 (Figure 4.3a). The long-term cover crops also tend to show a larger difference in ECa compared to the short-term cover crops (2018-10-29 in Figure 4.4). For the long-term chicory and lucerne, two deep rooting cover crops, this difference stays significant even in June and July 2019 but not for their short-term equivalent. Note that the magnitude of this difference is relatively small (about 2 mS/m) and hence, does not represent a large difference in soil moisture (only a few percent). The other shallower rooting cover crops, such as the red clover and cocksfoot, do not show any effect in June or July 2019 for both short and long-term variants.
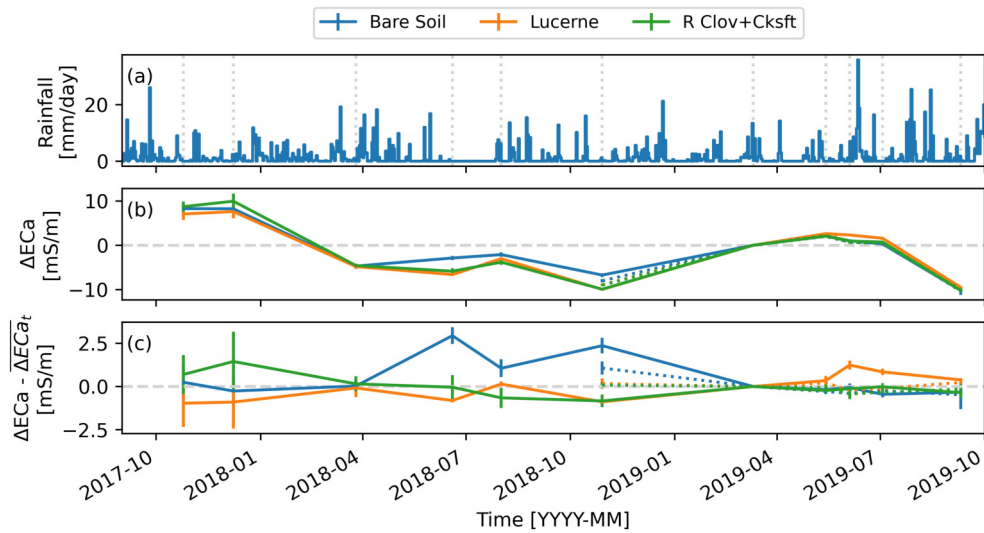
Figure 4.3 – Evolution of the difference in apparent electrical conductivity of VCP0.71 for bare soil, lucerne and red closer + cocksfoot (R Clov + Cksft) treatments in place for one-year (dotted lines) and two years (solid lines). (a) shows the daily rainfall. (b) shows the difference in apparent electrical conductivity compared to the reference date 2019-03-11. To make the difference between treatments more visible, the average difference for all treatments is computed for each survey ($\overline{\Delta ECa_t}$) and is subtracted from (b) leading to (c). Error bars represent the standard error of the mean.
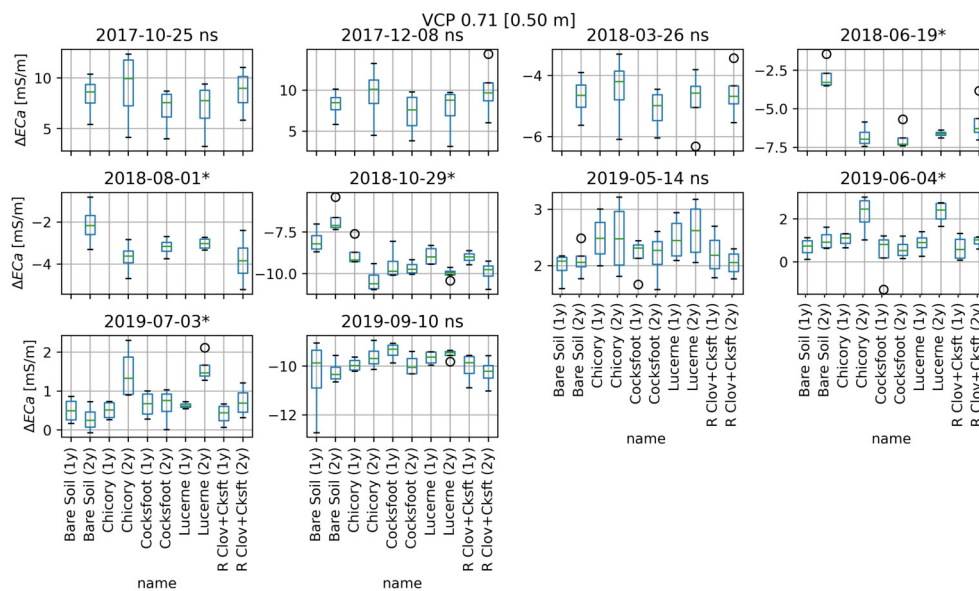
Figure 4.4 – Subplots of boxplots showing the differences in apparent electrical conductivity (ΔECa) compared to the reference date 2019-03-11. Long-term cover crops are indicated by (2y) and short-term by (1y). A star on top of the graph shows that there are significant differences (p<0.05) from an ANOVA test between the treatments. Non-significant results are denoted by 'ns'. Each subplot has its own vertical scale.

4.3.2   Compaction and irrigation

After inverting each survey, the difference in resistivity from June 2018 to August 2018 ($\Delta\rho$) is computed and divided by the resistivity of the first survey taken on 2018-06-12 (ρ_0) to obtain a relative difference. Figure 4.5 shows the relative difference in inverted resistivity ($\Delta\rho/\rho_0$ expressed as percentage) sections with yellow area associated with an increase in resistivity (drying) and blue area associated with a decrease in resistivity (wetting). All sections show a larger positive change, probably associated with soil drying close to the surface, extending no deeper than 0.7 m. The compacted wet treatment shows the shallowest drying by the crop, while the non-compacted treatments exhibits deeper drying. Figure 4.5a and c also clearly show the depth of drying is limited, probably by the compaction, compared to non-compacted treatments (Figure 4.5b and d). No treatments showed any major differences in resistivity deeper than approximately 1.5 m depth.
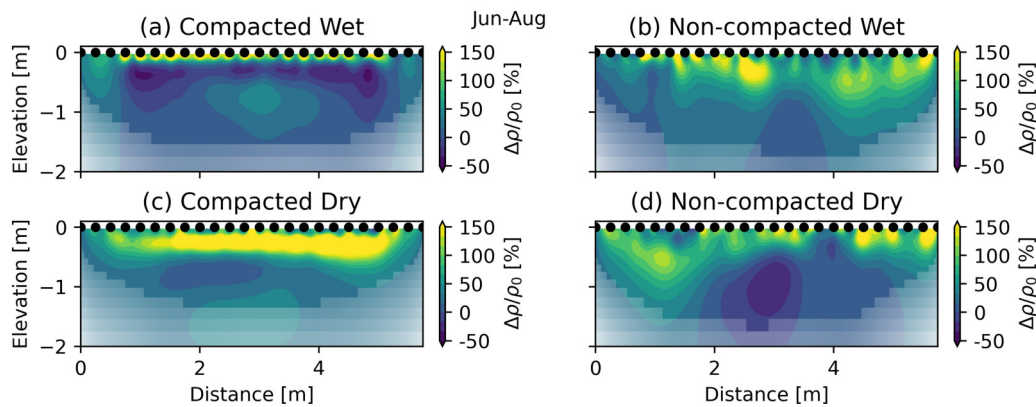
Figure 4.5 – Relative change in inverted resistivity ($\Delta\rho/\rho_0$) section between 2018-06-12 and 2018-08-03 showing the different treatments: (a) compacted wet, (b) non-compacted wet, (c) compacted dry and (d) non-compacted dry. Note that the resistivity is the inverse of the conductivity. The semi-transparent white overlay shows the sensitivity of the survey.

4.3.3   Tillage and nitrogen treatments

In October 2018, there was a significant ($p < 0.05$ by ANOVA) difference in absolute ECa between the plow and the direct drill treatments prior to any drying by the crops or application of N. The direct drill plots show a higher ECa compared to the plowed plots (data not shown). To remove the effect of this initial difference, the change in ECa is computed by subtracting the values measured on 2018-12-07 (reference date). Figure 4.6 shows that nitrogen levels only had a significant effect on ECa for a few days following the first fertilizer application where the ECa changes were correlated to the nitrogen rates (Figure 4.7). The nitrogen fertilizer increases the ECa proportionally to the application rates but because differences in ECa are used and there is a general ECa decrease throughout the season, the inverse relationship is observed. Despite

having no significant effect later on in the season, it can still be observed that the plots which did not receive additional nitrogen fertilizer (0 kg N/ha) are distinct from the other plots from May onwards in the plow treatment. This cannot be observed in the direct drill treatment. Figure 4.8 shows the main effect of tillage treatment. Both plow and direct drill treatments show a decrease through the season probably related to soil drying. We observe that the difference between direct drill and plow treatments increases after the second application of fertilizer for most EMI coil configurations, especially those which were more sensitive to deeper layers. These differences are not significant anymore after the 1st July. The nitrogen fertilizer rate had a significant impact on the yield (Figure 4.9). Nitrogen fertilizer was more effective at increasing yield in the plow treatment compared to the direct drill treatment, particularly at the higher rates of N. This effect is also seen in the development of the leaf area index (LAI) (Figure 4.10). Between mid-May and mid-June, the LAI in the direct-drill treatments continues to increase. In the plow treatments, the LAI reaches its maximum mid-May and does not substantially increase from mid-May to mid-June.
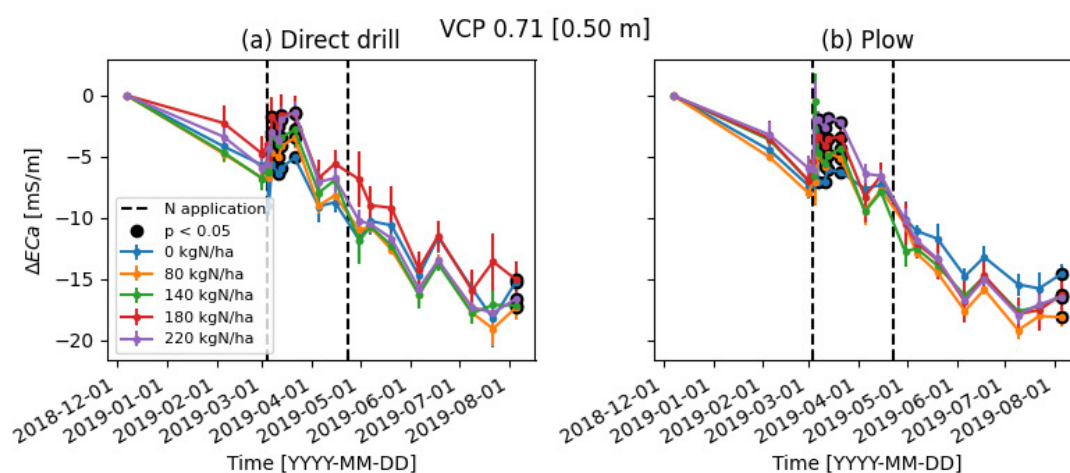
Figure 4.6 – Evolution of the differences in apparent conductivity (ΔECa) for VCP0.71 according to (a) direct drill and (b) plow treatment. The vertical dotted lines indicate when fertilizer was applied. Black dots show where the difference between the fertilizer treatments is significant (p < 0.05 by ANOVA). Error bars represent the standard error of the mean.
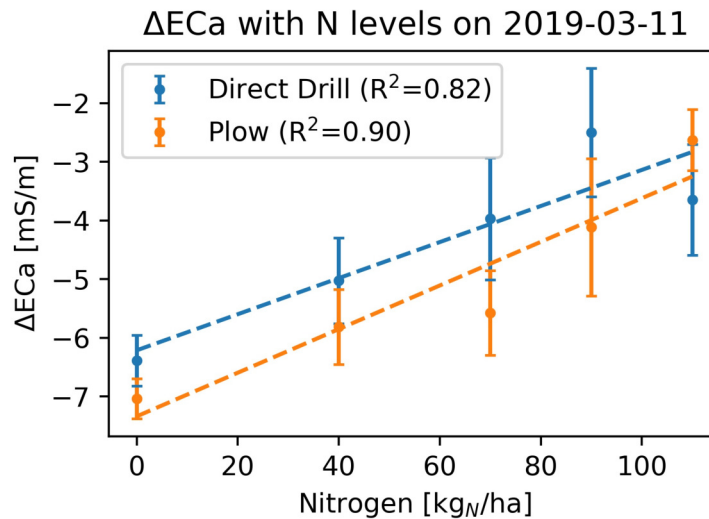
Figure 4.7 – Differences in apparent electrical conductivity (ΔECa) as a function of the amount of nitrogen after the first application (nitrogen applied on 2019-03-04). Note that differences are taken with respect to the reference date 2018-12-07 and not just before the nitrogen application. This is why large amount of fertilizer actually shows a smaller decrease in ECa as they compensate more the global ECa decreases from the reference date.
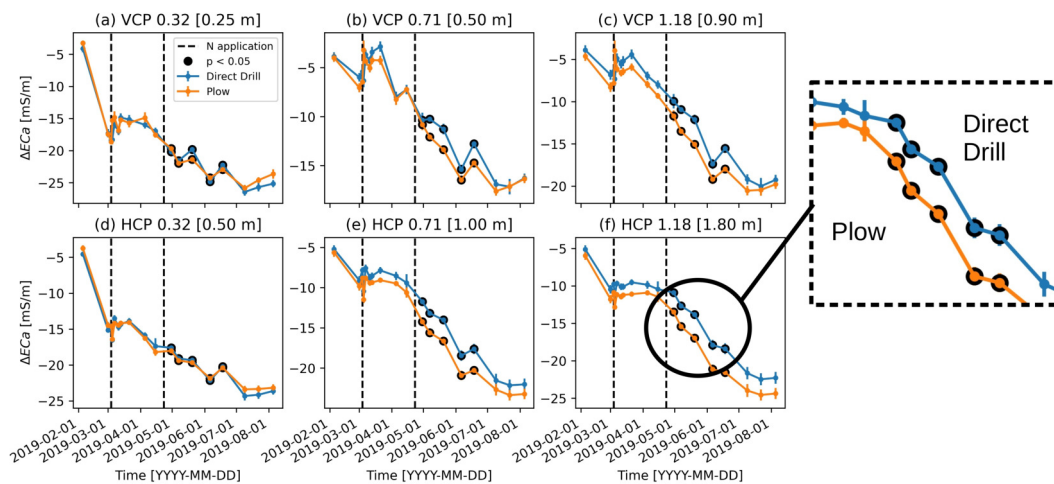
Figure 4.8 – Evolution of the differences in apparent electrical conductivity (ΔECa) with respect to the reference date 2018-12-07 for the six coil configurations of the CMD Mini-Explorer (a to f). All plots have been averaged between direct drill and plow treatment. Error bars represent standard error of the mean. Black dots show where the difference between direct drill and plow treatment is significant ($p < 0.05$ by ANOVA).
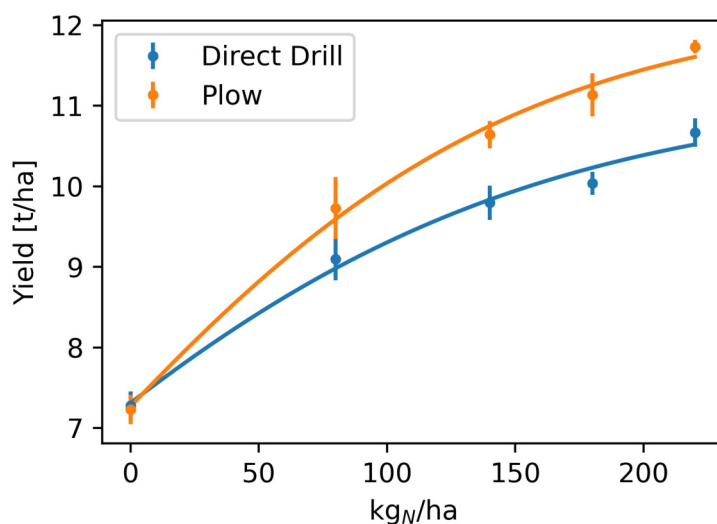
Figure 4.9 – Yield response to the amount of nitrogen fertilizer for the direct drill and plow treatments. Error bars represent the standard error of the mean. A sigmoid (a/(b+exp(-c*x + d))) has been fitted to both curves.
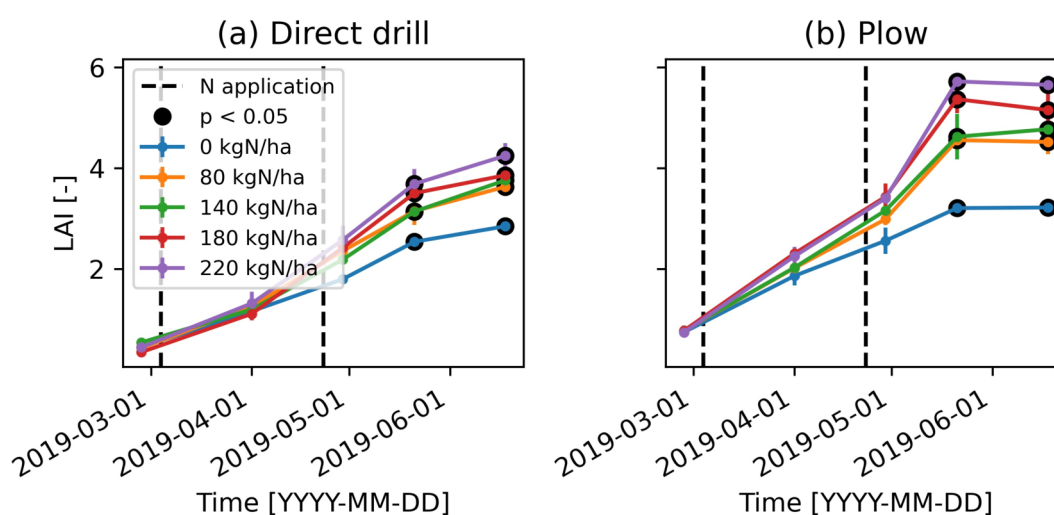
Figure 4.10 – Evolution of the leaf area index (LAI) between direct drill (a) and plow (b) treatments split by amount of nitrogen fertilizers applied. Black dots show where the difference between the fertilizer treatments is significant ($p < 0.05$ by ANOVA). Error bars represent the standard error of the mean.

4.4 Discussion

4.4.1 Capabilities

A single geophysical survey can be useful to map soil textural variation across the field and, in some cases, can be linked to soil moisture distribution (Calamita *et al.*, 2012). However, there is

little information on how it might impact crop productivity. Time-lapse geophysical surveys, in contrast, enable, to some extent, the removal the static effects of soil properties on the geophysical measurements. Changes in EC (or ECa), once temperature corrected, can then more easily be linked to changing states such as soil moisture or pore water ionic concentration. In the case-studies presented here, which took place in non-saline environments, we can reasonably link the changes in ECa to the changes in soil moisture due to crop-water uptake (evapotranspiration). We also observed that during short periods immediately following the application on mineral N, there was a sudden increase in EC probably due to an increase in pore water EC (Figure 4.6).

In the first case study, cover crops were found to have a significant effect compared to the bare soil in the first and second experiments. In November 2016, the tillage radish and white mustard had a larger effect than the vetch. However, after mowing, no more effect of the cover crops on the soil dynamics was observed. In the second experiment, both short-term and long-term cover crops show significant effect compared to the bare soil. Cover crops in place for two years tend to have a larger effect compared to cover crops grown for one season (Figure 4.4). After being cut down, most cover crop treatments do not show any difference compared to bare soil. Only the long-term chicory and lucerne, two deep-rooting cover crops, show a significant effect in June and July 2019 (Figure 4.3 and Figure 4.4). These ECa differences in the long-term chicory and lucerne treatments on 2019-06-04 (Figure 4.4) could be caused by an improved soil structure allowing better rainfall infiltration and possibly larger moisture storage. Ren *et al.* (2019) found that white mustard has a positive effect on the soil structure, promoting deeper root penetration of maize crop. However, the magnitude of the change (a few mS/m), once converted to soil moisture only represent a few percent, hence not constituting a substantial difference in soil drying compared to other treatments. Analysis of changes in ECa enhances the differences between cover crops, which would be less obvious with absolute ECa values as part of the signal would be impacted by various soil texture across the field.

Potatoes are particularly sensitive to drought stress. While Tang *et al.* (2019) have attempted to directly related ECa to soil moisture and potatoes tuber yield, the second case study presented here focused on the impact of traffic-induced compaction and irrigation treatment on the soil moisture. Time-lapse ERT between potato ridges reveals the limited depth of water uptake in compacted soil compared to non-compacted treatments. Plants in the non-compacted treatments can probably access water at a greater depth more easily (and thus dry the soil) in comparison to the compacted treatments. In wet treatments, crops rely mainly on the water stored in the uppermost 30-40 cm of soil. One major disadvantage of placing the electrodes in the furrows is that no information can be collected on what is happening inside the ridges. However, this setup enables us to better measure the effect of compaction as all ridges are compaction-free. Such information is potentially useful for agronomists to adapt agricultural practices, such as irrigation-schedules tailored to canopy and root development. Minimally invasive ERT or EMI

survey could reveal depth of drying of the crop and help estimate more accurately the amount of water needed for irrigation, leading to more cost-effective management of the water resource.

Time-lapse EMI in the third case study reveals that direct drill and plow treatments influence the soil moisture dynamics and the nitrogen uptake by the crop. From Figure 4.1c, it can be observed that direct drill resulted in patchier plots mainly due to the lower survival rate of the plants in the direct drill plots over winter. During the growing season, direct drill plots showed a somewhat smaller rate of decrease in ECa (Figure 4.8). It is probably the case that the direct drilled plots remained wetter due to a combination of lower evapotranspiration losses from a lower leaf area (Figure 4.10) and a more restricted root system. This is consistent with Sławiński *et al.* (2012) who found higher soil moisture in reduced tillage compared with conventional tillage, for three years of winter wheat monoculture on two different soils. The potential decrease in porosity in the plow treatment during the season could have increased the ECa. However, given that a general decrease in ECa is observed, this effect is probably minor compared to change in soil moisture. Nevertheless, it could potentially lead to an underestimation of the soil drying in the plow treatment based on ECa changes. The addition of nitrogen fertilizer caused a significant increase in ECa over a short period (Figure 4.6). The changes in ECa correlates well with the amount of nitrogen supplied (Figure 4.7). This is in accordance with the results of Eigenberg *et al.* (2002) who successfully use EMI for monitoring different nitrogen uptakes. However, this effect was only observed after the first application of fertilizer (2019-03-04) and not the second (2019-04-23). This could be because of a more rapid nitrogen uptake due to larger plants at the second application. In contrast, the LAI started to increase proportionally to the nitrogen level after the second application (Figure 4.10). This increase in LAI, potentially lead to larger soil drying and might be the cause of the significant differences observed between the tillage treatments (Figure 4.8). Yield response to the different rates was also larger for the plow than for the direct drill treatment (Figure 4.9). One possible explanation is that the larger root impedance in direct drill treatments led to a less effective use of nitrogen fertilizer Ge *et al.* (2019). However, without additional nitrogen, both plow and direct-drill treatments had similar yield. Overall, time-lapse EMI enables us to obtain information on the soil moisture and nitrogen dynamics taking place in different tillage treatments.

4.4.2   Limitations and recommendations

The cases we describe demonstrate that the minimal invasive operation of EMI and its high throughput are significant advantages of this method for agricultural applications. In some cases, EMI surveys can even be conducted while the crop is still in place (e.g. placing the instrument between the rows of wheat or the ridges of potatoes without damaging the crop). For its part, the greater resolution of ERT allows better recovery of depth-specific properties at the expense

of a more complex setup. The two methods have the advantage of sampling a relatively large volume of soil, producing more representative measurements than conventional soil sampling or soil moisture sensing. While both methods can be used for one-time survey, time-lapse studies clearly have great potential for agricultural studies as they enable the observation of the variation of states that can be related to plant development and plant productivity.

EMI instruments are sensitive to measurement drift and for our case-studies we let the instrument warm up to outdoor temperature for at least 30 min before starting the data collection (following Shanahan *et al.*, 2015). Additionally, the setup of a drift station, a place where measurements are collected at regular time interval, is recommended. More complex drift correction can also be applied (Robinson *et al.*, 2004; Delefortrie *et al.*, 2014). This procedure is essential for time-lapse surveys as it is likely that the drift of one survey will be different from another survey, inducing bias in the analysis. Temperature corrections are also essential in time-lapse surveys as mentioned in section 4.2.4 as the soil temperature is an important factor contributing to the soil EC.

Calibration of EMI, possibly by using an ERT array (Lavoué *et al.*, 2010; von Hebel *et al.*, 2019), help to transform qualitative EMI data to more quantitative values. However, it requires that ERT and EMI data span a sufficient range of EC values (in time or in space) in order to build a strong relationship, which can be a limitation in some situation. In our case, robust calibration equations were obtained for the wheat experiment using four time-lapse ERT arrays across the field and using a single time-lapse ERT array for the cover-crop experiments.

Multi-coil EMI instruments now enable the inversion of ECa data to depth-specific EC. However, this inversion remains challenging given the usual small number of coil configurations. Indeed, while ERT datasets usually consist of hundreds if not thousands of quadrupoles providing overlapping information on the same soil volume, EMI datasets usually rely on a few coil configurations. Smoothed Gauss-Newton solution (Whalley *et al.*, 2017), McMC methods (Shanahan *et al.*, 2015) or the shuffle complex algorithm (von Hebel *et al.*, 2014) are a few of the available methods for 1D inversion of EMI data.

While the above precautions are not needed with ERT instruments, the electrode setup and acquisition are more important. Electrodes, after initial installation, can be left in place while the crop is growing allowing time-lapse measurements to be taken at the same exact position. This enables ERT surveys to be inverted using difference inversion (LaBrecque & Yang, 2001). The drawback of that is that soils with high clay content will tend to swell and shrink, eventually leading to desiccation cracks around the electrodes (point of stress concentration) undermining the galvanic contact needed for ERT acquisition. Such effects have led some authors to explore the use of ERT to detect cracks in soils (Samouëlian *et al.*, 2003, 2004; Hassan & Toll, 2013). Using a mobile ERT array that is set up for each survey can be an alternative but require more precautions to not damage the growing crop during installation. Given that the electrodes are

unlikely to be at the same exact positions as previous surveys, a difference inversion cannot be used but inversion with constraint to a reference dataset can be adopted (as it is the case here). Once inverted, ERT sections also need to be temperature corrected.

Relating soil EC to soil properties or state is ultimately challenging. This is because EC is influenced by many factors (texture, density, pore water EC, soil moisture, temperature). These factors need to be controlled or accounted for to develop an EC value that relates the property of interest. Pedophysical relationships linking geophysical properties to soil properties are often site-specific and can be non-linear (Laloy *et al.*, 2011; Calamita *et al.*, 2012). While this manuscript does not attempt to convert change in EC to soil moisture content, we believe that the time-lapse approach and data processing carried out allow for the previous interpretations to be made. However, if changes in other soil properties, such as the decrease in porosity from tillage during the season, were to be observed with geophysical instruments, independent measurements of the soil moisture variation would be needed in order to better isolate the contribution of the change in porosity to the ECa variation.

The three case-studies presented in this work, were applied to relatively small plots from research sites. However, the geophysical methods proposed, particularly EMI has the potential to map much larger areas (Brogi *et al.*, 2019b). ERT systems as well, mounted on towed system (e.g. Veris Quad EC 1000) also allow mapping of large area. However, because ERT requires galvanic contact with the soil, it might be challenging to use a towed system without damaging a growing crop.

Finally, other geophysical methods such as acoustic/seismic (Lu, 2014), ground penetrating radar (Klenk *et al.*, 2015; Algeo *et al.*, 2018; Klotzsche *et al.*, 2019; Akinsunmade *et al.*, 2019) or even nuclear magnetic resonance (Paetzold *et al.*, 1985) are emerging methods that have potential for agricultural applications.

4.5   Conclusion

Time-lapse EMI and ERT surveys detect changes in EC that can more easily be related to variable states, such as soil moisture, compared to conventional static (one time) surveys. The collection of case studies reported here illustrate the effectiveness of time-lapse geophysics for a range of applications. The time-lapse approach helps to monitor cover crop effect on soil drying and image the reduced depth of water uptake in compacted soil for potatoes. Under winter wheat, a plow-based treatment showed larger decrease in ECa associated with larger soil drying compared to a direct drill treatment, which might explain the yield gap observed. Significant correlation between the different level of nitrogen and the ECa changes was also found but only for a short period of time. In contrast, yield and LAI showed a stronger response to nitrogen levels in plow than in direct drill treatment. While interpretation of geophysical data should

always be done carefully, we believe that the use of the time-lapse approach for EMI and ERT dataset have great potential to monitor the effects of a range of agricultural practices.

Acknowledgments

Chapter 5

Accounting for heterogeneity in θ - σ relationship: application to wheat phenotyping using EMI

Guillaume Blanchy[1], Christopher W. Watts[2], Rhys W. Ashton[2], Colin P. Webster[2], Malcolm J. Hawkesford[2], William R. Whalley[2], Andrew Binley[2]

[1] Lancaster University, Lancaster, Lancashire LA1 4YW, UK

[2] Rothamsted Research, Harpenden, Hertfordshire AL5 2JQ, UK.

Authorship statement

The PhD author collected geophysical data on the experiment, processed the data and wrote the manuscript. Other authors provided additional (non-geophysical) data and feedback on the manuscript. Andrew Binley and Richard Whalley provided additional ideas for the paper and edits on the manuscript.

Abstract

Geophysical methods, such as electromagnetic induction (EMI), can be effective for monitoring changes in soil moisture at the field scale, particularly in agricultural applications. The electrical conductivity (σ) inferred from EMI needs to be converted to soil moisture content (θ) using an appropriate relationship. Typically, a single global relationship is applied to an entire agricultural field, however, soil heterogeneity at the field scale may limit the effectiveness of such an approach. One application area that may suffer from such an effect is crop phenotyping. Selecting crop varieties based on their root traits is important for crop breeding and maximizing yield. Hence, high throughput tools for phenotyping the root system architecture and activity at the field-scale are needed. Water uptake is a major root activity and, under appropriate conditions, can be approximated by measuring changes in soil moisture from time-lapse geophysical surveys. We examine here the effect of heterogeneity in the θ-σ relationship using a crop phenotyping study for illustration. In this study, the θ-σ relationship was found to vary substantially across a field site. To account for this, we propose a range of local (plot specific) θ-σ models. We show that the large number of parameters required for these models can be estimated from baseline σ and θ measurements. Finally, we compare the use of global (field scale) and local (plot scale) models with respect to ranking varieties based on the estimated soil moisture content change.

5.1   Introduction

Over the past two decades there has been a growth in the use of geophysical methods in agriculture (Allred *et al.*, 2008). This has been driven, in part, by the need to assess variation in soil properties in a non-invasive manner over relatively large scales. Geophysical methods in such a context are a subset of proximal soil sensing approaches (Viscarra Rossel *et al.*, 2011). Measurements of properties, such as electrical conductivity, are typically treated as a proxy for a soil property or state of interest, e.g. soil texture, bulk density or soil moisture content. Such methods may also be used in a time-lapse manner to examine changes in soil properties or states, e.g. changes in texture or soil density due to land management practices. Typically, maps of a geophysical property are presented in a qualitative manner. Whilst this can be effective in some cases, the ability to estimate quantitatively the property, or state, of interest offers greater scope for a wider range of agricultural applications. To achieve such quantification, the relationship between the geophysical proxy and the soil property or state is required. Such relationships may be spatially variable, particularly over field scales typical in agricultural studies. Here, we assess such heterogeneity in a wheat phenotyping study, and propose practical methods to account for such variability.

5.1.1   Field-scale phenotyping bottleneck

Wheat is one of the main staple crops in the world. It has been bred over centuries for specific traits, most of which are above-ground characteristics. Given uncertain future climatic conditions, there are demands for more resilient breeds. A key component of such resilience lies in the root system of the crop. Deeper root systems are correlated with higher yield and higher resistance to drought (Wasson *et al.*, 2012). Usually the root system of a crop is assessed in the lab or in the greenhouse. However, field studies of the root system are essential to understand more about how each variety adapts to its environment. The typical approach of assessing the root system of a crop in the field is by direct sampling (Wasson *et al.*, 2014). Such methods are destructive, labour-intensive and expensive in a conventional breeding program with a large number of breeding lines. An alternative, less-invasive, and quicker approach is to consider the root activity rather than the quantity of roots. Such methods rely on observing changes in soil moisture to infer root activity (e.g. Michot *et al.*, 2003; Srayeddin & Doussan, 2009; Garré *et al.*, 2013; Beff *et al.*, 2013). Different methods to measure efficiently this change in soil moisture were explored by (Whalley *et al.*, 2017) for different wheat genotypes. Among them, geophysical methods, such as electrical resistivity tomography (ERT) and electromagnetic induction (EMI) appear promising as a means of measuring a proxy to observe the dynamics of soil moisture of the subsurface (Binley *et al.*, 2015). Shanahan *et al.* (2015) illustrate the use of EMI for differentiating soil drying from different wheat genotypes in a phenotyping context. In their study the relationship between the observed proxy (soil apparent electrical conductivity) and soil moisture content was assumed to be homogeneous across the study site. Huang *et al.* (2018) also use EMI as a proxy for plot-scale crop water of different chickpea genotypes. Other examples of the use of EMI in crop-related studies include Cassiani *et al.* (2012), von Hebel *et al.* (2014) and Moghadas *et al.* (2017).

5.1.2   Electromagnetic induction

The EMI method measures the soil apparent electrical conductivity (σ_a) in a non-contact/invasive manner. A standard EMI device is composed of a transmitter (Tx) coil and at least one receiver (Rx) coil. The transmitter coil generates a transient electromagnetic field. This primary field induces eddy currents in the ground; the magnitude of eddy currents generated is a function of the soil electrical conductivity, σ. The eddy currents then induce a secondary electromagnetic field. Both primary and secondary electromagnetic fields are measured by the receiver coils. The out-of-phase component of their complex ratio is used to compute the apparent electrical conductivity (σ_a) of the subsurface. EMI measurements can be made in vertical and horizontal coplanar orientations, with different depth-sensitivity functions. Several current instruments, such as the one used in this study (Mini-Explorer from GF-Instruments, Czech Republic), have

multiple receiver coils.

The relationship between depth-specific σ and measured σ_a, for a given coil orientation and the distance between the Tx and Rx, can be described using a simple function: the 'cumulative sensitivity function' (McNeill, 1980). A more accurate, but more complex, method based on Maxwell's equations (von Hebel et al., 2014; Andrade et al., 2016) can also be used to describe such a relationship. Using measurements made on a multi-coil device, depth-specific σ can be determined from inverse modelling of the σ-σ_a relationship. The inversion process seeks the best distribution of depth-specific σ that is consistent with all observed σ_a values for different coil spacings and orientations. A prerequisite, considered by some authors, for inversion is that the apparent values given by the different EMI configurations need to be calibrated with results from an ERT survey (e.g. Lavoué et al., 2010). More details about EMI inversion can be found in von Hebel et al. (2014).

EMI measurements have been extensively used to map field heterogeneities and produce detailed soil maps for the definition of management zones in precision agriculture (Corwin & Lesch, 2003; King et al., 2005; Brevik et al., 2006). More recently, multi-coil EMI instruments have provided greater depth-specific information in agricultural studies, allowing assessments of depth specific σ and their link to aboveground crop performance indicators (von Hebel et al., 2014; Brogi et al., 2019a).

5.1.3 Soil moisture content – electrical conductivity relationships

The soil electrical conductivity is controlled by a number of properties (soil texture, organic matter content) and states (soil temperature, pore water electrical conductivity, bulk density, soil moisture content). The soil structural state and its properties control σ through pore connectivity and porosity. Such properties are also inherently linked to soil moisture content (e.g. determining residual moisture content), which has a major effect on soil σ. Temperature effects can be accounted for given local vertical soil temperature profiles, which we assume to not vary spatially inside the same field, although effects of daily or seasonal variation in temperature may need to be accounted for. The electrical conductivity of the pore water also contributes to the soil σ. In temperate climates, the variation of the pore water electrical conductivity should be minimal in rain-fed settings. However, this has a greater impact in irrigated conditions as the irrigated water (e.g. groundwater sourced) is likely to have a different ionic composition and temperature than the pore water in the surface layers of soil. In semi-arid environments, pore water conductivity effects may be significant due to enhanced salinity arising from high evaporative fluxes (Corwin & Lesch, 2005). Note that even in rain-fed environment, increase in pore-water electrical conductivity can occur due to fertiliser application.

Archie's law (Archie, 1942), developed for oil reservoir investigations, is a commonly used

empirically derived model that relates the soil condition to the bulk σ. Waxman & Smits (1968) extended Archie's law by accounting for the effect of clay minerals (forming surface electrical conductivity). Several other approaches have been developed specifically for soils (e.g. Rhoades *et al.*, 1976). Laloy *et al.* (2011) compared a range of models for soil electrical conductivity, adopting the term "pedo-electrical" model to differentiate this from classical petrophysical approaches. Following (Laloy *et al.*, 2011), the relationship between σ and soil moisture content (θ) can be expressed as:

$$\sigma = a\theta^n + b \tag{5.1}$$

where a, b and n are empirical parameters that depend on soil properties. Following Garré *et al.* (2011), a is influenced by the pore water conductivity, soil texture and porosity; b by the soil surface conductivity; n is controlled by the soil texture. When the exponent n is close to 1, Equation 5.1 can be approximated by a linear relationship.

The parameters of Equation 5.1 may be obtained from laboratory measurements on field samples (e.g. Shanahan *et al.*, 2015) or directly in the field, for example using a trench and soil moisture sensors (Michot *et al.*, 2003; Garré *et al.*, 2013; Beff *et al.*, 2013). Both methods provide information on a relatively small volume that might not be representative of the entire field. Indeed, from field-scale observations, the different soil textural properties also impact the θ-σ relationships, either when using σ_a (Stanley *et al.*, 2014) or with depth-specific σ (Jayawickreme *et al.*, 2010). Equation 5.1 is usually appropriate when the soil moisture change is large and the soil heterogeneity is small. However, if significant soil heterogeneity exists, the variation in the parameters in Equation 5.1 may need to be accounted for. This effect may be particularly important in phenotyping studies (the determination of specific traits of crop varieties) since the differences in soil moisture change between crop lines (varieties) may be smaller compared to other studies where different species are used. Whether depth-specific or apparent values (like in this study) are considered, estimates of small changes in soil moisture are likely to be affected by heterogeneity in the θ-σ relationship (Equation 5.1).

Furthermore, in a phenotyping context, a better prediction of the soil moisture or change in soil moisture from EMI is important as it can help to make the variety ranking similar to the one obtained with direct soil moisture observations. Of course, if direct soil moisture data are available, there is little value in additional geophysical proxy measurements. However, in this study, the direct measurements allow us to determine what the maximum achievable information on soil moisture content obtainable from EMI measurements might be.

Therefore, this study aims to: (1) quantify the spatial heterogeneity of θ-σ relationships at the field-scale; (2) determine its impact on the phenotype ranking of wheat lines; (3) explore approaches to account for such effects using simplified but practical approaches. The investigation utilises a dataset of σ and θ measurements collected during a winter wheat field experiment.
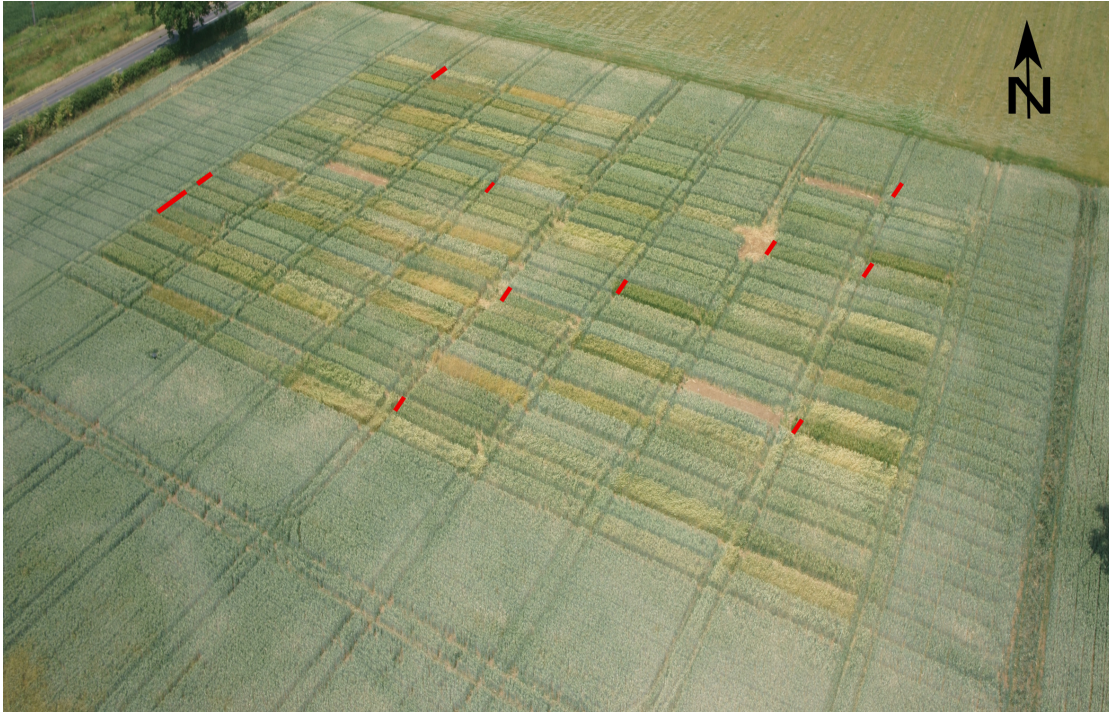
Figure 5.1 – Aerial picture of the field showing the 216 plots (each 9 m x 1.8 m) sown with winter wheat in 2016. Plots marked in red are equipped with ERT arrays.

5.2   Material and methods

5.2.1   Field layout

Measurements were made during the 2016-2017 growing season at the Warren Field experimental farm (Woburn, UK 52°01'06.5"N 0°35'29.0"W) operated by Rothamsted Research. The soil at the site is classified as a sandy clay loam (Distric Cambisol with 54% sand, 20% silt and 26% clay, more details in Shanahan *et al.* (2015). The field was sown with winter wheat at the end of 2016 and harvested in August 2017 (Bai *et al.*, 2019). In the experiment, 71 lines of wheat and one fallow treatment (all with 3 replicates) were randomly distributed in 3 blocks. An aerial photograph showing the field experiment and the 216 plots is shown in Figure 5.1. Out of the 216 plots (each 9 m by 1.8 m), 12 plots (4 varieties) were equipped with a 24-electrode electrical resistivity tomography (ERT) array (0.25 m spacing) placed along the middle of each plot. ERT data were used to calibrate EMI measurements following Lavoué *et al.* (2010). All plots were equipped with a 1.5 m long neutron probe access tube positioned 1 m from the edge of the plot. The ratio counts from the neutron probe were converted to soil moisture content using a field calibration (+/- 0.01 cm3/cm3). In the field, temperature sensors recorded soil temperature at (0.1, 0.2, 0.3, 0.4, 0.6, 1 m depths). They were used to correct the electrical conductivity from the ERT and EMI using the ratio model (Ma *et al.*, 2011) with a 2% increase per degree Celsius.

5.2.2 Field measurements

Three sets of EMI measurements were collected on each plot with a Mini-Explorer instrument (GF Instruments, Brno, Czech Republic) according to the guidelines provided in Shanahan *et al.* (2015). They were then averaged to obtain a mean for each plot. Surveys were conducted on dates (expressed in ISO 8601 format): 2016-10-08, 2017-03-02, 2017-03-16, 2017-04-03, 2017-04-27, 2017-05-16 and 2017-06-01. Data from some plots were discarded because of two high voltage cables buried under the field. The filtering used the standard deviation of the three sets of EMI data for each plot.

The Mini-Explorer contains three receiver coils with separations 0.32 m, 0.71 m and 1.18 m from the transmitter coil. Measurements in the two modes (horizontal coplanar mode (HCP) and vertical coplanar mode (VCP)) were obtained. Therefore, six measurements of apparent conductivity were made. The normalised sensitivity pattern (McNeill, 1980) of each configuration is shown in Figure 5.2a (note that in Figure 5.2a and hereafter the notation, for example, HCP0.32, is used to identify coil orientation and spacing: HCP with a 0.32 m coil spacing). Figure 5.2b shows example soil moisture data from the neutron probe taken at seven depths. For each depth, the grey lines denote the limits used to compute the local sensitivity weights used in the computation of the apparent soil moisture content.

ERT measurements were collected using a 48 Syscal Pro (Iris Instruments, Orléans, France) on similar dates to the EMI (2017-03-02, 2017-03-16, 2017-04-03, 2017-04-27, 2017-05-16, 2017-06-01 and 2017-06-23). Neutron probe measurements were collected on 2017-03-16, 2017-04-05, 2017-04-26, 2017-05-18, 2017-06-23. Nitrogen fertiliser (Nitram 37.5% N) was applied on 2017-04-10 and 2017-04-25 as pellets. Whenever possible ERT and EMI measurements were collected on the same day. Neutron probe datasets were collected as close as possible to the ERT/EMI dataset, either on the same day or before/after an interval of a few days, thus minimizing disturbance from any rainfall events. Note that the neutron probe dataset of mid-May was taken after a large overnight rainfall event. This had an impact on the shallow measurements (0.15 and 0.30 m depths) but did not influence the deeper measurements. Note also that nitrogen fertiliser was applied just before the measurement at the end of May. However, because of its application as dry pellets and the lack of large rainfall events, it is unlikely that it had fully dissolved into the soil at the time of the end of May survey. This could have caused a significant increase in the pore water electrical conductivity and hence in our EMI/ERT measurement, however, no sharp increase in observed electrical conductivity is apparent. At the end of the field campaign, four different datasets of ERT, EMI and neutron probe measurements were available to derive pedophysical relationship for each plot. Despite the limited number of time-lapse data collected on the same plot, the larger number of plots screened enables us to capture well the temporal and spatial variability across the field.
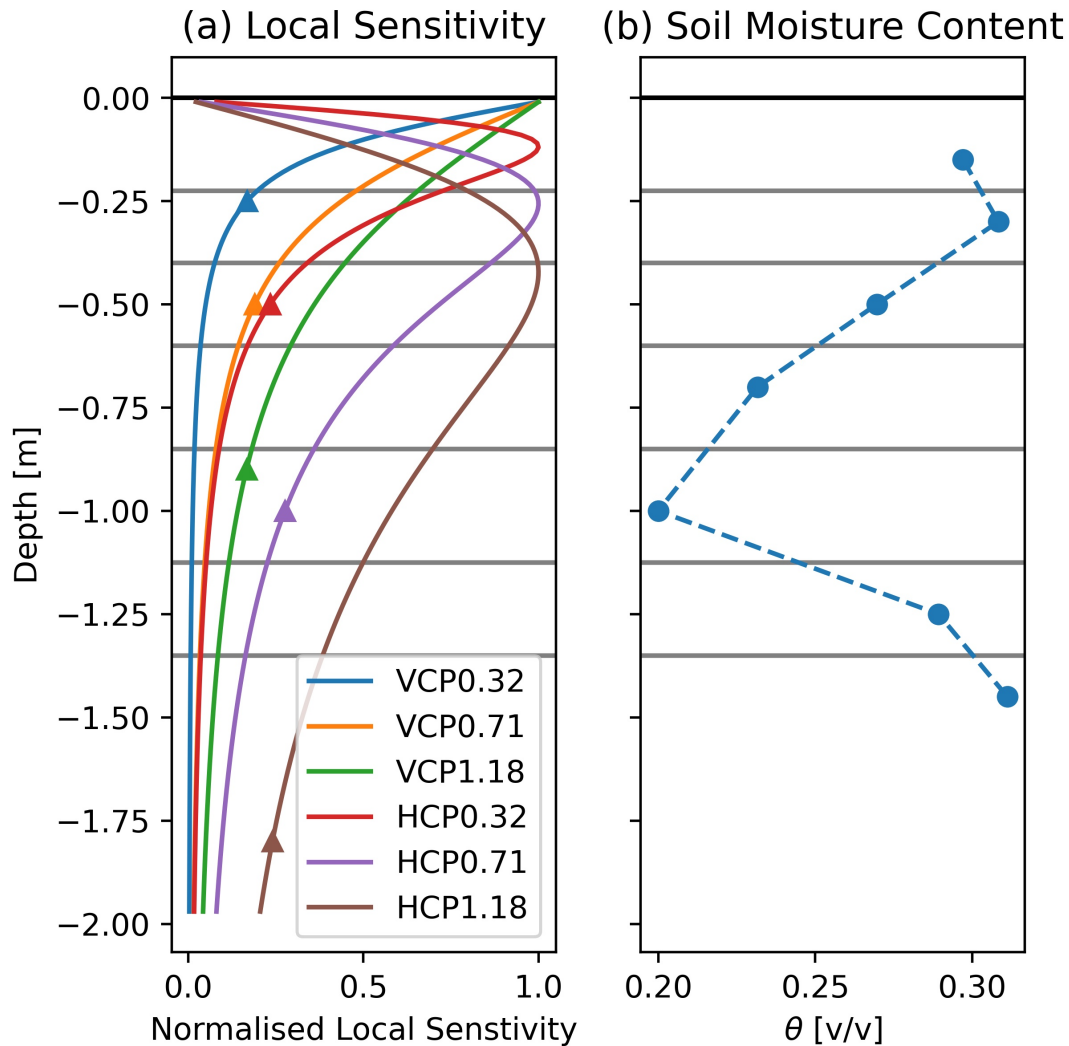
Figure 5.2 – (a) Normalised local sensitivity pattern for the six pairs of coil orientations / coil separations available on the Mini-Explorer instrument. The triangles show the depth above which there is 70% cumulative sensitivity (commonly referred to as the effective depth of investigation). (b) shows a measured soil moisture content profile by neutron probe. To build the apparent soil moisture content, each depth-specific θ measurement is multiplied by the integrated EMI sensitivity corresponding to its depths (between the grey lines) and then summed (see Section 3.1).

5.3 Results

5.3.1 Apparent soil moisture content

To allow comparison with observed apparent conductivity measurements and to avoid any inversion artefacts that can arise from EMI inversion, an 'apparent' soil moisture was computed based on the weights of the EMI cumulative sensitivity function (Figure 5.2a) following the approach given by Martini *et al.* (2017). The θ measurements of a given profile (Figure 5.2b) were multiplied by their respective depth-specific normalised local sensitivity and then summed to obtain an apparent soil moisture content (θ_a). The shape of the normalised sensitivity function is determined by the same parameters as for the EMI: the coil orientation (HCP or VCP) and the coil spacing (0.32, 0.71 or 1.18 m). Thus, for each pair of coil orientation/coil spacing, a different θ_a was obtained, for comparison with the observed σ_a from EMI. The apparent soil moisture content θ_a is given by

$$\theta_a = \sum_{i}^{n} \theta_i s_i \tag{5.2}$$

where, θ_i is the measured soil moisture content of layer i and s_i is the sensitivity of the layer i derived by integrating the cumulative sensitivity function between the top and the bottom depths of the layer (Figure 5.2). Note that the sum of s_i for the profile is equal to 1. n is the number of layers.

5.3.2 Evolution

Figure 5.3a shows the different collection times as well as selected weather data during the experiment. Figures 5.3b, c and d show the evolution of the different observed and computed below-ground variables. Note the clear difference between the averages of the fallow and cropped plots, demonstrating a substantial effect of the crop in the soil moisture changes over time, i.e. crop water uptake accounts for a substantial change in soil moisture. Note that the σ_a from EMI shows a peak around 2017-03-01 and 2017-06-01. This can be explained by the large amount of rainfall on the previous day. Note that no soil moisture content data were collected on 2017-06-01, hence the series does not show a similar increase. The analysis uses the data from the four following dates for which EMI, ERT and neutron probe measurements were all available: 2017-03-16, 2017-04-05, 2017-04-26, 2017-05-18.
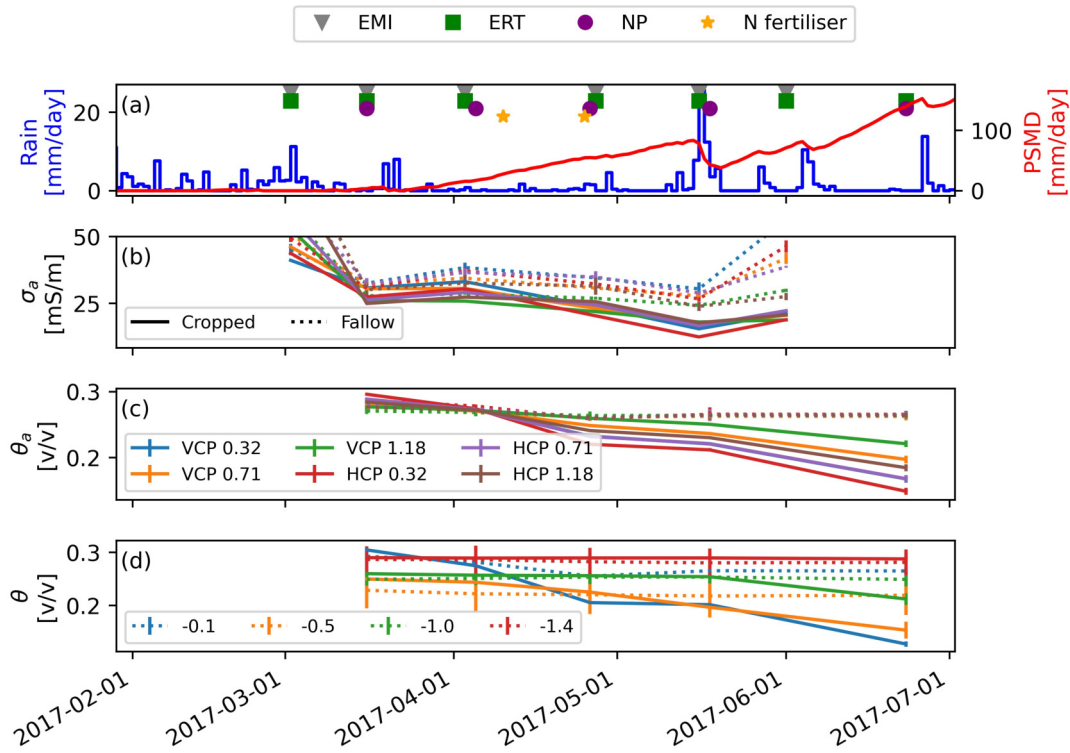
Figure 5.3 – (a) Rainfall and potential soil moisture deficit (PSMD) with markers corresponding to the collection date of the ERT, EMI and neutron probe (NP) dataset.(b) Evolution of σ_a from EMI. (c) Evolution of computed θ_a. Note that VCP0.32 line is mostly under to HCP0.71 at this scale. (d) Evolution of the measured soil moisture content from neutron probe for selected depths. Error bars are standard error of the mean (sometimes too small to be visible on the graph). Dotted lines are averages of the fallow plots while solid lines are averages of the cropped plots.

5.3.3   Time-lapse approach

Time-lapse monitoring of σ allows the removal of stationary effects of the soil (soil organic matter, soil texture) on the θ-σ relationship (e.g. Robinson *et al.*, 2012b; Shanahan *et al.*, 2015). This approach relies on the measurements of a baseline (in this case, where no crop effect is present), which is usually made at the beginning of the growth season when the field is at or near field-capacity. All subsequent surveys can be compared to this baseline, consequently revealing the main drying pattern mainly driven by root activity. For the experiment presented here the baseline data was measured on 2017-03-16. There are two ways to compute changes from the baseline conditions: (1) by computing the difference; (2) by computing the relative change. Assuming a linear relationship between θ and σ (n=1 in Equation 5.1) the following equations can be written. The difference is simply the difference between σ and σ_{ref}:

$$\Delta\sigma = \sigma - \sigma_{ref} = (a\theta + b) - (a\theta_{ref} + b) = a\Delta\theta \qquad (5.3)$$

where σ_{ref} and θ_{ref} are the baseline σ and θ, respectively. The relative change is the difference between σ and σ_{ref} normalised by the baseline σ_{ref} (Equation 5.4). It is given by:

$$\frac{\Delta\sigma}{\sigma_{ref}} = \frac{a\Delta\theta}{a\theta_{ref} + b}. \tag{5.4}$$

Computing differences (Equation 5.3) removes the effect of 'offset' b but retains 'slope' a, which may vary across the site. In contrast, working with relative change (Equation 5.4) retains the effects of a and b, unless b is relatively small. In the latter case, Equation 5.4 can clearly be simplified to link directly the relative change in σ with the relative change in θ as:

$$\frac{\Delta\sigma}{\sigma_{ref}} = \frac{\Delta\theta}{\theta_{ref}} \tag{5.5}$$

The expressions above were used to explore ways in which the variation of a and b within a site can be accounted for.

5.3.4   Observations

Figure 5.4 shows the different relationships between σ_a and θ_a for three plots with the same variety in the field site. The variation between the three responses (expressed as absolute, difference or relative change) reveals the effect of spatial variability across the site, highlighting the limitation of adopting a single global relationship.
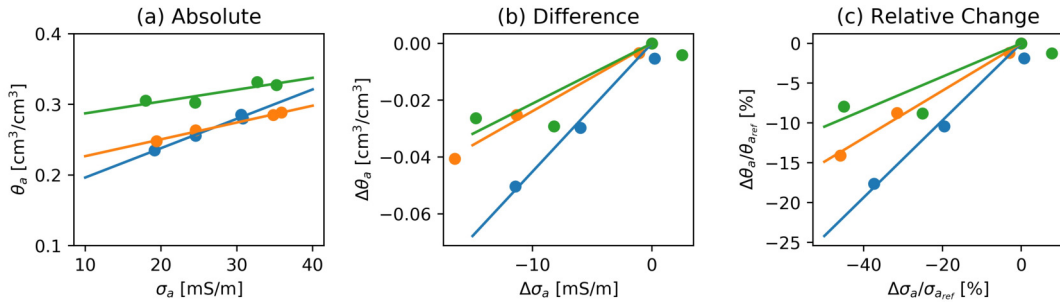
Figure 5.4 – θ-σ relationships between θ_a and σ_a collected in the field in three example plots with the same variety expressed as: (a) absolute, (b) difference and (c) relative change. Data for each plot are differentiated by a different colour symbol/line.

Figure 5.4 shows the distribution of θ_a and σ_a in April 2017 and their respective difference with respect to the baseline in March 2017 (2017-03-16). From Figure 5.5, it can be seen that the patterns for both absolute and differences are different. This illustrates the effect of different θ-σ relationships observed in Figure 5.4. Both patterns in σ_a and θ_a values remain consistent for the different collection dates.
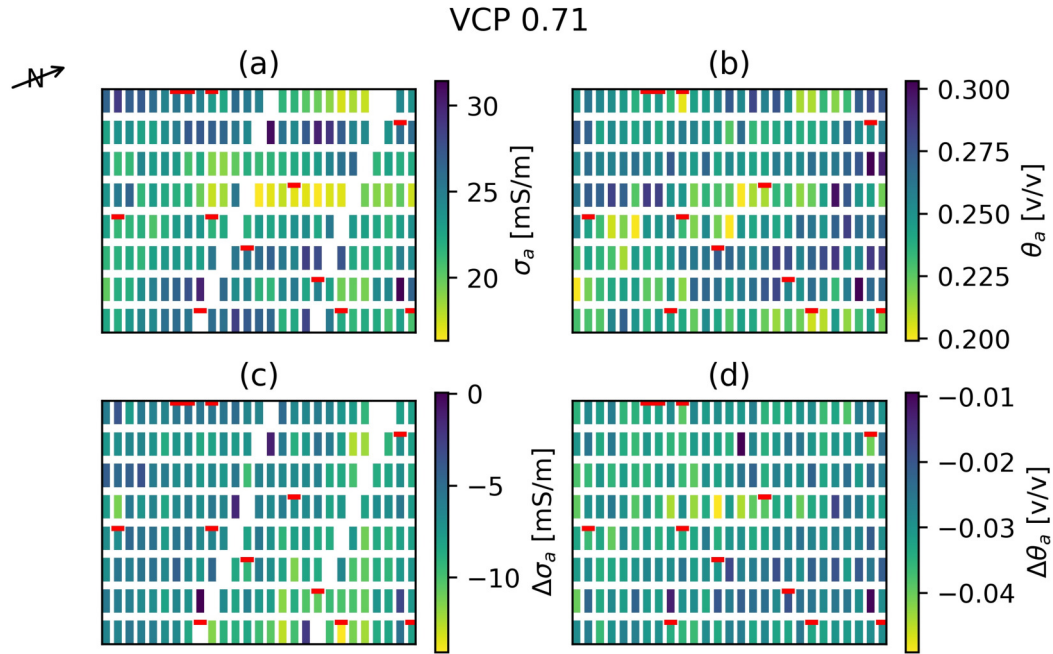
Figure 5.5 – General schematic layout of the random block experiment (not to scale) on 2017-04-17. One rectangle represents one 9 m by 1.8 m plot. Plots marked with a red line were equipped with an ERT array. The σ_a value for each plot is the average of three replicates. (a) Shows the distribution of σ_a (VCP0.71 with an effective depth of 0.5 m). (b) Shows the corresponding θ_a from neutron probe measurements. (c) and (d) show the difference in σ_a and θ_a, respectively, from the baseline measurement of 2017-03-16. Spatial heterogeneity exists in both variables and even in their differences. Blank plots in the EMI maps are plots affected by buried high-voltage cables.

5.3.5   Development of local model

Typically, a few samples from the field are collected to build a global unique relationship between θ and σ. We can express this relationship as:

$$\sigma = a_g\theta + b_b \tag{5.6}$$

$$\Delta\sigma = a_g\Delta\theta \tag{5.7}$$

where the global a_g and b_g parameters are identical for all the plots. However, for a heterogeneous field, using this global relationship may lead to substantial errors in the estimation of soil moisture content changes. In order to overcome this, we explored local models allowing the assignment of a unique θ-σ relationship for each plot. (M1) Linear local model: based on

Equation 5.1 assuming n=1. This model has two plot-specific parameters: i is the plot number, the slope is a_i and the offset is b_i

$$\sigma = a_i\theta + b_i \tag{5.8}$$

Figure 5.6 illustrates, using all measurements, how well the linear global model and linear local model (M1) perform. There is a clear (and expected) improvement of the prediction of soil moisture content with the linear local model. Note that an exponential model (not shown here) following Equation 5.1 was also fitted and has similar performance to the linear model (R^2=0.37 for the global exponential model; R^2=0.82 for the local exponential model). Consequently, the linear model is adopted hereafter.
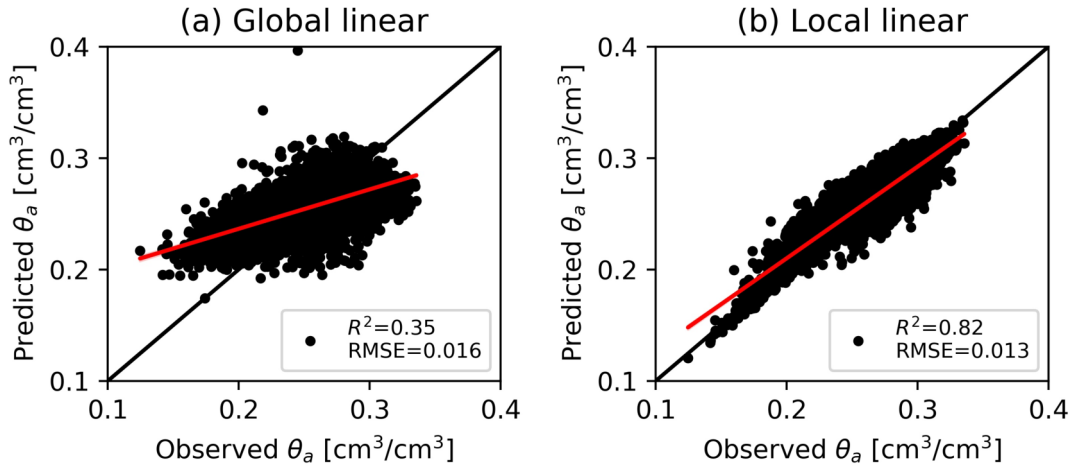
Figure 5.6 – Both graphs show the observed θ_a vs the predicted θ_a from (a) the global linear model (Equation 5.6) and (b) the local linear model (Equation 5.8).

As seen in Figure 5.6, the local linear model outperforms the global linear model but increases the number of parameters needed. More importantly, a full set of monitored soil moisture content values is needed, making the geophysical proxy approach redundant. As a first step to reduce the number of local parameters, we introduce two new models. (M2) Multi-offsets model: a linear model where each plot has its own offset b_i but share a common slope a_g,

$$\sigma = a_g\theta + b_i \tag{5.9}$$

(M3) Multi-slopes model: this model only applies to differences in values and is based on Equation 5.3, each plot having its own slope a_i. This model has one parameter per plot (slope),

$$\Delta\sigma = a_i\Delta\theta \tag{5.10}$$

Mathematically, the multi-offsets model (M2) produces a set of parallel σ-θ relationships similar

to Figure 5.4a while the multi-slopes model leads to a set of conical $\Delta\sigma$-$\Delta\theta$ relationships similar to Figure 5.4b. Both use fewer parameters than the local linear model (M1). The rationale for these simpler models is the need to reduce the number of parameters needed and increase our ability to predict them using a set of baseline measurements.

5.3.6 Development of predicted local (plocal) models

All local models (M1 to M3) require large amount of information for each plot and have limited practical use in a field phenotyping application. As stated above, if direct measurements of soil water were available in a field experiment there would be no benefit or value in using alternative geophysical proxy measurements. However, they allow us to determine what the maximum achievable information on soil moisture content obtainable from EMI measurements might be. As a more practical solution we explore a range of alternative approaches where the local θ-σ relationship is known for a subset of plots and the geophysical data are used to predict those local relationships for the other plots (plocal).

Predictors of the local parameters

The first step in developing predicted local (plocal) models is to identify the best estimates of the local parameters among baseline measurements. Figure 5.6 shows the relationship between the different local parameters from each model (M1 to M3) and the baseline σ_a and θ_a. It can be observed for the linear local model (M1) that the local offsets (b_i) are well related to baseline θ_a^{ref} and that the slopes (a_i) are more related to σ_a^{ref}. The multi-offsets (M2) and multi-slopes (M3) models aim to amplify those trends by reducing the number of local parameters. Using multiple local offsets but a global slope (Equation 5.9), the multi-offsets model (M2) displays a stronger relationship with the baseline θ_a^{ref} (R^2=0.86) than the linear model (R^2=0.40). Using multiple local slopes and no offsets (Equation 5.10), the multi-slopes model (M3) displays a stronger relationship with the baseline σ_a^{ref} (R^2=0.33) than the linear model (R^2=0.27).

VCP 0.71
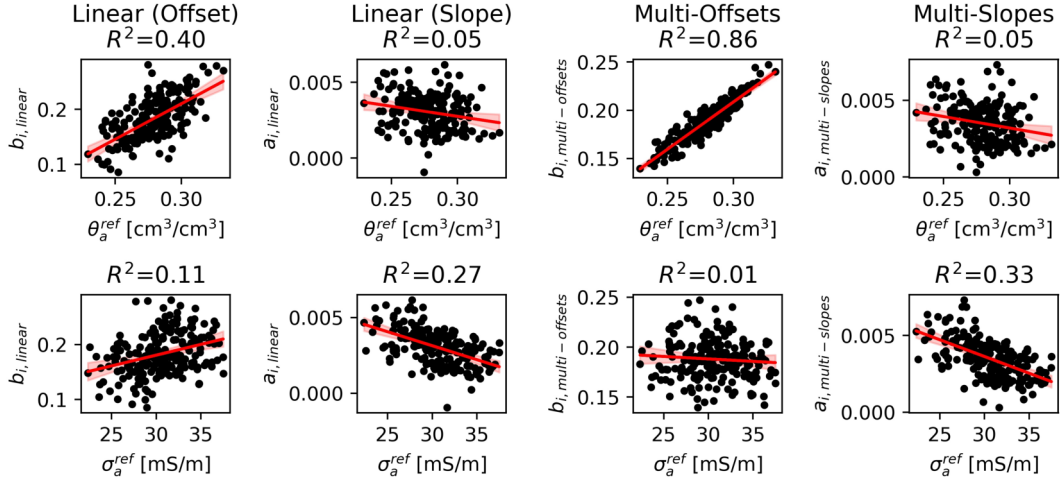
Figure 5.7 – Relationships between the local parameters of the three local models (M1 to M3) and the two baseline measurements σ_a^{ref} and θ_a^{ref} for VCP0.71. The first two columns on the left shows the local offsets b_i and the local slopes a_i of the local linear model (M1) against the baseline measurements. The 3rd column shows the local offsets b_i of multi-offsets model and the 4th column shows the local slopes a_i of the multi-slopes model against the baseline measurements. The red line is the line of best fit with its 95% confidence interval (red shaded region).

Figure 5.6 allows the identification of the best predictor for each local parameter. Given local parameters from a subset of plots, a linear relationship between them and their best predictor is derived and used to predict the value of the local parameters for the other plots. Those predicted local parameters are then used in one of the models (M1 to M3). This process and the results are shown below for the multi-offsets (M2) and the multi-slopes (M3) models (M1 not shown). Hereafter, the subset of plots is composed of the 12 plots equipped with an ERT array as they are randomly distributed in the field. The choice of plots is somewhat arbitrary: another set of plots could have been selected but they should span the largest possible range of σ and θ observed in the field.

Multi-offsets model

The multi-offsets (M2) model incorporates a local offset, b_i, but a global slope, a_g (Equation 5.9). As an illustration, Figure 5.8a compares, for a subset of plots (black line and dots), the multi-offsets model with its corresponding global model for VCP0.71. The global model compared here corresponds to Equation 5.6 where both slope, a_g and offset b_g are uniform across the field. The multi-offsets model improves the accuracy of the predicted θ_a compared to the global model (R^2=0.92 vs 0.37) due to the inclusion of the local parameters b_i (Figure 5.8a). Both models are fitted on all the plots available. In order to decrease the amount of data needed to obtain these local offsets, a linear relationship between the local offsets b_i and the baseline θ_a^{ref} is derived
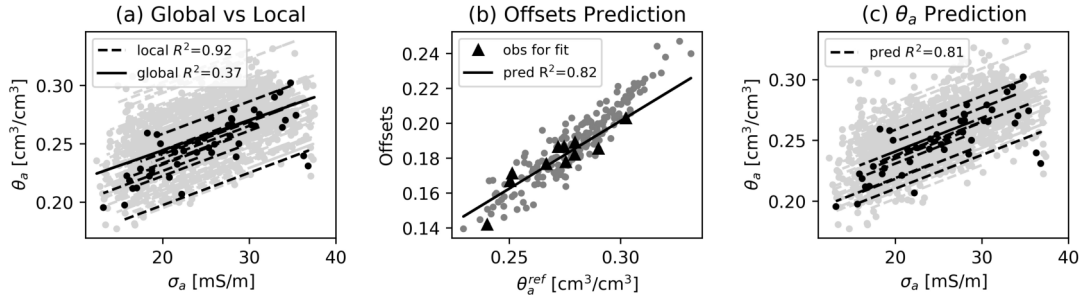
Figure 5.8 – Multi-offsets model fitted with apparent values (VCP0.71). The grey dots show all the data available on the 216 plots. They represent the maximum number of information achievable if both σ and θ are monitored on all the plots. In a more practical situation, only a subset of plots (black dots) are monitored for both σ and θ. (a) Shows the relationship fitted with the multi-offsets model (local) as well as a global linear model, both fitted on the 216 plots. (b) Shows the local offsets b_i vs the baseline θ_a^{ref}. The black line corresponds to a linear relationship fitted on the subset of plots. This relationship is used to predict the offsets for all the other plots. (c) Shows the multi-offsets model using the predicted offsets (plocal) from (b). In subplots (a) and (b) the black dots and dashed lines are used to illustrate the behaviour of some plots as plotting all lines will make the graph unreadable.

using the data from a subset of plots (Figure 5.8b). This b_i – θ_a^{ref} relationship is then used to predict b_i for all the plots. Finally, in Figure 5.8c, those predicted offsets are used in the plocal multi-offsets model to obtain θ_a. In this case, the R^2 of the multi-offsets model with the predicted parameters (0.81) is better than for the global fit (0.37).

The multi-offsets model focuses on the absolute values and not the differences. For the latter the multi-slopes model is adapted further.

Multi-slopes model

The multi-slopes model (M3) presented in Figure 5.9 tries to fit a local model $\Delta\sigma_a$ and $\Delta\theta_a$ (Equation 5.10). Figure 5.9a shows a comparison of the multi-slopes model and its global equivalent. In this case the global model contains a unique slope for the whole field. Similar to Figure 5.8, the introduction of a local parameter (slope a_i) improves the strength of the relationship from R^2 0.71 to 0.86. In Figure 5.9b, a linear relationship is derived between the local slopes a_i and the baseline σ_a^{ref} based on a subset of plots (R^2 0.64). This a_i-σ_a^{ref} relationship is then used to predict the values of a_i for all the other plots. Finally, those predicted slopes are used in Figure 5.9c in the multi-slopes model to predict $\Delta\theta_a$ for all plots. The multi-slopes model with the predicted local parameters (plocal) has a higher R^2 (0.68) than the global fit (0.71).
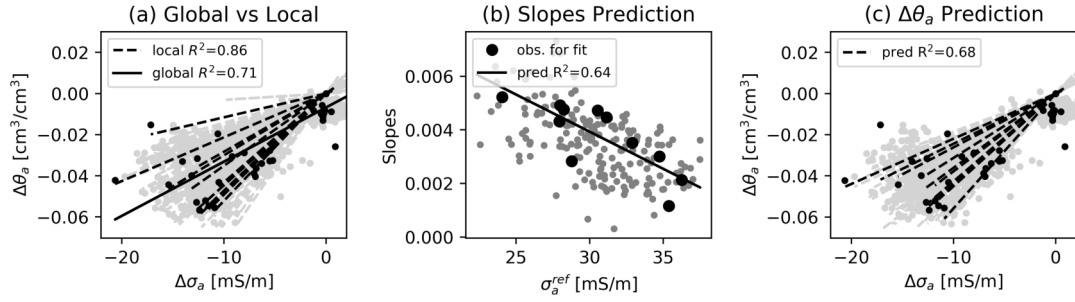
Figure 5.9 – Multi-slopes model fitted with differences in apparent values (VCP0.71). The grey dots show all the data available on the 216 plots. They represent the maximum number of information achievable if both σ and θ are monitored on all the plots. In a more practical situation, only a subset of plots (black dots) are monitored for both σ and θ. (a) Shows the multi-slopes model as well as a global relationship with a unique slope for all 216 plots (global). (b) Shows the local slopes according to the baseline σ_a^{ref}. The black line corresponds to a linear relationship fitted on a subset of plots. This relationship is used to predict the local slopes for all the other plots. (c) Shows the multi-slopes model using the predicted slopes from (b) (plocal). In subplots (a) and (b) the black dots and dashed lines are used to illustrate the behaviour of some plots as plotting all lines will make the graph unreadable.

5.3.7 Quality of the predicted local models

Figure 5.10 shows the quality of the prediction of M1, M2 and M3 using the predicted local parameters (plocal). The multi-offsets (M2) and multi-slopes (M3) models which only have one local parameter show better R^2 (M1: 0.16, M2: 0.53, M3:0.60) and a lower root mean squared error (RMSE) (M1: 0.04, M2: 0.02, M3: 0.03) than the plocal linear model (M1) which has two local parameters. That means that the predicted soil moisture content from the multi-offsets (M2) or multi-slopes (M3) models is more accurate than from the linear model (M1).
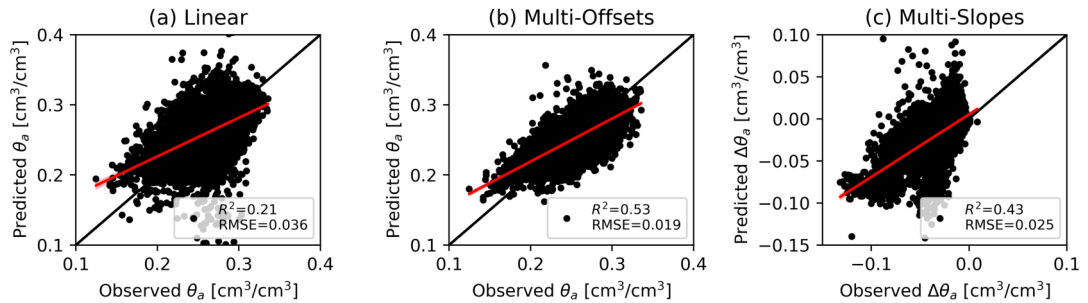
Figure 5.10 – Quality of the predicted θ_a vs the observed θ_a from (a) linear, (b) multi-offsets and (c) multi-slopes models with predicted local parameters. The red line is the line of best fit with its 95% confidence interval (red shaded region). Both multi-offsets and multi-slopes models have one local parameter while the linear model has two.

5.3.8   Choice of the size of the subset of plots for plocal models

The size of the subset of plots needed for the plocal models needs to be chosen carefully. Figure 5.11 shows the effect of the number of selected plots on the RMSE of the prediction for the multi-offsets (M2) and the multi-slopes (M3) models. In this case, the RMSE does not change much if more than 10 plots are included in the subset.
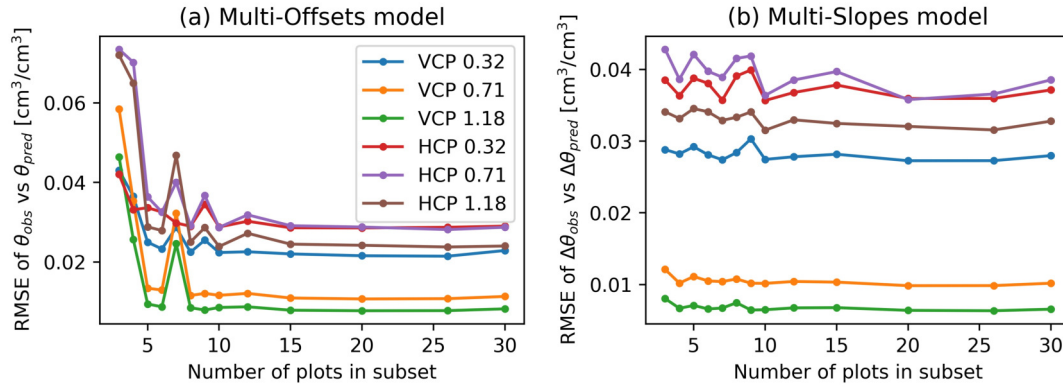
Figure 5.11 – Effect of the size of the subset of plots on the predictions of the plocal multi-offsets (a) and multi-slopes (b). After sorting the plots according to the baseline σ_a, a subset of a given number of plots is selected at regular interval on the whole range of baseline values.

5.3.9   Effect on the variety ranking

In a phenotyping context, we expect similarity in the rank of varieties whether observed (from neutron probe) or predicted (from EMI) soil moisture values are used. To assess the ranking improvement the predicted values of the global, local and plocal models are averaged by variety. Then the Spearman's rank correlation is computed between the observed and the predicted θ_a (or $\Delta\theta_a$). The Spearman's rank correlation has the advantage to be directly related to the ranking of the variety which is a commonly used metric in crop breeding. A high value for this coefficient means, in our case, that higher predicted θ_a is associated with higher observed θ_a or that larger predicted θ_a differences are associated with larger observed θ_a differences, from examining absolute values or differences, respectively.

Figure 5.12a shows the Spearman's rank correlations for the multi-offsets (M2) model using the baseline θ_a^{ref} as predictor of the local offsets. Figure 5.12b shows the Spearman's rank correlations for the multi-slopes (M3) model using the baseline σ_a^{ref} as predictor of the local slopes.

Using the data in this study, the global models offer poor correlation compared to the local models, due to the heterogeneity of the σ-θ relationship. This is true for all coil configurations. The plocal models, i.e. the models using the predicted local parameters, show higher correlation compared to their global equivalent. For the multi-offsets model the improvement between global
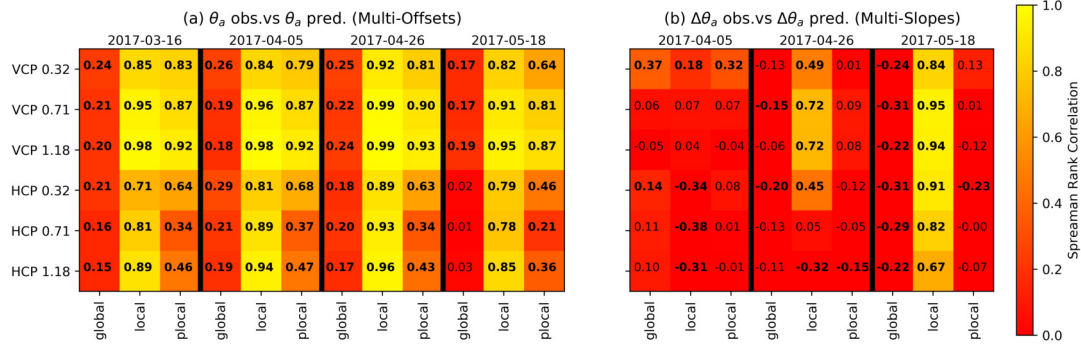
Figure 5.12 – Improvement in variety ranking in terms of the Spearman's rank correlation coefficient for (a) the multi-offsets and (b) the multi-slopes models. Each row of the table corresponds to a coil configuration. The columns are grouped by dates and subdivided into global, local and plocal models. The global models use field-specific parameters, the local models use plot-specific parameters estimated using all the data available. The plocal model use the predicted plot-specific parameters estimated from baseline measurements (as in Figure 5.8b and Figure 5.9b). Bold numbers denote a significant correlation ($p < 0.05$).

and the plocal is substantial (Figure 5.12a). When considering changes in soil moisture content (Figure 5.12b), the correlation with the global model is sometimes negative. This is a concern as it means that an increase in σ_a can be associated with a decrease in θ_a following application of the global model. The local multi-slopes models increases this correlation substantially, especially for later dates. However, the plocal multi-slopes model shows relatively poor correlation even if it can compensate for the negative correlation observed in the global model in some cases.

5.4   Discussion

5.4.1   Methodological limitations

The approach presented in this manuscript relies on apparent and not depth-specific electrical conductivity measurements to avoid the uncertainty arising from EMI inversion. Hence, we converted soil moisture content to apparent values using the practical cumulative sensitivity function (McNeill, 1980). However, the latter can have limitations especially on heterogeneous conductive soils. To estimate the errors that can arise from using the cumulative sensitivity function, Maxwell's equations can be used to reconstruct sensitivity functions based on a synthetic two layers profile comparable to what is observed in the field (Callegary et al., 2007). Both sensitivity functions are then used to compute the apparent soil moisture content. The maximum discrepancy between the two approaches is 0.01 cm3/cm3, which is similar to the neutron probe accuracy (0.01 cm3/cm3). Given the magnitude of the errors, this probably has a more important impact on the changes in soil moisture content than on the absolute values. This might

explain why the multi-slopes model works less well than the multi-offsets model in this study.

The dynamics of the soil moisture is complex and isolating the effect of root activity is challenging. Whenever possible, measurements were collected at increasing potential soil moisture deficit and away from significant rainfall events (Figure 5.3). The drying observed in cropped plots compared to fallow plots suggests a substantial effect of the root activity (Figure 5.3). However, the proposed approach does not aim at univocally measuring root water uptake but rather at comparing soil moisture variation mainly induced by root activity for the different varieties.

The models described in the manuscript are simple linear models. More complex relationships can be used to relate soil moisture to electrical conductivity. For example, an exponential model was initially tested and showed similar performance to the linear model (see section 3.5), hence the simplest model is chosen. In the linear models presented, the slope can be related to the soil surface conductivity while the offset is more a function of the pore water conductivity. Both are functions of the soil texture and porosity (Garré *et al.*, 2011). We do not have the information to investigate further the impact of these soil properties on the pedophysical parameters we derived for this field.

This study assumes that the samples taken on each plot (EMI, NP) are representative of the entire plot and that no substantial heterogeneity exists within the plot itself. While we have no data to assess that this assumption is fulfilled for all the plots, the inverted ERT sections, which span 5.75 out of the 9 meters of the plot length, suggest that this is the case.

One can question if the plot is the appropriate scale at which to investigate the variability of the θ-σ relationships. The use of variogram analysis can certainly help to determine the appropriate length-scale at which the heterogeneity occurs. However, this method was not explored in this study as our approach relies on the plot-scale for practical reasons and to be consistent with additional phenotyping measurements at the site.

Finally, it has been assumed that the root system of the crop itself did not significantly contribute to the soil bulk apparent conductivity. While there is evidence that suggests that coarser roots can effect the soil bulk electrical conductivity (Amato *et al.*, 2008; Mary *et al.*, 2017), finer herbaceous roots have been found to have a signal in magnitude similar to the effect of grain size or soil moisture content (Amato *et al.*, 2009). Nevertheless, recent studies were able to isolate the electrical signature of roots themselves (Tsukanov & Schwartz, 2020). This could have great potential for phenotyping applications.

5.4.2   Ranking performance

Fitting a global model with field-specific parameters to all the data can lead to a satisfactory prediction of the soil moisture content particularly if the differences expected between the treatments are large such as for different types of vegetation (Jayawickreme *et al.*, 2010), between

fallow and cropped plots or between different soil types. However, when comparing a large number of similar varieties this global model may be limited (Figure 5.12). In a phenotyping application, as here, using of such a relationship may lead to false ranking of variates when using geophysical data (Figure 5.12). As observed by Farahani *et al.* (2005) for non-saline soil, higher σ_a is not always associated with higher soil moisture. Taking into account differences, it can also be seen that a large reduction in σ_a is also not always associated with a large reduction in θ_a. The negative correlations sometimes observed are of concern as they lead to very different varieties ranking whether we consider σ_a or θ_a (Figure 5.12). The use of local parameters in the σ-θ relationship increases the Spearman's rank correlation for later dates as the soil moisture differences from the baseline become larger. The large number of parameters needed to fit the local models (linear, multi-offsets or multi-slopes) can be reasonably reduced using a relationship between the local parameters and the baseline σ_a or θ_a fitted on a subset of plots. The resulting plocal models that use those predicted parameters increase the accuracy of the prediction compared to global models (Figure 5.10). The coefficient of determination (R^2) is often similar or higher to the ones of the corresponding global models but the ranking assessed (using the Spearman's rank correlation) is usually better (Figure 5.12). Note that the R^2 achieved are all below 0.6 which is relatively poor compared to what could potentially be achieved with a local relationship for all the plots (Figure 5.6b). Indeed, this improvement is mainly limited by the quality of the relationship between the local parameters and the predictors (Figure 5.8b and Figure 5.9b). Hence, the need to select plots which span a wide range of conductivities to be monitored for both σ and θ in order to have a more robust fit that is representative of the entire field.

5.4.3   Local models and parameters predictability

As seen in Figure 5.6, the offsets of the linear or multi-offsets models are mainly related to the baseline θ_a. There is also a slight positive trend between the baseline σ_a and the offsets of the linear model but it is relatively weak compared to θ_a and it completely vanishes in the multi-offsets model. The simplification of the linear model to a multi-offsets model amplifies this dependence on the baseline θ_a. Wetter plots tend to stay wetter compared to other plots surveyed at the same time. This can be seen on Figure 5.4a where each plot follows its own increasing line. This strong offset effect also explains why the relative change approach described earlier does not work well in this case. Given Equation 5.3, the offset is not negligible and so the equation cannot be simplified to Equation 5.4. That is why differences (Figure 5.4b) and relative changes (Figure 5.4c) are similar. If the offsets were negligible, Figure 5.4c would show a single line.

The local slopes of the local linear model are well correlated with the baseline σ_a. Considering differences, the multi-slopes model also shows good correlation between the local slopes and the
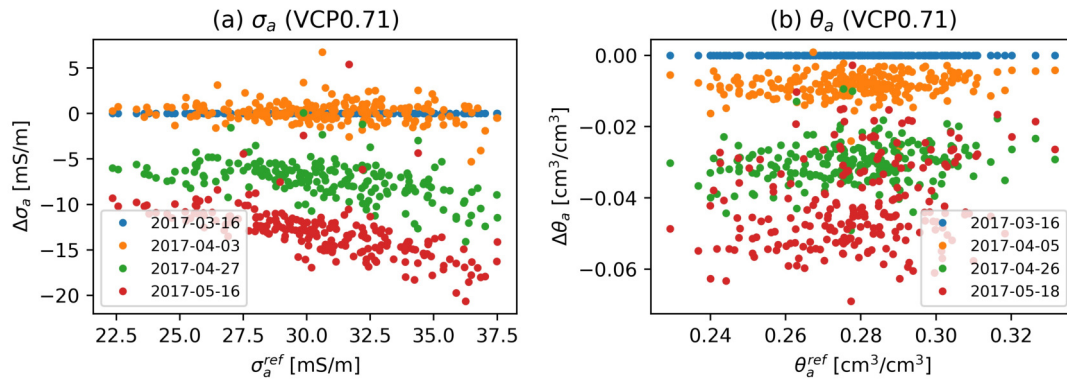
Figure 5.13 – Differences in σ_a (a) and θ_a (b) for VCP0.71 plotted against their respective baseline measurements for the different survey dates (different colours). There is larger decrease in σ_a for higher σ_a^{ref} in (a) while such a downward trend cannot be seen for θ (b).

baseline σ_a. The conical shape of the data shown in Figure 5.4b and Figure 5.9a for the differences illustrates how different plots have different slopes. Stanley *et al.* (2014) show how the slopes of the σ-θ relationships vary between two sites with contrasting textures: sites with higher clay content, for example, result in greater values than those from sandier locations.

The multi-offsets and multi-slopes models have one contrasting assumption. The former assumes a unique slope for the entire field while the latter uses plot-specific slopes. Having both plot-specific offsets and slopes leads to the local linear model but its local parameters are difficult to predict using baseline measurement (Figure 5.6) and hence leads to poor estimates (Figure 5.10). As the relationship between σ_a-θ_a is largely offset dominated, we decided to fix the slope in the multi-offsets model to reduce the number of local parameters. For the differences, the effect of the offsets disappeared (Equation 5.3) and only the effect of the slopes has an impact on the relationship. This leads to the multi-slopes model (Equation 5.10).

As seen in Figure 5.13, the differences in observed σ_a are well correlated with the baseline readings. Larger reductions in σ_a are seen on plots with higher baseline σ_a (Figure 5.13a). Note that such a trend is not observed for θ_a (Figure 5.13b). The fact that the σ_a differences are still function of the baseline reveals that the baseline σ_a contains some information on how the σ_a is likely to change: larger reductions are expected in areas of higher baseline σ_a. This behaviour explains why the starting σ_a could be a good predictor of the slopes in the multi-slopes and linear models. Indeed, as the plots with higher baseline σ_a show a larger increase in σ_a with time for the same increase in θ_a, they need to have a smaller slope to compensate. Smaller slopes are then found for higher baseline σ_a (Figure 5.9b and Figure 5.6). We believe this is related to the heterogeneity of the soil texture of the field where some areas are richer in clay than others.

Plots with higher baseline σ_a tend also to have smaller offsets as well (Figure 5.6). But this relationship is not strong enough to be used for parameter prediction and θ_a is preferred as the

predictor (Figure 5.8b). Also, the prediction of the local parameters using the baseline readings is much better in the multi-offsets model (Figure 5.8b R^2=0.82) than in the multi-slope model (Figure 5.9b R^2=0.64). This can explain why the multi-slopes model using predicted local parameters show only a slight improvement in variety ranking compared to the multi-offsets model (Figure 5.12).

The multi-offsets and multi-slopes models are simplified ways to account for the variability due to the spatial heterogeneity of the θ-σ relationship. By reducing the number of local parameters compared to a local linear model, the local parameters are more correlated with baseline measurements and hence easier to predict based on a subset of plots. In that way, they increase the ranking of the varieties and the accuracy of the predicted θ_a compared to global models.

5.4.4 Improvement of the time-lapse approach

A key bottleneck in using the local models (M1 to M3) is the predictability of the large number of local parameters they require. In this study an approach was chosen where both variables (θ_a and σ_a) are recorded on a subset of plots. In this case the same 12 plots that served for the ERT calibration of the EMI data were arbitrarily chosen as they are well distributed across the field and span the whole range of observed baseline values. In our case, a sample of 12 was a large enough number to reach the minimum RMSE achievable (Figure 5.11). Given the local parameters found on the selected plots, a relationship can be derived using the baseline σ_a or θ_a. This relationship can then be used to predict the values of the local parameters for the other plots. We believe that geostatistical tools can also be used to determine the number of sampling locations. However, we have not tested these in this paper.

Considering the above, we propose an improvement to the time-lapse approach described earlier to monitor the changes in soil moisture for large crop breeding experiment. After the first baseline EMI survey, plots with contrasting σ_a are selected and equipped with soil moisture sensors (such as neutron probe access tube). The data collected on those plots will allow the estimation of the parameters for the multi-offsets and multi-slopes models. Those parameters can then be expanded to the other plots using the baseline measurements (Figure 5.8b and Figure 5.9b). The new approach is as follows.

1. Baseline survey on all the plots to acquire σ_a^{ref} and θ_a^{ref}: - multi-slopes: EMI with all configurations (σ_a^{ref}); - multi-offsets: soil moisture measurements for all depths available to build an apparent soil moisture content measurements (θ_a^{ref})

2. Selection of plots with contrasting σ_a to be equipped with θ sensors

3. Time-lapse EMI on all the plots and time-lapse θ on the selected plots: collection of multiple σ_a-θ_a datasets

4. Fit the multi-slopes (Equation 5.10) and multi-offsets (Equation 5.9) models on the selected plots to obtain the value of the local parameters: slope a_i for multi-slopes and offset b_i for multi-offset

5. Fit of linear relationship between those local parameters and the baseline value of the selected plots as in Figure 5.8b and Figure 5.9b: a_i σ_a^{ref} and b_i θ_a^{ref}

6. Those linear relationships are then used to predict the local parameters a_i and b_i on the other plots using their respective baseline measurements σ_a^{ref} / θ_a^{ref}

This new approach offers a trade-off between equipping all the plots with soil moisture sensors in order to fit a local models and using a unique global relationship for the entire field. Note that if a multi-offsets model is to be derived, baseline θ data are still needed as they are the best predictors of the local offsets.

5.4.5   Analysis of the residuals

An increase in residuals can arise due the large number of local parameters. However, as Figure 14 shows, there is no substantial increase in the distribution of those residuals for the predicted local models compared to the global and local models. We can also see from Figure 5.8b and Figure 5.9b that even if the relationship is not perfectly fitted, the predicted parameters tend to stay in a reasonable range, avoiding the generation of outliers. Note that the residual for the multi-slopes model are smaller than the residuals for the multi-offsets as the range of $\Delta\theta_a$ (0 to -0.07) is smaller than the range of θ_a (0.15 to 0.35).
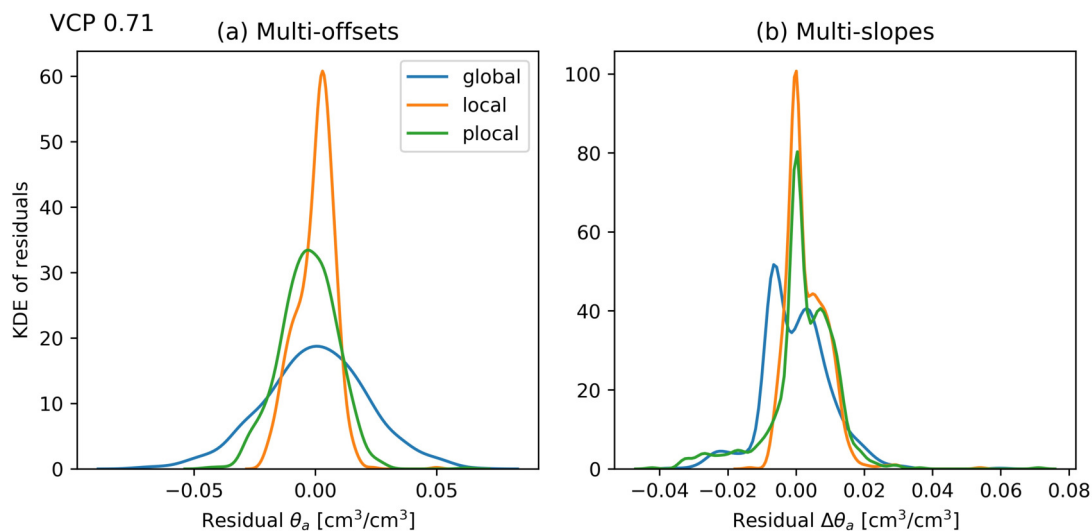
Figure 5.14 – Kernel density estimate (KDE) of the residuals for the multi-offsets (a) and the multi-slopes (b) models for VCP0.71. For each the global model represent a global (field-scale) linear relationship while the local models use plot-specific parameters. The plocal model is the local model with the plot-specific parameters predicted from baseline θ_a or σ_a.

5.5   Conclusions

High-throughput geophysical tools, in this case time-lapse EMI, offer great potential as a proxy measurement of soil moisture differences. When measurements are collected over increasing soil drying during crop growth, they may be linked to root activity in non-irrigated crop breeding field trials. The usual time-lapse approach is useful for removing the static effects of soil electrical conductivity but can be limited for ranking a large number of similar varieties in a heterogeneous environment. The spatial heterogeneity of the σ-θ relationship at the field scale has an impact on the ranking of the varieties and using a field-specific global relationship can lead to misleading interpretation. The proposed multi-offsets and multi-slopes models try to account for this heterogeneity by using plot-specific parameters that can be estimated from the baseline measurements. This improves the variety ranking between EMI and neutron probe data. A practical approach is proposed for such studies in which a baseline EMI survey is used to target sites for soil moisture monitoring, thus enhancing the ability to formulate predictions of the local σ-θ relationships. Although all the processing presented here was done with apparent conductivity measurements, however, the same process can be applied to depth-specific (inverted) measurements.

Acknowledgements

Chapter 6

Time-intensive geoelectrical monitoring under winter wheat

Guillaume Blanchy[1,2], Nicolas Virlet[2], Pouria Sadeghi-Tehran[2], Christopher W. Watts[2], Malcolm J. Hawkesford[2], William R. Whalley[2], Andrew Binley[1]

[1] Lancaster University, Lancaster, Lancashire LA1 4YW, UK

[2] Rothamsted Research, Harpenden, Hertfordshire AL5 2JQ, UK

Authorship statement

The PhD author set up the geophysical acquisition system, processed the data and wrote the manuscript. Other co-authors provided additional (non-geophysical) data and feedback on the manuscript. Andrew Binley provided additional ideas for the paper and edits on the manuscript.

Abstract

Several studies have explored the potential of electrical resistivity tomography to monitor changes in soil moisture associated with the root water uptake of different crops. Such studies usually use a set of limited below-ground measurements throughout the growth season but are often unable to get a complete picture of the dynamics of the processes. With the development of high-throughput phenotyping platforms, we now have the capability to collect more frequent above-ground measurements, such as canopy cover, enabling the comparison with below-ground data. In this study hourly DC resistivity data were collected under the Field Scanalyzer platform at Rothamsted Research with different winter wheat varieties and nitrogen treatments in 2018 and 2019. Results from both years demonstrate the importance of applying the temperature correction to interpret hourly electrical conductivity (EC) data. Crops which received larger amounts of nitrogen showed larger canopy cover and more rapid changes in EC, especially during large rainfall events. The varieties showed contrasted heights although this does not appear to have influenced EC dynamics. The daily cyclic component of the EC signal was extracted by decomposing the time series. A shift in this daily component was observed during the growth season. For crops with appreciable difference in canopy cover, high frequency DC resistivity monitoring was able to distinguish the different below-ground behaviors. The results also highlight how coarse temporal sampling may affect interpretation of resistivity data from crop monitoring studies.

6.1   Introduction

6.1.1   Field phenotyping

Senapati & Semenov (2020) show that European wheat varieties still have genetic potential to be exploited through breeding programs. Traits such as optimal root water uptake are present in the genetic population but still need to be selected and transferred into commercial varieties via crop breeding. To create new varieties with desirable traits (e.g. high yield, short stem, deep rooting, etc.), crop breeders cross other varieties which exhibit one or several of the desired traits. This process generates large number of different genotypes (or lines). To select which genotype possesses which traits, all lines are grown and their respective phenotype (i.e. the combination of all traits) is assessed. The lines which show desired traits are selected and can potentially become new varieties. Although this is a simplistic description of crop breeding techniques, it provides a context for this study.

One of the usual step to assess crop phenotype is to grow the different lines in large field fields. This step can be labor-intensive due the large number of lines to screen, leading to a "phenotyping bottleneck" (Furbank & Tester, 2011). To relieve it, new tools are being developed

(Araus & Cairns, 2014; Atkinson *et al.*, 2019). Among them, automated high throughput phenotyping platforms (HTPPs) permit the collection of many above-ground traits automatically (Prasanna *et al.*, 2013). An example of such infrastructure is the Field Scanalyzer facility at Rothamsted Research (Virlet *et al.*, 2017). Despite this progress, there has been less advance in the development of below-ground methods (Atkinson *et al.*, 2019). Geophysical methods, such as ERT, electromagnetic induction and ground penetrating radar, have been identified as promising candidates to fill this gap (Araus & Cairns, 2014; Atkinson *et al.*, 2019).

6.1.2   Geoelectrical monitoring in agriculture

Geophysical methods can image near-surface processes at multiple-scales (Binley *et al.*, 2015) and hence have a great potential for agricultural applications, e.g. for assessing the spatial and temporal distribution of soil water. Geoelectrical methods, and more specifically electrical resistivity tomography (ERT), has proven useful in imaging variation in soil moisture in several field applications (Michot *et al.*, 2003; Srayeddin & Doussan, 2009; Whalley *et al.*, 2017). ERT data are usually collected at regular time intervals enabling to separate the static and dynamic components of the soil electrical conductivity. The dynamic component is usually dominated by the change in soil moisture caused by various processes, in particular plant water uptake and evaporation. The static component is usually linked to soil textural properties such as clay content. Such time-lapse studies have been used to investigate the root zone moisture interaction for different ecosystems (Jayawickreme *et al.*, 2008). At smaller scales, ERT monitoring has been applied in orchards to investigate, in 2D and 3D, the soil moisture dynamics influenced by the root water uptake and irrigation strategies (Cassiani *et al.*, 2015; Consoli *et al.*, 2017; Vanella *et al.*, 2018). In herbaceous plants, time-lapse ERT was used to determine the spatial pattern of root water uptake of corn and sorghum in irrigated conditions (Srayeddin & Doussan, 2009) as well as corn with cover crops (Michot *et al.*, 2003). More recently, Coussement *et al.* (2018) used 2D ERT monitoring to measure the effects of a tree border on the soil moisture of a corn field. At the plot scale, Whalley *et al.* (2017) used time-lapse ERT to differentiate root water uptake of different wheat varieties.

All the studies above used time-lapse monitoring which usually involves collecting a few sets of ERT measurements during the growth season of the crop or around specific irrigation events. As such, they provide a few snapshots of the soil electrical conductivity, showing the effects of the seasonal processes. Hourly monitoring over long periods are rare but it has the potential to offer more insight into the dynamics of plant-soil-water interactions. For example, Vanella *et al.* (2018) use hourly 3D ERT monitoring to image the effects of full irrigation and partial root zone drying on an orange tree. They highlight that access to time-intensive monitoring provides more information on the soil moisture dynamics than less frequent measurements under specific

transient conditions. Mares *et al.* (2016) linked the diurnal pattern of soil electrical conductivity with the sap flow movement in pine trees. At the laboratory scale, Werban *et al.* (2008) monitored at hourly intervals the soil moisture beneath a lupin plant using 2D ERT and estimated the root water uptake of the plant. In addition to being able to follow the dynamics of specific events, hourly measurements have the potential to look at daily dynamics. Finally, another advantage of hourly scale sampling is that it is closer to the scale at which physiological processes of the plant take place. Given the wide availability of automated monitoring ERT instrumentation, high frequency below-ground geophysical measurements may offer more information for crop breeding studies.

To analyze the value of geoelectrical monitoring under HTPP in a phenotyping context, this paper focuses on the following research questions. (i) What is the potential of geophysical tools for monitoring below-ground dynamics? (ii) How can geophysically-derived below-ground information be linked to above-ground traits dynamics? (iii) What are the capabilities and limitations of geoelectrical monitoring for phenotyping applications?

6.2   Material and methods

6.2.1   Experimental setup

The experiments were carried out at Rothamsted Research, UK (51°48'34.56"N, 0°21'22.68"W) in Great Field, under the Field Scanalyzer platform area (Virlet *et al.*, 2017). The platform covers a flat area of 0.12 ha. The soil is described as a Luvisol (WRB) and is composed of a loamy top layer (0.3 m) over a more clayey layer with flints (Batcombe). The soil drainage can be impeded by this second layer especially in the areas around the platform due to heavy traffic during the construction. Two experiments were conducted during the growing season in 2017–2018 (hereafter referred to as 2018) and 2018–2019 (hereafter referred to as 2019) under rainfed conditions.

In 2018, three different varieties of winter wheat (*Triticum aestivum* L. var. Mercia Rht3, Mercia RhtC and Shamrock) were sown on 2017-10-30 (all dates are expressed in ISO 8601 format) in "sowing plots" of 0.6 m length by 1 m width with a planting density of 350 seeds/m2 and were grown under normal UK rate nitrogen (200 kgN/ha). Each "sowing plot", made up of two subplots, 0.6 m by 0.5 m, was sown with the same variety. Two continuous "sowing plots" of the same variety, were grouped to form a plot unit for this experimentation. This design was inherited from a larger experiment taking place in the same field. Each plot was equipped with 10 stainless steel electrodes of 0.1 m length with 0.15 m inter-electrode spacing. The electrodes were entirely buried (end of the electrode at 0.1 m below the surface) between the rows of wheat, hence not in contact with the plants. The pins of two nearby plots were attached to an array

of 24 pins (4 pins were discarded). The two ERT arrays were connected to an ERT monitoring system. The aim of this experiment was to identify any differences in soil electrical conductivity between the varieties.

In 2019, four plots of a nitrogen/variety trial sown on 2018-10-25 where equipped with an ERT array. Two varieties, Crusoe and Istabraq, were grown in plot of 3 m by 1 m under low and high nitrogen fertilization (50 kgN/ha and 350 kgN/ha as dry pellets, respectively). The first application of nitrogen 50 kgN/ha was made on 2019-03-08 and the second application was made on 2019-04-10. Figure 6.1 shows the four plots being monitored. Each plot was equipped of 12 stainless steel electrodes of 0.1 m length with 0.3 m inter-electrode spacing. As in the 2018 setup, the electrodes were entirely buried between the rows of wheat, avoiding contact with the plants. The pins of two nearby plots were attached to a 24 pins array that was connected to the ERT monitoring system.
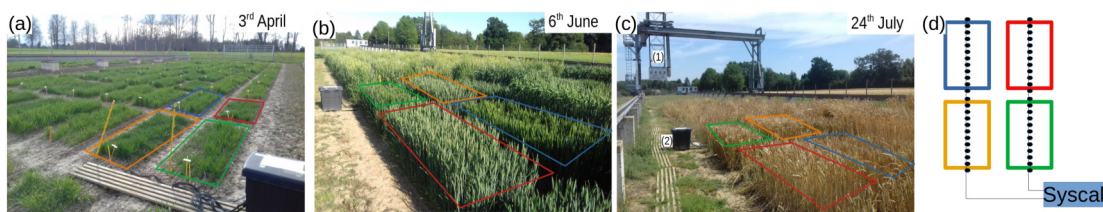
Figure 6.1 – Photographs of the experiment under the Field Scanalyzer facility at Rothamsted Research in (a) April, (b) June and (c) July 2019. (c) Shows the box containing the different sensors (marked (1) and black box marked (2) contains the ERT monitoring system connected to arrays in the four plots. The variety and nitrogen treatment of the plots are identified by colored rectangles: (blue) Crusoe 50 kgN/ha, (orange) Istabraq 350 kgN/ha, (green) Crusoe 350 kgN/ha, (red) Istabraq 50 kgN/ha.(d) shows the plan of the installation for 2019.

6.2.2 Above-ground variables

The above ground data were collected by the Field Scanalyzer platform (Virlet et al., 2017). The growth parameters were collected from RGB camera (Prosilica GT3300, Allied Vision, 3296 x 2472 pixels) for the canopy cover and from the 3D laser scanner (Fraunhofer Institute) for height.

Canopy cover values were derived from the RGB images and expressed as a percentage of the image covered by green pixels belonging to the plot canopy (Sadeghi-Tehran & Hawkesford, 2017). The height of the crop was obtained from the 3D cloud points using the 98th percentile of the vertical coordinates of the cloud points (adapting from Lyra et al., unpublished). The height and canopy cover of the crops were available for both 2018 and 2019.

6.2.3   Geophysical data processing

Electrical resistivity tomography (ERT)

ERT measurements were collected using a remotely controlled Syscal Pro 48 (Iris Instruments, Orléans, France) at hourly intervals. In both years, the measurement sequence used was a dipole-dipole configuration (using one and two electrode spacing between the current/potential dipole and, respectively, eight and six levels between the current and potential dipoles) with electrode spacing of 0.15 m (2018) and 0.3 m (2018). Reciprocal measurements were included in the sequence after each normal set. Additional dummy quadrupoles (40 for the entire sequence) were also added to optimize the sequence (specific to the Syscal instrument); in total, the sequence for both years was composed of 496 quadrupoles (124 per plot).

In 2018, the system was operational between the end of May to July to capture rainfall events when the wheat was fully mature (between flowering and harvest). In 2019, the ERT monitoring system ran successfully from February to the end of August (flowering around 14th June) with a few data gaps. At the end of May, current injection errors were noted and so the instrument was replaced with another Syscal Pro 48 to allow monitoring until September. We noticed that the data from this second device had higher reciprocal errors than the original one, in particular for larger dipoles. Despite this, the datasets from both instruments show consistency in dynamics by reacting to rainfall events and showing similar daily fluctuations.

The ERT data collected were processed using the ResIPy software (Blanchy *et al.*, 2020b) that makes use of the Occam's based R2 inversion code (Binley, 2015). Because of the short electrode spacing compared to the length of the electrode, the nodes of the mesh corresponding to the electrode were positioned at 60% of the electrode length (Rücker & Günther, 2011). Given the relatively small number of quadrupoles per plot, surveys were combined in batches of 24 (a day) and a power-law error model was fitted for each batch using the binned reciprocal errors. This approach ensures a sufficient number of data points to obtain a robust error model, while allowing the error model to vary throughout the season.. Each dataset was then inverted independently in a batch mode. The difference inversion method of LaBrecque & Yang (2001) did not work well for our dataset when applied over the entire season either using a single background survey or applied over consecutive surveys. For 2019, it produced satisfactory results until May, before large changes in electrical conductivity occurred. After May 2019, the difference approach was not able to reproduce the small variations in electrical conductivity observed at hourly intervals in the apparent data. This was partly due to the higher reciprocal errors observed after May that forces the inversion towards a smooth solution. Inverting independent surveys and constraining them to the background survey produced better results for the earlier dates. However, after May 2019, this approach produced inverted sections that were too biased towards the background image. For this reason we decided to invert each survey independently with its own error model.

Although this approach does not take advantage of difference or background regularization option that could potentially reduce time-lapse artifacts, it still produces inversions that shows clear temporal dynamics. Each inverted section was then averaged into a 1D profiles per plot used in the rest of the study. The 1D profiles were computed for ease of comparison between plots.

EC temperature correction

It is essential that the temperature correction is applied to be able to distinguish between soil moisture and temperature effects on electrical conductivity. The variation in bulk electrical conductivity with temperature is due primarily to two factors: the change in the ion mobility and the change and on the viscosity of the pore water (Hayley et al., 2007). To account for the effect of temperature, different models have been developed. Ma et al. (2011) compared the different corrections found in the literature and concluded that a ratio model performs well in the range 3 to 47 °C. Beyond this range, the empirical model proposed by Sheets & Hendrickx (1995), which appears in the corrected form in Corwin & Lesch (2005), is more appropriate. Hayashi (2004) explored the range of applicability of the ratio model and concluded that this model is applicable within the 0-30°C temperature range, which is similar to the conclusion of Ma et al. (2011).

Given that our soil temperature lies within the 0-30°C range, we applied the ratio model to our data with a 2% increase per degree:

$$\sigma_{25} = \frac{\sigma_T}{1 + 0.02 * (T - 25)} \tag{6.1}$$

where σ_{25} is the equivalent electrical conductivity at 25 °C, σ_T is the bulk electrical conductivity measured at the temperature T in °C. Note that this model makes the correction factor dependent on $\sigma 25$. For our study we used the hourly soil temperature values measured at five depths (0.1, 0.2, 0.3, 0.5, 1 m) under grass from the Rothamsted weather station (e-RA Rothamsted electronic archive) located about 100 m from the experimental plots. The temperatures were linearly interpolated with depth to match the depths of the inverted electrical conductivities. The effect of the temperature correction can be seen in Figure 6.2. All inverted conductivity values presented hereafter have been temperature corrected using this relationship.

6.2.4 Time series analysis

The decomposition of the time series of electrical conductivities was applied to the 2019 dataset because it is longer and allows analysis of seasonal change (not possible with the shorter 2018 dataset). For a selected depth, the series of interest is composed of temperature corrected inverted electrical conductivities from February to September 2019. The signal is broken down into three

components using an additive model:

$$Y(t) = T(t) + S(t) + e(t) \tag{6.2}$$

where $Y(t)$ represent the raw signal, $T(t)$ represent the trend, $S(t)$ is the daily component, $e(t)$ is the residual. All components are dependent on time t. Note that the daily component is sometimes referred as the seasonality of the time series and represents repeating short-term cycles in the series. This decomposition is simple but enables the identification of different aspects of the signal. To decompose the signal, the algorithm proceeds as follows:

1. The period of the short-term cycles of the signal is identified. In this case, the signal shows a short-term cycle every 24h (daily).

2. A moving average is applied on the series with a window size corresponding to this period, this produces the trend.

3. The trend is subtracted from the raw signal and the resulting values are averaged for each period to form the daily component.

4. The residuals are obtained by subtracting the trend and the daily components from the raw data.

The algorithm was implemented using the '`seasonal_decompose()`' function of the statsmodels Python package (Seabold & Perktold, 2010).

6.3   Results

6.3.1   Effect of the soil temperature variations

Figure 6.2 shows the impact of the temperature correction by analyzing the cross-correlation between the soil temperature at 0.15 m depth and the corresponding averaged inverted conductivity from the plot of Crusoe 50 kgN/ha. The temperature correction has two main effects. First it increases the overall electrical conductivity to bring it to an equivalent electrical conductivity at 25°C. That allows us to compare different dates throughout the season. Second it decreases the cross-correlation between the two variables.

6.3.2   Inverted profiles

Figure 6.3 shows examples of the inverted resistivity section and their corresponding averaged inverted conductivity profiles for 2018 and 2019 experiments. For a given year, all profiles show similar values and pattern due to the proximity of the plots.
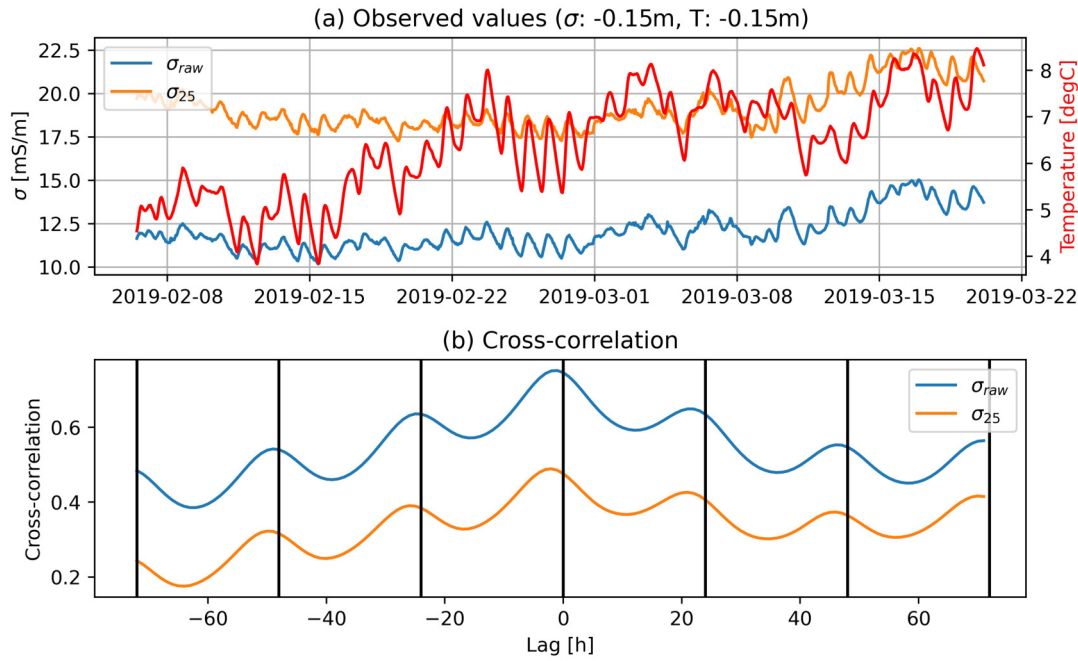
Figure 6.2 – (a) Example inverted conductivities values with and without the temperature correction. (b) Cross-correlation between the inverted electrical conductivity (corrected or not) and the soil temperature at 0.15 m depth. The inverted conductivities are extracted from the Crusoe 50 kgN/ha plot of the 2019 experiment. Similar graphs can be observed on the other plots.
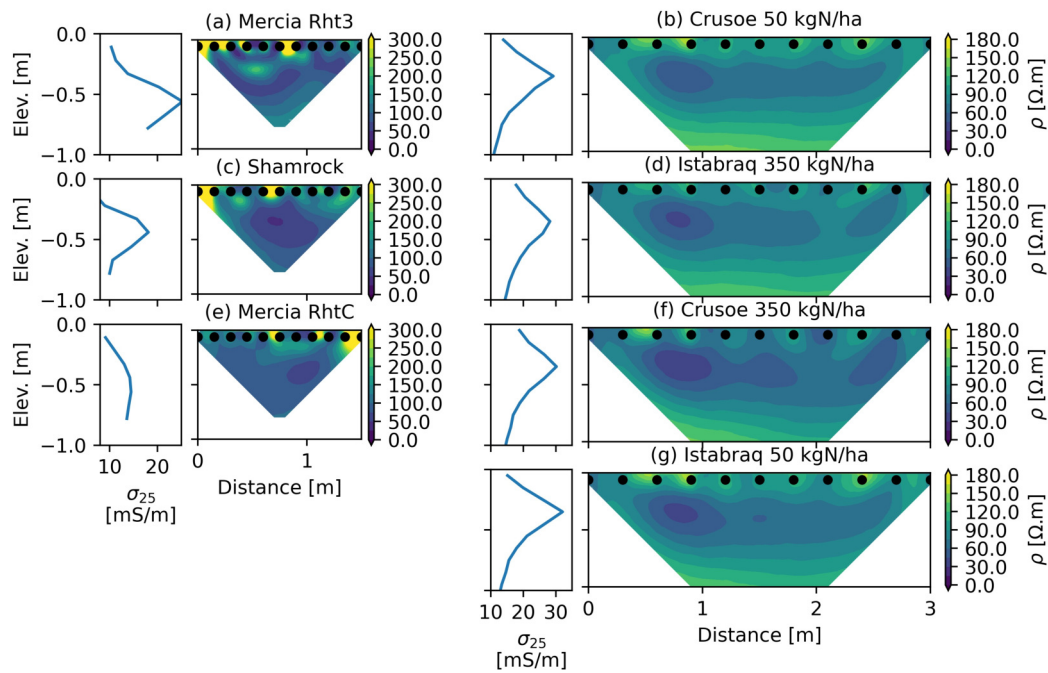
Figure 6.3 – Inverted resistivity sections and their corresponding temperature corrected averaged 1D profile for the three plots in 2018 (a,c,e) and the four plots in 2019 (b,d,f,g). Both taken on 15th June. Note that the resistivity and conductivity scales are different between 2018 and 2019.

6.3.3   Seasonal variations

Figure 6.4 and Figure 6.5 illustrate the time course of the different variables during the 2018 and 2019 experiments. In 2018, the ERT monitoring system successfully captured a large rainfall event that took place at the end of May. All varieties reached full canopy cover at the end of May and maximal height around mid-June. Figure 6.4d shows clearly the large increase in electrical conductivity due to the rainfall and the progressive soil drying afterwards. This effect is strongly attenuated at the depth of 0.44 m (Figure 6.4e). The daily averaged rates of decrease in electrical conductivity at 0.22 m between 2018-06-05 and 2018-07-01 are -0.12 m.S-1.d-1(Mercia Rht3), -0.10 m.S-1.d-1(Shamrock) and -0.15 m.S-1.d-1 (Mercia RhtC). Figure 6.4c shows clearly the different heights of the varieties with Mercia Rht3 being a dwarf variety while Mercia RhtC is a tall variety.
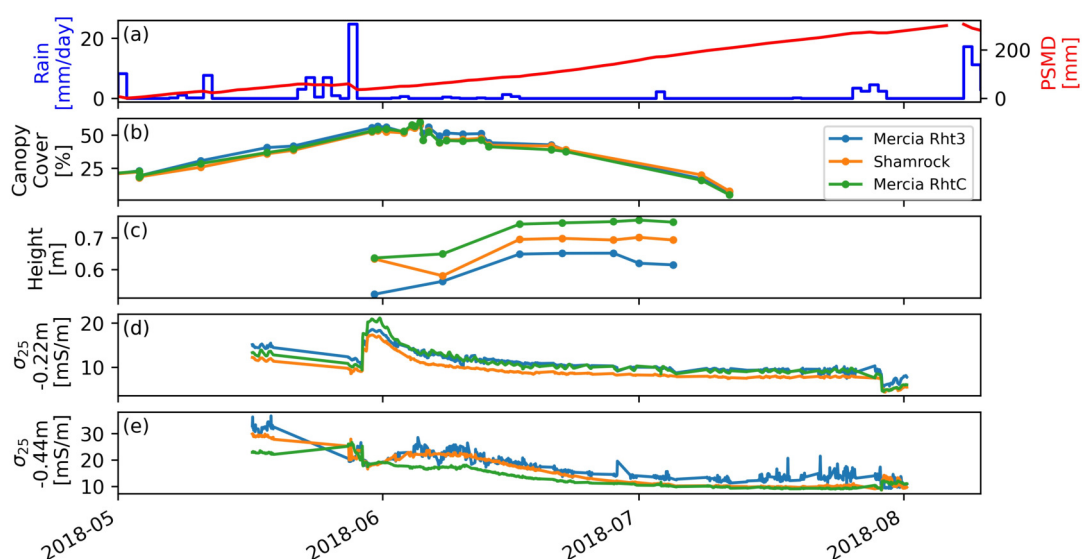
Figure 6.4 – Time course of different variables on the 2018 experiment with three different winter wheat lines (Rht3 Mercia, RhtC Mercia, Shamrock). (a) Daily precipitation and potential soil moisture deficit (PSMD). (b) Canopy cover development derived from RGB picture. Maximum canopy cover is reached from end of May and senescence start in the beginning of July. Canopy cover does not reach value higher than 80% because of the gaps between the subplots. (c) Increasing height of the crops. (d,e) Inverted temperature corrected electrical conductivity for each variety at 0.22 m and 0.44m depths, respectively.

Figure 6.5 shows the time course of the different variables collected in 2019. Figure 6.5a shows daily precipitation and potential soil moisture deficit (PSMD). The PSMD was obtained from meteorological variables measured at the Harpenden weather station (full methodology at: http://www.era.rothamsted.ac.uk/Met/derived_variables#PSMD). From the end of April,

the canopy cover of the two high N plots exceeded the canopy cover of the low N plots and reached a maximum by mid-June, irrespectively of the variety (Figure 6.5b). The canopy cover started to decrease in the beginning of July as an effect of the senescence. In contrast, the height of the crops appears to be related to the variety and less influenced by the nitrogen treatments (Figure 6.5c). Note however, that Istabraq 50 kgN/ha is slightly smaller than Istabraq 350 kgN/ha at the end of the season.

Figure 6.5d and Figure 6.5e show the temperature corrected inverted conductivity at depths of 0.15 m and 0.45 m, respectively. The shallower depth (Figure 6.5d) shows a peak around 2019-03-20 after the first application of fertilizer and then the electrical conductivity of all four plots starts to decrease coinciding with the measured increase in canopy cover. Two other peaks can be observed around 2019-05-10 and 2019-06-25 after significant rainfall events (Figure 6.5a). During these two events, Istabraq 350 kgN/ha and Crusoe 350 kgN/ha show larger increases in conductivity but also a more rapid decrease over the following days. A later rainfall event occurred at the end of August but no dramatic decrease in conductivity is seen following this as the crop has been harvested mid-August. The slight decrease observed could be attributed to the usual drying of the soil. The deeper depth presented in Figure 6.5e shows a more attenuated response to that in Figure 6.5d: no clear difference between the nitrogen treatments or the varieties can be seen. However, the two major rainfall events of 2019-05-10 and 2019-06-25 appear to drive a slight increase in electrical conductivity at depth, albeit much weaker than that seen at the shallow depth. Note also the increase in electrical conductivity for Crusoe 350 kgN/ha around 2019-03-20 at -0.45 m.
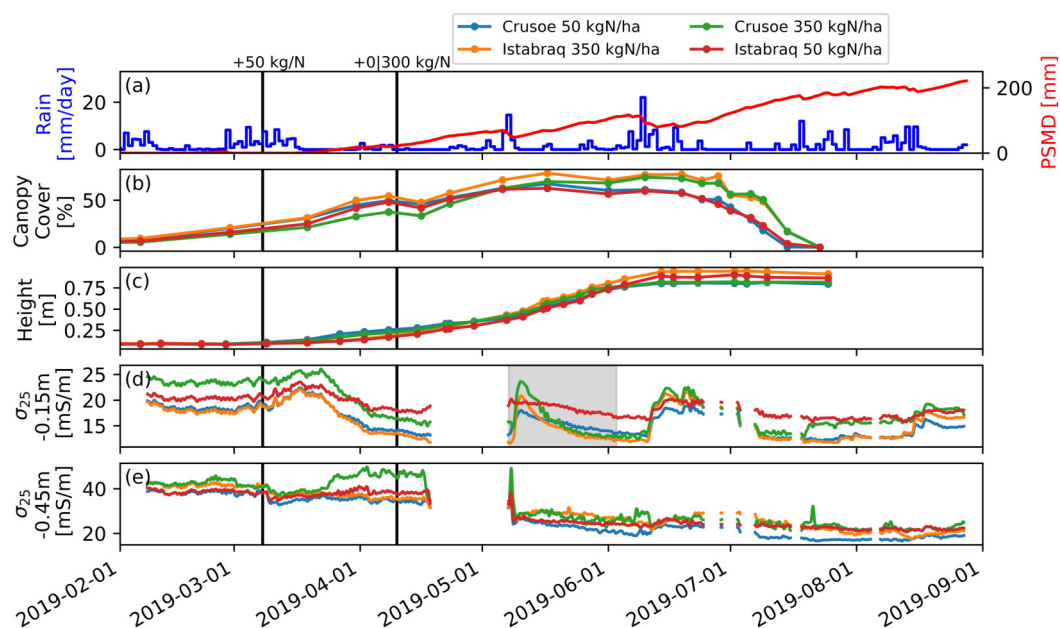
Figure 6.5 – Time course of different variables on the 2019 experiments with two winter wheat varieties (Istabraq and Crusoe) and two different nitrogen treatment (50 and 350 kgN/ha). (a) Daily precipitation and potential soil moisture deficit (PSMD). (b) Developing canopy cover determined from RGB picture. (c) Increase in crop heights over time. (d,e) Time course of the temperature corrected inverted electrical conductivity under the four crops. Note that a moving average of window 3 has been applied on the (d) and (e) to reduce the noise and remove outliers. The shaded area in (d) can be viewed enlarged in Figure 6.8. The two vertical black lines show when the nitrogen fertilizer was applied (2019-03-08 and 2019-04-10).

6.3.4   Time series analysis

Figure 6.6 shows the decomposition of a selected portion of the temperature-corrected and inverted conductivity curves during the first rainfall event, May 2019. The observed signal (Figure 6.6a) comprised a general trend (Figure 6.6b), a daily component (Figure 6.6c) and a residual component (Figure 6.6d) using the additive model described earlier. The diurnal characteristic of the signal is clearly shown by this analysis (Figure 6.6c) decreasing during the day and increasing during the night (shaded areas). This cycle is common to all four plots in May 2019.
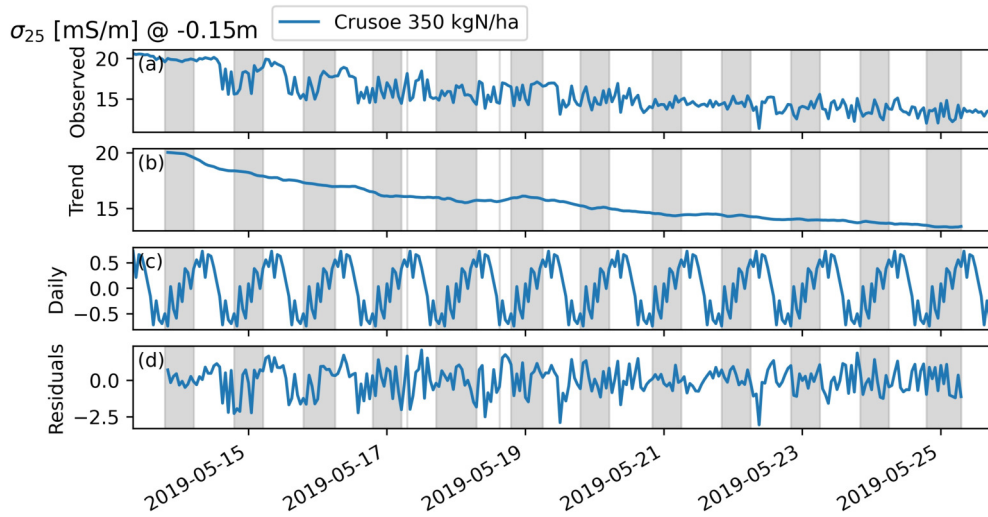
Figure 6.6 – (a) Portion of the temperature corrected inverted conductivity signal at 0.15 m depth after the main rainfall event of mid-May. Shaded areas represent the night. The signal is decomposed in three additive components: the trend (b), the daily component (also called seasonality) (c) and the residuals (d).

The same additive decomposition can be applied to different moving time windows of 7 days with two-day offsets between the windows. The daily component extracted is shown for each window in Figure 6.7 for the 0.15 m depth. The advantage of applying the decomposition on smaller time windows compared to the whole signal is that it allows us to see the evolution of the daily component through the season. In Figure 6.7, it can be seen that the lower part of the daily component (strong blue), initially around 6h00 in February progressively shifts down to 17h00 by the end of April, when the crops start to grow a mature canopy and extract more water from the soil. This shift is subtle but consistent among consecutive weeks. Note as well that in February and March (Figures 6.7b and c), the decrease in electrical conductivity occurs mainly during the night which is the opposite of what is observed later in the season, in May for instance (Figure 6.6c).
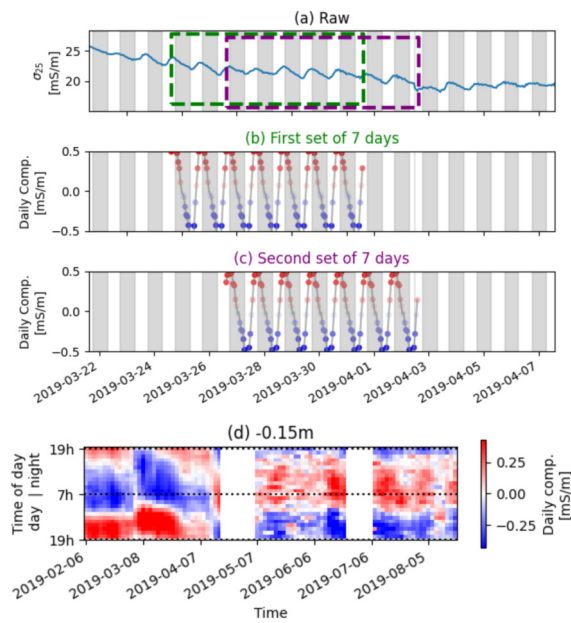
Figure 6.7 – Evolution of the daily component of the additive model fitted on a several moving windows of a week (7 days) with a two-day offset between consecutive windows. (a) Observed data (here the temperature corrected inverted conductivity at 0.15 m depth) and two windows. The first window of a week is extracted, and the additive decomposition is applied. The cyclic component is displayed in (b). A second window is chosen two days later, and the same process is repeated (c). The shaded area represents night. (d) Evolution of the daily components for each moving window over the whole growing season during night (19h – 7h) and day (7h - 19h). Moving windows spanning no data intervals have been removed.

6.3.5   Reaction to rainfall event

Figure 6.8 shows an enlarged graph during a major rainfall event at the end of May 2019. It illustrates how the shallow electrical conductivity of the two crops which, received larger amounts of nitrogen fertilizer, increase immediately after the large rainfall and then decrease at a greater rate over the following days. The average decrease rates in electrical conductivity are computed between 2019-05-11 and 2019-05-29 for each plot. When grouped by N treatments, high N plots decrease faster (-0.47 mS.m^{-1}.d^{-1}) than low N plots (-0.15 mS.m^{-1}.d^{-1}). This behavior was mainly observed at depths shallower than 0.2 m. The rates of decrease in electrical conductivity of the four plots correlated well (R^2=0.57) with their respective maximum canopy covers (Figure 6.5b) but not with their heights (R^2<0.01). Subsequent (albeit smaller) rainfalls do not have any visible impact on the electrical conductivity.
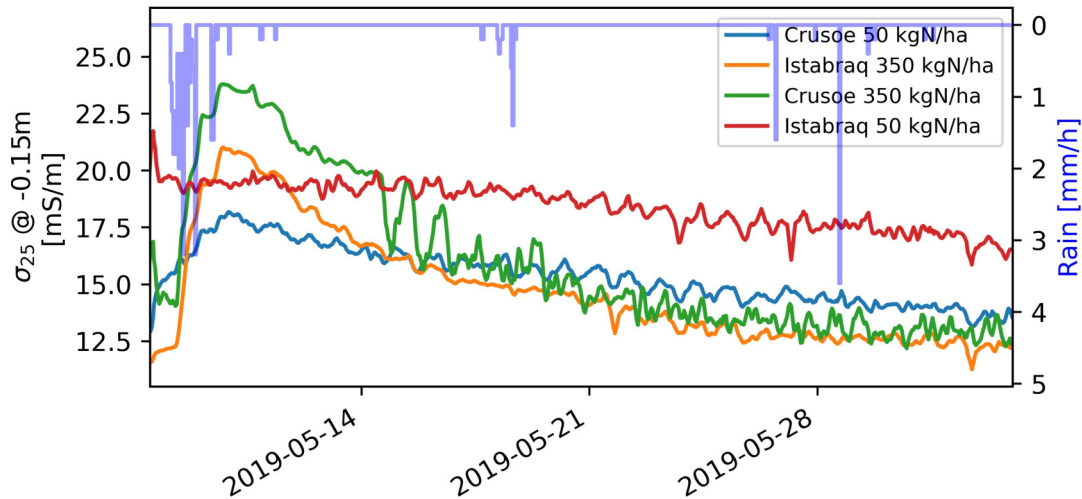
Figure 6.8 – Enlargement of the grey shaded area of Figure 6.5d showing the evolution of the inverted conductivity of the four crops under the Scanalyzer in 2019 during and after the major rainfall event at the end of May 2019. Note the faster decrease in electrical conductivity of the crops which received more nitrogen.

Table 6.1 – Summary of the yield of the different varieties in both years.

Winter Wheat Variety	N fertilizer	Year	Grain yield @ 85% [t/ha]	Straw yield @ 85% [t/ha]	Total biomass @ 85% [t/ha]
Mercia Rht3	-	2018	2.0	5.4	7.4
Shamrock	-	2018	5.6	7.9	13.5
Mercia RhtC	-	2018	6.5	8.1	14.6
Crusoe	50 kgN/ha	2019	10.0	10.7	20.7
Istabraq	50 kgN/ha	2019	10.5	10.1	20.6
Crusoe	350 kgN/ha	2019	12.0	11.8	23.8
Istabraq	350 kgN/ha	2019	13.6	13.6	27.2

6.3.6   Yield

For each year, the grain and straw dry weights were measured and converted to yield in t/ha at 85% dry matter (Table 6.1). The yield in 2018 was much smaller compared to 2019. This can be explained by the lack of rain in 2018 and several bird damages. In 2018, Mercia RhtC (tall variety) had the largest grain and straw yield while Mercia Rht3 (dwarf variety) had the lowest. In 2019, the two plots which received more nitrogen fertilizer had a higher grain and straw yield compared to those which only received one application of fertilizer. For the same rate of nitrogen fertilizer, Istabraq had higher yield than Cruose. In 2018, there was no clear relationship between the grain yield and the daily rate of decrease in shallow electrical conductivity after the large rainfall event (R^2=0.08). In contrast, in 2019, larger grain yield was associated with larger daily rate of decrease in shallow electrical conductivity after the major rainfall event at the end of May (R^2=0.52).

6.4   Discussion

6.4.1   Implementation of geoelectrical monitoring

The inversion of long-term time-lapse electrical resistivity data is challenging. In 2019, the procedure was made more difficult because of the higher reciprocal errors of the replacement instrument, used after May. Difference and background-constrained inversion were tested but both could not reproduce the diurnal dynamics observed in the apparent conductivity data during the entire season and most failed to converge at the end of the growing season. Difference inversion performed well when applied on the data collected before the first nitrogen application but failed to reproduce the variations observed in the apparent values afterwards. Difference inversion is usually effective when the surveys shared a high systematic error and a low random error but that might not be the case in this study. As a simpler approach, each survey was inverted individually with a power-law error model based on the binned reciprocal error of the batch of 24 consecutive surveys. We noticed that the inclusion of an error model greatly helps the inversion to converge and would recommend the addition of reciprocal measurements in automated sequence for this purpose. In applications of difference inversion type schemes, a different type of error model that reduces systematic errors can be considered (Lesparre *et al.*, 2019).

One important challenge that we met with the inversion of hourly geoelectrical data, was to be able to retain the day-night pattern observed in the apparent resistivity measurements following their inversion. In this study we successfully retrieved this pattern for shallower depths, but we noted that deeper depths do not show similar daily fluctuations (Figure 6.5e). Figure 6.9 compares the evolution of the apparent and inverted values for shallow and deeper depths. Apparent values show a daily pattern for shallow and for deep depths while the daily pattern is only visible in the shallow depth for the inverted values.. The current study mainly focuses on shallower depths as they exhibit faster responses to meteorological events but also because most of the root system of winter wheat usually lies above 0.3 m depth (see, for example, Hodgkinson *et al.* (2017)). Without detailed root data for our experiments we have to assume this to be the case here. Additionally, another reason for only observing the daily pattern at shallow depths is the structure of the soil texture. Indeed, the higher clay content of the soil below 0.3 m might have substantially slow down water fluxes and hence attenuated the fluctuations. This is a potential limitation of the current study site and the experiment would benefit from a repeat in a well-drained environment to see if these daily fluctuations can be observed deeper.
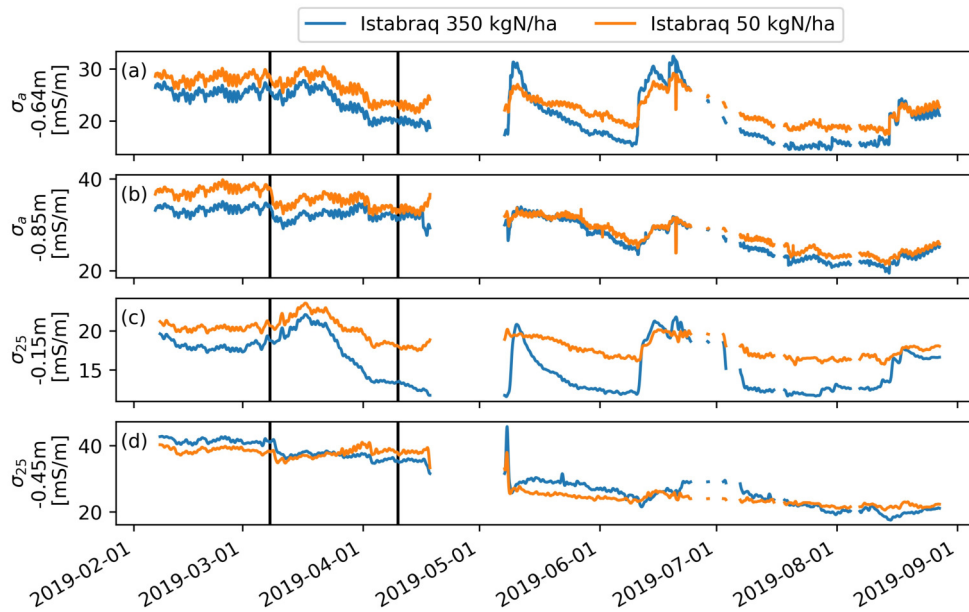
Figure 6.9 – Comparison between two apparent conductivities (a) and (b) and two inverted temperature corrected conductivities (c) and (d) for the two plots of Istabraq in 2019. Both (c) and (d) were smoothed by a moving average (window=3). Note that the inverted conductivities at deeper depths do not show strong daily fluctuation compared to the apparent resistivity data (compare plot (d) with (b)) but rather an attenuated version of the seasonal dynamics.

Finally, an important factor when measuring hourly electrical conductivity is the effect of soil temperature as shown by the cross-correlation plot of Figure 6.2b. The diurnal pattern of temperature strongly influences electrical conductivity, particularly at shallow depths. Applying the usual temperature correction using the ratio model (Equation 6.1) helps to reduce this effect and decreases the cross-correlation (Figure 6.2b).

6.4.2   Coupling with other above-ground variables

In 2018, the different wheat varieties did not show large difference in term of canopy cover which can be attributed to the lack of rain during the canopy expansion phase (Figure 6.3b). This might explain why no large difference in the dynamics of the inverted conductivities were observed between the varieties (Figure 6.3d and e). Figure 6.4d shows that the conductivity at -0.22 m under Mercia RhtC decreased slightly faster after a major rainfall event which might be linked to the larger canopy cover of the variety. In other field trials Hodgkinson *et al.* (2017) observed that the dwarf wheat variety (Mercia Rht3) has a deeper root system but that this does not lead to larger root water uptake. No links could be found between the yield and the dynamics of the electrical conductivity in 2018.

In contrast, large differences in canopy cover were observed in 2019 between the plots. The

dynamics of the electrical conductivity is clearly related to the development of the canopy cover when no major rainfall events occur (Figure 6.5b and c).

Figure 6.8 shows that the plots receiving more nitrogen show a larger increase in electrical conductivity during the rainfall event. One explanation could be that part of the nitrogen from the last application was still in the soil in granular form, and not yet in a form available to the crop. With the rainfall, it was dissolved again in the soil solution and caused a surge in the electrical conductivity. We did observe a small peak after the first application of fertilizer (Figure 6.5d). Once dissolved, the nitrogen is quickly taken up the roots resulting in a faster decrease of the soil electrical conductivity.Figure 6.6 This newly absorbed nitrogen can then be allocated to the growth of the crop, leading to an expansion of the canopy cover (Figure 6.5d). The decrease in electrical conductivity could also be due the crop water uptake which depends on the canopy cover. However, the rate of uptake of the different crops is likely to be comparable given their similar canopy cover prior to the event. In this study, separating the two effects is difficult without independent measure of the soil moisture.

There was no strong correlation between crop height and electrical conductivity. The crop height was more influenced by the variety and less by the nitrogen treatment. In contrast, the yield of the crops which received more nitrogen was much greater compared to those receiving less. However, for a given level of nitrogen (either 50 or 350 kgN/ha), Istabraq shows a slightly higher yield than Cruose. For example, Istabraq 350 kgN/ha has a higher grain yield (13.6 t/ha) than Crusoe 350 kgN/ha (12 t/ha).

6.4.3   Diurnal cycles

As previously stated, no direct measurements of soil moisture content were collected during these two experiments. However, the relationship between the electrical conductivity and the soil moisture content was known for the soil under the Scanalyzer. With it we can relate the electrical conductivity data from the graphs above to soil moisture content. However, given the suspected contribution of the nitrogen fertilizer to the electrical conductivity (mainly around large rainfall events), the focus here has been on electrical conductivity variation.

Diurnal patterns are present in the apparent conductivities measured (Figure 6.9a and b). Once inverted, and temperature corrected, those diurnal cycles are still visible mainly for shallower depths and attenuated for deeper depths (Figure 6.5d and e). In order to see if these patterns are related to crop activity, partitioning of the time series was performed. However, we acknowledge that univocally attributing the changes in electrical conductivity to root water uptake is not possible in this study.

Figure 6.6c shows that the daily component for all the plots tends to decrease during day and increase during night in May. Note that earlier in the season the opposite trend was observed

(Figure 6.6) when the crop had probably less effect on the dynamics of the soil moisture. The daily component is arguably noisy, and we explain this partly because of the noise in the original signal (Figure 6.6a) but also because this daily component is extracted as the mean of the periodic difference between the raw signal and the trend. One main limitation of the additive decomposition is that the daily component cannot vary in amplitude from one day to another. We hypothesize that this daily component is mainly influenced by the root water uptake of the crop - which follows a diurnal cycle as seen, for instance, in Verhoef *et al.* (2006) or Werban *et al.* (2008). The nightly increase observed from May could be due to soil moisture replenishment or hydraulic lift (Horton & Hart, 1998).

The same decomposition approach was applied on moving windows throughout the whole season (Figure 6.7) and revealed a shift from April onward in the daily component of the signal. This progressive shift appears at a time when the crops start to grow larger canopy cover and show large decrease in electrical conductivity (Figure 6.5d). Note also that the diurnal component of the signal was still strong in February when the crops were small and showed a decreasing electrical conductivity during night-time. Such a strong daily component in the signal for earlier dates is unexpected. It could be related to the fact that the temperature correction did not completely remove the cross-correlation between temperature and electrical conductivity (Figure 6.2). In this case there may be a residual effect of the temperature cycle that remains in the series. This effect is overcome later in the season by larger effects of the diurnal soil moisture dynamics.

6.5   Conclusion

This study shows hourly electrical resistivity monitoring applied to small scale agricultural plots with different wheat varieties and nitrogen treatments. A high cross-correlation with the soil temperature and the hourly electrical conductivity makes it essential for the application of a temperature correction. However, diurnal patterns in the electrical conductivity remains and our analysis suggest that this diurnal pattern is mainly influenced by plant activity particularly when the crops are fully grown. Distinguishing differences between varieties remains challenging, and we did not observe any large differences in electrical conductivity either in 2018 or 2019 experiments. However, the effect of nitrogen uptake could be clearly seen in the dynamics of the electrical conductivity during large rainfall events. We acknowledge the limitation of the approach to monitor a few experimental plots, but we believe that higher time resolution has enabled us to gain deeper insight into soil-plant dynamics than the usual coarser time-lapse monitoring, in particular during large rainfall and subsequent drying events but also at the daily scale. Specifically, the ERT monitoring system provided non-invasive depth-specific information that can be related to some above-ground measurements. As such, it offers a unique perspective

into the soil-water-plant interactions which is essential for breeding more resilient varieties.

Acknowledgments

Chapter 7

Discussion and Conclusion

7.1 Introduction

To help tomorrow's agriculture meet its productivity and sustainability goals but also to become more resilient to climate change induced stresses, such as drought, we need to adapt our agroecosystems. Improving agricultural practices is one aspect of this adaptation. Using management practices such as the ones defined by the FAO (http://www.fao.org/conservation-agriculture/en/) for conservation agriculture has potential to relieve the challenges we are facing. While the effectiveness of such practices can be partially estimated based on above-ground measurements, it is also essential to estimate the impact of these practices on the below-ground soil-plant-water interactions. However, monitoring soil moisture change at the field-scale is challenging. Satellite-based imagery often offers a resolution that is too coarse while 'point-like' sensors, such as TDR, are expensive to install in field-scale setups and constrained due to their measurement support volume. Soil coring is destructive, labour-intensive and prevents repeated measurements over the same area over time. In this context, geophysical methods offer a potentially powerful solution to study soil moisture processes at the field-scale with minimally invasive sensors. Using a time-lapse approach, geophysical methods have the potential to provide information on the change in soil moisture in relation to the different management practices and hence help to better characterise the effect and value of the practice on the agroecosystem.

Apart from developing and refining agricultural practices, another aspect concerns the crop itself. Crop breeding, which consists of creating and selecting the best varieties of a crop, initially relied mainly on above-ground traits that are easily measurable. However, in order to select varieties that are more resilient to water-related stresses, more information on the root system of the crop needs to be collected. While this information is easily available in greenhouse experiments, at the field-scale acquiring information on the root system, or its interaction with the soil, can be difficult, time-consuming and destructive in some cases. The use of geophysical methods, especially ERT and EMI, has proven useful in detecting soil drying driven by water uptake of different varieties in field-scale setups (Shanahan *et al.*, 2015; Whalley *et al.*, 2017). However, in large field experiment, the effectiveness of the approach might be hindered by different local pedophysical relationships due to the field heterogeneity. In addition to large-scale field trials, we have also focussed on high-throughput field phenotyping platforms, that offer crop breeders a more controlled and automated field environment to test the varieties. Under such a platform, our work aimed at estimating the potential of time-intensive geoelectrical monitoring at detecting plant-induced moisture change but also understanding how this information can be linked to the dynamics of other above-ground traits collected by the automated platform.

Among the various geophysical techniques available, we used a combination of two well-established geoelectrical methods, ERT and EMI, to explore the potential of time-lapse geophysics for agricultural studies. The potential, illustrated throughout this thesis by multiple

experiments, is summarised in the next section.

7.2   Papers summary

7.2.1   Agricultural practices

EMI and ERT have been widely used in agricultural studies, mainly as a proxy of a soil property or state of interest. However, the use of a time-lapse approach is less widespread. Chapter 4 used the time-lapse approach to infer the impact of several agricultural practices on soil moisture change. The aim was to gain information on soil moisture availability in relation to the agricultural treatments applied. Following a specific data collection and processing methodology, we interpreted the change in EC as a proxy for change in soil moisture. While we acknowledge that this assumption would benefit from independent soil moisture measurements, it has, nevertheless, proven adequate in other studies (Shanahan *et al.*, 2015; Whalley *et al.*, 2017) and in our own work Chapter 5. Moreover, it does not preclude a qualitative interpretation of the results.

In the cover crops study, white mustard was found to substantially dry the soil in depth in the 2017 experiment compared to other shallower-rooted cover crops. The long-term experiment in 2018, showed similar results but also highlighted the larger drying of cover-crops grown over two seasons compared to cover crops grown during one season. In both experiments the soil drying due to the cover crops vanished a few months after their destruction and hence probably had a minimal effect on the main cash crop. In the study of the effect of soil compaction on irrigated potato crops, inverted ERT sections revealed the shallower depth of drying of compacted treatments. This is an important agronomical observation as it might impact the effectiveness of the irrigation to which potatoes are particularly sensitive.

In a combined study of tillage and fertiliser use on winter wheat, differences between normal tillage and conventional tillage were observed using time-lapse EMI. Despite an initial higher EC in the direct drill (probably due to reduced porosity), the decrease in EC during the season was lower than for normal tillage. This could be explained by the easier water uptake in the normal tillage treatment that led to larger soil drying. The different nitrogen treatments had a significant short-term effect just after the application, probably due to an increase in pore water EC. However, later in the season, only LAI and yield show significant relationships to the amount of nitrogen received. The yield and LAI response to nitrogen was higher in the normal tillage than the direct drill treatment, possibly because the compact medium restricted root development and diverted plant resources to the roots. The ephemeral effect of the nitrogen treatments on the EC supports our assumption of a primarily soil moisture driven EC, however, Chapter 6 also demonstrated that nitrogen application can amplify the EC response after large rainfall events.

Overall, EMI and ERT used in a time-lapse fashion, enabled us to infer, qualitatively, differences in soil moisture changes between different agronomical practices relevant for a more sustainable agriculture. A more quantitative interpretation is explored in Chapter 5, which analysed the impact of the heterogeneity of the pedophysical relationship on the ranking of wheat varieties at the field-scale.

7.2.2   Field-scale heterogeneity

As shown in Chapter 5, when large number of similar varieties are tested in a field-scale setup, the time-approach can be limited. This is due to the heterogeneity of the relationship between soil moisture and EC or change in soil moisture and change in EC. In the experiment on Warren Field in 2017 (Chapter 5), it was observed that these pedophysical relationships changed slightly from plot to plot across the field. While this has a limited impact when differences between treatments are large enough (e.g. for different crops or different agricultural treatments like in Chapter 4), in the case of several wheat varieties on a heterogeneous setup, this can have an important effect.

Indeed, considering a single pedophysical relationship in this setup led to a different ranking of the varieties (ranking is an essential indicator of the variety performance for crop breeders). This finding shows an important limitation of the time-lapse approach in this case. Another finding is that the parameters of these local pedophysical relationship can be approximated using soil moisture and ECa values measured initially (reference) when the effect of crop is negligible. This enabled us to develop multi-offsets and multi-slopes models that helped, to some extent, in alleviating the issue. A new practical approach was also proposed in order to take the effect of this field variability in the experiment design. While this issue is probably exacerbated in field phenotyping trials, we believe that the approach described makes the time-lapse geophysical approach more accurate if one disposes of the means to put it in place.

Chapter 5 demonstrates that pedophysical relationships, in addition to being site-specific, can also show substantial variability inside the same field and that this might hinder the potential of the method for field phenotyping applications. In addition to large field-scale experiments, the use of smaller controlled platform also enable high-throughput phenotyping of different varieties. The value of geophysical monitoring to collect below-ground phenotyping information is explored in the next section.

7.2.3   Time-intensive ERT monitoring

An automated high-throughput field phenotyping platform (HTPP) such as the Field Scanalyzer described in Chapter 6 is a powerful tool for field phenotyping. While the scale of the experiment is smaller than conventional field-scale phenotyping trials, such as the one described in

Chapter 5, HTPP offers a wealth of above-ground information useful to crop breeders. Chapter 6 complemented these above-ground data with time-intensive ERT measurements on two wheat varieties crossed with two nitrogen treatments. Automated hourly ERT measurements were collected and processed over the entire growth season revealing the below-ground EC dynamics of the different plots. In addition to the general seasonal decrease in EC, shorter-term events, caused by rainfall could also be observed. In this experiment, separating the contribution of soil moisture and nitrogen fertiliser to the soil EC is challenging. While we believe the seasonal trend observed was mainly controlled by the change in soil moisture from crop uptake, a faster EC decrease after large rainfall events could be partially attributed to nitrogen uptake by the crop. As such ERT monitoring was able to image two root functions (water uptake and nutrient uptake) while being unable to distinguish them from each other. The effect of nitrogen treatments was also temporarily observed in the Pastures field experiment (Chapter 4) but only after the first application.

In the Scanalyzer experiment, while similarity in the dynamics of above-ground variables could be found, overall the EC dynamics was more impacted by the nitrogen treatments than by the different varieties. The high-temporal resolution of ERT monitoring also highlighted a shift in the diurnal component of the shallow EC variation when the crop started to growth rapidly. We believe that this shift demonstrates the progressively larger impact of the crop-induced diurnal soil moisture dynamics. However, only independent soil moisture measurements could confirm this hypothesis.

In addition to automated ERT monitoring, a series of EMI surveys were also conducted under the Scanalyzer on a monthly basis, however, the influence of the static metallic structure of the gantry and railings could not be confidently accounted for even in a time-lapse fashion. It appears that the contribution of the Scanalyzer infrastructure to the EMI-measured ECa field varied between the different EMI surveys, possibly because of temperature (heating/cooling of the structure). This made the EMI results unsuitable for statistical analysis. Overall, time-intensive geoelectrical monitoring enabled the observation of below-ground EC variation patterns at different time-scale and also to relate them to above-ground variables.

Throughout this thesis, geophysical methods have been applied on multiple specific agricultural studies, revealing potentials and limitations of the approach. The next section proposes to transversally use these findings to put in perspective the use of geophysical methods in agriculture.

7.3   Geophysics and agriculture: a good match?

7.3.1   Practicality of geophysical survey for agriculture

Geophysical surveys offer a unique intermediate scale between point measurements from soil sensors/samples and aerial/satellite imaging. In this work, EMI and ERT methods have been adapted to the specific scale of various field experiments. ERT arrays have been designed to fit in agricultural plots with electrode spacing ranging from 0.15 (Chapter 6) to 0.5 m (Chapter 4), demonstrating the scalability of the method. The EMI sensor chosen, the CMD Mini-Explorer, was also perfectly suited to study the root zone in agricultural setups with effective depths of investigation ranging from 0.25 to 1.8 m. However, time-lapse ERT often requires a fixed setup which can only be installed on a limited number of plots (Chapter 5), that is one of the reasons why it is used in conjunction with EMI, which can easily be expanded to larger number of plots. Figure 7.1 shows the scales of the methods used in this work.
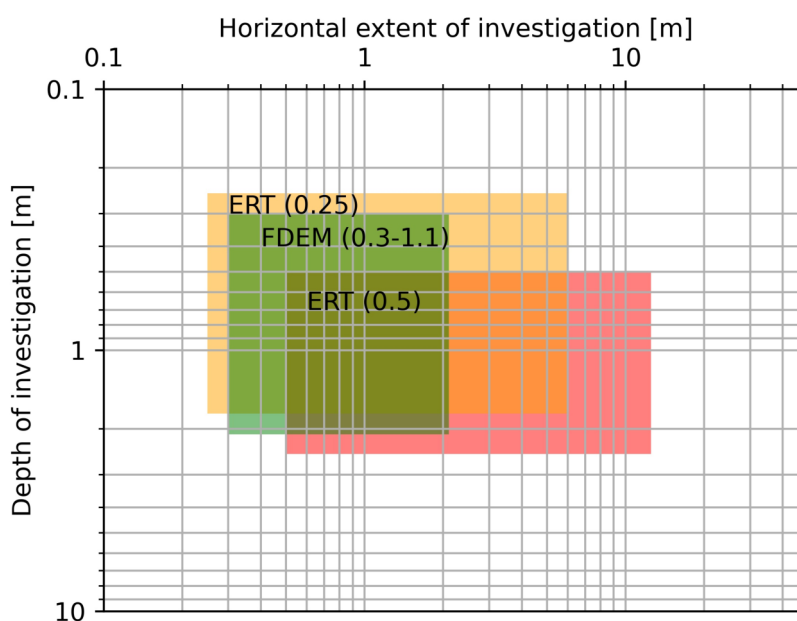
Figure 7.1 – Updated version of Figure 1.1, demonstrating the scales of investigation showcased in the studies of this thesis. Electrical resistivity tomography (ERT) and Frequency Domain Electromagnetic (FDEM also abbreviated EMI in the thesis) are shown. The spacing between electrodes (ERT) or coils (FDEM) is given between parenthesis in meters.

The relative scalability of geophysical methods brings another advantage: the sampling size,

i.e. measurement support volume. In comparison to conventional soil sampling techniques, geophysical measurements can sample a larger soil volume, making them more representative. Having more representative measurements is certainly an advantage for field trials experiment which relies on statistical design to show differences between varieties (Chapter 5) or agricultural practices (Chapter 4). Point-like sensors, such as TDR, have a smaller sampling volume and hence are more sensitive to local soil heterogeneity, presence of stones or voids. However, geophysical methods are not completely immune to these. Indeed, dessication cracks around ERT electrodes constitute an important issue when the electrode are left in place over the season. In our experiments, this sometimes occurred, and we had to reposition the electrode or discard the quadrupoles associated with it.

Also, compared to conventional sampling, the implementation of EMI and ERT methods used in this work, is much less invasive. ERT arrays were, most of the time, left in place without disturbing crop growth. EMI measurements were easily carried out between the rows of wheat, sugar beets, potatoes or cover crops without damaging the crop (Chapter 5 and Chapter 4). Compared to soil coring that usually require some soil disturbance (of the core but also of the area around), this is a significant advantage, as it allows repeated measurements to be taken at the same position during the growth season and hence better monitoring of plant-induced change in soil moisture.

These three main advantages: scalability, representative volume and minimal invasiveness, are essential aspects that make geophysical methods practical for agricultural studies (Chapter 4) and especially suited to high-throughput field phenotyping (Chapter 5, Chapter 6). However, we acknowledge that all experiments presented in this work used a plot design which facilitated data collection. Indeed, access to ERT arrays and collection of EMI measurements could be done from the paths around the plots without disturbing it. In a field setup without a plot design, such access will be constrained and hence EMI measurements might be limited to the main tram lines, which will be more affected by traffic-induced compaction. In addition, the crop itself can make data collection more difficult by preventing easy access to the soil surface. For instance, EMI data collection in tall crops, such as maize, will require some adaptation to manipulate the instrument between the rows. Crops sown at higher density or not in rows, might also prevent EMI measurements to be collected at the soil surface. An ERT setup might be easier to deal with this if they are installed before crop growth but their removal prior to harvest can potentially lead to unwanted crop damage. On this concern, electrode burying can be helpful and allows removal of ERT arrays after harvest.

Another practical (but constrained) aspect of geophysical methods is that often the geophysical variable measured is sensitive to a wide range of soil parameters and states. For geoelectrical methods, this is an advantage as this makes EC relevant for the study of a wide range of important agronomic variables (e.g. soil texture, soil moisture, salinity) and, at the same time,

a drawback as separating the contribution from these different factors is challenging. This is particularly the case in Chapter 6 where the contribution from the fertiliser and change in soil moisture could not be separated. The wide sensitivity of geophysical measurements to soil characteristics often complicates their interpretation. To simplify this interpretation, the time-lapse approach was used to account for the static contributing factors, as developed in the next section.

7.3.2   Time-lapse approach

The time-lapse approach is particularly useful for geoelectrical methods that measure soil EC. Indeed, while static EC surveys have been widely used for the creation of soil maps and the delineation of soil management zones for precision agriculture, the time-lapse approach enables the assessment of the contribution of static soil properties (porosity, soil texture) to enhance the more dynamic characteristics (soil moisture, pore water EC, soil temperature), hence, somewhat simplifying the interpretation of the geophysical variable.

In this work, pore water EC was assumed to be constant as all studies took place in rainfed setup in non-saline soils. However, we realised that this assumption can be wrong after the application of nitrogen fertiliser (Chapter 4, Chapter 6). The increase in pore water EC due to fertiliser can have a strong impact on the ECa measured even if it vanishes after a few days due to rapid nitrogen uptake by the crop (Chapter 4). However, in Chapter 6, the application of nitrogen fertiliser enhances the EC variation after substantial rainfall events. In this last case, a rapid decrease in EC after rain events is likely dominated by the N uptake by the crops rather than moisture uptake. While it is impossible to separate the two with our experimental setup, they both illustrate different root functions: nutrient acquisition and water uptake.

Another important factors affecting time-lapse survey is the soil temperature. Controlling for soil temperature between different surveys was done routinely using the correction 2% per degree Celsius equation described by Ma *et al.* (2011). Multiple correction equations exist, few based on empirical relationships. The correction chose in this work has been selected because it is commonly used and physically-based. Accounting for temperature variation is essential for time-lapse surveys. This is especially the case for time-intensive surveys (Chapter 6), where the interpretation of diurnal patterns, relies on the preliminary temperature correction.

Assuming constant pore water EC and accounting for soil temperature, leaves a change in EC mainly driven by soil moisture. Careful collection of time-lapse surveys away from important rainfall events, enables the measurement of a change in EC mainly influenced by plant transpiration (under vegetated areas). This approach has been successfully used to assess the impact of different agricultural practices (Chapter 4) such as compaction, cover crops and tillage with nitrogen treatments. We believe that this approach is more robust than approaches relying on empirical pedophysical relationships to relate soil moisture and soil EC (Calamita *et al.*, 2015).

Indeed, these relationships vary substantially from one site to another and often assume that the entire investigated site conforms to this relationship. Some of this site-specificity might be due to local textural properties which are usually alleviated by considering change in EC as a proxy of change in soil moisture (Chapter 4). However, this relationship, can in some cases also vary within the same field (Chapter 5).

As demonstrated by Chapter 5, field heterogeneity can also impact time-lapse based soil moisture estimates. It has been observed that the parameters of the plot-specific pedophysical relationships varied across the same field. This issue is especially important for field phenotyping applications as, ideally, variety ranking from geophysically-based estimates should be as close as possible to moisture sensors-based ranking (Chapter 5). The non-random distribution of the pedophysical parameters, enabled us to design models to account for this heterogeneity and hence improve the discriminating capability of the time-lapse approach for comparing different varieties of the same crop. However, these models rely on initial measurements of the soil moisture and ECa for all the plots which might not always be feasible.

The interpretation of geophysical variables always needs to be done carefully. Even if a time-lapse methodolody enables a relative simplification of the approach, it also has its limitations. With the increasing use of geophysical methods in interdisciplinary research (such as agrogeophysics), there is a need to ensure accessible and reproducible data processing of the geophysical variable as it is a prerequisite to further interpretation.

7.3.3   Geophysical data processing: interdisciplinary research and open-source software

To ensure an accessible and reproducible workflow, two different software tools have been developed collaboratively during this work. ResIPy (for ERT processing) and EMagPy (for EMI processing).

ResIPy is built as a Python wrapper around the well-established R* codes (Binley, 2015) for resistivity inversion. It proposes powerful data filtering and error modelling options in an accessible graphical user interface (GUI). It also has interactive forward modelling capabilities that enable to design a survey (electrodes, setup, measurement sequence) and synthetically assess its ability to recover the expected resistivity pattern. In addition to the interface, ResIPy provides an Python application programming interface (API) that can be used for automated tasks in scripts. The combination of the GUI and the API makes ResIPy well suited to non-specialists as well as more advanced users. It is also a potentially powerful tool for teaching purposes. Appendix A provides more details about ResIPy as well as several case studies demonstrating its capabilities.

EMagPy is built entirely in Python and focuses on the filtering, calibration and inversion

of EMI measurements. It is also composed of an intuitive GUI and a powerful Python API for more automated tasks. In addition to common filtering options, EMagPy contains functions to calibrate EMI measurements against depth-specific EC measurements (Lavoué *et al.*, 2010). Calibration of EMI measurements is important for a quantitative use of the data (von Hebel *et al.*, 2019) but also to facilitate convergence of the inversion. Indeed, with some multi-coil EMI device such as the CMD Mini-Explorer, each coil has its own calibration equation and might overestimate or underestimate the ECa systematically (von Hebel *et al.*, 2019; Shanahan *et al.*, 2015). Finally, EMagPy provides different inversion algorithms and forward modelling approaches to invert EMI data. We envisage that the software could be used in interdisciplinary research by non-specialists and also for teaching purpose, while promoting good practices in EMI data processing. More details on EMagPy can be found in Appendix B along with several case studies demonstrating its capabilities.

Accessible and reproducible processing of geophysical data is useful, even more in interdisciplinary projects. It enables inversion of geophysical measurements into depth-specific values but also paves the way to more quantitative interpretation. Two important aspects that makes geophysical measurements more relevant for electrical imaging of the root function as discussed in the next section.

7.3.4   Root function imaging

Imaging root architecture is invaluable for crop breeders as the root system controls nutrients and water access which has implication for crop yield (White *et al.*, 2015). For instance, access to deep water has been correlated with higher yield (Lopes & Reynolds, 2010; Ober *et al.*, 2014). However, the geophysical methods used in this work, ERT and EMI, are, so far unable to directly detect roots, especially fibrous roots of annual crops. In contrast, woody roots have a stronger impact on the EC because of their less electrically conductive bark and can potentially be detected in-situ using other geophysical methods (Mary *et al.*, 2020).

While direct field root imaging would certainly be a valuable trait for crop breeders, this work focuses on imaging the root functions which also has agronomical value. The main root function targeted here is the root water uptake as soil moisture variation are a strong driver of the soil EC. However, inferring root water uptake from change in soil moisture can be ambiguous. Indeed, redistribution processes occurring within the soil further complicate the soil moisture patterns. Also, large water depletion does not necessarily occur where more roots are present. This last point is a clear limitation of the work developed here and prevents us from directly linking root architecture to root function. However, monitoring depth-specific root activity can still give us useful information on the maximum depth where water extraction is taking place (e.g. limited extraction depth in compacted treatment in Chapter 4) and on the overall magnitude of the

drying compared to other treatments (e.g. direct-drill vs conventional tillage in Chapter 4 or different wheat varieties in Chapter 5). Also, assuming similar soil conditions, the shape of the soil drying profile under wheat can be related to the general distribution of root biomass (White et al., 2015) and hence, can be used to distinguish between varieties (Whalley et al., 2017).

While soil moisture content is easily measurable, soil matric potential is more useful as it controls root water uptake. Whalley et al. (2017) noticed that under dry conditions, small change in soil moisture content can result in large changes in matric potential to which ERT and penetrometer methods were most sensitive. However, acquisition of penetrometer measurements was difficult in dry environments and limited to shallow depths. ERT is not as high-throughput as EMI, which limits its use in field-scale phenotyping trial. In this work, the relationship between matric potential and geophysical variable was not investigated mainly because dry enough conditions were not encountered. However, it is an area that might need further investigation as the larger sensitivity of ERT to matric potential compared to EMI might be due to the inherent differences in how both methods measure soil EC. Indeed, as matric potential decreases, the current pathways in the soil are modified which can potentially explain the greater sensitivity of ERT.

The work presented here, mainly focuses on monitoring change soil moisture content. However, nutrient uptake (mainly from nitrogen fertiliser) was observed as well in some experiments (Chapter 6 and Chapter 4). Being able to follow fertiliser uptake by the crop or leaching in the field using geophysical methods constitute a great potential for agricultural applications. It would, however, requires independent soil moisture measurements to isolate the fertiliser-induced pore water EC contribution.

Overall, the time-lapse approach demonstrated its effectiveness at detecting soil drying differences between cover crops (Chapter 4). Similarly, different soil drying patterns of similar crops with different agricultural practices could also be observed using the approach (Chapter 4 and Chapter 6). However, detecting differences between different varieties of the same crops can be challenging due to soil heterogeneity and the small differences in water uptake between the varieties (Chapter 5).

We envisage that similar approaches using time-lapse EMI calibrated with ERT could be used for other crops or agricultural practices provided that the expected change in soil moisture is large enough between the treatments. Application to more saline environment might be more difficult due to the challenge in separating soil moisture and pore water EC contributions. While this might be alleviated by additional independent soil moisture measurement, other geophysical methods such as NMR might also be an alternative to provide an unambiguous soil moisture estimate. Finally, while the contribution of the fibrous roots themselves has been assumed negligible compared to soil EC, a knowledge gap remains on their exact impact on the geophysical measurements. New acquisition methods and processing techniques might help to relieve the

limitations of this work and provide ways in which research could be expanded.

7.4   Perspectives

7.4.1   Acquisition methods

The time-lapse approach using EMI calibrated with ERT described in this work is well adapted to field-scale plots. While EMI measurements can be collected relatively quickly, they still require an operator to walk into the field and position the EMI device on the ground between the crop. This can potentially limit the number of measurements collected in a given time. Air-launched GPR methods can potentially help relieve these limitations Lambot *et al.* (2006) by not requiring direct contact with the surface. Such systems can be installed on motorized vehicle to map field-scale soil moisture (Jadoon *et al.*, 2010; Lambot *et al.*, 2008). However, (Vereecken *et al.*, 2014) noted that the air-launched method as a shallower depth of investigation (10-20 cm) then ground-based GPR. Recently, the use of UAV (a.k.a drones) along with air-launched GPR provided an even less-invasive and more high-throughput approach. Wu *et al.* (2019) successfully used this approach to map soil moisture at the field-scale early on in the season when the crop is little. However, this air-launched method is sensitive to terrain roughness for frequency above 700 MHz. Higher flight altitude also decreases the signal-to-noise ratio. In addition, the impact of a growing crops on the GPR signal has not been studied yet. However, as demonstrated by Wu *et al.* (2019), this method is very fast and enable shallow soil mapping of a field without any crop disturbance.

Another way to prevent crop disturbance at the time of sampling is to rely on automated acquisition system such as ERT systems. Such automated system uses permanently installed electrode and performs regular data collection. In Chapter 6, we used a custom-made automated system with surface electrodes for monitoring soil moisture content under the Scanalyzer platform. While this setup was adapted for the platform, the mandatory connection to the grid and the necessity of internet access (wifi) for remote control makes it less suited for more isolated field monitoring. Other instruments, such as automated ERT monitoring systems developed by the British Geological Survey, might be more adapted to isolated and long term studies. For example, such as system was successfully used to monitor soil moisture dynamics in an active railway embankment (Chambers *et al.*, 2014). While installing an automated system at large scale will be expensive, having a permanent ERT monitoring setup on a target area for several years can be very useful to study the effect of agricultural practices such as direct drill for which the agroecosystem can take several years to fully adapt to. In addition, the high-temporal resolution of such system, might reveal plant-induced soil moisture patterns (Chapter 6) or help to better analyse the soil moisture interaction between trees and crop in agroforestry systems

(Mulyono *et al.*, 2019).

Also, while most field ERT setups used 2D arrays for practical reason, the use of 3D arrays might better account for the lateral heterogeneity and potentially lead better soil moisture estimate (Beff *et al.*, 2013). In addition to surface electrodes, borehole electrodes could also be added to help somewhat compensate the loss of sensitivity at depth (Garré *et al.*, 2011) in small plots experiment (Vanella *et al.*, 2018). While such setups are likely to be more invasive and less practical than 2D arrays for field-scale applications, their use is potentially more adapted to controlled field environment such as the Scanalyzer platform (Chapter 6).

Similar to ERT, EMI lacks sensitivity at depth. However, EMI inversion could somewhat benefit from additional measurement configurations. Mester *et al.* (2011) showed that most information about the subsurface can be obtained by using different coil orientations, while different inter-coil spacing have moderate impact and changing frequencies (8–15 KHz) have a minor influence. While the orientation of the transmitter and receiver coils is usually fixed within rigid-boom multi-coil instruments, their relative orientations to the ground surface can be changed. One can imagine an intermediate orientation between HCP and VCP that would have a different EM response and hence bring additional measurements. This might be challenging as the equations for such intermediate response have not been derived and hence the forward modelling of such intermediate configuration would be more complex.

Another limitation of the geoelectrical methods used in this study is their somewhat complex relationship to soil moisture content. In Chapter 6 or Chapter 4, change in EC was sometimes influenced by both soil moisture content and pore water EC even if a time-lapse approach is considered. NMR does not suffer from this effect as it is directly sensitive to the number of protons in the soil, hence offering independent measurements of soil moisture content. While nuclear magnetic resonance has been widely used in lab-scale studies (Borisjuk *et al.*, 2012) or for ground-water investigation and aquifer characterisation (Binley *et al.*, 2015), the method has rarely been used in agricultural studies (Paetzold *et al.*, 1985), possibly because of its shallow depth of investigation and more complex setup compared to geoelectrical methods. However, new inversion methodology might help make the method more adapted to vadose zone studies (Costabel & Günther, 2014).

Another approach to further tighten the link between the geophysically-derived change in soil moisture and crop uptake in future studies is the use of isotope-based methods. For instance, Corneo *et al.* (2018) used isotopes to study root water uptake of four wheat genotypes. They found that even if the majority of roots were in the top 10 cm, the water extraction at greater depth in the soil profile was mainly controlled by the soil types. Association of isotope-based methods and ERT in a controlled setup could enable to better understand soil moisture redistribution processes taking place. Corneo *et al.* (2018) shows as well than even if soil moisture change can be linked to root activity, they cannot be used to infer root architecture precisely.

This is further supported by Zhang *et al.* (2020) who showed that similar root length densities can, in some cases, show significant difference in drying profiles. Indeed, while change in soil moisture reflects the interaction between the root system of the crop and the surrounding soil, knowledge of the root architecture itself can offer a broader view of the genotype resilience to potential water stress as demonstrated in Figure 7.2. Hence, direct assessment of the root system itself is also valuable.
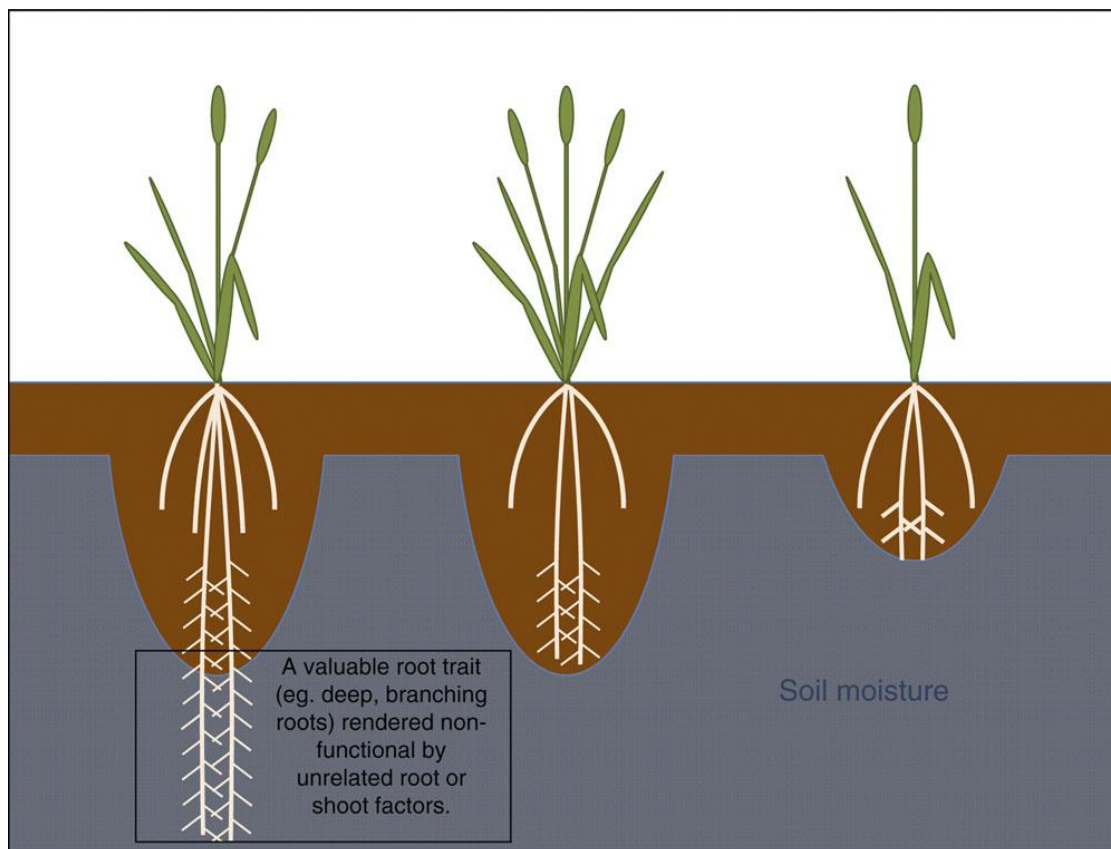
Figure 7.2 – Schematic representation of different root architectures and soil drying profiles. One can observe that some deep root traits cannot always be measured by soil drying solely. Reproduced from Wasson *et al.* (2012).

7.4.2 Direct root sensing

Direct root sensing using geophysical methods aims at detecting roots with a minimally invasive approach. Among geoelectrical methods, mise-à-la-masse (MALM) has been successfully used to obtain information on woody root system of vine (Mary *et al.*, 2020). However, this approach relies on the preferential longitudinal electrical conductivity of woody roots and cannot be easily applied to fibrous roots of annual crop where electric currents leakages occurred all along the length of the roots. However, other electrical properties of the roots can be used for imaging purpose. The electrical polarisation generated from the roots themselves can be used to observe root architecture at the lab scale using SIP (Weigand & Kemna, 2017) and have potential

to be applied in field-scale setup (Weigand & Kemna, 2018). However, the longer acquisition time of SIP measurements might constitute an obstacle for high-throughput field phenotyping applications.

In contrast, ground-based GPR (in contrast to air-launched GPR described above) measurements are quicker than SIP. Similar to MALM, GPR has been useful for identification of woody roots from trees due to their large contrast in electrical permittivity compared to the surrounding soil (Guo *et al.*, 2013). While fibrous roots might not offer the same contrast, their presence in densely sown plots should, in theory, have an impact on the overall permittivity measured. Liu *et al.* (2018) demonstrated using different pixel-based metrics that a link between root biomass and GPR signal could be established for some field-site. However, this approach requires more research and the impact of soil moisture content on the pixel-based estimates would gain to be further investigated.

While the approaches described above attempt to recover root parameters at the field-scale, other approaches focus on lab-scale setup. For instance, computed tomography (CT) has been used to recover root architecture of sugar beets (Mooney *et al.*, 2012). For similar purpose, nuclear magnetic resonance imaging (MRI) can also be used. Lab MRI, due to its immense development for medical purpose, is a well-established method that offer high-resolution imaging of given samples. (Borisjuk *et al.*, 2012) offered a review of MRI for plant based studies and highlighted the potential of the method for microscopic scale. While these methods can accurately identify roots, they can be less accurate at discriminating them from water filled pores in some cases. Moreover, CT and MRI are, for now, unsuited for field-scale study. The heavy and expensive setup they required cannot be operated at large scale and substantial research would be needed to make the methods more portable. However, they remain interesting methods to be combined with lab-based geophysical measurements such as MALM and SIP to study soil-plant-water interactions.

In addition to various acquisition methods that offer new perspective for agrogeophysics in term of soil moisture estimation or direct root detection, improvement in geophysical data processing is also an important aspect that can shape the future of the field.

7.4.3   Data Processing

Processing of geophysical data and especially inversion helps improve their interpretation. If information on the soil moisture profile or the soil layering is available, it might be useful to incorporate this prior knowledge into the geophysical processing workflow. Additionally, the use of a coupled or a joint approach (e.g. Hinnell *et al.*, 2010) might help to constrain geophysical inversion results to possible expected output. The use of multiple geophysical methods (e.g. NMR with ERT/EMI, GPR with ERT/EMI) provide a larger amount of information on the

subsurface and their combined processing via different multi-geophysical frameworks such as SimPEG (Cockett *et al.*, 2015) or pygimli (Rücker *et al.*, 2017) has the potential of producing more robust inverted geophysical results.

The coupled approach is well suited to the integration of hydrological model in the geophysical workflow processing. From our own experience, this coupling enables the recovery of synthetic root distribution, provided sufficient knowledge of hydrological parameters in the soil profile exists. Using Hydrus-1D, we simulated different rooting patterns and the resulting soil moisture dynamics during a full growth season using real meteorological variables. On selected dates, the soil moisture profiles was extracted from the simulation and converted to EC using a pedophysical relationship. The depth-specific EC profiles was then converted to ECa measurements by means of the forward EM model. Using a non-parametric approach (Houska *et al.*, 2015), we then used the simulated ECa values to find back the parameter controlling the root distribution. This approach successfully recovered root parameters using synthetic data, however, it did not work as well for field data mainly because of the different pedophysical relationships observed across the field (Chapter 5) but also because of the uncertainty on the soil hydraulic parameters of each soil layers. We believe, however, that the approach might be more successful in controlled environment where a greater knowledge of the soil parameters is available. The approach would also benefit from a thorough analysis of the uncertainty.

In addition to the inclusion of hydrological models, electrical models of the root system can also be considered for more accurate conversion of EC to soil moisture content. Indeed, so far, the contribution of the roots to the EC measured has been neglected. Rao *et al.* (2019) developed an electrical model of the root system and, using synthetic simulations, demonstrated that the presence of roots increases the uncertainty of the electrical conductivity measured. This effect was larger in sand (increase of 4 to 18% in EC uncertainty for every 1% increase in root/sand ratio) than for loamy medium (0.2 to 1.5%). The study further demonstrated that the effect is proportional to the surface area of the roots and their electrical contrast with the soil. While the exact contribution of the roots to the EC might be difficult to quantify in field-scale setup, this numerical study provides essential order of magnitude of the uncertainty that could be expected.

Aside from more complex modelling, data processing of geophysical variables can also benefit from advances in the field of data sciences. For instance, convolutional neural network could be used to faster inverse modelling Maxwell-based EMI response (Moghadas, 2020). Deep neural networks can also be used to invert crosshole GPR data (Laloy *et al.*, 2020) or for predicting soil moisture estimate based on geophysical variable (Cimpoiaşu *et al.*, 2020). However, these machine-learning approaches require large training dataset which might not always be available. Hence, there is a need to federate geophysical research on the root zone (e.g. `http://geo.geoscienze.unipd.it/growingwebsite/`) to build these large database covering different soil types and conditions.

7.5   Concluding remarks

Ensuring sustainable food production and its resilience to climate change stresses is a complex challenge from which key components take place at the field-scale. Different agricultural practices, such as cover crops or direct drill, have the potential to make our agroecosystems more sustainable. However, measuring the impact of these practices on the soil moisture dynamics in field-scale setups is a challenge. Crop breeding incorporating below-ground traits also has the potential to develop varieties more resilient to climate-induced water stress. However, acquiring root information in the field-scale is challenging.

In this work, two well-established geophysical methods, ERT and EMI, were used in a time-lapse fashion over multiple experiments to try to meet these challenges. Time-lapse ERT and EMI revealed the limited depth of root drying under potatoes and the ephemeral impact of cover crops on the soil moisture dynamics. Time-lapse EMI enabled to enhance the different dynamics between normal tillage and direct drilled plots in terms of both soil moisture and nitrogen uptake. It was shown that direct-drill plots had weaker response to different nitrogen levels compared to normal tillage but also keep a higher soil moisture content compared to normal tillage.

The time-lapse approach used throughout this work, enabled to enhance change in EC mainly driven by water uptake and hence imaging one of the main root functions. However, this approach can be impacted by the heterogeneity of the pedophysical relationship which can hinder the discriminating capability to distinguish different varieties in field phenotyping trials. However, it has been demonstrated that, in some circumstances, it can be compensated by simple multi-offsets and multi-slopes approaches and adapted survey designed.

Time-intensive ERT monitoring enabled observation of the hourly dynamics of the soil EC and its reaction to large rainfall events impacted by nitrogen applications. In this case, EC only based approach was limited as unable to distinguish between the fertiliser or the soil moisture contribution. On the long term, some correlations between above-ground variables and the EC dynamics were observed as well.

While being very practical for the experimental setups described in this work, the time-lapse geoelectrical monitoring can have limited practicability in non-experimental setups where other less-invasive methods (e.g. air-launched GPR) might be more adapted. Also, while our approach mainly focused on plant-induced soil drying, there is still incentive at developing complementary methods for direct root imaging. Modelling interactions between soil, plant and water by mean of a more complex framework integrating hydrological and root electrical models might help better understand the value of geophysical measurements for agriculture.

While more complex geophysical data acquisition and processing might further improve the usefulness of geophysical methods in agricultural studies, one should not forget that other non-geophysical approaches (e.g. neutron probe, penetrometer, TDR) exists and might as well pro-

vide a simple and effective solution for the field-scale challenges presented. Furthermore, the collection of auxiliary variables on soil, water or plant parameters are always useful to refine the interpretation of the geophysical data.

In conclusion, the capabilities of time-lapse EMI and ERT monitoring but also their limitations have been studied for imaging root functions in a number of different agricultural experiments. They both provide practical and valuable insights into the "hidden half" of the plant and are important assets of the emerging field of agrogeophysics. A field, that we believe, can contribute to shape a more sustainable agriculture for tomorrow.

Appendix A

ResIPy, an intuitive open source software for complex geoelectrical inversion/modeling

Guillaume Blanchy[1], Sina Saneiyan[2], James Boyd[1,3], Paul McLachlan[1], Andrew Binley[1]

[1] Lancaster Environment Centre, Lancaster University, Lancaster, UK

[2] Department of Earth and Environmental Sciences, Rutgers, The State University of New Jersey, Newark, NJ, United States

[3] British Geological Survey, Keyworth, Nottingham, UK

Authorship statement

GB and SS contributed to the GUI. GB, SS, JB and PM contributed to the API. GB specifically contributed to the R2 and Survey classes. JB specifically contributed to the mesh generation and handling. SS specifically contributed to the IP part of the API and GUI. PM specifically contributed to the sequence generation of the API and the testing of the GUI. GB, SS, JB and PM wrote the paper. AB wrote all the Fortran executables and provided feedback on the manuscript.

Code availability

The open-source code (GPL license) is available on GitLab: `https://gitlab.com/hkex/pyr2`.

Abstract

Electrical resistivity tomography (ERT) and induced polarization (IP) methods are now widely used in many interdisciplinary projects. Although field surveys using these methods are relatively straightforward, ERT and IP data require the application of inverse methods prior to any interpretation. Several established non-commercial inversion codes exist, but they typically require advanced knowledge to use effectively. ResIPy was developed to provide a more intuitive, user-friendly, approach to inversion of geoelectrical data, using an open source graphical user interface (GUI) and a Python application programming interface (API). ResIPy utilizes the mature R2/cR2 inversion codes for ERT and IP, respectively. The ResIPy GUI facilitates data importing, data filtering, error modeling, mesh generation, data inversion and plotting of inverse models. Furthermore, the easy to use design of ResIPy and the help provided inside makes it an effective educational tool. This paper highlights the rationale and structure behind the interface, before demonstrating its capabilities in a range of environmental problems. Specifically, we demonstrate the ease at which ResIPy deals with topography, advanced data processing, the ability to fix and constrain regions of known geoelectrical properties, time-lapse analysis and the capability for forward modeling and survey design.

A.1   Introduction

Geoelectrical methods are powerful and well-established tools for non-intrusive characterization of subsurface geoelectrical properties. These methods were developed in the early 1900s for mineral resource exploration (Schlumberger, 1920). However, electrical resistivity tomography (ERT) and induced polarization (IP) are now extensively used in a wide range of environmental studies. Applications include monitoring landslides (Uhlemann et al., 2018), precision agriculture (Vanella et al., 2018), assessing permafrost degradation (Mewes et al., 2017), determining hydraulic properties (Benoit et al., 2019), imaging of landfill sites (Ntarlagiannis et al., 2016), monitoring groundwater-surface water interactions (McLachlan et al., 2017) and monitoring of bio-mediated soil stabilization (Saneiyan et al., 2019). As geoelectrical methods become embedded in cross-disciplinary studies there is a need for relatively easy to use data inversion tools, which retain levels of complexity required for modeling of more sophisticated applications.

The translation of geoelectrical measurements to geoelectrical properties requires the use of inverse methods. These methods aim to find the best distribution of geoelectrical parameters that is consistent with observed measurements. This involves minimizing the misfit between the set

of four electrode measurements and the predicted response from a geoelectrical model. Because of the non-linear nature of the problem, the inversion proceeds in an iterative manner until the misfit between the predicted response and the measurements are within a given tolerance. Forward modeling can also be used to generate synthetic data given a synthetic geoelectrical model (workflow shown with red arrows in Figure A.1). Typically, the measurements are composed of a set of transfer resistances (or apparent resistivities) from different four electrode configurations (quadrupoles). If the induced polarization (IP) method is used, the chargeability (in time-domain IP surveys) or phase angle (in frequency domain IP surveys) is also recorded in addition to the transfer resistance. At low frequencies (below 10Hz, i.e. the usual operation frequencies of resistivity/IP instruments) chargeability and phase angle have a linear relationship and the complex transfer impedance can be derived from time domain IP measurements. Therefore, the inversion seeks to find the resistivity (or complex resistivity – in the case of an IP survey) distribution that can explain the measurements. For more details about the inverse methods used here, see Binley & Kemna (2005) and Binley *et al.* (2005).

Several established tools exist for inverting geoelectrical data (Pidlisecky & Knight, 2008). Some codes are specialized for inverting monitoring (time-lapse) measurements (Karaoulis *et al.*, 2013) or for including hydrological or other geophysical information in the inversion (Johnson *et al.*, 2017; Nath *et al.*, 2000). Most non-commercial tools are built around command-line software implementations that require significant experience to operate effectively, which can be challenging for new users, and limits use in an educational environment. There is a growing interest in open source codes within the scientific community, as they provide both users and developers access to comment and advance codes, allowing contributions from multiple developers. More significantly, perhaps, is the increasing demand for the sharing of tools for reproducible science. An open source approach allows users to tailor a given code to suit their needs. Successful examples of open source codes in geophysics include pyGIMLI (Rücker *et al.*, 2017) and SIMPEG (Cockett *et al.*, 2015) both providing a Python application programming interface (API). In the spirit of open source provision, we developed ResIPy (formerly named pyR2) to facilitate processing, modeling and inversion of geoelectrical data. ResIPy is written in Python and is open source (source code is available on a GitLab repository: `https://gitlab.com/hkex/pyr2`). The software handles importing, filtering, error modeling of geoelectrical data and makes use of the freely available R2, cR2 and R3t codes (`http://www.es.lancs.ac.uk/people/amb/Freeware/Freeware.htm`) for modeling/inversion of data. R2, cR2 and R3t are mature codes for resistivity and IP problems but lack any graphical user interface. (Befus, 2018) recently documented a Python wrapper for R2. In contrast, ResIPy offers full IP capability and data quality control features, and has been developed to suit educational/training needs. ResIPy also has 3D capabilities (Boyd *et al.*, 2019) but these will not be detailed in this 2D-focused manuscript. R2 and cR2 are finite element based, allowing the incorporation of complex topography and modeling of bounded regions. They allow
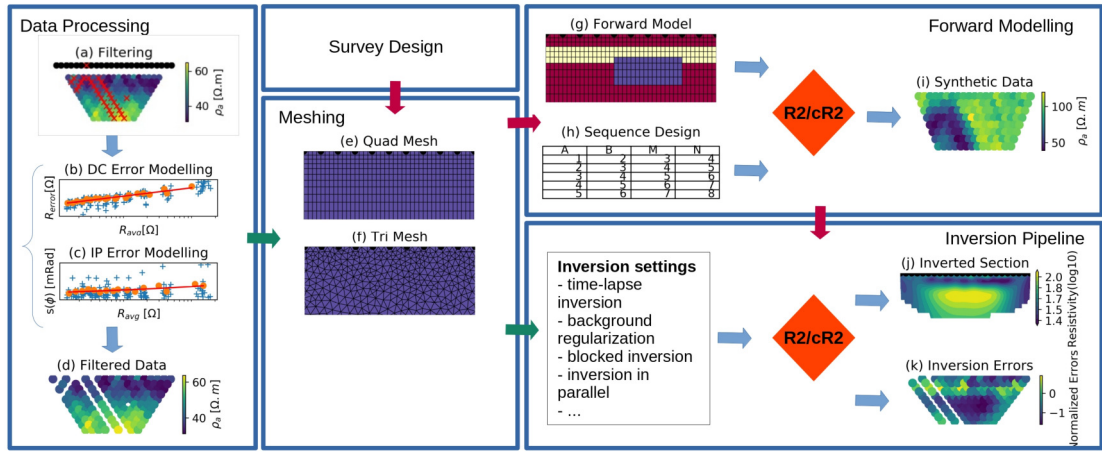
Figure A.1 – Diagram of the capabilities of ResIPy. Inversion workflow (green arrows): data can be imported and bad measurements or electrodes can be filtered out (a). If reciprocal measurements are present an error model can be fitted for DC resistivity (b) and for IP (c). A quadrilateral (e) or triangular (f) mesh is then generated. The mesh and the filtered data (d) are sent to the inversion pipeline. Different inversion settings can be defined such as blocking regions of the mesh or time-lapse settings. The resulting inverted section is then produced with R2/cR2 (j) along with diagnostic pseudo section of the normalized error of the inversion (k). Modeling workflow (red arrows): based on a hypothesis, a mesh is created and a synthetic model designed (d). After creating a sequence (e) the forward response can be computed (f) using R2/cR2. Those synthetic data can then be sent to the inversion pipeline to be inverted.

full flexibility of electrode assignment; accommodating, for example, surface electrode and borehole electrode based surveys. Inverse modeling in the codes is conducted using a weighted least squares objective function coupled with a range of regularization options, including time-lapse data analysis (Binley, 2015).

R2 was developed for solving DC resistivity problems. cR2, in contrast, is tailored for IP problems by formulating the problem in terms of complex resistivity (Binley & Kemna, 2005). Both codes require specifically formatted text files for data input, specification of forward or inverse model settings, and mesh construction. ResIPy removes the need for such text input in a graphic user interface (GUI), whilst assisting the user in pre- and post-processing stages. Use is made of the freely available meshing code Gmsh (Geuzaine & Remacle, 2009) for complex mesh construction. The underlying philosophy of ResIPy is to retain the necessary sophistication of geoelectrical inversion whilst enhancing the accessibility to a wider range of users. Moreover, ResIPy provides an environment for training that may be refined and customized to meet user needs. Hence, ResIPy is particularly well suited for educational purposes. Its intuitive interface, open source nature and wide capabilities allow new users to explore, at their pace, geoelectrical data analysis. Figure A.1 shows the main capabilities of ResIPy.
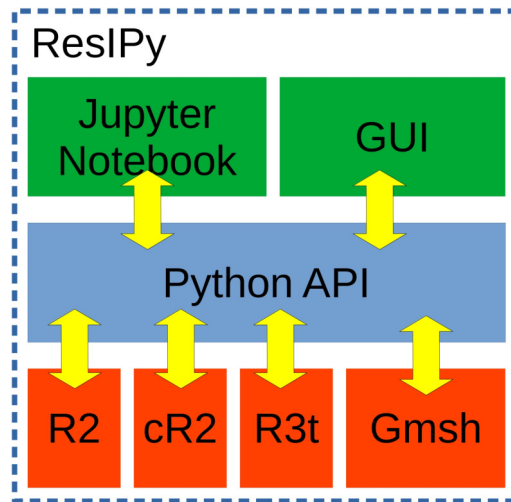
Figure A.2 – ResIPy internal working with three main layers. On top, the visualization layer. In the middle the Python API that is in charge of all calling the executable. At the base are the compiled executable R2, cR2 and Gmsh.

We first describe the general design of the code with the API and GUI. Then, data processing and mesh generation options are explained. Finally, different aspects of ResIPy are illustrated through different environmental field and synthetic cases.

A.2   Structure of the code

A.2.1   Software design

ResIPy is made of three layers (Figure A.2). The bottom layer is composed of the compiled inversion codes R2 (and R3t) and cR2 that are called during inversion or forward modeling for DC resistivity and complex resistivity, respectively. This layer also contains the software Gmsh (http://gmsh.info) that is used to generate triangular meshes. The middle layer is composed of the Python API. This interface contains a set of functions that acts as a wrapper around the executables, facilitating the writing of their input files (R2.in, cR2.in, mesh.geo) and the reading of their outputs. The Python API also contains specific processing routines such as for filtering the data or performing advanced error modeling of DC and IP data. A detailed list of the API functions can be found in Appendix.

The top layer is composed of visualization tools that provide a graphical environment to the user. The Python API is object-oriented and has several classes. The main class is called R2 (R2.py) which manages the data processing and inversion. The GUI initiates an R2 object each time a new inversion/modeling problem is started. Next is the Survey class (Survey.py) that handles one dataset for one survey. Multiple surveys (e.g. from a time-lapse experiment), can be handled inside the same R2 object using the R2.surveys attribute. Finally, the Mesh class

(meshTools.py) handles the tasks associated with the construction of the finite element mesh (e.g. mesh generation, mesh refinement, electrode positioning, etc.). Each `R2` object contains an instance of the Mesh class in `R2.mesh`. More details about the mesh as well as a full overview of the classes and their respective methods are provided in Appendix A.

The Python API is documented within the code according to scipy/numpy docstring guidelines (https://docs.scipy.org/doc/numpy-1.15.0/docs/howto_document.html). The advantage of this approach is that html documentation can be easily compiled and updated using the Python documentation generator Sphinx (https://hkex.gitlab.io/pyr2). The GUI also provides help through the interface (tool tips), which allows the user to learn more about different aspect of the inversion and error modeling.

A.2.2   Standalone graphical user interface

The standalone GUI is written in PyQt5, making it easy to modify and therefore allows for future development. Moreover, graphs are plotted using matplotlib (Hunter, 2007) and can be exported at every step. The GUI uses a series of tabs (Figure A.3) that allows a non-linear workflow and takes the user through the necessary stages of importing and filtering data (or creating synthetic data for forward modeling), generating a mesh and inverting data. The import tab is used to load geoelectrical and topographical data. Geoelectrical data can be imported directly using a number of standard formats (e.g. IRIS Instruments Syscal files, Res2DInv files, and the standard R2 and cR2 input files) or manually imported using the "Custom Parser" tab. Additionally, topographical data can be entered manually or loaded from a comma separated value (csv) file at "Electrode (XYZ/Topo)" tab. After importing data, the user can continue through the workflow, as outlined in the following sections, or move directly to inversion using default settings with the "Invert" button in the "Importing" tab. Using default settings allows the user to generate reliable images in most cases, which may be a useful for novice users or for fast assessment of data (e.g. in the field). It is important to note that all inversion parameters available to R2 and cR2 can be accessed and modified under the "Inversion settings" tab. For instance, the user can change the regularization type, whether the inversion converts data to logarithmic values, data error estimates, smoothing anisotropy and the maximum number of iterations. Help is provided for each parameter, with further details available in the R2 and cR2 manuals (http://www.es.lancs.ac.uk/people/amb/Freeware/Freeware.htm). Furthermore, under advanced settings the user has the option to do batch inversions in parallel on multicore machines.
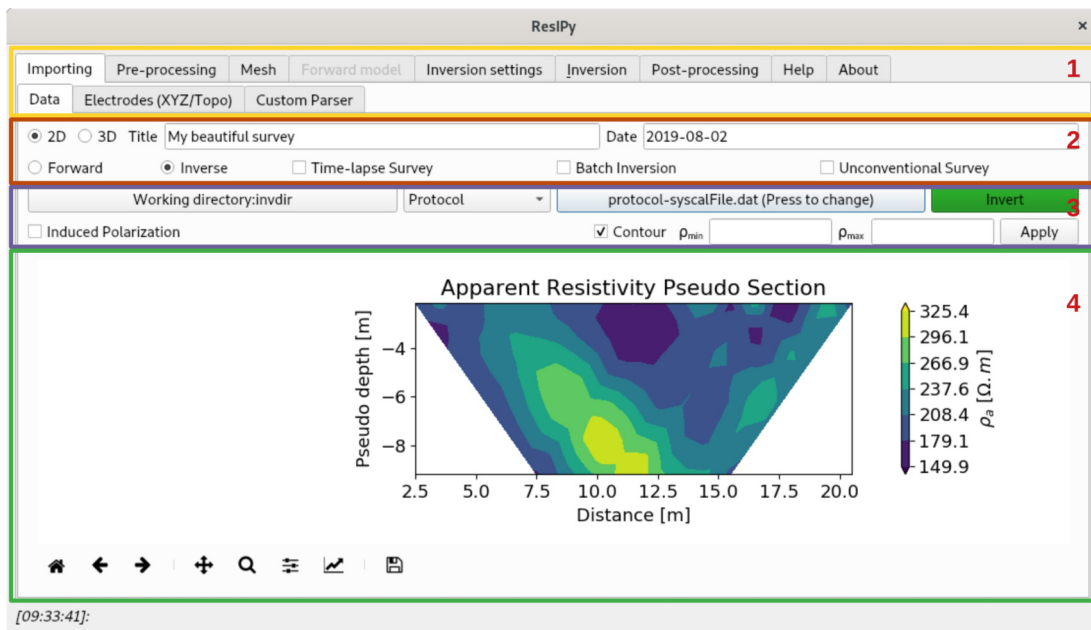
Figure A.3 – General layout of the standalone graphical user interface with (1) different tabs for each processing step, (2) Options for type of survey and inverse/forward modeling , (3) Data import and IP check, (4) pseudo-section plot of the imported data.

A.2.3   Data quality control

ResIPy is capable of rigorous data cleaning and quality control, this can either be done automatically or with user control. Both approaches take into account whether reciprocal measurements are present in the dataset or not. In the GUI, data quality control options are available under the "Pre-processing" tab.

Automatic data cleaning/filtering

The first step of data cleaning in ResIPy is the `basicFilter()` method, which removes the following measurements: (1) infinity or NaN values, (2) duplicates, (3) invalid measurements (e.g. quadrupoles were current electrodes are also potential electrodes – A or B at same position as M or N). If there are reciprocal measurements in the input file, ResIPy automatically calls `reciprocal()` and calculates reciprocal errors. The number of measurements with a relative reciprocal error above 20% are also notified to the user (using the API), but are not discarded by default. The above mentioned methods are also called when a dataset is manually added using `addData()` (e.g. when a reciprocal dataset is added separately).

User-controlled quality control methods

In addition to automatic data cleaning step, ResIPy has several user-controlled quality control methods implemented in the code API as well as the GUI. These methods are divided into two categories: (1) data cleaning/filtering and (2) data error analysis.

Data cleaning User-controlled data cleaning/filtering is carried out in multiple separable steps. All the processing is available in the GUI under "Pre-processing" tab. If reciprocal measurements are present, the following methods can be used to clean up dataset: (1) `filterRecip(percent)`, where 'percent' is a desired percentage value to remove measurements with high error (2) `removeUnpaired()` to remove quadrupoles that do not have a reciprocal pair. In the GUI, these methods can be found in "Reciprocal Filtering" tab under "Pre-processing" tab. The error probability distribution histogram is also provided to help visualization of dataset quality (Figure A.4c). Additionally, the user can select and remove unwanted measurements (regardless of reciprocity) by using `manualFiltering()` method (also available in the GUI under "Manual/Reciprocal Filtering" tab in "Pre-processing"). This interactive method allows the user to manually pick and remove data points within the GUI. Furthermore, the user can eliminate all measurements carried out by a specific electrode (Figure A.4a and b). Further user-controlled data cleaning/filtering is limited to filtering datasets with chargeability/phase values ("Phase Filtering" tab in "Pre-processing"). Quality control is particularly important for IP applications given the smaller signal to noise ratio, compared to DC resistivity problems (Slater & Lesmes, 2002; Zarif *et al.*, 2017).

To give the user full control of the IP data cleaning/filtering, different methods are implemented in the code. In the GUI, the user can apply the available filtering methods and see the results in an interactive Raw versus Filtered graph (Figure A.5). All the phase angle filters can be used separately and are reversible at this stage. In the GUI, the user can select the "Reset all phase filters" button to reset back to the state after manual/reciprocal filtering.

Data error analysis In addition to the data cleaning, ResIPy is capable of data error modeling for DC resistivity and/or IP data. Data error analysis tabs in the GUI ("Resistance Error Model" and "Phase Error Model") are only available when there are reciprocal measurements within the input dataset(s).

Resistance error model:

Observed errors are based on individual measurement reciprocal errors accord-
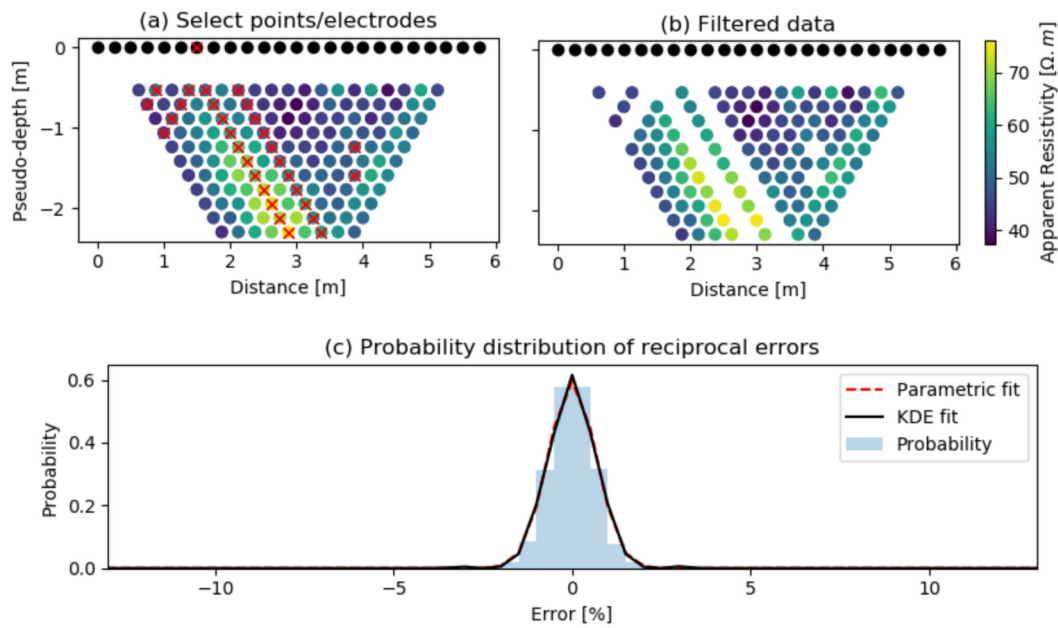
Figure A.4 – Interactive manual filtering. (a) Pseudo section with selected unwanted data points (crossed out in red), (b) Pseudo section with removed data points (user must hit "Apply" button to remove the crossed out data points). And (c) probability distribution of the reciprocal error with parametric and non parametric fit (Kernel Density Estimate = KDE).
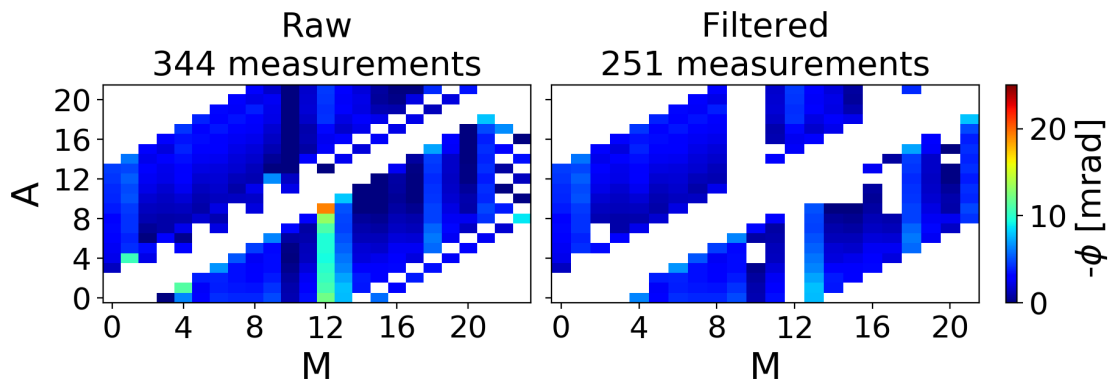
Figure A.5 – Interactive phase angle (ϕ) filtering diagrams. (left) Raw measurements (no filters). (right) Filtered dataset (including both automatic and user-controlled filtering). Each measurement is represented by a colored pixel where the y coordinate is position number of the first current electrode (A) and x coordinate is position number of first potential electrode (M) for a 4 electrode (A-B/current pair, M-N/potential pair) quadrupole (Flores Orozco et al., 2013). White pixels represent no measurement at that location.
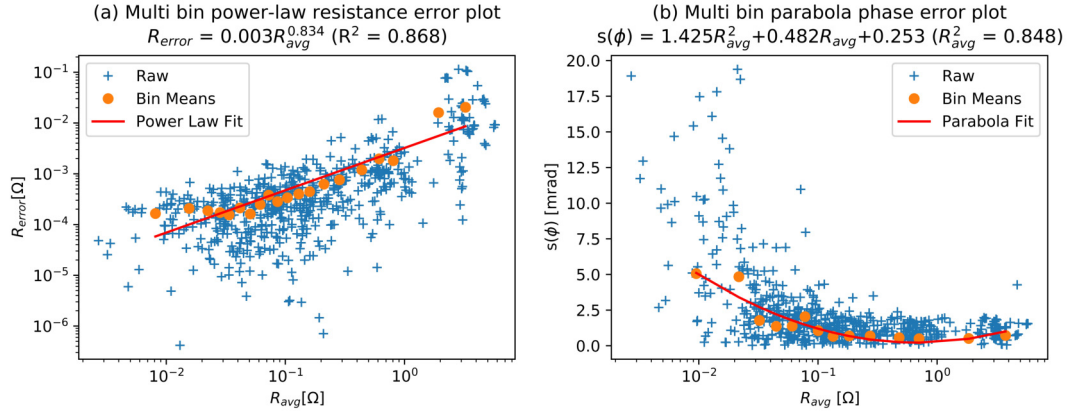
Figure A.6 – Multi-bin error models. (a) Resistance error model (linear), (b) Phase angle error model (parabola). Other options are also available to choose within the GUI.

ing to:

$$R_{error} = |R_{normal} - R_{reciprocal}| \tag{A.1}$$

To calculate an error model (linear or power-law), ResIPy uses multi-bin analysis (for more details of the method, see Koestel *et al.* (2008) and Mwakanyamale *et al.* (2012)) where errors (Equation A.1) are binned into 20 bins of equal count and sorted based on average resistance error R_{avg} [Ω], given by

$$R_{avg} = \frac{|R_{normal} + R_{reciprocal}|}{2} \tag{A.2}$$

Phase error model: Observed errors are based on phase angle discrepancies between normal and reciprocal measurements ($s(\phi)$ [mrad])

$$s(\phi) = |\phi_{normal} - \phi_{reciprocal}| \tag{A.3}$$

and are plotted versus individual normal measurement resistances (R_{normal} [Ω]). Phase error models (power-law and parabolic) are calculated using multi-bin analysis (Mwakanyamale *et al.*, 2012; Flores Orozco *et al.*, 2012); where phase angle discrepancies have been binned into 20 equal count bins and sorted based on R_{normal} [Ω]. The final error model fit formula is written on top of the graph with the coefficient of determination (R2) (Figure A.6). For more details about all the methods used in this section, see section A.4.

A.2.4   Meshing

In ResIPy, two types of 2D finite element meshes can be used: structured quadrilateral (see section A.2.4) or unstructured triangular (see section A.2.4). Regardless of elemental shape, the mesh elements tend to be finer near the electrodes and get coarser at greater distances from the electrodes. This is to address the need for greater discretization in areas of high potential gradient. The mesh is composed of a finer mesh defined by the electrode locations which is encompassed in a coarser mesh with a larger lateral and depth extent (for semi-infinite boundary problems). This is because the mesh boundaries are non-flux (Neumann). In a normal field setting, current from the electrodes will propagate beyond the survey bounds; R2 and cR2 model electrical current flow for the entire mesh assigned to the problem. Hence, in order to reliably model current flow, the mesh boundaries need to be sufficiently far away from the electrode positions. Note there are exceptions where such infinite boundaries are not appropriate (e.g. a non-infinite boundary would exist if conducting electrical surveys near cliff faces, or in laboratory tank experiments). For those specific cases a customized mesh can be imported in to the ResIPy workflow.

The lateral extent of the fine mesh region is dependent on the X (horizontal) coordinates of electrodes (which are represented as nodes in the mesh). The fine mesh region extends to the following depth estimated using

$$Z_{min} - \frac{2X_{max}}{3}, \tag{A.4}$$

where Z_{min} is the lowest elevation of electrodes in the surface or borehole array, and X_{max} is the distance between the longest quadrupole in the survey. Note that this is not a depth of investigation, for example as computed by the method of Oldenburg & Li (1999), but rather a conservative estimate of it to facilitate meshing.

Quadrilateral mesh

ResIPy defines a quadrilateral mesh as an array of X and Z coordinates (i.e. a structured grid), and an array of elevation values with the same length as the X

array. The mesh is composed of a fine region defined by the survey geometry with a coarser surrounding region (because of the infinite boundaries). Only the finer mesh region is displayed in the GUI. The number of nodes between the electrodes can be adjusted in the GUI (Figure A.8). In the API, the mesh growth factors in the Z direction can be adjusted with `zf` and `zgf` attributes for the fine and the coarse region respectively. In the X direction, a growth factor for the coarse region can also be set in the API (`xgf`). In the case of buried electrodes (e.g. cross-borehole surveys), the X and Z coordinates of the electrodes are inserted into the quadrilateral mesh after the main mesh generation scheme.

Triangular mesh

Triangular meshes allow application to more complicated geometry (e.g. topography and geometrical features within the region of study). In ResIPy, the `trian_mesh()` function generates the mesh by calling Gmsh.exe to perform the meshing process. The `trian_mesh()` function provides an input file for gmsh (.geo) and parses the output (.msh).

Similar to the quadrilateral mesh, it is possible to control the mesh refinement by specifying a characteristic length associated with each electrode node. Smaller characteristic lengths will result in a finer mesh. Similar to the quadrilateral mesh, the user can specify a growth factor that controls the increase in element size with depth. With both quadrilateral and triangular meshes it is advisable to avoid fine elements in areas with low sensitivity, as they will not add anything to the interpretation of the inverted model but will increase computation time. These two parameters can be set in the GUI using slider or in the API using the and `cl_factor` attributes of the `R2.createMesh()` method.

Both quadrilateral and triangular mesh options are available in ResIPy to encompass the capabilities of the R2/cR2 codes. A quadrilateral mesh is generated faster than a triangular mesh in ResIPy and output from a structured mesh (e.g. the array of resistivities following inversion) can be easier to work with (e.g. to extract vertical or horizontal resistivity profiles). However, triangular meshes are more versatile, can account for complex topography and are computationally more efficient. Consequently, triangular meshing is recommended in ResIPy.
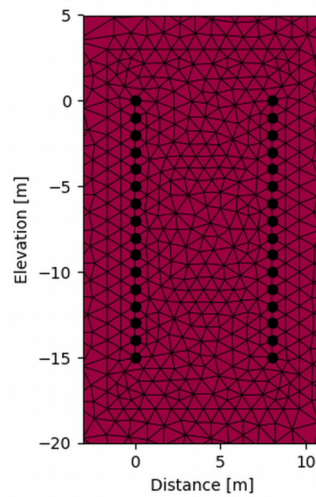
Figure A.7 – Example of a pair of borehole arrays in a whole space problem. Note that the view is cropped and that the real mesh extends much further away from in all directions. Also note that the mesh shown in coarsely discretized for illustration purposes.

Whole space problems In some cases, it might be appropriate to assume the electrodes are buried at such an extensive depth that current flow does not interact with the surface or any other boundaries. In such cases, ResIPy offers a scheme whereby electrode coordinates are inserted into a fine triangular mesh region with a larger surrounding region (Figure A.7).

Region definition

For generating a forward model for survey design, or for inverse modeling of a survey with known subsurface boundaries, ResIPy allows the user to define different regions within the mesh. These regions can be assigned a specific resistivity and phase angle values. Regions can be selected in the GUI using an interactive plot picker and table system (Figure A.8). In some cases, the user may wish to prevent regularization in the inversion across certain boundaries, for example if there is a known geological boundary. To do this the user can specify that these regions are different zones. In this paper, we make a clear distinction between the term 'region' which is a spatial group of elements, and the term 'zone' which is a special case of a region where the regularization is suppressed along its boundaries. The example in subsection A.3.4 considers a river with a fixed river resistivity, and the example in subsection A.3.1 considers how to generate and invert synthetic data
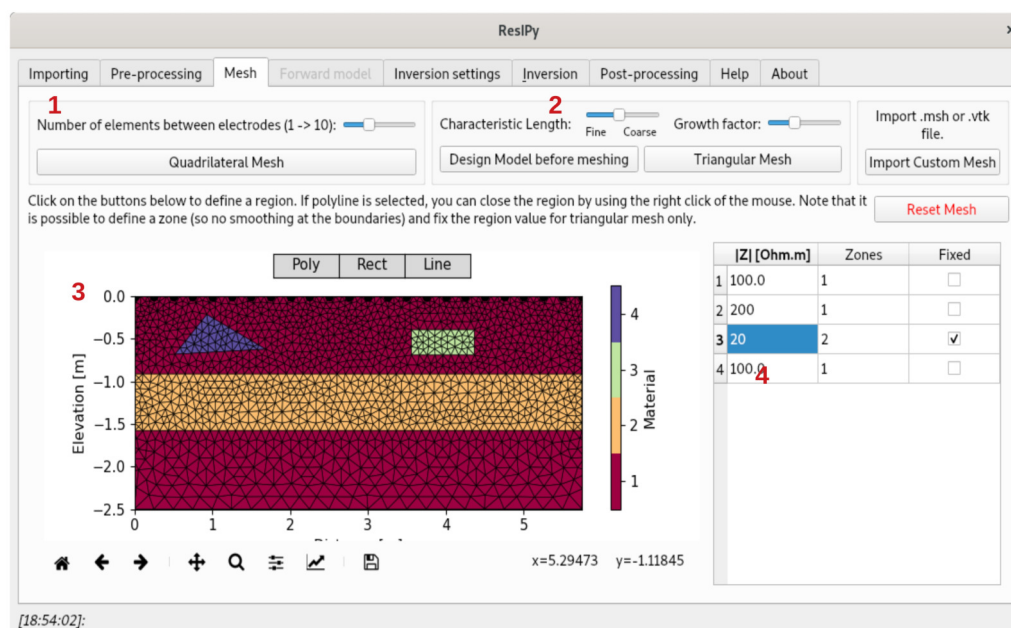
Figure A.8 – The interface allows for both quadrilateral (1) and triangular (2) mesh generation. The interactive mesh display allows to draw regions of different shapes (3) and specify their properties using the panel on the right panel(4).

using the forward modeling capabilities.

A.3 Applications

The following examples demonstrate the capabilities of ResIPy. Each of the examples aims to expose particular aspects of ResIPy relevant for the case study. For each example the steps to reproduce the results in the GUI along with the lines of code in the API that does the same are provided. This aims to make the link between the GUI and the Python API more obvious. Further examples are available in the GitLab repository (https://gitlab.com/hkex/pyr2/tree/master/examples).

A.3.1 Survey design

Knowing the measurement response for a given model is a powerful tool to assess method limitations. This is particularly useful when trying to optimize the survey design for an intended target, or for determining if detecting a parameter of interest is realistic or not. Forward modeling can be done in the ResIPy API using the `R2.forward()` method, or in the GUI by selecting "Forward" check box in the

main importing tab. ResIPy offers four types of sequences: dipole-dipole, Wenner, Schlumberger, multiple-gradient. The user has also the possibility to import and generate their own custom sequence. Note that R2/cR2 are capable of modeling any quadrupole sequence or combination of sequences.

The sensitivity of the array to a certain target will depend on quadrupole configuration; hence, for survey design this is an important consideration. For example, Wenner arrays tend to favor sensitivity to horizontal features rather than vertical ones (Binley, 2015). Additionally, the electrode spacing of the survey will dictate the ability of the array to resolve a given target, as the array spacing controls spatial resolution and depth of investigation. Arrays with smaller electrode spacing have a shallower depth of investigation than larger arrays but have higher spatial resolution. Therefore, in the case of surveys with a known target but unknown location, arrays with different electrode spacing and quadrupole configurations can be trialed through forward modeling to find a setup that is best suited to the problem.

The following example compares the sensitivity of a Dipole-Dipole and a Wenner sequence to resolve a shallow target. The target, a rectangular feature buried at 1 m depth with dimensions of 3 m by 1 m (Figure A.9a), can be defined in the "Mesh tab" using the interactive plot or using the API method R2.addRegion(). The resistivity of the target is set to 10 Ohm.m whilst the background resistivity is set to 100 Ohm.m. The sequence is chosen in the "Forward Model" tab or using the k.createSequence() method from the API. Given a starting model (Figure A.9a) and a sequence, the forward model can be run. The measurements produced are displayed as a pseudo-section (Figure A.9b and c). In this case 5% noise is added to the measurements to simulate a more realistic scenario. The synthetic data are then inverted to see how much information can be recovered from them (Figure A.9d and e). Figure A.9 shows that a dipole-dipole array is better suited to this kind of problem compared to a Wenner array. In Figure A.9d (Wenner array), a low resistivity region can be observed but its location is widespread. Figure A.9e (dipole-dipole array) more closely resembles the input resistivity model, and the low resistivity region is better collocated with the placement of the target.

```
k = R2(typ='R2')
k.setElec(np.c_[np.linspace(0, 24, 24), np.zeros((24, 2))])
k.createMesh(typ='quad')
target = np.array([[7,-2.2],[12,-2.2],[12,-5],[7,-5]])
k.addRegion(target, 10, -3) # target definition
k.createSequence(params=[('wenner_alpha',1),
                         ('wenner_alpha',2),
                         ('wenner_alpha',3),
                         ('wenner_alpha',4),
                         ('wenner_alpha',5),
                         ('wenner_alpha',6),
                         ('wenner_alpha',7),
                         ('wenner_alpha',8),
                         ('wenner_alpha',9),
                         ('wenner_alpha',10)])

k.forward(iplot=True, noise=0.05) # add 5 % noise
k.invert(iplot=True)
k.showResults(index=0, attr='Resistivity(Ohm-m)', sens=False)
k.showResults(index=1, attr='Resistivity(Ohm-m)', sens=False)

# now for the dipole dipole
k.createSequence([('dpdp1', 1, 8)])
k.forward(iplot=True, noise=0.05)
k.invert(iplot=True)
k.showResults(index=1, attr='Resistivity(Ohm-m)', sens=False)
```

This example uses synthetically generated data to optimize the design of the survey. Once this step is done, the survey is carried out and field/lab measurements are collected. The following examples demonstrate how those measurements are processed with ResIPy.

A.3.2   2D resistivity with topography

Castle Hill in Lancaster (UK) is the site of a first century Roman fort (Wood, 2017). At the site there are no remains of the Roman fort walls above the ground but targeted archaeological investigations have found traces of the walls foundations. The aim here is to map the extent of walls around the site using several ERT cross transects. Only one of those transects is used here. In this example, the steep topography of the hill strongly impacts the inversion results, i.e. if topography is not included in the mesh, the inversion outputs unrealistic results containing artifacts. The results are displayed in Figure A.10 where the high resistivity anomaly on the top of the slope corresponds to the walls foundations. All transects together help to define the positions of the walls and hence the extent of the Roman fort. GUI:

1. Importing data: exact electrode locations can be added in the "Electrodes
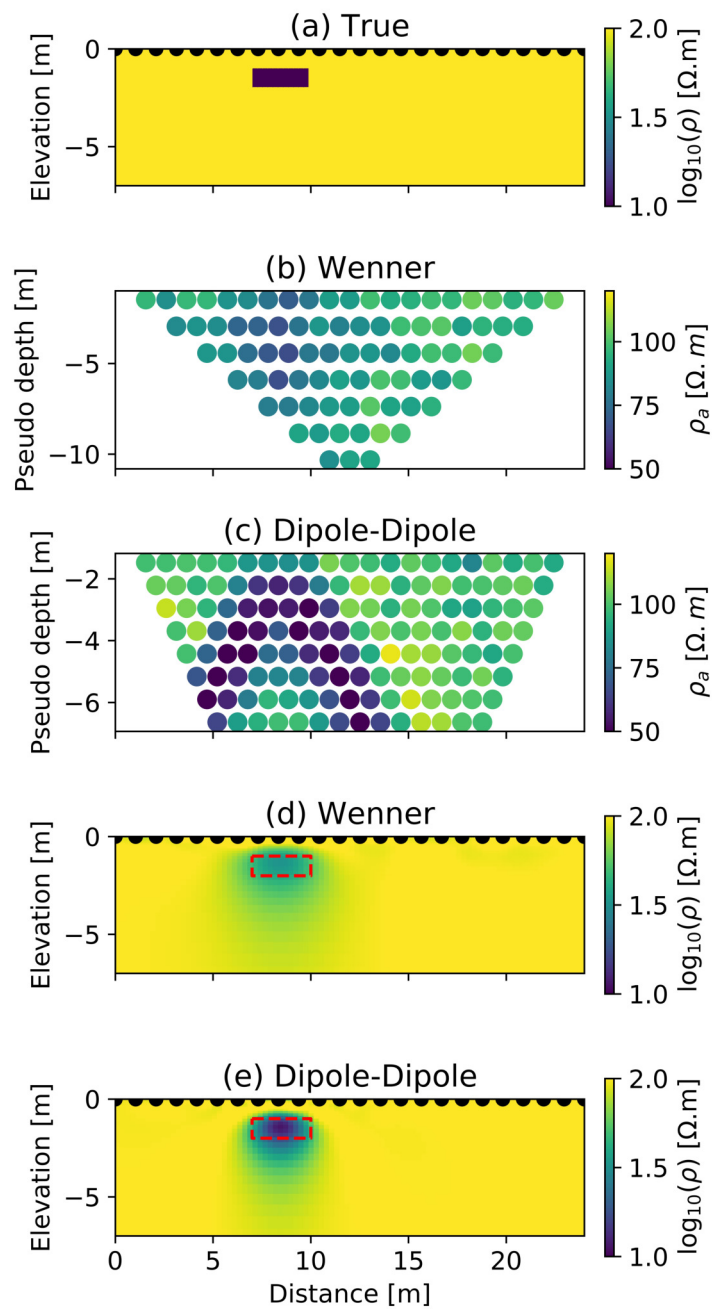
Figure A.9 – Forward modeling in ResIPy. (a) The original resistivity model for which measurements are computed. (b) and (d) the pseudo and inverted section of apparent resistivities for a Wenner array respectively, (c) and (e) the pseudo and inverted section for a Dipole-Dipole array. The red dashed line in (d) and (e) shows the true position of the target.
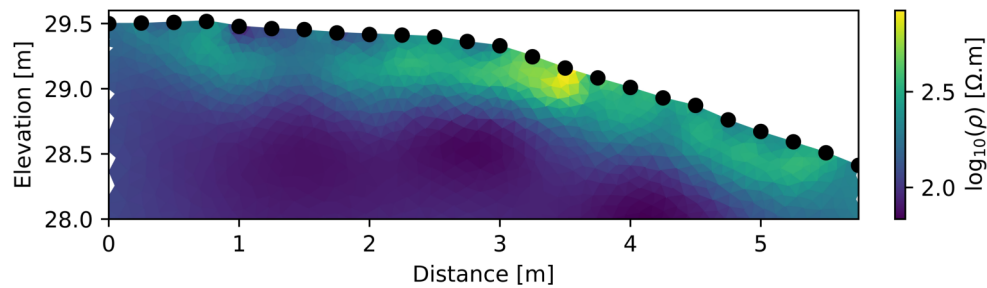
Figure A.10 – Inverted section of one of the ERT transects crossing over the wall. A zone of higher resistivity approximately 3.5 m along the transect agrees well with other excavations nearby, and probably represents the remains of wall foundations.

  (XYZ/Topo)" tab

2. (optional) choose mesh type: we use triangular mesh

3. Inversion

  The same can be achieved using the API:

```
k = R2() # initiate an R2 instance
k.createSurvey('syscalFileTopo.csv', ftype='Syscal') # import data
k.importElec('elecTopo.csv') # importing the electrodes positions
k.fitErrorPwl() # fit a power law
k.err = 'True' # tells the inversion to use the error model we've fitted
# (done automatically in the GUI) this will set a_wgt and b_wgt at 0
k.createMesh(typ='trian') # create quadrilateral mesh
k.invert() # run the inversion
k.showResults() # show the inverted section
```

A.3.3   2D IP

Recently, it has been shown that IP is a capable tool for monitoring soil strengthening involving calcite precipitation in both lab and field scale (Saneiyan et al., 2018, 2019). Here we use data reported by Saneiyan et al. (2019) to show how the IP filtering options available in ResIPy can enhance inversion quality. To illustrate the processing capabilities of ResIPy we first invert a dataset where the raw IP measurements are used directly without data filtering. Second, we show how data filtering can enhance the final inversion. Note that for IP problems the inverse model can be displayed as an image of resistivity magnitude and phase angle, or as an image of real conductivity and imaginary conductivity. The resistivity magnitude and phase angles are parameters directly derived from the measured impedances. The real and imaginary conductivity are derived from the magnitude

and the phase angle. The advantage of imaginary conductivity over phase angle is that it provides an unbiased estimate of the polarization of the medium.

Inversion without data cleaning

Similar to the previous section, we can approach the problem with either using GUI or straight from API: GUI:

1. Importing data: code automatically detect "IP" values, if a known file type is chosen (e.g. Syscal)

2. (Optional) choose mesh type: we use triangular mesh

3. Inversion.

   API:

```
k = R2(typ='cR2') # initiate an R2 instance (considering there is IP data in the input data)
k.createSurvey('IP_MICP_ALL.csv', ftype='Syscal') # import data
k.createMesh(typ='trian') # create triangular mesh
k.invert() # run the inversion (and write cR2.in and protocol.dat automatically)
k.showResults(attr='Phase(mrad)') # show the inverted section
```

For this case, without data cleaning, the inversion of the phase angle did not converge within 10 iterations (observed by consistent unrealistic and very high RMS misfit values per iteration) and the inversion results did not show meaningful subsurface structures. In order to apply data quality control, we then follow the steps reported in Saneiyan *et al.* (2019).

Inversion with data cleaning and error analysis

The steps are similar to previous but here we include data quality control routines, filtering and error analysis. GUI:

1. Import data: IP_MICP_ALL.csv.

2. Reciprocal filtering: removing data points with $> 5\%$ reciprocal error

3. Phase filtering ("Phase Filtering" tab in "Pre-processing"):

   (a) Removing nested measurements (measurements where M or N are in between A and B)

   (b) Phase range filtering: setting $0 < \text{-}\phi < 20$

4. Error modeling:

   (a) Resistance error model: power law

   (b) Phase error model: power law

5. (Optional) choose mesh type: we use triangular mesh

6. Inversion

API:

```
k = R2(typ='cR2') # initiate an R2 instance (considering there is IP data in the input data)
k.createSurvey('IP_MICP_all.csv', ftype='Syscal') # import data
k.filterRecip(percent=5) # removing datapoints with > 5% reciprocal error
k.filterNested() # removing nested measurements
k.filterRangeIP(0,20) # setting phase shift range to 0 < -$\phi$ < 20
k.fitErrorPwl() # adding resistance power-law error model to data
k.fitErrorPwlIP() # adding phase power-law error model to data
k.err = 'True' # using error models (DC and IP) - automatically done in the GUI when fitting the error m
k.createMesh(typ='trian') # create triangular mesh
k.param['a_wgt'] = 0 # "a_wgt" = 0 when there is individual resistance error
k.param['b_wgt'] = 0 # "b_wgt" = 0 when there is individual phase error
k.param['tolerance'] = 1.14 # based on data, field site and experience
k.param['min_error'] = 0.001 # based on data, field site and experience
k.invert() # run the inversion (and write cR2.in and protocol.dat automatically)
k.showResults(attr='Magnitude(Ohm.m)') # show the inverted real conductivity section
k.showResults(attr='Phase(mrad)') # show the inverted phase shift section
```

This time the data was successfully inverted (resistivity RMS misfit = 1.47 and phase RMS misfit = 1.11 in 3 iterations). Figure A.11 shows the final inversion plots.

According to Saneiyan *et al.* (2019), the phase angle anomaly below -3.5 m is the area impacted by microbial induced carbonate precipitation (MICP) processes and ResIPy successfully shows this in the inversion plots. Saneiyan *et al.* (2019) show that a consistent increase in the phase angle below -3.5 m is observed during a 15-days experiment, confirming the impacted area by MICP has been detected by the IP survey successfully.

A.3.4 River: blocky resistivity inversion

ERT has been used in a number of studies for characterizing riverbeds, lakebeds and canals using waterborne and fixed arrays for both static and time-lapse investigations (Ball *et al.*, 2006; Crook *et al.*, 2008; Ward *et al.*, 2013). In this example, we demonstrate how ResIPy allows the user to create a blocky region corresponding to the river and therefore better resolve the subsurface. In this case ResIPy
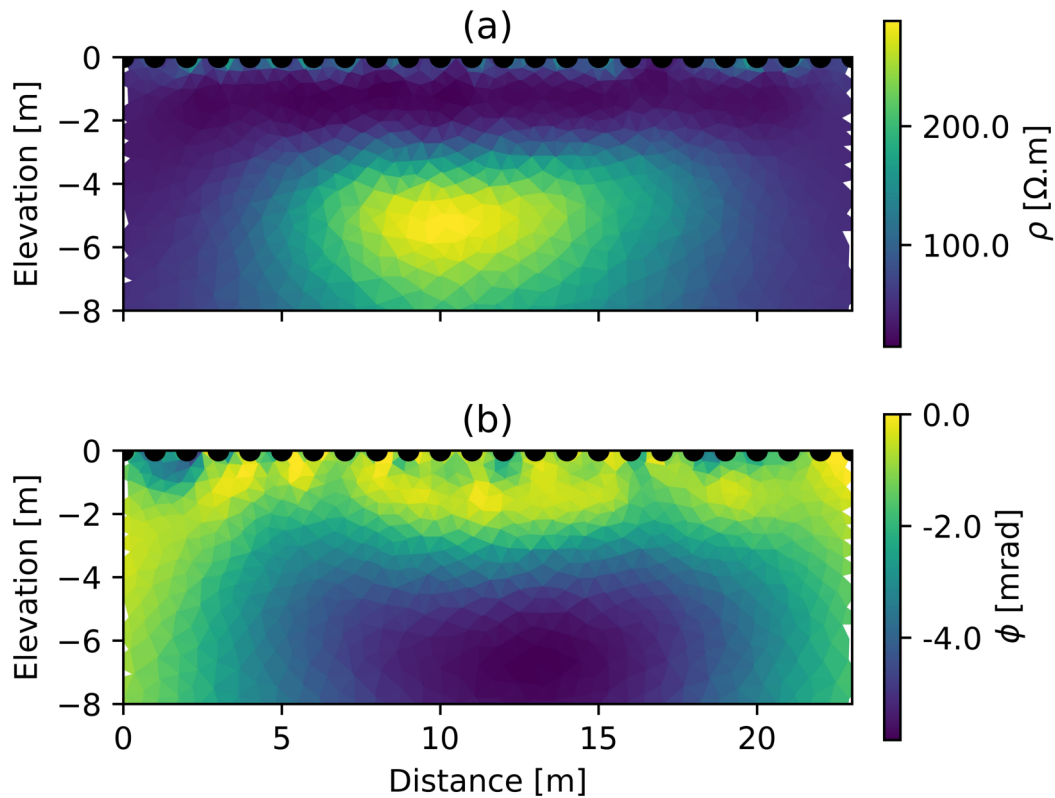
Figure A.11 – Inverted IP plots. (a) resistivity plot, (b) phase angle plot.

allows the resistivity of elements of the mesh representing the river water column to be fixed, and regularization at the boundary between the river and surrounding region to be suppressed (i.e. using zones for regularization). The survey used here was collected using a transect that spanned the chalk fed river Lambourn (UK) and part of an adjacent riparian wetland. The inverted section is shown in Figure A.12. GUI:

1. Importing the data using the 'Protocol' file type

    (a) Inputting the topography file for the electrodes

    (b) Burying the substream electrodes

    (c) Adding additional topography points to define where the river intersects the river bank

2. Meshing: triangular meshing is selected

    (a) Use the interactive plot to select a region corresponding to the river, define it as a separate (and fixed) zone and assign it a starting resistivity
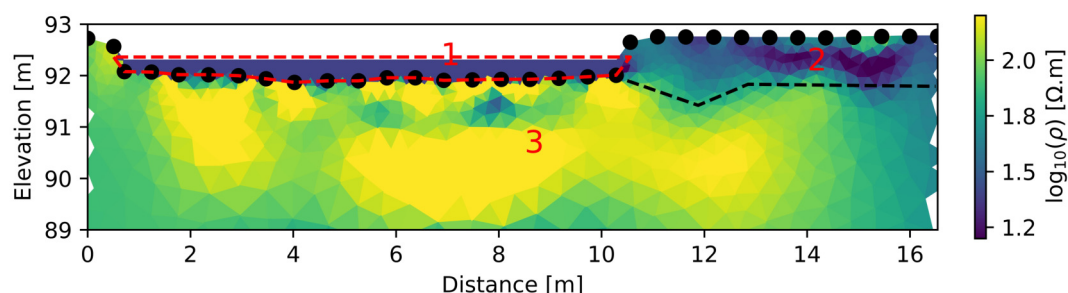
Figure A.12 – Inverted section showing (1) the river water corresponding to the fixed region surrounded by red dashed lines, (2) the peat layer, more conductive and (3) the gravels beneath more resistive. The block dashed line is an interpretation of the interface between the peat and the gravels.

of 25 Ohm.m (value independently measured in the river)

3. Invert

API:

```
k = R2()
k.createSurvey('river-protocol.dat', ftype='Protocol')
# following lines will add electrode position, surface points and specify if electrodes
# are buried or not. Similar steps are done in the GUI in (a), (b), (c)
x = np.genfromtxt('river-elec.csv', delimiter=',')
k.setElec(x[:,:2]) # electrode positions
surface = np.array([[0.7, 92.30],[10.3, 92.30]]) # additional surface point for the river level
buried = x[:,2].astype(bool) # specify which electrodes are buried (in the river here)
k.filterElec([21, 23, 22, 2, 3]) # filter out problematic electrodes 21 and 2
k.createMesh(typ='trian', buried=buried, surface=surface, cl=0.2, cl_factor=10)
xy = k.elec[1:21,[0,2]] # adding river water level using 2 topo points
k.addRegion(xy, res0=25, blocky=True, fixed=True) # fixed river resistivity to 25 Ohm.m
k.param['b_wgt'] = 0.05 # setting up higher noise level
k.invert()
k.showResults(sens=False, vmin=1.2, vmax=2.2, zlim=[88, 93])
```

A.3.5   Time-lapse monitoring of soil drying due to root water uptake

ResIPy allows users to perform inversion of time-lapse resistivity and IP surveys as well as batch surveys. These options need to be selected in the GUI before importing data. In both cases (time-lapse or batch survey) the user must select a directory containing the datasets rather than single data files (ResIPy automatically will ask for an import directory). Note that all files are imported in alphabetical order. For difference inversion, all surveys are automatically matched to keep only the quadrupoles common to all surveys.

A specific option to run the inversions in parallel is available in "Advanced" tab under "Inversion Settings" tab. In this case multiple inversions will be run on

different logical processors, which will significantly speed up the total inversion process (if a multi core machine is used). Note that this consumes more memory for large meshes.

The dataset used in this example is a series of ERT surveys made between March to May 2017 at a wheat field maintained by Rothamsted Research at Woburn, UK. The aim of this study is to monitor the root water uptake of different wheat varieties for the purpose of selecting resilient lines (Whalley *et al.*, 2017). ERT arrays were installed under different wheat varieties and left in place during the season. Regular ERT measurements were collected and converted to soil moisture content to observe the depth of the soil moisture depletion due to root water uptake. In this example, four ERT surveys of one variety are inverted using a time-lapse routine inversion (difference inversion) that specially invert for change in resistivity (LaBrecque & Yang, 2001). All changes in resistivity are expressed as percentage difference compared to the background survey (15th March 2017). The inverted sections illuminate the drying pattern of the variety throughout the growing season (Figure A.13).

In the GUI:

1. Importing data (for time-lapse: checking the 'Time-lapse' survey check box)

2. Fitting a power-law error model (applied on all data points for all time steps, the same global error model will then be used for computing error for each survey)

3. Create a triangular mesh

4. Inversion settings: in the advanced setting tab, we checked parallel inversion (i.e. multiple instances of the executable are run at the same time to speed up the inversion).

5. Inversion

API:

```python
k = R2() # initiate an R2 instance
k.createTimeLapseSurvey('timeLapse/', ftype='Syscal') # import data
k.fitErrorPwl() # fit a power-law
k.err = 'True' # tells the inversion to use the error model
k.createMesh(typ='trian', cl=0.5) # create a triangular
# mesh with a characteristic length of 0.5
```

```
k.invert(parallel=True) # run the inversion in parallel
k.showResults(index=0) # show the first inverted section
k.showResults(index=1) # show the second inverted section
k.showResults(index=1, attr='difference(percent)') # show the
# differences between the first and second survey
```
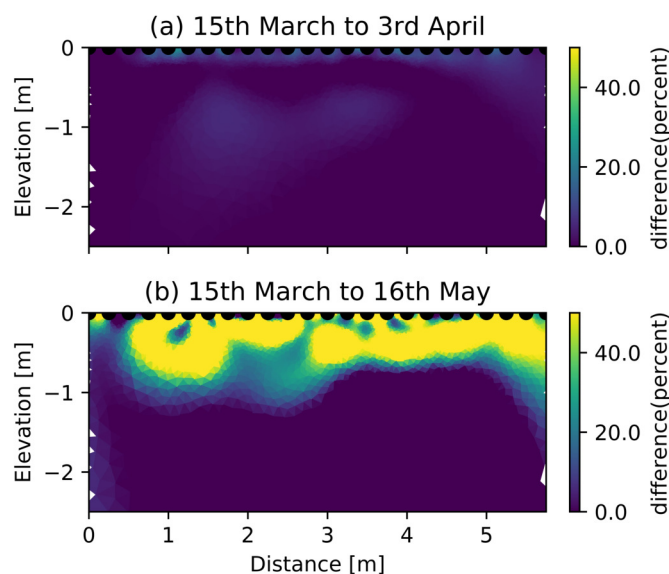

Figure A.13 – Time-lapse inverted section showing the differences from the background (15th March 2017) to (a) 3rd April and (b) 16th May 2017. There is an increasing resistivity in the subsurface, interpreted as an increasing drying due to root water uptake by the wheat. The change in resistivity reveals the depth of the drying which varies for different wheat varieties (Whalley *et al.*, 2017).

A.4   Conclusion

ResIPy is a geophysical data analysis, modeling and inversion tool that simplifies the problem and allows users to have full control over sophisticated modeling/inversion parameters in an intuitive graphical user interface. ResIPy provides a platform for multi-disciplinary projects in which reliable results are produced in an easy to follow nonlinear user interface. ResIPy allows modeling and inversion of 2D and 3D resistivity and IP data, and is ideally suited for educational purposes. While most available inversion codes/software are capable of basic data filtering, ResIPy provides a thorough data cleaning routine. We have illustrated some of the key features of ResIPy, showing, for example, how data filtering and error modeling can enhance data inversion, especially for IP surveys. ResIPy has been successfully used in multiple field and modeling situations using both the GUI and

the API.

We believe this open source project will not only increase the usability of the mature R2/cR2 inversion/modeling codes, but also improve the accessibility of geophysics in interdisciplinary projects while also providing a powerful open source tool for teaching purposes.

Acknowledgements

We would like to thank the members of Lancaster – Rutgers Hydrogeophysical Knowledge Exchange group (HKEx) for their valuable feedback throughout this project.

Computer Code Availability

The data used in the examples and compiled standalone executables of the software are all available on the GitLab repository: https://gitlab.com/hkex/pyr2. Documentation of the API along with examples can be found at https://hkex.gitlab.io/pyr2.

Appendix

Below can be found a table summarising the main methods and functions available in ResIPy API. The list of arguments (signature) of the methods/functions are not displayed for the sake of simplicity but detailed help can be found in the documentation online (https://hkex.gitlab.io/pyr2/api.html).

Table A.1 – API methods in ResIPy

class	methods/attributes	what it does
R2 (R2.py)	createSurvey()	Import single survey dataset from file
	createTimeLapseSurvey()	Import time-lapse datasets from directory
	createBatchSurvey()	Import batch datasets from directory
	setElec()	Set the electrodes
	importElec()	Import electrodes position from file
	manualFiltering()	Manually select outliers point on the pseudo-section
	filterDip()	Filter dipole
	filterData()	Filter data (used in the outlier removal)
	fitErrorPwl()	Fit a power law error model resistivity (inherited from Survey)
	fitErrorLin()	Fit a linear error model resistivity (inherited from Survey)
	fitErrorPwlIP()	Fit a power law error model IP (inherited from Survey)
	fitErrorLinIP()	Fit a linear error model IP (inherited from Survey)
	fitErrorParabolaIP()	Fit a hyperbola error model to IP (inherited from Survey)
	createMesh()	Create a mesh (quadrilateral or triangular)
	showMesh()	Display the mesh
	addRegion()	Add a region of specific resistivity to the mesh
	createModel()	Interactive region definition
	createSequence()	Create sequence for forward modeling
	importSequence()	Import sequence for forward modeling
	forward()	Run the forward model
	write2in()	Write the .in file with all inversion settings
	write2protocol()	Write the protocol.dat file with the measurements
	invert()	Run the inversion
	showResults()	Show the inverted section
Mesh (meshTools.py)	show()	Display the mesh with the default attribute
	add_e_nodes()	Add electrode node indexes to mesh
	summary()	Prints summary information about the mesh.
	assign_zone()	Assigns 2D zones to the mesh.
	computeElmDepth()	Calculate depth to datum for each element
	write_vtk()	Writes a .vtk file
	write_attr()	Writes a tabbed file with element attributes
	paraview()	Show mesh in Paraview application if available
Functions in meshTools.py	import_vtk()	Import a .vtk file and returns an instance of Mesh
	quad_mesh()	Create a quadrilateral mesh (called by R2)
	trian_mesh()	Create a triangular mesh (called by R2)
	custom_mesh_import()	Import a .msh, .vtk, .dat mesh format and return mesh instance.
	systemCheck()	Returns and prints information about the user's system; Operating system, number of logical CPU cores detected and memory available.

Appendix B

EMagPy: open-source standalone software for processing, forward modeling and inversion of electromagnetic induction data

Paul McLachlan[1], Guillaume Blanchy[1], Andrew Binley[1]

[1] Lancaster Environment Centre, Lancaster University, Lancaster, UK

Authorship statement

GB and PM wrote the code, the Jupyter notebook for the cases and the manuscript. AB contributed to writing the manuscript and supervised work on the field case studies.

Code availability

The code and data is available under the GPL-licence at [https://gitlab.com/](https://gitlab.com/hkex/emagpy) [hkex/emagpy](https://gitlab.com/hkex/emagpy). In addition, documentation can be found at [https://hkex.gitlab.](https://hkex.gitlab.io/emagpy/) [io/emagpy/](https://hkex.gitlab.io/emagpy/).

Abstract

Frequency domain electromagnetic induction (EMI) methods have had a long history of qualitative mapping for environmental applications. More recently, the development of multi-coil and multi-frequency instruments is such that the focus has shifted toward inverting data to obtain quantitative models of electrical conductivity. However, whilst collection of EMI data is relatively straightforward, the inverse modeling is more complicated. Furthermore, although several commercial and open-source inversion codes, exist, there is still a need for a user-friendly software that can bring EMI inversion to non-specialist audience. Here the open-source EMagPy software is presented as an intuitive approach to modeling EMI data. It comprises a graphical user (GUI) interface and a Python application programming interface (API). EMagPy implements both cumulative sensitivity and Maxwell-based forward operators and can model data for 1D and quasi-2D/3D cases using either deterministic or probabilistic methods. The EMagPy GUI has a logical 'tab-based' layout to lead the user through data importing, data filtering, inversion, and plotting of raw and inverted data. In addition, a dedicated forward modeling tab is presented that allows generation of synthetic data. In this publication necessary considerations, and background, of EMI theory are described before EMagPy's capabilities are presented through a series of synthetic and field-based case studies. Firstly, the performance of cumulative sensitivity and Maxwell-based forward models, and the influence of measurement noise are assessed for synthetic cases. Then the importance of data calibration for a riparian wetland dataset, the ability to include a priori information for a river-borne survey and the potential for monitoring soil moisture in a time-lapse example are all investigated. It is anticipated that EMagPy offers a user-friendly tool suitable for novice and experienced

practitioners alike, and its intuitive nature mean it can provide a useful tool for teaching purposes.

B.1   Introduction

B.1.1   Applications of electromagnetic induction

Ground-based frequency domain electromagnetic induction (EMI) methods use phenomena governed by Maxwell's equations to infer information about the electrical conductivity (EC) of the subsurface. As EC is the reciprocal of electrical resistivity, EMI methods can provide comparable information to electrical resistivity methods. However, given that they do not require direct coupling with the ground, they can be more productive than standard electrical resistivity tomography (ERT) methods, particularly for surveying large areas (e.g. Frederiksen et al., 2017; Huang et al., 2017a). EMI measurements are typically expressed in terms of apparent electrical conductivity (ECa) and have a long history of being used to reveal spatial patterns of a number of hydrogeologically and agriculturally important properties and states; e.g. salinity (Corwin, 2008), water content (Corwin & Rhoades, 1984; Williams & Baker, 1982; Sherlock & McDonnell, 2003), clay content (Triantafilis & Lesch, 2005; ?) and soil organic matter (Huang et al., 2017a). Furthermore, some studies have used repeated (i.e. time-lapse) measurements of ECa to reveal temporal patterns, e.g. for soil water content monitoring (Robinson et al., 2012b; Huang et al., 2016, 2017d; Martini et al., 2017).

In addition to ECa mapping, the development of multi-frequency and multi-coil instruments has enabled the potential to invert EMI data to provide quantitative models of depth specific EC. For instance, by obtaining multiple EMI measurements with different sensitivity patterns, models of EC can be obtained. EMI inversions can be formulated as the minimization of the difference between measured and synthetic ECa values generated from forward model calculations. Most EMI inversion algorithms use a 1D forward model based on either the linear cumulative sensitivity (CS) function proposed by McNeill (1980) or non-linear full solution (FS) forward model based on Maxwell's equations (e.g. Wait, 1982; Frischknecht, 1987). Moreover, some EMI inversion programs, such as EM4Soil (Monteiro San-

tos, 2004) and the Aarhus Workbench (Auken *et al.*, 2015), implement 1D forward modeling and address issues of 2D/3D sensitivity by using lateral constraints to encourage laterally smoothed images when; these methods are typically referred to as quasi-2D/3D inversion.

As with ECa mapping, EMI inversion has also been used in a wide range of applications, see Table B.1. It is important to note differences in how EMI data are collected, processed and modeled as different approaches will ultimately yield different inversion results. For instance, whether the EMI device is operated at ground level or an elevated level has implications for its sensitivity patterns (e.g. Andrade *et al.*, 2016). Moreover, although the use of FS forward models is generally advocated for, especially in high salinity or clay rich environments (e.g. Koganti *et al.*, 2018; Zhao *et al.*, 2019), CS forward models are still commonly used (e.g. Huang *et al.*, 2016; Saey *et al.*, 2016). The distinctions between FS and CS forward models, and limitations of CS forward models, are important to consider and consequently are investigated in this work. Lastly, whether EMI data has been calibrated will influence results. For instance, calibration of EMI measurements has been used to account for factors relating to device setup and/or above ground features (e.g. vegetation) to provide more confidence (i.e. lower data total misfit) in inverted models. Calibration is commonly done with either electrical methods, ERT or vertical electrical sounding (see Lavoué *et al.*, 2010; von Hebel *et al.*, 2019, 2014) or soil sampling, using trenches or cores (see Jadoon *et al.*, 2015; Zare *et al.*, 2015; Huang *et al.*, 2016). Furthermore, it has also been argued that calibration of EMI data is a prerequisite for inversion (e.g. Lavoué *et al.*, 2010; Moghadas *et al.*, 2017).

There are several established commercial programs for processing and inverting frequency domain EMI data. Commercial programs include the Aarhus workbench (Auken *et al.*, 2015), and EM4Soil (Monteiro Santos, 2004). In addition, several open source software codes exist, such as the Matlab-based open-source GUI for EMI data, FEMIC (Elwaseif *et al.*, 2017), and the Python-based open-source codes SimPEG (Heagy *et al.*, 2017) and pyGIMLi (Rücker *et al.*, 2017). Open-source software has several benefits over commercial software: it permits

Table B.1 – Non-exhaustive list of environmental studies using inverted EMI data. HCP refers to horizontal co-planar, VCP refers to vertical co-planar and PRP refers to perpendicular orientation (all of which are defined in the text).

Reference	Application	Survey acquisition	Calibration	Inversion details
Martinelli & Duplaá (2008)	Chemical pollution	GEM-2 SLEM: Six frequencies between 2575 and 47025 Hz	None	EM1DFMFW (Farquharson et al., 2003) with FS
Brosten et al. (2011)	Hydraulic conductivity	GEM-2, Height: 1 m HCP1.22 At 15 frequencies between 10 and 60 kHz	None	FEMIC with FS
von Hebel et al. (2014)	Structure	CMD Mini-Explorer Height: 0 m, VCP0.32, VCP0.71, VCP1.18, HCP0.32, HCP0.71, HCP1.18 At 30 kHz	ERT	SCE-UA with FS and CS
Davies et al. (2015)	Coastal salinity	DUALEM-421S Height: 0.2 m HCP1.0, PRP1.1, HCP2.0, PRP2.1, HCP4.0 PRP4.1 At 9 kHz	None	EM4Soil with FS
Jadoon et al. (2015)	Soil salinity	CMD Mini-Explorer Height: 0.05 m VCP0.32, VCP0.71, VCP1.18, HCP0.32, HCP0.71, HCP1.18 At 30 kHz	Soil sampling	FS
Shanahan et al. (2015)	Soil moisture	CMD Mini-Explorer Height: 0 m, VCP0.32, VCP0.71, VCP1.18, HCP0.32, HCP0.71, HCP1.18 At 30 kHz	ERT	McMC inversion with CS
Zare et al. (2015)	Soil salinity	DUALEM-421S Height: 0.2 m HCP1.0, PRP1.1, HCP2.0, PRP2.1, HCP4.0 PRP4.1 At 9kHz	Soil sampling	EM4Soil with CS and FS
Christiansen et al. (2016)	Archaeology/ stratigraphy	DUALEM-421S, Height: 0.2 m HCP1.0, HCP2.0, HCP4.0, PRP2.1, PRP1.1, PRP4.1 At 9 kHz	ERT based	Aarhus Workbench with FS

Table B.2 – (continued)

Reference	Application	Survey acquisition	Calibration	Inversion details
Huang *et al.* (2016)	Soil moisture	DUALEM-421S Height: unknown HCP1.0, HCP2.0, HCP4.0, PRP2.1, PRP1.1, PRP4.1 At 9 kHz	Soil sampling	EM4Soil with CS and FS
Saey *et al.* (2016)	Stratigraphy	DUALEM-421S Height: 0.16 m HCP1.0, HCP2.0, HCP4.0, PRP2.1, PRP1.1, PRP4.1 At 9 kHz	None	CS function
Frederiksen *et al.* (2017)	Stratigraphy	DUALEM-421S Height: 0.285 m HCP1.0, HCP2.0, HCP4.0, PRP2.1, PRP1.1, PRP4.1 At 9 kHz	None	Aarhus Workbench with FS
Huang *et al.* (2017a)	Soil organic carbon	DUAELM-21S Height: 0.075 m HCP1.1, HCP2.1 PRP1.1, PRP2.1 At 9 kHz	None	EM4Soil with FS and CS
Huang *et al.* (2017b)	Soil moisture	DUAELM-21S Height: 0.075 m HCP1.1, HCP2.1 PRP1.1, PRP2.1 At 9 kHz	None	EM4Soil with FS and CS
Whalley *et al.* (2017)	Soil moisture	CMD Mini-Explorer Height: 0 m, HCP/VCP s=0.32, 0.71, 1.18 m At 30 kHz	ERT	Gauss-Newton smoothed time-lapse with CS
Koganti *et al.* (2018)	Soil salinity	DUALEM-21S Height: 0.45 m HCP1.0, HCP2.0, PRP2.1, PRP1.1 At 9 kHz	Soil sampling	EM4Soil with CS and FS
Martinez *et al.* (2018)	Soil moisture	DUALEM-21S HCP1.0, HCP2.0, PRP2.1, PRP1.1 At 9 kHz	None	EM4Soil with CS and FS
von Hebel *et al.* (2019)	Stratigraphy	CMD Mini-Explorer Height: 0 m, VCP0.32, VCP0.71, VCP1.18, HCP0.32, HCP0.71, HCP1.18 At 30 kHz	ERT	SCE-UA with FS

better reproducibility, it is free and it allows the user to interrogate the source code and, where necessary, adapt and customize for their own application. Moreover, despite their availability, there is still a need for a comprehensive open-source software capable of bringing EMI inversion to a non-specialist audience. Given the increasing application of geophysics in multi-disciplinary projects, the need of a flexible and intuitive software for EMI inversion is a necessity.

In this work a Python-based open source EMI inversion software, EMagPy, is introduced. EMagPy has capabilities to generate synthetic data, filter and calibrate field data, and perform quasi-2D/3D inversions. The inversion algorithms utilize either Maxwell-based FS forward models or CS forward models, and provide the capability to obtain smoothly and sharply varying models of EC. EMagPy provides a tab-based, user-friendly interface to that makes it accessible for novice users, making it ideal for teaching and training purposes. This manuscript provides a summary of the theoretical background to the software and highlights its capabilities through several case studies. Specifically, the case studies investigated are: (1) the performance of CS and FS forward models, (2) the impact of noise and height on the inversion results, (3) the impact of EMI calibration on a riparian wetland data set, (4) EMI inversion of a river-borne data set with a priori knowledge of river stage and EC , and (5) time-lapse inversion of EMI data from an agricultural experiment to characterize soil moisture change.

B.2   Material and methods

B.2.1   EMI Background

EMI devices operate by passing an alternating current through a transmitter coil to generate a primary electromagnetic field (H_p). This time-varying primary electromagnetic field interacts with the subsurface to induce eddy currents which in turn generate a secondary electromagnetic field (H_s). H_p and H_s are then recorded by the receiver coil, see Figure B.1. The ratio of H_s and H_p is expressed as a complex number with an in-phase component (P) and an out-of-phase, or quadrature, component (Q). The ratio H_s/H_p is dependent on both the instrument set-up (e.g. operating frequency, coil separation and coil orientation) and subsurface con-

ditions (e.g. magnetic, conductive and dielectric properties). At the frequencies used, dielectric properties can generally be ignored; furthermore, given that in most environmental settings the subsurface can be considered non-magnetic such that the magnetic permeability of the subsurface is can be equal to the magnetic permeability of free space ($\mu_0 = 1.257$ x 10^{-8} H/m).
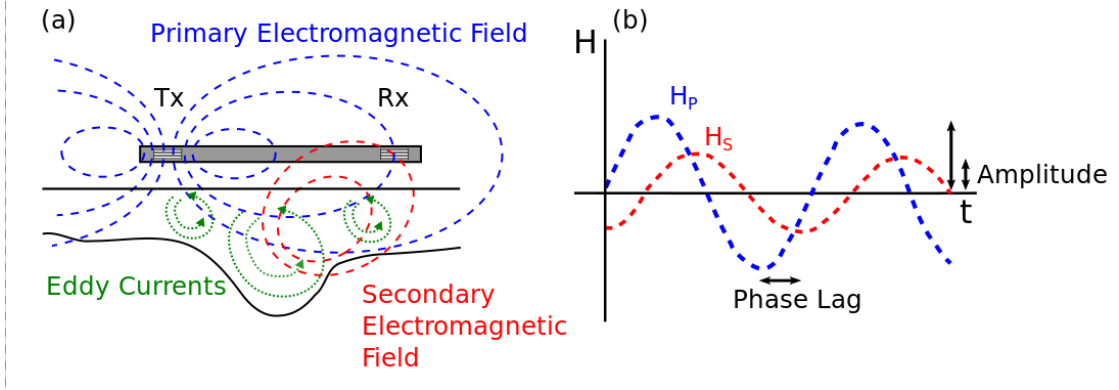
Figure B.1 – (a) Schematic of an EMI device with one transmitter coil (Tx) and one receiver coil (Rx) over a ground with a highly conductive medium overlying a more resistive medium. The transmitter emits a transient primary magnetic field (H_p) that induces eddy currents in the ground. These eddy currents generate a secondary electromagnetic field (H_s). (b) Both primary and secondary electromagnetic field are sensed by the receiver coil and from the complex ratio of their signals, information about the subsurface can be inferred.

For any given ground properties, the obtained H_s/H_p is dependent upon the separation distance between the transmitter and receiver coil, the operation frequency and the orientation of coils. The most commonly used orientations are referred to as coplanar loops in which both the transmitter and receiver coils are orientated either horizontally (HCP) or vertically (VCP), with respect to ground. Another coil orientation is the perpendicular orientation (PRP) in which the transmitter and receiver loops are oriented at 90 degrees from one another. In addition, many devices are multi-coil or multi-frequency, meaning that measurements with different sensitivity patterns can be obtained by the same instrument, often simultaneously, and used for inverse modeling.

Most EMI instruments express their measured H_s/H_p values as values of apparent electrical conductivity (ECa). This term was introduced by McNeill (1980) to provide a more comprehensible measurement with the same units as EC, i.e., S/m. McNeill (1980) derived a linear relationship describing the Q value expected

from a homogeneous subsurface electrical conductivity. The relationship therefore links the Q value of an assumed homogeneous subsurface to an ECa (i.e. the EC of a corresponding homogeneous ground). It is commonly referred to as the low induction number (LIN) approximation as it assumes that the device is being operated for cases where the induction number (β) is low ($\beta << 1$). The induction number is given by:

$$\beta = s\sqrt{\frac{\omega\mu_0 EC}{2}}, \tag{B.1}$$

where ω is the angular frequency ($2\pi f$) and s is the coil separation. The LIN approximation proposed by McNeill (1980) is given by:

$$EC_a = \frac{4}{\omega\mu_0 s^2}Q \tag{B.2}$$

It can be clearly seen from equation 1 that large frequencies and higher EC ground will violate the $\beta \ll 1$ specification proposed by McNeill (1980). Moreover, other more conservative β values of < 0.3 (Wait, 1982) and < 0.02 (Frischknecht, 1987) have also been proposed to determine when conditions can qualify as LIN. It is also important to note that the LIN approximation assumes that the EMI device is operated at ground level above a subsurface with a homogeneous EC; therefore it may be invalid for heterogeneous environments (see Callegary *et al.*, 2007; Lavoué *et al.*, 2010) or when the device is operated above the ground. Nonetheless, development of such a relationship has been essential in advancing the EMI method.

B.2.2   Forward modeling

To invert EMI data, forward models that provide accurate theoretical responses for any given combination of ground properties and device specifications are required. In EMagPy forward responses can be calculated using CS or FS based forward models. The CS forward models, also proposed by McNeill (1980), provide a linear simplification of the non-linear FS forward models, both approaches are discussed below.

In EMagPy the CS and FS forward models are 1D, i.e. it is assumed that the subsurface comprises continuous horizontal layers and there is no topographic vari-

ation at the field site. Although EMI sensitivity patterns are inherently 3D, 1D approaches are more computationally efficient and inversions can be completed in parallel. Moreover, full 3D inversion approaches would require overlapping measurement footprints, hence a denser sampling, which might not always be the case for applications aiming to cover large areas. In contrast, a 1D inversion approach does not require a consistent survey patterns to ensure overlapping measurements. Moreover, as with other inversion software that use 1D forward models (e.g. EM4Soil and the Aarhus Workbench), EMagPy contains methods to mitigate 2D/3D effects. For instance, anomalous data can be removed, running averages can be calculated, and quasi 2D/3D inversions can be conducted (i.e. by enforcing lateral smoothing in the inversion). Applying a running average is particularly useful to smooth consecutive measurements with overlapping footprint. This prevents over-estimation of the resolution of the survey.

Nonetheless, for completenesss, it is also important to briefly mention other approaches to account for 3D effects. For instance, Flores Orozco *et al.* (2012) proposed a method that uses spatially average EMI measurements to determine subsurface 3D EC structures, Benech *et al.* (2016) used a combination of 1D and subsequent target 3D inversions and Guillemoteau *et al.* (2017) proposed a linearized 3D forward model and highlight its performance over standard 1D FS forward models. However, at the time of writing, EMagPy focuses on the common 1D approach for reasons of computational efficiency, simplicity and flexibility.

Cumulative sensitivity forward model

McNeill (1980) provided CS forward model functions that describe the relative contribution of materials below a specific depth to an overall ECa value when a device operates under LIN conditions. These CS functions assume that the sensitivity of the instrument is solely a function of the depth and coil separation and does not depend on the subsurface EC, or the operating frequency of the device. The CS responses for VCP, HCP and PRP orientations are as follows:

$$R_{VCP}(z) = \sqrt{4z^2 + 1} - 2z, \tag{B.3}$$

$$R_{HCP}(z) = \frac{1}{\sqrt{4z^2 + 1}}, \tag{B.4}$$

$$R_{PRP}(z) = 1 - \frac{2z}{\sqrt{4z^2 + 1}}, \tag{B.5}$$

where z is the depth normalized by the coil separation, s. From equations B.3 and B.4 the sensitivities for different coil separations for the specifications of the CMD Mini-Explorer and CMD Explorer (GF Instruments, Brno, Czech Republic) can be calculated, see Figure B.2. For instance, it can be seen that measurements made with coils in the VCP orientation are more sensitive to the shallow subsurface and measurements made in HCP orientation are sensitive to deeper depths. These functions are commonly used by manufacturers to provide information about the depth sensitivity of their instruments; i.e. the rule of thumb states VCP measurements have an effective depth of 0.75 times the coil separation and 1.5 times for HCP measurements which is approximately equal to the depth above which 70% of the signal is obtained (see also Callegary *et al.*, 2007).
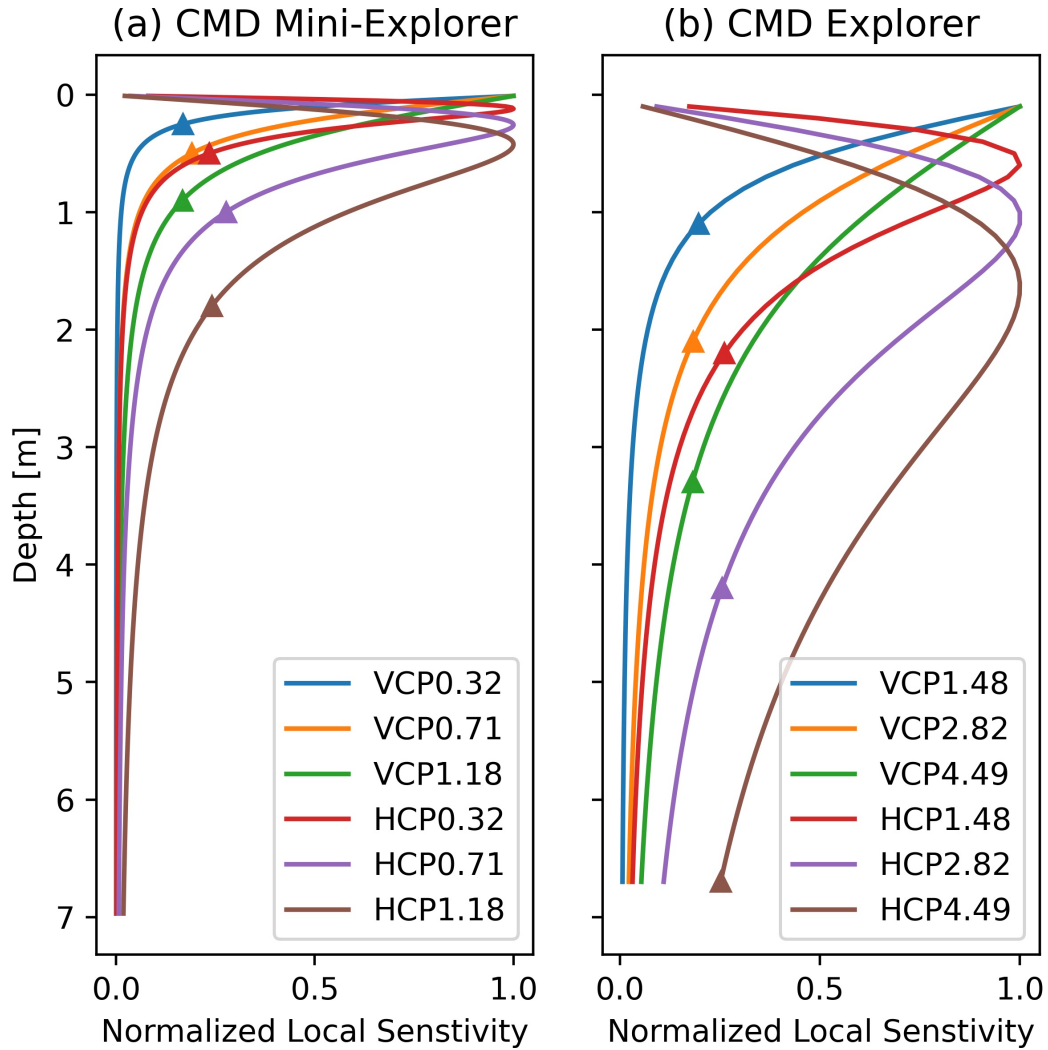
Figure B.2 – Normalized local sensitivity pattern of the coil configurations of two multi-coils instruments: (a) CMD Mini-Explorer and (b) CMD Explorer. Each coil configuration is first determined by its orientation (VCP/HCP here) and the Tx-Rx coil separation with units of meters. The triangles on each curve corresponds to the effective depth range supplied by the manufacturer.

As with the LIN approximation, the CS functions have been fundamental in advancing the EMI methods. Furthermore, despite the availability of inversion algorithms based on the FS forward model, the use of CS forward model in EMI applications is still common (see Table B.1). This is largely due to their simplicity and efficiency in the inversion process compared to non-linear FS forward solutions. Furthermore, although, as with the LIN approximation, the CS forward model was developed for application when EMI devices are operated at ground level, several studies have used it to model the response of devices operated at some elevation

by re-scaling the CS function (see **?**).

Full Maxwell forward model

In order to calculate a non-simplified response of the ground, in terms of HS/HP, FS forward models must be used. The FS forward models used in EMagPy rely on the assumption that electromagnetic fields propagate only due to conduction currents., which is valid at low frequencies. The Maxwell-based FS response is provided by Wait (1982) and can be used to determine the response of an EMI instrument over a 1D layered earth consisting of N layers:

$$Q_{VCP} = \mathfrak{Im}\left(\frac{H_s}{H_p}\right)_{VCP} = \mathfrak{Im}\left(-s^2 \int_0^\infty R_0 J_1(s\lambda)\lambda d\lambda\right), \qquad (B.6)$$

$$Q_{HCP} = \mathfrak{Im}\left(\frac{H_s}{H_p}\right)_{HCP} = \mathfrak{Im}\left(-s^3 \int_0^\infty R_0 J_0(s\lambda)\lambda^2 d\lambda\right), \qquad (B.7)$$

$$Q_{PRP} = \mathfrak{Im}\left(\frac{H_s}{H_p}\right)_{PRP} = \mathfrak{Im}\left(-s^3 \int_0^\infty R_0 J_1(s\lambda)\lambda^2 d\lambda\right), \qquad (B.8)$$

Where $\mathfrak{Im}$ denotes that only the imaginary component is considered, J_0 and J_1 are Bessel functions of zeroth and first orders, respectively, and R_0 is the reflection factor, which is dependent on the thickness and EC of each layer. The reflection factor is calculated at the interface of each layer, including between the air and the first layer. It can be obtained recursively from the infinite N^{th} layer, given that beyond N can be assumed homogeneous and therefore $R_{N+1} = 0$, and the following:

$$R_n = \frac{\frac{\Gamma_n - \Gamma_{n+1}}{\Gamma_n + \Gamma_{n+1}} + R_{n+1}e^{-2\Gamma_{n+1}h_{n+1}}}{1 + \frac{\Gamma_n - \Gamma_{n+1}}{\Gamma_n + \Gamma_{n+1}}e^{-2\Gamma_{n+1}h_{n+1}}}, \qquad (B.9)$$

where $\Gamma_n = \sqrt{\lambda^2 + i\omega\mu_0 EC_n}$, and h_n and EC_n are the thickness and the EC of the nth layer. R_0 is obtained by assuming the EC of layer 0 is 0 S/m to reflect the air. Furthermore, the FS forward models can be modified to account for cases when the device is operated above the ground, in EMagPy this done by modeling the 'air gap' as a layer with an EC of 0 mS/m, the same approach is also used for the CS functions. The integrals in equations B.6, B.7 and B.8 represent the

Hankel transform and can be calculated by linear filtering (Guptasarma & Singh, 1997; Anderson, 1979). As noted, most devices provide measurements as an ECa, value, therefore in order to use the FS forward model the obtained Q values from equations B.6, B.7 and B.8 need to be converted to ECa values. The nature of this translation is crucial, as discussed below.

B.2.3 Comparison of ECa values and forward models

Although the LIN approximation can be used to obtain ECa values that comprehensibly represent the subsurface EC, the non-linear relationship between subsurface EC and Q has led several authors to develop methods that provide a more representative ECa values, especially when LIN assumptions are not valid. For instance, although most manufacturers state that their EMI devices operate under LIN conditions and use the LIN approximation to obtain ECa values, Beamish (2011) demonstrated that LIN assumptions are perhaps only valid at low EC values (< 12 mS/m). Typically, for EMI devices operating at low to moderate induction numbers (e.g. low frequency devices with short coil separations operating above low EC ground, see equation 1) the in-phase (P) component of the signal is unstable and approaches to obtain a more representative ECa value focus only on the Q component (e.g. Andrade *et al.*, 2016; Guillemoteau *et al.*, 2016; von Hebel *et al.*, 2019). At higher induction numbers, methods typically focus on both the P and Q components (e.g. Huang & Won, 2000; Guillemoteau *et al.*, 2015). This is done because at higher Q values the relationship between Q and EC is non-monotonic and methods relying on Q values alone will provide misleading ECa values. Because of the generally weakly magnetic subsurface in environmental cases, and the characteristic instability of P measurements for devices operating under, or near, LIN conditions, in EMagPy a method akin to Van Der Kruk *et al.* (2000), Andrade *et al.* (2016), von Hebel *et al.* (2019) is used to compute a more representative ECa. This is done by minimizing the absolute difference between an observed Q value, Q_{target}, and a Q value for an equivalent homogeneous subsurface conductivity, Q_{homo}:

$$min([Q_{target} - Q_{homo}]). \tag{B.10}$$

The ECa value obtained from this method therefore closely matches the EC of a homogeneous subsurface. As this optimization can be subject to localized minima, in EMagPy it is initialized with the LIN approximation. To avoid confusion, in EMagPy ECa values obtained from Q values via the LIN approximation are referred to as LIN-ECa whereas ECa values obtained via Equation B.10 are referred to as FS$_{EQ}$-ECa, this distinction is important and is discussed further below. Moreover, as noted above, the relationship between Q and EC is not monotonic at high EC values. For instance Figure B.3, shows the relationship of LIN-ECa and FS$_{EQ}$-ECa with EC for the specifications of the 4.49 m coil separation of the GF Instruments CMD Explorer operated in HCP mode. It is evident that beyond 728 mS/m Q begins to decrease, furthermore at such conductivities the device is now operating at moderate induction numbers ($\beta = 0.54$). This has a number of important implications that practitioners ought to be aware of, the first being that if the subsurface EC is too high, inversion using only ECa or Q values will yield unreliable results and approaches considering P values ought to be used (e.g. Guillemoteau *et al.*, 2016). Moreover, at high subsurface EC values Q values become more similar, this means that in higher EC environments, measurement or calibration errors may have more influence on the ability to obtain accurate models of EC.
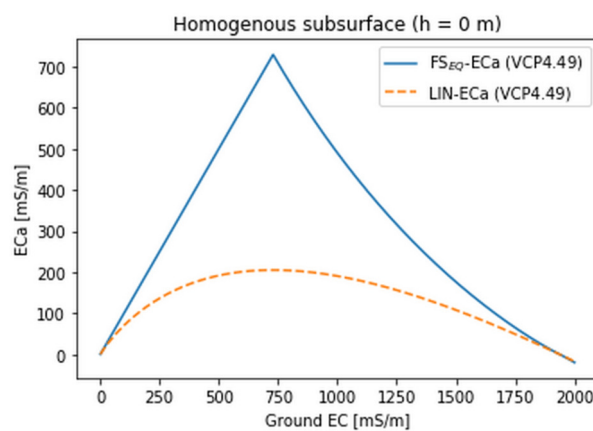
Figure B.3 – Relationship between ground EC and ECa calculated using the LIN approximation and FS$_{EQ}$ methods.

Additionally, although the FS_{EQ}-ECa method provides a more representative ECa, provided the subsurface EC is low enough, the key importance when inverting EMI data using the FS forward model is that modeled ECa are obtained from Q using the same method used to convert Q to ECa by the EMI device. For instance, although in most cases devices use the LIN approximation, some EMI devices use a custom calibration. For example, GF Instruments use a manufacturer calibration based on a linear fit through the Q values obtained at sites of known subsurface EC. In addition, different GF Instruments calibrations exist when their devices are operated at ground level and 1 m, such that measurements made at 1 m elevation are more similar to measurements made on the ground surface. This would mean, for instance, that if ECa values using the GF Instruments 1 m calibration were converted to Q using the LIN approximation they would be significantly higher than actually measured and would yield incorrect inversion results.

Furthermore, although the CS is also based on LIN assumptions, the ECa values obtained from CS forward models may differ from the ECa obtained from LIN approximation of Q values measured in the field. This means that under certain scenarios use of the CS forward model could result in erroneous inversion. In this work a distinction between an ECa value from equation 2 (LIN-ECa), an ECa value from equation 6-10 (FS_{EQ}-ECa) and from the equations 3-5 (CS-ECa) is made, see Figure B.4.
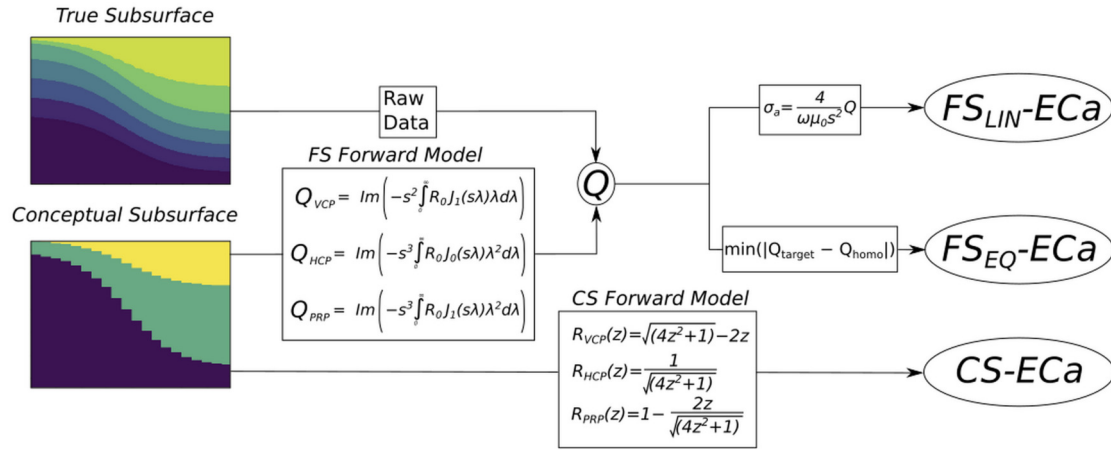
Figure B.4 – The different routes for obtaining ECa values. For field cases all devices obtain a Q value which is typically transformed into an ECa using either the LIN-ECa or some other manufacturer calibration (e.g. the GF instruments linear calibration). Some authors (e.g. von Hebel *et al.*, 2019) opt to convert their field obtained Q values using a minimizing approach (FS$_{EQ}$-ECa). For modeled cases there are two principle routes to obtain ECa values from a model subsurface: (1) Q values may be calculated from the FS forward model, they would then typically be converted to LIN-ECa or FS$_{EQ}$-ECa, and (2) CS-ECa values can be obtained directly using the CS forward model.

To highlight the distinctions of ECa values defined here, and hence stress the importance of their difference, they can be computed for a variety of synthetic cases. In Figure B.5, FS$_{EQ}$-ECa, LIN-ECa and CS-ECa are calculated for the device specifications of the largest coil separation (4.49 m) of the CMD Explorer operated in VCP mode above homogeneous and heterogeneous subsurfaces, at ground level and at 1 m elevation. For the homogeneous case, data are generated for subsurface EC of 1 to 100 mS/m in 1 mS/m increments, the heterogeneous case data is generated for a two layer model with a layer 1 thickness of 0.5 m, an upper layer EC of 1 to 100 mS/m in 1 m/Sm increments and a constant layer 2 EC of 50 mS/m.
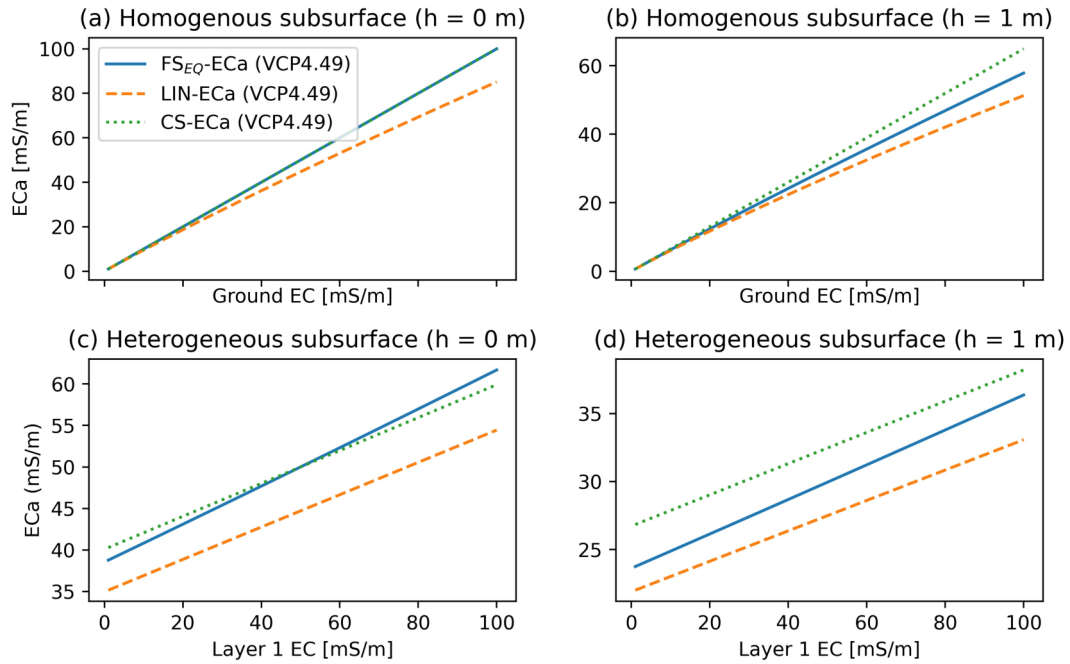
Figure B.5 – Differences between CS-ECa, FS$_{EQ}$-ECa and LIN-ECa for a homogeneous and a heterogeneous case. (a) shows the differences over a homogeneous medium with increasing EC, (b) shows the differences over an increasing homogeneous medium when the device is operated at 1 m, (c) shows the differences over a heterogeneous medium with a fixed layer 1 thickness of 0.5 m and a fixed layer 2 EC of 50 mS/m, and (d) shows the differences over a heterogeneous medium with a fixed layer 1 thickness of 0.5 m and a fixed layer 2 EC of 50 mS/m when the device is operated at 1 m elevation. In all plots h is the device height above ground level.

Firstly, it can be seen from Figure B.5a that, for a homogeneous subsurface EC when the device is at ground level, the FS$_{EQ}$-ECa and CS-ECa values lie on a 1:1 line, whereas the LIN-ECa deviates from this line at higher EC values. In comparison, when the device is operated at 1 m elevation (Figure B.5b) FS$_{EQ}$-ECa, LIN-ECa CS-ECa all show increasing deviation at higher subsurface EC values, with the FS$_{EQ}$-ECa being intermediate between the higher CS-ECa and the lower LIN-ECa. Furthermore, these values are broadly comparable for low conductivities (< 20 mS/m), for the ground level and 1 m elevation cases. When the device is operated at ground level (Figure B.5c), for the heterogeneous case, the LIN-ECa is significantly lower than the other two values. Furthermore, the FS$_{EQ}$-ECa and CS-ECa match when the upper layer conductivity is 50 mS/m (i.e. homogeneous subsurface). When the device is operated at 1 m elevation (Figure B.5d) for the heterogeneous case all ECa values differ from each other across the layer 1

conductivity range.

These observations demonstrate that under certain conditions the CS function may be inappropriate to model with LIN-ECa values obtained from the field, i.e. when the subsurface has high EC values, is strongly heterogeneous or when the device is operated above ground. Moreover, if FS_{EQ}-ECa is taken as the most accurate representation of the subsurface EC, it can be seen that LIN-ECa underestimates the subsurface EC in the case of higher EC values and heterogeneous environments. However, as noted above, so long as the translation between Q and ECa is consistent for the EMI device and FS forward model, the derivation of ECa using this method is not a requisite for accurate inversion. Furthermore, this FS_{EQ}-ECa requires more computational overhead than the LIN-ECa method as it requires minimization of equation 10.

B.2.4   Calibration of EMI data

In addition to considering ECa values, it is important to note that in many cases EMI devices are only seen to provide qualitative measurements of conductivity because of instrument calibration difficulties (Triantafilis *et al.*, 2000; Sudduth *et al.*, 2001; Gebbers *et al.*, 2009; Abdu *et al.*, 2007; Nüsch *et al.*, 2010). For instance, external influences such as presence of the operator, zero-leveling procedures, field set up or above ground features not accounted for in the inversion (e.g. vegetation), can influence the measurements significantly. Therefore, in order to permit quantitative modeling of EMI data several authors have advocated for the need of data calibration (e.g. Lavoué *et al.*, 2010; von Hebel *et al.*, 2014). Proposed calibration methods have included collection of intrusive soil samples (e.g. Triantafilis *et al.*, 2000; Moghadas *et al.*, 2012), use of ERT (e.g. Lavoué *et al.*, 2010; von Hebel *et al.*, 2014) or use of measurements made at multiple elevations (e.g. Tan *et al.*, 2019).

In this work the method using ERT is implemented, whereby depth-specific models of electrical resistivity are used to calculate a forward EMI model response which is then paired with a set of EMI measurements made along the ERT transect. Although it is possible to invert ERT data with several inversion programs, the

calibration implementation in EMagPy is designed so it can directly use ERT models produced by its sister code, ResIPy (https://gitlab.com/hkex/pyr2; Blanchy *et al.*, 2020b). Clearly, there is an implicit assumption here that the ERT-derived electrical conductivities are the true subsurface values, and that the footprint of EMI and ERT measurements are similar or can be accounted for by lateral averaging.

B.2.5 Inversion methods

Typically, inversions of EMI data are done using deterministic or probabilistic methods. In most cases (e.g. Monteiro Santos, 2004; Guillemoteau *et al.*, 2016; Mester *et al.*, 2011) deterministic strategies employ gradient-based minimization techniques to produce a single best solution. Such approaches are popular as they provide a relatively fast method to invert data. However, although calculating the Jacobian (sensitivity) matrix is straightforward for the linear CS forward models, for FS forward models the problem must be linearized. The other common set of approaches involves probabilistic methods (e.g. Minsley, 2011; Shanahan *et al.*, 2015; Moghadas *et al.*, 2017; Moghadas & Vrugt, 2019) whereby posterior parameter distributions can be obtained and used to characterize uncertainty. Recently, neural network methods have also been applied for inverting EMI measurements (Moghadas, 2020).

Data and model misfit

In EMagPy the inverse problem can be solved to produce either sharply or smoothly varying models of EC. The sharp inversion solves the inverse problem with both conductivities and depths as parameters, whereas the smooth inversion uses fixed depths and solves only for conductivities. In both cases the data misfit is defined as the difference between observed values and predicted values from the forward model solutions. As the smooth inversion typically produces a model containing more EC values than measurements it requires regularization with a model misfit term, which determines the smoothness of neighboring layers. In comparison, the sharp inversion, although a model misfit term can be used, the inverse problem is generally set such that the problem is over-determined, i.e. the number of param-

eters (depths and conductivities) is less than the number of measurements. The total misfit is given by:

$$\Phi = \Phi_d + \alpha\Phi_m, \tag{B.11}$$

where Φ_d is the data misfit, Φ_m is the model misfit and α is a smoothing parameter determining the influence of Φ_m on the total misfit, i.e. ordinarily this would be set to 0 for cases where a sharp model is warranted. The inversion problem can be solved by minimizing either the L1 or the L2 norm objective functions for each 1D profile. The data misfit for both norms are obtained by:

$$\Phi_d = \frac{1}{N}\sum_{i=1}^{N}|d_i - f_i(m)|, \tag{B.12}$$

$$\Phi_d = \frac{1}{N}\sum_{i=1}^{N}(d_i - f_i(m))^2, \tag{B.13}$$

where N is the number of coil configurations per profile, d is the observed values and $f(m)$ is the predicted values from the forward model with parameter set, m. Similarly, the model misfits for L1 and L2 norms, respectively, are obtained by:

$$\Phi_m = \frac{1}{M}\sum_{i=1}^{M-1}|EC_j - EC_{j+1}|, \tag{B.14}$$

$$\Phi_m = \frac{1}{M}\sum_{i=1}^{M-1}(EC_j - EC_{j+1})^2, \tag{B.15}$$

where M is the number of layers in the model and EC_j is the conductivity of layer j.

Optimization methods

In EMagPy, the total misfit can be minimized using three groups of methods (see Table B.3): using either (1) a Gauss-Newton method, (2) optimization from the scipy package (Virtanen et al., 2020), or (3) McMC optimization from the spotpy package (Houska et al., 2015). The Gauss-Newton implementation involves obtaining the Jacobian (sensitivity) matrix. Given its linear nature (i.e. sensitivity is not

dependent upon EC) this approach is straightforward for the CS function, however for the FS function the sensitivity is calculated for an assumed subsurface EC and if the initial EC model does not match the data well the solution can perform poorly. The Gauss-Newton implementation requires fixed depths and requires a large α value to produce smooth solutions. As the Jacobian matrix for the CS function does not depend on the layer conductivity, the solution is reached in one iteration, however for the FS the Jacobian matrix can be updated for a number of iterations until the solution reaches convergence. Such an approach is relatively quick and given that the Jacobian matrix is consistent for the implementation of the CS forward model it has been shown to perform well in time-lapse inversion applications (e.g. Whalley *et al.*, 2017).

Table B.3 – Minimization methods employed within EMagPy. Minimization method.

Minimization method	Description	Implemented features	Package used
Gauss-Newton	Gradient based method.	FS and CS forward model, L2 data and model misfit.	-
Nelder-Mead	Simplex heuristic search method.	CS and FS forward model, L1 and L2 data and model misfit.	scipy
L-BFGS-B	Approximation of BFGS method, with bounds. This method uses an estimate of the inverse Hessian matrix.	CS and FS forward model, L1 and L2 data and model misfit.	scipy
Conjugate Gradient	Gradient method for non-linear problems.	CS and FS forward model, L1 and L2 data and model misfit.	scipy
SCE-UA	Shuffled Complex Evolution Algorithm McMC based method.	CS and FS forward model, L1 and L2 data and model misfit.	spotpy
DREAM	Differential Evolution Adaptive Metropolis Algorithm McMC based method.	CS and FS forward model, L1 and L2 data and model misfit.	spotpy
ROPE	Robust Parameter Estimation McMC method	CS and FS forward model, L1 and L2 data and model misfit.	spotpy

Through the optimize function from scipy, EMagPy can minimize Equation B.11 using the Nelder-Mead (Nelder & Mead, 1965), L-BFGS-B (Byrd *et al.*, 1995) or

conjugate gradient (Fletcher & Reeves, 1964) algorithms. However, it is important to note that a broader range of algorithms exist though the scipy package and can be implemented if needed. These methods can be used for both the CS and FS forward models and are adapted to both smooth and sharp inversions. Their implementation is based on the function `scipy.optimize.minimize()` from the scipy python package that is used to minimize the objective function. Each method has its own convergence criteria (see scipy documentation) The McMC-based approach also minimizes an objective function but relies on different sampling approaches to find a solution. This implementation is based on the Python spotpy package (Houska *et al.*, 2015) that provides several solvers for parameter optimization such as SCE-UA (Duan *et al.*, 1994), DREAM (Vrugt & Ter Braak, 2011) or ROPE (Bardossy & Singh, 2008). One advantage of this approach is that it produces posterior distribution of the parameters from which a model uncertainty can be estimated (Figure B.6). In EMagPy, the posterior distribution is based on the 10% best samples (i.e. the models with the lowest total misfit) and the error for each model parameter is estimated using the standard deviation of this posterior distribution. Although this method was primarily implemented to obtain sharp models of EC, it can also be used for smooth models.
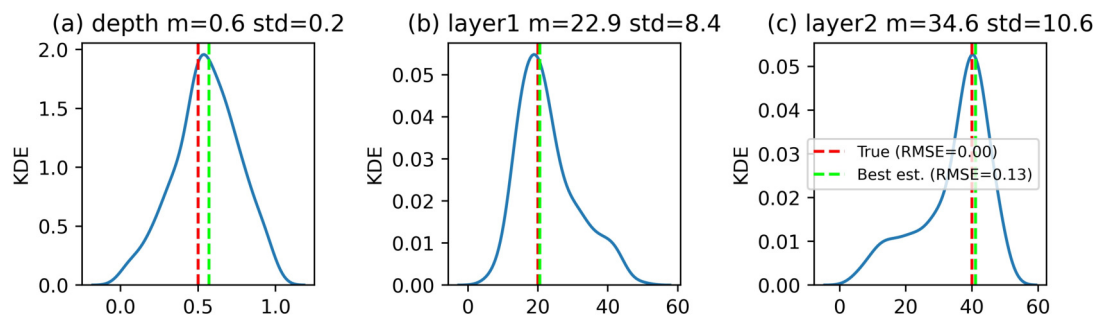
Figure B.6 – Example of a two layers, one varying depth model inverted using the McMC solver. Each subplot shows the posterior distribution of the parameters after sampling (3000 samples, 1 chain) for (a) the depth, (b) the EC of layer 1 and (c) the EC of layer 2. m is the mean and std is the standard deviation of the distribution (meters for depth and mS/m for layer1 and layer2). The red dashed line represent the true value while the green dashed line represent the best estimate (the one with the lowest misfit).

The quality of the inversion can be assessed visually by plotting the predicted

ECa values from the inverted model and the observed ECa for each profile using either `showMisfit()` or `showOne2one()` methods. The former will plot data as a profile showing the measured ECa values as points and the modeled EC values as lines, whereas the latter will plot measured and modeled ECa values and a 1:1 line. It is also possible to directly plot the root-mean-square error for each profile on top of the inverted section using `showResults(rmse=True)`. This makes it easy to quickly identify how suitable models are for explaining the different EMI observations.

B.2.6 EMagPy capabilities

EMagPy has been designed to provide both a Python application programming interface (API) and a graphical user interface (GUI). The Python API can be used in Python scripts or in Jupyter notebooks and enables automated tasks. The GUI provides an intuitive interface for the inversion and modeling of multiple datasets. In EMagPy, the code is structured around two main classes, a Survey and a Problem class. The Survey class that contains information related to the survey (such as the ECa values and their locations) and several display functions. Whereas the Problem class handles the forward and the inverse modeling and displays the results. Multiple surveys can be imported, to allow for time-lapse inversion. If geographical information (e.g. x and y coordinates) is available, map plots can be used to show the raw or inverted data. Raw data can also be displayed as 2D pseudo-sections of ECa measurements to highlight general patterns in the data. In this approach, pseudo-depths are taken as the maximum effective depth, i.e. the 70% sensitivity cut-off of the cumulative sensitivity functions (Figure B.4). Figure B.7 summarizes the capabilities of EMagPy. A more exhaustive list of API methods can be found in Appendix.
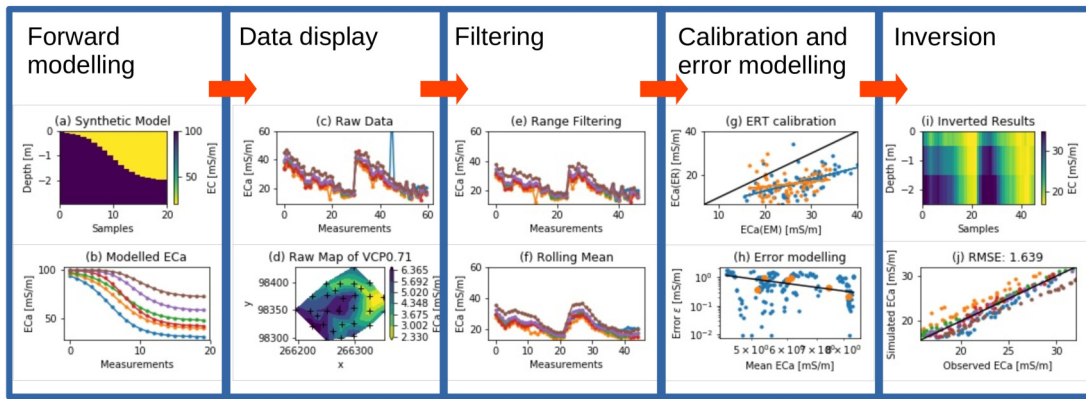
Figure B.7 – Capabilities of EMagPy workflow. Given a defined depth-specific EC model (a), synthetic apparent ECa can be modeled (b). Alternatively, field measurements can be imported and displayed as line plot (c) or map (d). Range filtering (e) and rolling mean (f) are among the options available to filter the measurements. If an ERT transect has been collected, a quantitative calibration of the measurement can be done (g). If cross-over points were collected, an error model can be derived (h). (g) shows the inverted data and (j) how well the modeled ECa fits the observed ECa.

Along with a pure Python API, EMagPy offers a graphical user interface (GUI) composed of several tabs exploiting the capabilities of the API (Figure B.8). The purpose of the interface is to provide a standalone intuitive user-friendly tool.
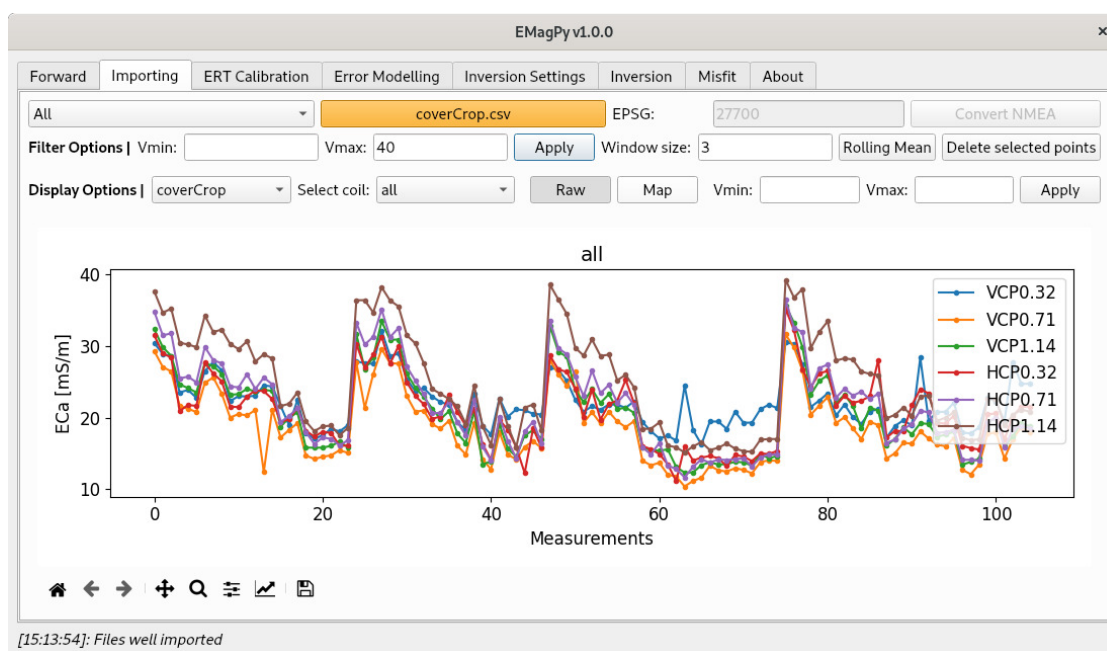
Figure B.8 – EMagPy graphical user interface is composed of several tabs that guide the user through the EMI processing workflow. At first the measurements are imported and filtered or alternatively they can be synthetically generated in the 'Forward' tab. Then an ERT calibration (if available) can be performed and an error model can be fitted if there are cross-over points. Then in the "Inversion Settings" tab the number of layers and their depths is defined as well as other inversion options. The inversion results are displayed in the 'Inversion' tab and the 'Post-processing' tab helps to assess the quality of the inversion.

B.3   Case studies

The following case studies presented here are included to demonstrate the ability of EMagPy for forward modeling and inversion. In addition, the Python code of the case studies presented below is available on the Gitlab repository of the project for anyone to reproduce (`https://gitlab.com/hkex/emagpy/-/blob/master/jupyter-notebook/em-paper.ipynb`).

B.3.1   Impact of different forward models on inversion

The first case demonstrates EMagPy's forward modeling capabilities and investigates the difference between FS and CS forward models for a heterogeneous subsurface. Data were generated from the synthetic model displayed in Figure B.9a, i.e. a two layer model comprising an upper layer with an EC of 10 mS/m and a

lower layer with an EC of 50 mS/m. Data were generated in terms of LIN-ECa using the FS forward model for the instrument properties of the CMD Explorer operated at ground level and 1 m before being inverted using either the FS forward model or the CS forward model. The FS_{LIN} forward models were used as in most devices express their measurements in terms of LIN-ECa. It can be seen for both 0 m and 1 m elevations the FS results match the synthetic model in terms of depth and EC. In comparison, although the CS results pick up the depth reasonably well for the 0 m elevation case, the EC values of the second layer are not well resolved.

```python
# parameters for the synthetic model
nlayer = 2 # number of layers
npos = 20 # number of positions/sampling locations
conds = np.ones((npos, nlayer))*[10, 50] # EC in mS/m
x = np.linspace(0.1, 2, npos)[:,None]
depths = 0 + 2/(1+np.exp(-4*(x-1))) # depth of model

# defines coils configuration, frequency and height above the ground
coils0 = ['VCP1.48f10000h0', 'VCP2.82f10000h0', 'VCP4.49f10000h0',
          'HCP1.48f10000h0', 'HCP2.82f10000h0', 'HCP4.49f10000h0']
coils1 = ['VCP1.48f10000h1', 'VCP2.82f10000h1', 'VCP4.49f10000h1',
          'HCP1.48f10000h1', 'HCP2.82f10000h1', 'HCP4.49f10000h1']

# forward modeling
ks = []
for i, coils in enumerate([coils0, coils1, coils0, coils1]):
    k = Problem()
    k.setModels([depths], [conds])
    _ = k.forward(forwardModel='FSlin', coils=coils, noise=0)
    ks.append(k)
k.showResults() # display original model
k.show() # display ECa computed from forward modeling

for k, fm in zip(ks, ['FSlin','FSlin','CS','CS']):
    k.setInit(depths0=[0.5], fixedDepths=[False],
              conds0=[20, 20], fixedConds=[False, False]) # set initial values
    # invert using ROPE solver (RObust Parameter Estimation)
    k.invert(forwardModel=fm, method='ROPE', regularization='l1',
             bnds=[(0.01, 3), (0, 80), (0, 80)], rep=1000, njobs=-1)
```
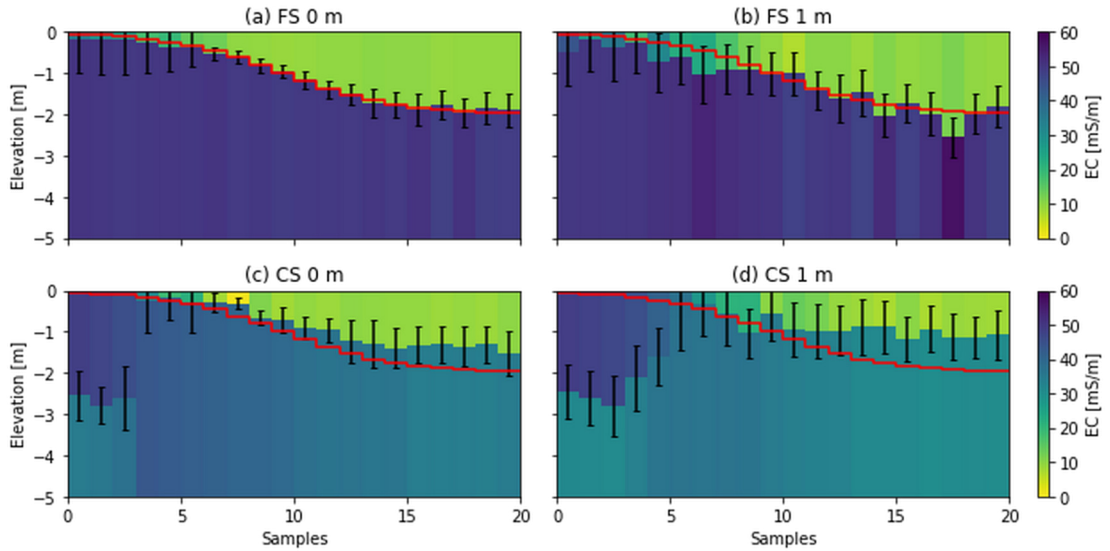
Figure B.9 – Inverted model with (a) FS_{EQ} at 0 m, (b) FS_{EQ} at 1 m, (c) CS at 0 m, (d) CS at 1 m. The red lines denote the true interface between the two layers of 10 and 50 mS/m from top to bottom. The error bars show the standard deviation of the posterior distribution (based on the 10% best sample).

B.3.2   Impact of measurement noise on inversion

To investigate the influence of measurement noise on the inversion when the device is operated at ground level and at 1 m, data were generated for a two layer model with an undulating interface. The upper layer EC was set at 20 mS/m and the lower layer EC was set at 100 mS/m, synthetic data were then generated using the FS forward model and corrupted with 2% Gaussian noise. Data with, and without noise, were then inverted. It was observed that in the noise-free cases, when the device is at 0 m and 1 m, the synthetic model is resolved relatively well Figure B.10. This is also true for the data containing noise when operated at ground level but when elevated at 1 m elevation the inversion performs much poorer. Importantly, as can be observed from the error bars the models that poorly match those in the synthetic model are characterized by similar uncertainty as those that match well; this implies that interpretation in such environments may be ambiguous.

```
# parameters for the synthetic model
nlayer = 2 # number of layers
npos = 20 # number of sampling locations
conds = np.ones((npos, nlayer))*[20, 100]
x = np.linspace(0.1, 2, npos)[:,None]
depths = 0.65 + 0.15* np.sin(x*np.pi*2)
# define coils configuration, frequency and height above the ground
coils0 = ['VCP1.48f10000h0', 'VCP2.82f10000h0', 'VCP4.49f10000h0',
```

```
         'HCP1.48f10000h0', 'HCP2.82f10000h0', 'HCP4.49f10000h0']
coils1 = ['VCP1.48f10000h1', 'VCP2.82f10000h1', 'VCP4.49f10000h1',
         'HCP1.48f10000h1', 'HCP2.82f10000h1', 'HCP4.49f10000h1']

coils = [coils0, coils0, coils1, coils1]
noises = [0, 0.05, 0, 0.05]
ks = []

# generate ECa using forward model
for i in range(4):
    k = Problem()
    k.setModels([depths], [conds])
    _ = k.forward(forwardModel='FSlin', coils=coils[i], noise=noises[i])
    ks.append(k)

# invert
for k in ks:
    k.setInit(depths0=np.array([0.5]), fixedDepths=[False])
    k.invert(forwardModel='FSlin', method='ROPE', regularization='l1',
            bnds=[(0.05, 2.5), (5, 150), (5, 150)], rep=1000, njobs=-1)
```
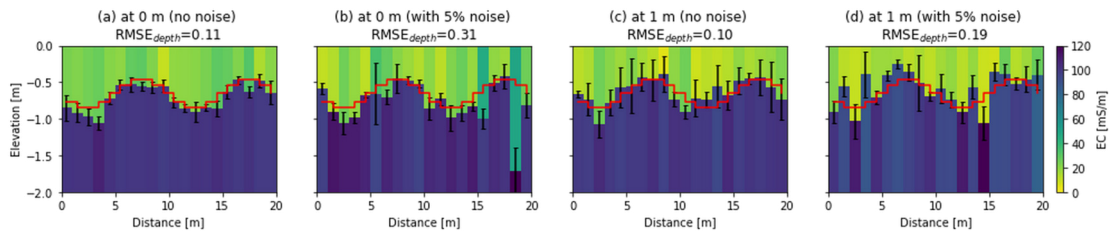

Figure B.10 – All inversions are performed with the ROPE solver on a two-layer model with a varying depth. (a) Inversion with 0% noise with device on the ground. (b) Inversion with 5% noise on the ground. (c) Inversion with 0% noise at 1 m above the ground (d) Inversion with 5% noise at 1 m above the ground. The red line represents the true interface between the two layers. The error bars show the standard deviation of the posterior distribution (based on the 10% best sample).

B.3.3   Comparisons of raw and ERT calibrated data from a riparian wetland

In this case study, data collected from a riparian wetland using the CMD Explorer are used to highlight how calibration of data can improve inversion performance. The riparian wetland is characterized by peat and underlying gravel and revealing the depth of the peat is of interest in characterizing the hydrology of the site (see Chambers *et al.*, 2015; **?**). ERT data were collected with a Syscal Pro 96 (Iris Instruments, Orleans, France) with 96 electrodes spaced of 0.5 m using a dipole-dipole sequences comprising 2342 measurements. An inverted EC section was obtained using ResIPy (Blanchy *et al.*, 2020b). EMI data were calibrated by com-

puting ECa values for each column of the quadrilateral mesh ERT model; to pair ERT derived ECa values with the EMI data, measurements were binned based on their position along the ERT transect using a bin width of 2 m. Linear regressions were then fitted through the paired measurements to obtain calibration coefficients. It can clearly be seen that when not calibrated (Figure B.11a), the inversion fails to reveal the pattern of the peat, however when calibrated (Figure B.11b) the peat depth and EC more closely resembles the ERT image (Figure B.11c).

```
fnameEC = datadir + 'boxford-calib/eri_ec.csv'
fnameECa = datadir + 'boxford-calib/eca_calibration.csv'

# non calibrated
k1 = Problem()
k1.createSurvey(fnameECa)
k1.show()
k1.setInit(depths0=np.arange(0.05, 3, 0.02))
k1.invert(forwardModel='FSlin', alpha=0.01, method='L-BFGS-B', njobs=-1)

# ERT calibrated
k2 = Problem()
k2.createSurvey(fnameECa)
k2.calibrate(fnameECa, fnameEC, forwardModel='FSlin') # plot calibration
k2.calibrate(fnameECa, fnameEC, forwardModel='FSlin', apply=True) # apply the calibration
k2.setInit(depths0=np.arange(0.05, 3, 0.02))
k2.invert(forwardModel='FSlin', alpha=0.001, method='L-BFGS-B', njobs=-1)
```
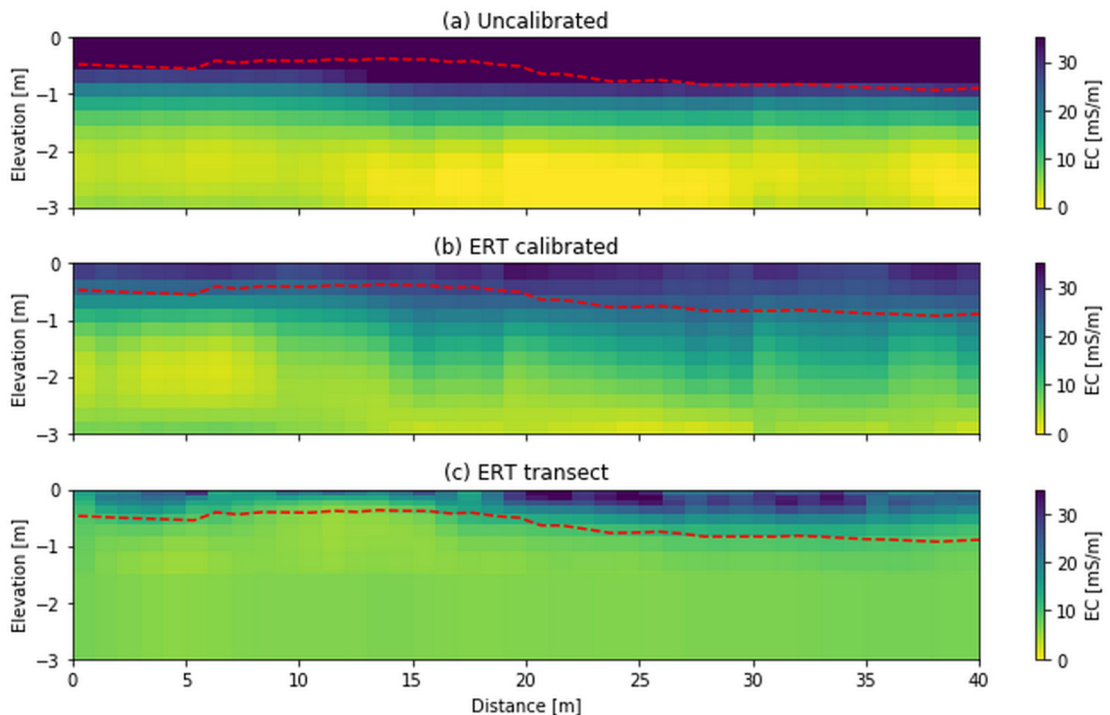

Figure B.11 – Smoothly inverted non-calibrated (a) and calibrated (b) EMI data with the corresponding ERT inversion (c). The dashed red line shows the true depth of the peat intrusive penetration measurements.

B.3.4   Riverbed data with prior knowledge or river stage and electrical conductivity

EMagPy also permits the fixing of initial model parameters within the inversion. This may be useful if a priori knowledge is available, i.e. structural information obtained from intrusive or geophysical methods (e.g. seismic refraction or ground penetrating radar). In such cases, smoothing is automatically disabled between layers with fixed and non-fixed conductivities. Prior information is available in the case of river-borne surveys where the depth and EC of the river can easily be measured. In recent years there has been increasing interest in the use of geophysics to interrogate groundwater-surface water interaction studies (see McLachlan *et al.*, 2017). In this case, EMI data was collected from a site characterized by zones of groundwater up-welling, which have been shown previously to be sites of nitrate loading from legacy agricultural pollution (Binley *et al.*, 2013). EMI data were collected using a CMD Explorer mounted on an inflatable kayak, 0.2 m above the surface of the water using both HCP and VCP orientations. River depths were determined from a pressure logger (see Binley *et al.*, 2013) and river EC (48 mS/m) was determined with an EC meter. In Figure B.12 ECa values from the river-borne survey were inverted with fixed river depth and fixed EC for the top layer corresponding to river water. Furthermore, to account for 2D effects the data was smoothed with a running average across 20 measurements (6 m) and a 2D lateral smoothing factor was used in the inversion. It can be seen that the EC of the riverbed is higher on the upstream side; this is in broad agreement with hydraulic head data presented in Binley *et al.* (2013). The hydraulic head profile in Figure B.12c shows high vertical hydraulic gradients; Binley *et al.* (2013) interpreted this to be a zone of significant up-welling of the more conductive, nitrate rich, groundwater. Furthermore, although the application of river-borne EMI is not novel (e.g. Butler *et al.*, 2004; Mansoor *et al.*, 2006), this is the first application demonstrating the ability of EMI inversion to remove the effect of the water column.

```
k = Problem()
k.createSurvey(datadir + 'leith/leith_emi_heads.csv')
k.rollingMean(window=20)
wdepths = k.surveys[0].df['depth'].values # measured water depths
```
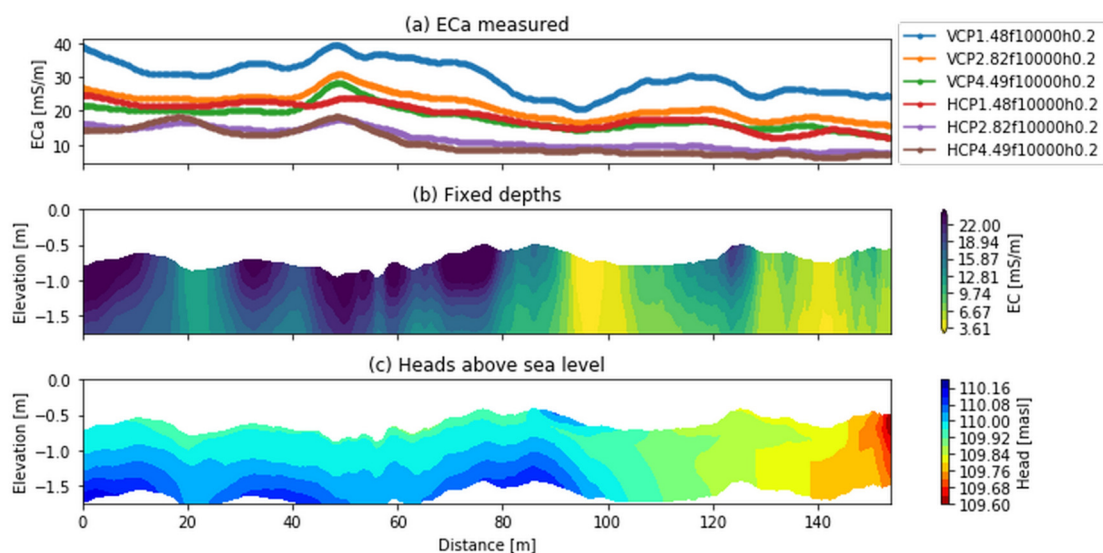
Figure B.12 – (a) ECa values measured from a CMD Explorer on a boat along the river. (b) Inverted EC values given a fixed depth and a fixed EC of the top layer representing the river water (only the river bed conductivity is shown). (c) Hydraulic heads in the river bed from Binley *et al.* (2013). Upstream is at 0 m and downstream at 160 m distance.

```
k.show(dist=True)
depths = wdepths[:,None] + np.arange(0, 3.1, 0.15)
conds0 = np.ones(depths.shape[1]+1)*20
fixedConds = np.zeros(depths.shape[1]+1, dtype=bool)
conds0[0] = 48 # river water EC measured (mS/m)
fixedConds[0] = True # river EC fixed
k.setInit(depths0=depths, conds0=conds0, fixedConds=fixedConds)
k.invert(forwardModel='FSlin', alpha=0.7, beta=0.7) # beta > 0 will cause lateral smoothing
```

B.3.5   Time-lapse monitoring of agricultural soil moisture

In the last case study, the capability of EMagPy to perform time-lapse EMI inversion is shown for an experiment to monitor soil moisture. Soil moisture changes can provide crop breeders important information for selecting resilient varieties. Usually a pedophysical relationship (Laloy *et al.*, 2010) is used to convert the geophysical variable (ECa or depth-specific EC) to soil moisture. However, such a relationship can be heavily site-specific and susceptible to textural properties. A more robust approach involves using changes in ECa to estimate changes in soil moisture as textural properties can be assumed stable (Shanahan *et al.*, 2015). In this case study, changes in soil moisture are inferred from changes in inverted EC beneath different wheat varieties. Here, EMI data are inverted for changes in EC using EMagPy's Gauss-Newton solver, see Appendix 1 of Whalley *et al.*

(2017) for more details. ECa measurements were collected using a CMD Mini-Explorer on different winter wheat plots (9 x 1.8 m) in the same field during the growth season. At the same time, soil moisture measurements were obtained using a neutron probe. Note that all ECa values were calibrated using an ERT array and temperature corrected. Figure B.13a shows the inverted EC in March 2017 while Figure B.13e shows the volumetric water content measured by neutron probe. Figures B.13b, B.13c and B.13d show the change in EC, in mS/m, from the EC in Figure B.13a, and Figures B.13f, B.13g and B.13h show the changes in water content, in relation to Figure B.13d. Larger decreases in EC are observed at shallower depths throughout the growing season and coincide well with decreases in soil water content (Spearman Rank Correlation = 0.70 with p < 0.01). These patterns are attributed to crop growth and water uptake in the shallowest soil. Furthermore, this example highlights how, although the background patterns in modeled EC and water content do not match (e.g. due to textural heterogeneity), the changes in both parameters offer a more fruitful relationship.

```
fnames = [
        datadir + 'timelapse-wheat/2017-03-16.csv',
        datadir + 'timelapse-wheat/2017-04-03.csv',
        datadir + 'timelapse-wheat/2017-04-27.csv',
        datadir + 'timelapse-wheat/2017-05-16.csv']
k = Problem()
k.createTimeLapseSurvey(fnames) # import all surveys
k.setInit(depths0=np.linspace(0.1, 2, 10)) # smooth multiple fixed depths model
k.computeApparentChange() # compute change in ECa compared to first survey
k.invert(forwardModel='CSgn', alpha=0.07) # Gauss-Newton routine
```
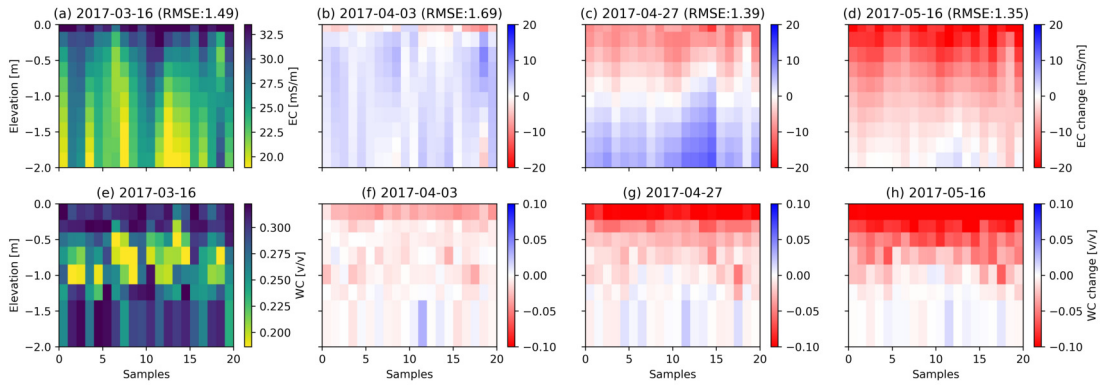
Figure B.13 – Evolution of the inverted change in electrical conductivity throughout the growth season (a to d) and of the measured soil moisture content (e to h). EC and WC changes are expressed as absolute difference relative to 2017-03-16 (models a and e). Deeper and larger decrease in EC is observed throughout the season mainly (b, c and d) following the change in soil moisture (f, g and h) mainly driven by root water uptake. Date format is YYYY-MM-DD (ISO 8601).

B.4 Conclusions

EMI has multiple applications to investigate the subsurface and is increasingly being used in multidisciplinary projects. Such applications are anticipated to increase and it is hoped that the intuitive graphical user interface and Python API of EMagPy will provide a user-friendly and versatile tool. It was demonstrated that although the CS forward model may perform well in low conductivity, homogeneous environments, the FS is often more appropriate. It was also demonstrated that measurement error can be more problematic in cases where devices are operated above the ground and that inversion can aid in the convergence and interpretation of EMI models. Additionally, the potential to include a priori knowledge was demonstrated and the ability of EMagPy to carry out time-lapse inversion was highlighted. It is anticipated that the graphical user interface provides a ready to use tool that will be beneficial for novices, experts or for educational and training purposes. Moreover, the accessible and well documented API provides the opportunity for experienced users to implement additional features.

Acknowledgments

Appendix

Table B.4 – Main API methods used in EMagPy.

API method	Short description
`Problem.show()`	Show apparent values as scatter plot
`Problem.showMap()`	Show spatial distribution of apparent values for given coil
`Problem.calibrate()`	Calibration of ECa value given depth-specific EC dataset
`Problem.invert()`	General inversion routine
`Problem.showResults()`	Show inversion results as a transect
`Problem.showSlice()`	Show the slice for the selected inverted layer
`Problem.showOne2one()`	Show 1:1 graph of modeled vs observed apparent EC
`Problem.showMisfit()`	Show the observed and the modeled ECa

Appendix C

Landwards: Hydrogeophysics for agriculture: capabilities and limitations

Guillaume Blanchy[1,2], Chris Watts[2], Richard Whalley[2], Andrew Binley[1]

[1] Lancaster Environment Centre, Lancaster University, Bailrigg, Lancaster LA1 4YW, UK

[2] Rothamsted Research, West Common, Harpenden AL5 2JQ, UK

Authorship statement

The PhD author wrote the manuscript. Chris Watts, Richard Whalley and Andrew Binley provided comments and edits on the manuscript.

C.1   Introduction

Wheat is one of the most important global crops, being grown on more land than any other commercial crop, and currently providing 20% of total calories consumed by humans worldwide, being second only to rice. A 60% increase in demand is expected by 2050, as the global population increases towards 10 billion. As part of the Designing Future Wheat project1, scientists are seeking to identify traits tolerant to UK drought and temperature stress scenarios. We need to know how soil structure and the availability of nutrients and water interact with genotypes to permit deep rooting. To facilitate this study, agricultural engineers are developing a number of practical and innovative technologies for in-field above and below ground phenotyping, including use of drones, robots and other ground-based systems. One of the more challenging aspects of this study is to discover how wheat roots interact with the soil. Here we explain how we are using hydrogeophysics methods to non-destructively rapidly screen hundreds of wheat varieties in the field.

C.2   What is hydrogeophysics?

Many people in the UK will associate geophysics with archaeology from the popular TV series Time Team. In fact, geophysics is a very broad discipline of Earth sciences. Hydrogeophysics focusses on the investigation of properties and processes in the Earth that are related to hydrology (the study of Earth's water). Hydrogeophysics uses a range of techniques, many of which were developed for mineral exploration, to 'look into the ground' and improve our understanding of where water is, where it is moving and what is controlling it. Methods based on sensing electrical properties are popular in hydrogeophysics because the presence of water (or its movement) can be detected by changes or variation in electrical properties (a wet soil conducts electricity easier than a dry soil). We can measure electrical properties of the soil without disturbing it, which makes the technique particularly attractive in agriculture. In fact, commercial systems are available today using arrays of coulter-electrodes towed behind a tractor to measure soil
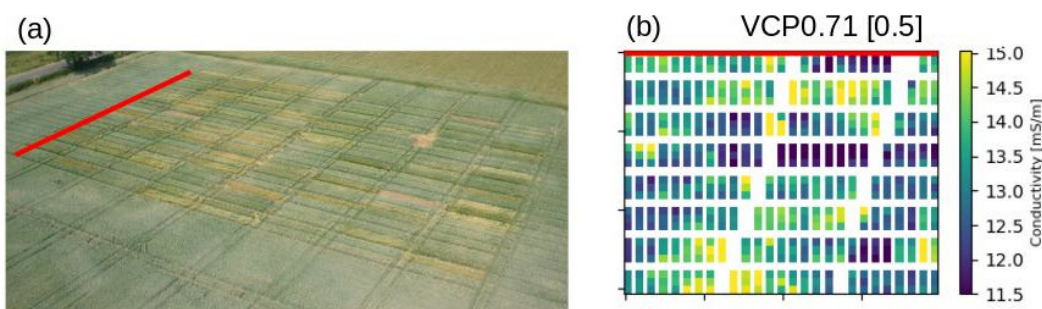
Figure C.1 – (a) picture of the 216 plot field experiment consisting of 71 wheat varieties + fallow plot replicated three times. (b) Background measurement of apparent electrical conductivity measured at 0.5 m depth with the VCP0.71 coil configuration revealing field patterns associated with different soil textures. Note 2 diagonal lines represent previously unknown buried high voltage cables.

electrical conductivity (the property of the soil that describes the ease at which electrical current will move through it). Another method, called electromagnetic induction (EMI), doesn't need any contact with the soil and works a bit like a metal detector. It is actually used for very large scale studies, such as mineral prospecting, using sensors mounted on aircraft.

C.3 How are we using hydrogeophysics?

The attraction here, however, is that from EMI measurements close to the ground surface we can map variation in soil electrical conductivity at shallow depths (see Figure C.1). And since the presence of water effects soil conductivity then perhaps we can monitor changes in the amount of soil water (due to uptake by crops) without even touching the soil. If we can do this then perhaps we can assess how different varieties of wheat extract water from the soil (how much and how deep?).

C.4 How does EMI work?

We are currently using a CMD mini-explorer electromagnetic conductivity sensor (GF Instruments, supplied by Allied Associates, Dunstable, UK). This device is composed of a tube with different coils inside: one transmitter coil (Tx) and three receiver coils (Rx1, Rx2 and Rx3) (Figure C.2). EMI instruments measure
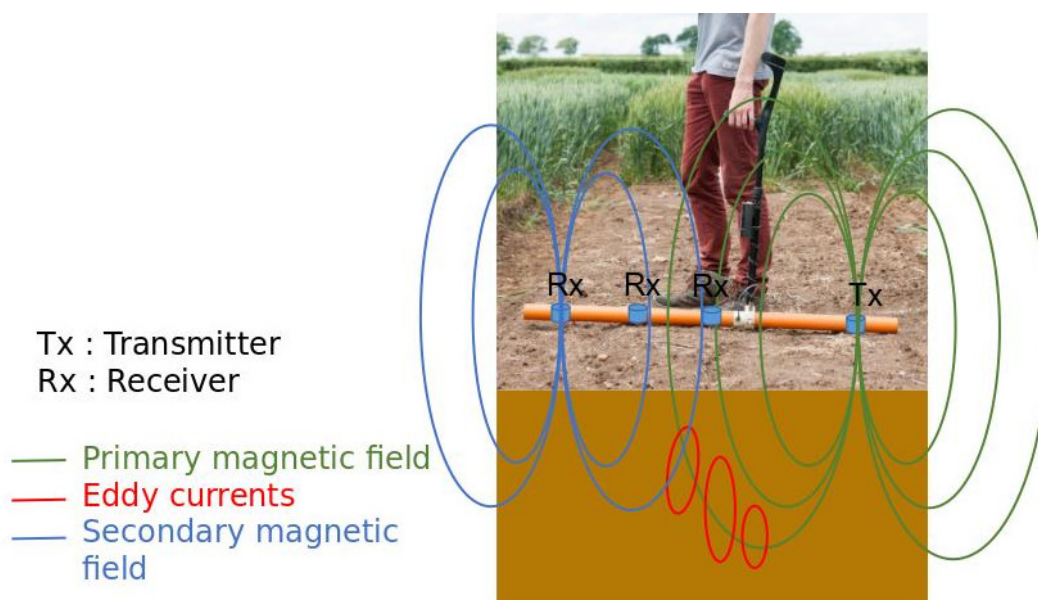
Figure C.2 – Figure 2: Internal working of the EMI device (CMD Mini-Explorer). The primary field is created by the transmitter. Electrical conductors in the soil create 'eddy currents' which can be sensed by a secondary magnetic field at the receiver coils.

an apparent electrical conductivity, σa. This represents the weighted average of soil electrical conductivity σ over a depth range that depends on the separation distance between the transmitter and receiver coils, as well as their orientation. The transmitter coil creates an electromagnetic field, which when it enters the soil creates a signal that can be sensed on the receiver coils and allow us to determine the ground electrical apparent conductivity. Multi-coils devices allow the recording of different apparent conductivities over different depths. We can use these measurements in a type of mathematical modelling called inverse modelling to obtain a depth-specific electrical conductivity.

C.5   How to use it to measure root water uptake?

Soil moisture is a dynamic property under growing crops, dominated by root water extraction driven in turn by evapotranspiration. To monitor soil drying we use EMI surveys carried out regularly throughout the growing season to compare different varieties of wheat. The first set of measurements are taken shortly after the crop emerges but when the soil is at field capacity: this is called the background survey. All subsequent surveys are expressed in changes in electrical conductivity to the
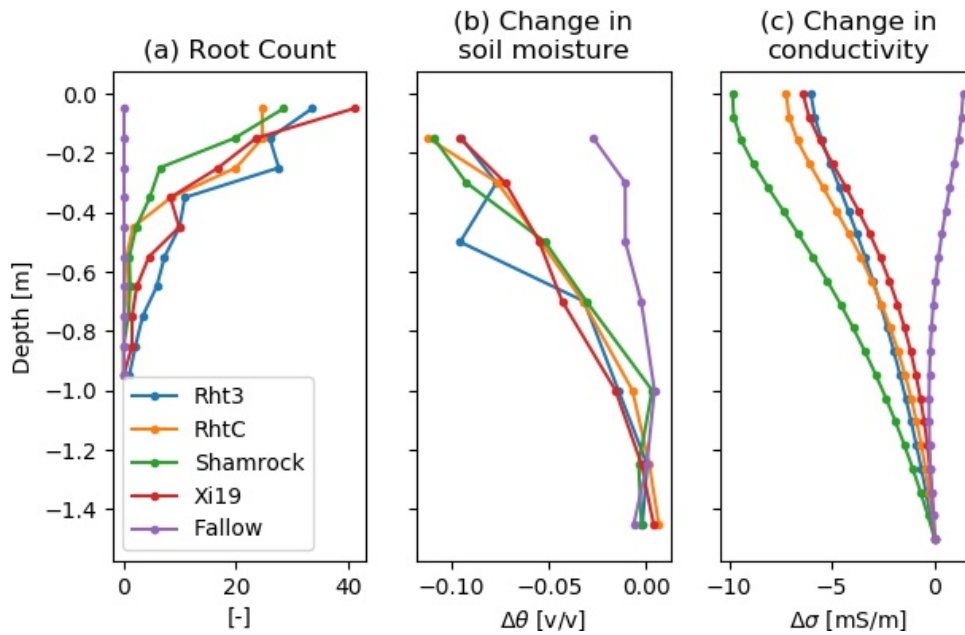
Figure C.3 – Profiles of different wheat lines and fallow plot in term of (a) root count, (b) change in soil moisture from neutron probe and (c) change in electrical conductivity from EMI.

initial background survey. As all other soil properties stay virtually the same so changes in electrical conductivity are mainly driven by the changes in soil moisture, that can be related to root water uptake. The one exception is soil temperature which is measured continuously allowing a correction factor to be applied to the EMI output. Additional measurements such as soil moisture content from neutron probes and root counts from the soil cores have been recorded to be compared to the EMI results. Figure C.3 shows how the change in electrical conductivity from EMI is related to the change in soil moisture (from neutron probe). There is a particularly clear distinction in this case between the fallow plots and the cropped plots. Both electrical conductivity and soil moisture change also show very good agreement with the root counts obtained from soil coring. Note that all the different wheat varieties are very similar mainly because of there wasn't any major water stress during this growth season (2017).

C.6   What are the limitations of this approach?

During this work we have identified that the relationship between the transformed electrical conductivity and soil moisture content is highly site specific. Hence, there is a need to establish a relationship for each field or even for different loca-

tions within the same field if the field soil is heterogeneous. e.g. clay-rich area will present a much higher increase in electrical conductivity with increasing soil moisture compared to sandy soil. Looking at change with time allows to overcome some of the static effects of the soil but not all.

The second main limitation is that apparent conductivity data measured from the EMI device needs to be post-processed to build a depth-specific electrical conductivity profile. This process called 'inversion' is well established for other hydrogeophysical methods but still to be improved for EMI. This forms part of my PhD.

C.7   Conclusion

In conclusion, hydrogeophysics provides a potentially useful tool for wheat root phenotyping under field conditions. In this article we have focused on the EMI method and shown how it offers us a high-throughput, non-invasive screening technique to compare soil drying profiles of different wheat varieties throughout the growing season. However, field-specific relationships are needed to obtain more accurate soil moisture results and the inversion of apparent conductivity to depth-specific electrical conductivity can still be improved. Overall, this method has a great potential for agricultural applications.

Aknowledgements

Appendix D

Geophysical methods to assess soil characteristics

Ho-Chul Shin[1], Guillaume Blanchy[2], Ian Shield[1], Peter Fruen[1], Timothy Barraclough[1], Christopher W Watts[1], Andrew Binley[2] and William R. Whalley[1]

[1] Rothamsted Research, Harpenden, Hertfordshire AL5 2JQ, UK

[2] Lancaster University, Lancaster, Lancashire LA1 4YQ, UK

Authorship statement

GB contributed to write the EMI section of this paper. HCS wrote the main part of the manuscript. HCS, IS, PF, TB, CWW, AB and WRW participated in the work presented in this chapter. AB contributed to write the ERT section and the section on geophysical properties. AB and WRW provided comments and edits on the chapter.

D.1 Introduction

In this chapter we explore the use of geophysical methods to assess soil physical characteristics. Several geophysical methods can be used for this purpose, such as electrical resistivity, induced polarisation, electromagnetic induction methods, ground penetrating radar, nuclear magnetic resonance as well as methods based on seismic wave analysis (Table D.1). Most geophysical methods do not directly measure soil characteristics but rather physical properties that may be related to properties or states of interest. Relationships to convert the physical property measured to the soil characteristics of interest play an essential role in using geophysical tools for soil science. It is also important to note that different soil characteristics can affect the same physical property which complicate the interpretation the geophysical results. For instance, soil moisture and salinity can both increase the soil electrical conductivity. Different methodological strategies can be used to separate these multiple effects.

With the exception of ground penetrating radar, geophysical methods used in soil studies originate from mineral and oil exploration. The scalability of the methods has allowed application to shallow investigation of the subsurface. Growth in their use in hydrology expanded in the 1990s (e.g. Binley *et al.*, 2015) and, more recently, have been widely integrated in many agronomy investigations (e.g. Allred *et al.*, 2008). Static surveys (i.e. conducted at one point in time) can be effective for mapping variation of soil properties; the adoption of time-lapse surveys can help reveal changes to states (e.g. soil moisture) or properties (e.g. density) over time.

Electrical resistivity methods measure the subsurface electrical resistivity distribution using an array of electrodes, typically on the ground surface. Such methods can be used for mapping spatial patterns of electrical resistivity using mobile arrays but are commonly used with a fixed array of electrodes to determine a 2D (vertical section) or 3D image of the subsurface (Binley, 2015). The term electrical resistivity tomography (ERT) is commonly used in reference to imaging with a fixed array of electrodes. Samouëlian *et al.* (2005) provides an introduction to ERT for soil studies, while the recent review of Cimpoiaşu *et al.* (2020) describe

the application of geoelectrical methods for root studies. Electromagnetic induction (EMI) relies on the measurement of the electromagnetic field from induced eddy currents to infer the subsurface electrical conductivity (the conductivity is the inverse of the resistivity). As a contact-less method, it is widely used for mapping large areas.Doolittle & Brevik (2014); Sudduth et al. (2005) and Corwin et al. (2006), amongst others, demonstrate the use of EMI for soil studies.

Electrical resistivity (or conductivity) methods can sometimes result in ambiguous interpretation because of the number of factors that can change the resistivity of a soil. Induced polarisation is an extension of the resistivity method that is sensitive to the storage of electrical charge, and consequently senses electrical characteristics of the soil grain surface, making it effective at differentiating variation in resistivity due to both pore water ionic content and clay content (Slater & Lesmes, 2002). The direct link between induced polarisation and grain surface characteristics has prompted a number of studies using induced polarisation to infer permeability of Earth materials (e.g. Weller & Slater, 2015).

Ground penetrating radar (GPR) sends radar pulses into the ground and records their multiple 'echos' to build an image of the subsurface revealing material with contrasting electrical permittivity. This can be extremely effective at mapping lithological boundaries or soil horizons. The speed of the radar wave is directly related to soil water content (as is exploited in the commonly used dielectric methods for soil moisture) and thus knowledge of the radar velocity allows the assessment of soil moisture. Analysis of radar velocity (and hence soil moisture) can be carried out at shallow depths using reflected signals or the direct wave that travels along the ground surface (e.g. Algeo et al., 2018). Like GPR, nuclear magnetic resonance (NMR), is also sensitive to water content in soils (Paetzold et al., 1985). In saturated soils NMR signals can be used to infer a pore size distribution and permeability. The method is based on the interaction of hydrogen nuclei moments and an externally applied magnetic field. Most applications of NMR have focussed on relative deep investigations (up to hundreds of metres), although recent advances in instruments are permitting very shallow depths of investigation, opening up opportunities for soil studies.

Table D.1 – A summary of the different geophysical methods for soil probing and their associated geophysical properties and soil characteristics that can be derived.

Method	Basic physical property affecting measurement	Soil characteristics
Electrical resistivity	Electrical resistivity	Saturation, porosity, clay content, ionic of concentration pore water, salinity
Induced polarisation	Chargeability	Clay content, grain surface area
Electromagnetic induction	Electrical conductivity	Saturation, porosity, clay content, ionic of concentration pore water, salinity
Ground penetrating radar	Electrical permittivity	Soil horizon boundaries, saturation
Nuclear Magnetic Resonance	Resonant properties of hydrogen nuclei	Saturation and pore size (in saturated soils)
Seismic probing	Elastic properties	Soil strength and internal stress

Seismic waves methods, from which acoustic methods belongs, relies on the analysis of the 'echos' of pressure waves through the soil. Seismic methods share some similarity with GPR which relies on an electromagnetic pulse. While geophysical methods were initially used to characterise lithological features, often to depths of 100s of metres such as for mineral exploration, their use in agriculture is focused on shallow layers, usually to the depth of crop roots (a few metres). Their minimal invasiveness and high-throughput offers great potential for non-destructive study of the soil characteristics for agriculture.

It is not possible to cover all these methods and approaches in a single chapter, instead we focus on three methods, which have specific value for soil investigations. For a more exhaustive overview of the different geophysical methods for agriculture, we redirect the reader to Allred *et al.* (2008). The first two methods we cover are electromagnetic induction and electrical resistivity, which are well established in agriculture. The third method is an emerging method based on acoustic to seismic coupling. The first of the two methods have been used in agriculture and soil science for both mapping soil characteristics, such as salinity and clay content, and for more detailed studies of soil processes, often related to water and solute movement. Methods based on the analysis of seismic waves are sensitive to the elastic properties of soil but also depend on soil water status and soil compaction.

D.2   Geophysical properties of soil

In practice geoelectrical methods such as EMI and ERT are sensitive to a number of properties that are reasonably constant (clay content, organic matter content) as well as ephemeral states such as soil temperature, pore water electrical conductivity, bulk density and soil water content. The soil structure affects electrical conductivity by virtue of pore connectivity and porosity. Archie's law (Archie, 1942), originally developed for oil reservoir investigations, is a commonly used empirically derived model that relates the soil condition to the bulk electrical conductivity. Waxman & Smits (1968) extended Archie's law by accounting for the effect of clay minerals (forming surface electrical conductivity). Several other approaches have been developed specifically for soils (e.g. Rhoades *et al.*, 1976). Laloy *et al.* (2011) compared a range of models for soil electrical conductivity, adopting the term "pedo-electrical" model to differentiate this from classical petrophysical approaches.

The electrical resistivity (respectively, conductivity) is a measure of how difficult (respectively, easy) an electrical current can flow through and is a property of the material independent of its dimension. And, the resistivity and conductivity are reciprocally related. Their MKS units are ohm metre (Ωm) and siemens per metre (S/m), respectively. A textbook introduction to the electrical resistivity and conductivity often refers to a direct current flow through a finite-length (L) rod with a uniform cross-section (A). Then, resistivity (ρ) and conductivity (σ) are defined as $\sigma = RA/L$ and $\rho = GL/A$ where $R = V/I = 1/G$; then, R, G, V and I are the resistance, conductance, voltage difference and current, respectively. When an alternating current with varying frequency is employed instead of a direct current, the electrical property can also be a function of frequency. However, for materials with conductivity in the range (1 – 1000 mS/m) usually measured by most electromagnetic induction devices, the electrical properties are largely independent of frequency. Therefore, the electrical conductivity measured by an electromagnetic induction equipment operating in low-frequency and low induction number is likely the same as the inverse of the electrical resistivity measured by a direct-current resistivity method (McNeill, 1980).

Soils are the result of various weathering processes acting on parent materials whose physical and chemical properties are altered consequently. Structurally, soils are made up with mineral matrix and interwoven voids (or pores). Most soil minerals are effectively electrical insulators with negligible electrical conductivity, except some rare exceptions. Therefore, soil electrical conductivity is usually associated with the pores having the moisture in various stages of saturation. Soil electrical conductivity is electrolytic in nature and hence is affected by the number and mobility of ions. The ease of movement of the ions is largely determined by the fluid viscosity. The viscosity of fluid depends on the temperature of the fluid. Therefore, the electrical conductivity is also affected by the temperature (McNeill, 1980).

The relation between the electrical conductivity and temperature is generally nonlinear. However, over normal ambient temperatures, the degree of nonlinearity is relatively small, a linear equation known as the ratio model is commonly used (McNeill, 1980):

$$\sigma(T) = \sigma(25)[1 + a(T - 25)], \tag{D.1}$$

where $\sigma(T)$ is the electrical conductivity measured at a temperature T ($^\circ$C) and $\sigma(25)$ is a reference electrical conductivity at a common temperature of 25 $^\circ$C. The level of change is determined by a temperature compensation factor a. Several different choices have been used for a. McNeill (1980) used a from a sodium chloride solution ($a = 0.022$ $^\circ$C^{-1}): i.e. 2.2% change per degree Celsius. Other values are $a = 0.0191$ $^\circ$C^{-1} based on 0.01 M KCL solution; $a = 0.025$ $^\circ$C^{-1} commonly used by geophysicists; for "2% increase of electrical conductivity per increase of temperature" frequently cited (Hayashi, 2004).

Temperature effects can be accounted for given local vertical soil temperature profiles, which can be assumed to have limited spatially variability within a site, although effects of daily or seasonal variation in temperature do need to be considered. The electrical conductivity of the pore water contributes significantly to the bulk conductivity of soil. In temperate climates, the variation of the pore water electrical conductivity should be minimal in rain-fed settings, but it may be

greatly affected by irrigation depending on the source of the irrigation water (e.g. groundwater sourced). In semi-arid environments, pore water conductivity effects may be significant due to enhanced salinity arising from high evaporative fluxes (Corwin & Lesch, 2005).

Soils can also be examined by using elastic waves which require a medium (or a matter) to propagate through: sounds (or acoustic waves) are also part of elastic waves. In this regard, soils are the media whose particles are disturbed while the elastic waves are propagated. The elasticity inherent in soils act as a restoring force.

The soil as a wave-propagating medium, for elastic waves, can be approximated as either purely solid or porous media. For solid elastic media without constituent pores, there are two types of elastic waves which are well-known primary (P)-wave and secondary (S)-wave, also known as shear wave. The P-wave is a compressional (or longitudinal) wave in that the movement of particles are in the direction of wave propagation. The S-wave is a transverse (or shear) wave in that the disturbed particles oscillate perpendicular to the direction of waves. By contrast, the electromagnetic waves are entirely transverse with different polarisation. As the names suggest, P-wave propagates faster than S-wave. These are body waves which means that the medium of interest is unbounded. When a boundary or surface is considered, in addition to body waves, so-called surface waves are encountered such as Rayleigh waves, Love waves, etc.

When the wave-propagating medium is porous, more waves can be present. If the pore network of a poroelastic (porous and elastic) medium is filled with a single fluid, e.g., either air-saturated or water-saturated, then we have three waves in total: two compressional waves and a shear wave. The phenomenon can be modelled by a two-phase poroelasticity theory pioneered by Biot (1956b). If the pores are occupied by two different fluid such as unsaturated soils, four distinct waves are encountered: three compressional waves and a shear wave, when there is a wave path through water in addition to those through the solid and air (Arora & Tomar, 2008; Lo & Sposito, 2013).

In the case of both geoelectrical and seismic probing of soil the first challenge

is to determine the basic physical property of soil. The second challenge is to interpret that basic physical property in terms of some soil property of interest (see Table D.1).

D.3   Electromagnetic Induction

The electromagnetic inductive (EMI) method is a non-invasive, high-throughput conductivity survey methods that can be done over large area with minimal setup (McNeill, 1980). Modern equipment can also be mounted on a mobile platform such as a non-conducting sled (Corwin & Lesch, 2005), therefore enabling more efficient survey of large areas. Also in soil with higher clay content, cracks can appear around the electrodes for the resistivity method (discussed later), resulting in poor galvanic contact; EMI does not suffer from this limitation (Sheets & Hendrickx, 1995). EMI methods are sensitive to electrical conductors, consequently, the method can be limited in very resistive environments (e.g. very dry clay-free soils).

EMI instruments are composed of at least two coils. One transmitter coil (Tx) and one receiver coil (Rx). The time-varying magnetic field arising from the alternating current in the transmitting coil at a certain frequency induces very small currents (eddy currents) in the ground. These currents generate a secondary magnetic field H_s which is sensed, together with the primary field H_p by the receiving coil (McNeill, 1980). Larger eddy currents will be induced in more conductive soil resulting in a larger secondary magnetic field. From the ratio between the primary and the secondary magnetic field, a value of the ground electrical conductivity can be obtained. This value is called 'apparent' electrical conductivity (often abbreviated ECa). Its apparent nature derived from the fact that it represents a weighted average of the depth-specific electrical conductivity.

Different coil configurations of the Tx and Rx coils are used. When the plane normal to both Tx and Rx coils is vertical to the surface of the ground, the direction of dipoles is horizontal: this configuration is known as the horizontal dipole mode (H) or the vertical co-planar mode (VCP). The other is the vertical dipole mode (V), also called the horizontal co-planar mode (HCP), where the plane normal to

the coil is horizontal. Both configurations can be achieved by a single instrument by simply rotating it ninety degrees. Additionally, the normal plane of the Tx and Rx coil can be perpendicular: this is called the perpendicular orientation (PRP). In this section we focus on the vertical and the horizontal dipole modes only.

The orientation and the distance between the Tx and Rx coil define the shape of the magnetic fields and hence the depth and the volume investigated by the EMI device. Larger coil separation between Tx and Rx results in a greater volume investigated. While original instruments had only one Tx and one Rx coil (such as EM38, EM35), more recent instruments (e.g. the GF Instruments CMD Mini-Explorer shown in Figure D.1) are multi-coil, meaning they incorporate multiple Rx coils and one Tx coil. This enables the simultaneous measurement from multiple Tx-Rx coil separations and hence different depths of investigation at one time.

Figure D.1 – Operator using a CMD Mini-Explorer (GF Instruments, Brno, Czech Republic) to survey a wheat field.

Analytical expression of the ratios of the secondary field to the primary magnetic field for a homogeneous subsurface can be derived from Maxwell's equation and are given by (McNeill, 1980):

$$\frac{H_s}{H_{pV}} = \frac{2}{(\gamma s)^2}[9 - (0 + 9\gamma s + 4(\gamma s)^2 + (\gamma s)^3)e^{-\gamma s}], \qquad (D.2)$$

for a vertical dipole mode, and

$$\frac{H_s}{H_{pH}} = 2(1 - \frac{3}{(\gamma s)^2} + (3 + 3\gamma s + (\gamma s)^2)\frac{e^{-\gamma s}}{(\gamma s)^2}), \qquad (D.3)$$

for a horizontal dipole mode. $\gamma = \sqrt{i\omega\mu_0\sigma}$ with μ_0 the free-space magnetic permeability, ω the angular frequency and i the imaginary unit. Use of μ_0 instead of μ (the magnetic permeability of the soil) means that we are largely concerned with non-magnetic environment.

The variable γ can be represented by the electrical skin depth δ with the relationship $\gamma\delta = \sqrt{2i}$. The skin depth is defined as the distance of travel at which an electromagnetic wave is attenuated by $1/e \cong 0.368$. The ratio of the coil spacing s (i.e. transmitter-receiver separation) to the skin depth B is known as the induction number B: i.e. $B = s/\Delta$. Then, the combined variable γs can be expressed by $\gamma s = B\sqrt{2i}$. Therefore, a low induction number ($B << 1$), which is common in most commercial electromagnetic induction devices, is a condition requiring that the coil spacing is much shorter than the skin depth and hence an important indicator of wave attenuation. A very conductive environment will increase the value of γ, decrease the skin depth δ and increase the induction number B, potentially breaking the low induction number condition.

Under the low induction number condition, the imaginary part (i.e. quadrature) of the ratios of H_s to H_p can be simplified to

$$(\frac{H_s}{H_p})_V \cong (\frac{H_s}{H_p})_H \cong= \frac{(\gamma s)^2}{4} = \frac{iB^2}{2} = \frac{i\omega\mu_0\sigma s^2}{4} \qquad (D.4)$$

for both dipole orientations, by the Taylor series expansion of $e^{\gamma s}$ with at least 5 terms. Therefore, at low values of induction number, the secondary magnetic field is a very simple function of ω, σ and s. When the operating frequency and coil spacings are arranged to ensure the low induction number for the range of conductivity of interest, the apparent electric conductivity σ_a (also denoted by ECa) can be determined by using the imaginary part of the ratio of H_s to H_p :

$$\sigma_a = \frac{4}{\omega \mu_0 s^2} \left| \frac{H_s}{H_p} \right|, \tag{D.5}$$

The condition of a low induction number ensures not only the aforementioned simple relationship to deduce the apparent conductivity, but also negligible magnetic coupling between the current loops. In addition, regardless of the value of the induction number, all current flows are assumed to be horizontal. In a horizontally layered soil (which is often assumed theoretically), the effect of the refraction of the current flows are assumed negligible, rendering further theoretical development more accessible. Therefore, the secondary magnetic field measured at the surface of a horizontally layered ground can be considered as the sum of all the contributions from each layer.

Under the condition of a low induction number ($B << 1$), the relative sensitivity of the vertical (S_V) and horizontal (S_H) dipole configurations to layers at various depths is known as (McNeill, 1980):

$$S_V(z) = 4z(4z^2 + 1)^{3/2} \tag{D.6}$$

$$S_H(z) = 2 - 4z(4z^2 + 1)^{1/2} \tag{D.7}$$

where z is a normalised depth: i.e. a depth divided by the coil spacing s. Therefore, s and the coil orientation are the sole factor affecting the relative sensitivity distribution with depth. Note that $S_H(z)$ peaks at the surface ($z = 0$): i.e. $S_H(0) = 2$, then gradually decreases (Figure D.1a). By contrast, $S_V(z)$ vanishes at the surface ($S_V(0) = 0$), peaks at $z = 1/\sqrt{8}$, i.e. $S_v(1/\sqrt{8} = 4\sqrt{2}/9$, then gradually decreases (Figure D.2a).

More useful may be its cumulative sensitivity function (CS_V, CS_H) which accumulates the relative contribution to the secondary magnetic field from all layers below a given depth :

$$CS_V(z) = \int_z^\infty S_V(z)dz = (4z^2 + 1)^{-1/2} \tag{D.8}$$

$$CS_H(z) = \int_z^\infty S_H(z)dz = (4z^2 + 1)^{1/2} - 2z \qquad (D.9)$$

which means all the layers below a depth of z-times coil spacings produce a relative contribution of $CS_V(z)$ or $CS_H(z)$ to the indicated meter reading of the apparent conductivity. At the surface, the complete contribution is made from all the depths; therefore, $CS_V(0) = CS_H(0) = 1$ (Figure D.2b). For cases when the EMI instrument is not operated on the ground, a rescaled version of the CS function can be used (?).
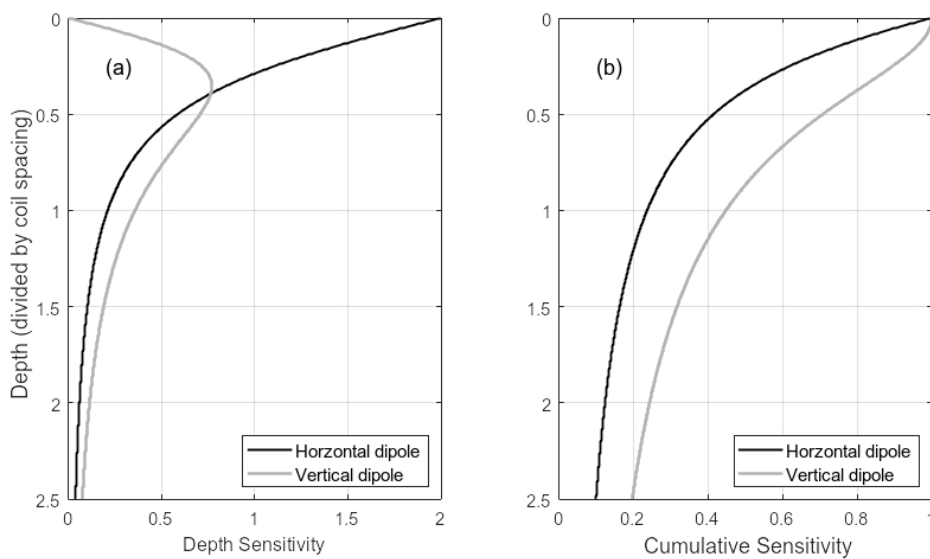
Figure D.2 – (a) Local sensitivity and (b) cumulative sensitivity of horizontal dipole and vertical dipole.

The reading from an electromagnetic induction meter on a horizontally layered earth model can be simply calculated by using the cumulative sensitivity functions, i.e., by adding up the contribution from each layer independently (e.g. JafarGan-domi & Binley, 2013): $\sigma_a = \sigma_1(1 - CS(z_1)) + \sum_{j=2}^{N-1} \sigma_j(CS(z_{j-1}) - CS(z_j)) + \sigma_n CS(z_{N-1})$, for $N \geq 2$. $\sigma_a = \sigma_1(1 - CS(\infty)) = \sigma_1$, for a homogeneous half-space ($N = 1$), where CS could be either CS_V or CS_H depending on the orientation of dipoles. The total number of the layers is N. The layer numbering is such that the one nearest to the surface is identified by $j = 1$. The normalised depth z_j is measured from the surface to the lower boundary of a layer j.

It is useful to know how much of secondary-field signals contributes from a body

of soils from the surface down to a certain depth. It is a complementary concept to the CS function. The normalised depth of soils with p ($p \leq p \leq 1$) contribution is $z = \frac{\sqrt{p(2-p)}}{2(1-p)}$ for a vertical dipole mode, $z = \frac{p(2-p)}{4(1-p)}$ for a horizontal dipole mode, The effective depth of investigation is commonly determined by setting $p = 0.7$ which amounts to about 1.59 and 0.76 times the inter-coil spacing for the vertical and horizontal dipole modes, respectively.

The cumulative sensitivity function (based on the low induction assumption) is still widely used but can be limited mainly in very conductive environment (Callegary *et al.*, 2007, 2012; Andrade *et al.*, 2016). Indeed, the shape of the cumulative sensitivity function does not depend on the electrical conductivity of the layers. An alternative approach consists in using Maxwell's equation that Wait (1982) derived for a 1D layered earth. This strategy has been successfully used in a number of studies (e.g. Lavoué *et al.*, 2010; von Hebel *et al.*, 2014, 2019; Hanssens *et al.*, 2019).

As discussed above, EMI instruments usually output apparent electrical conductivity values for each unique combinations of coil orientations and separations. Given multiple apparent values for one position, it is possible, using the shape of the CS function for instance, to rebuild the profile of depth-specific electrical conductivity. This process is called inversion and is widely employed in other geophysical methods. Inversion of EMI data can be challenging given the smaller number of measurements at each location, but when successful provides a vertical profile of electrical conductivity. While a full description of EMI inversion is out of the scope of this chapter, useful information is provided by von Hebel *et al.* (2019) and Monteiro Santos (2004). Commercial software such as EM4Soil (Monteiro Santos, 2004) or Aarhus workbench (Auken *et al.*, 2015) or open-source ones such as SimPEG (Heagy *et al.*, 2017) and pyGIMLi (Rücker *et al.*, 2017) are examples of software able to perform EMI inversion.

D.3.1   Applications of EMI

The apparent measurement of electrical conductivity from EMI instruments have been extensively used for mapping different properties and states such as soil

salinity (Corwin, 2008), water content (Corwin & Rhoades, 1984), soil texture (Triantafilis & Lesch, 2005) or soil organic matter (Huang *et al.*, 2017a). EMI mapping of agricultural field can serve to delineate management zones (King *et al.*, 2005; Rossi *et al.*, 2018; Moral & Serrano, 2019). Hence enabling spatial tailored crop management for precision agriculture.

Often, a key issue remains to understand how the electrical conductivity is related to a soil property of interest. For instance, (Korsaeth *et al.*, 2008) showed that maps of electrical conductivity obtained from EMI measurements could be used to map soil organic matter. This was because soil organic matter was proportional to the soil water content by virtue of the relationship between soil organic matter and porosity. Identically linking apparent electrical conductivity to soil moisture content is challenging and often results in site-specific relationships. Calamita *et al.* (2015) presents a review of the different soil moisture content – electrical conductivity relationships from multiple studies.

A way forward is the use of time-lapse surveys that enables the isolation of the dynamic component of the electrical conductivity which can be related, under some circumstances, to the change in soil moisture (Robinson *et al.*, 2012a; Martini *et al.*, 2017). The time-lapse approach consists in subtracting a reference survey from other surveys, hence allowing the removal of the static contribution of electrical conductivity from soil texture, for example.

To allow quantitative application, EMI measurements often needs to be calibrated against other soil conductivity data, for example from electrical resistivity surveys (Lavoué *et al.*, 2010; Shanahan *et al.*, 2015). Figure D.3 shows soil drying by wheat estimated with EMI, ERT, neutron probe and penetrometer measurements. The temporal patterns of soil drying compare well with those obtained with a neutron probe.
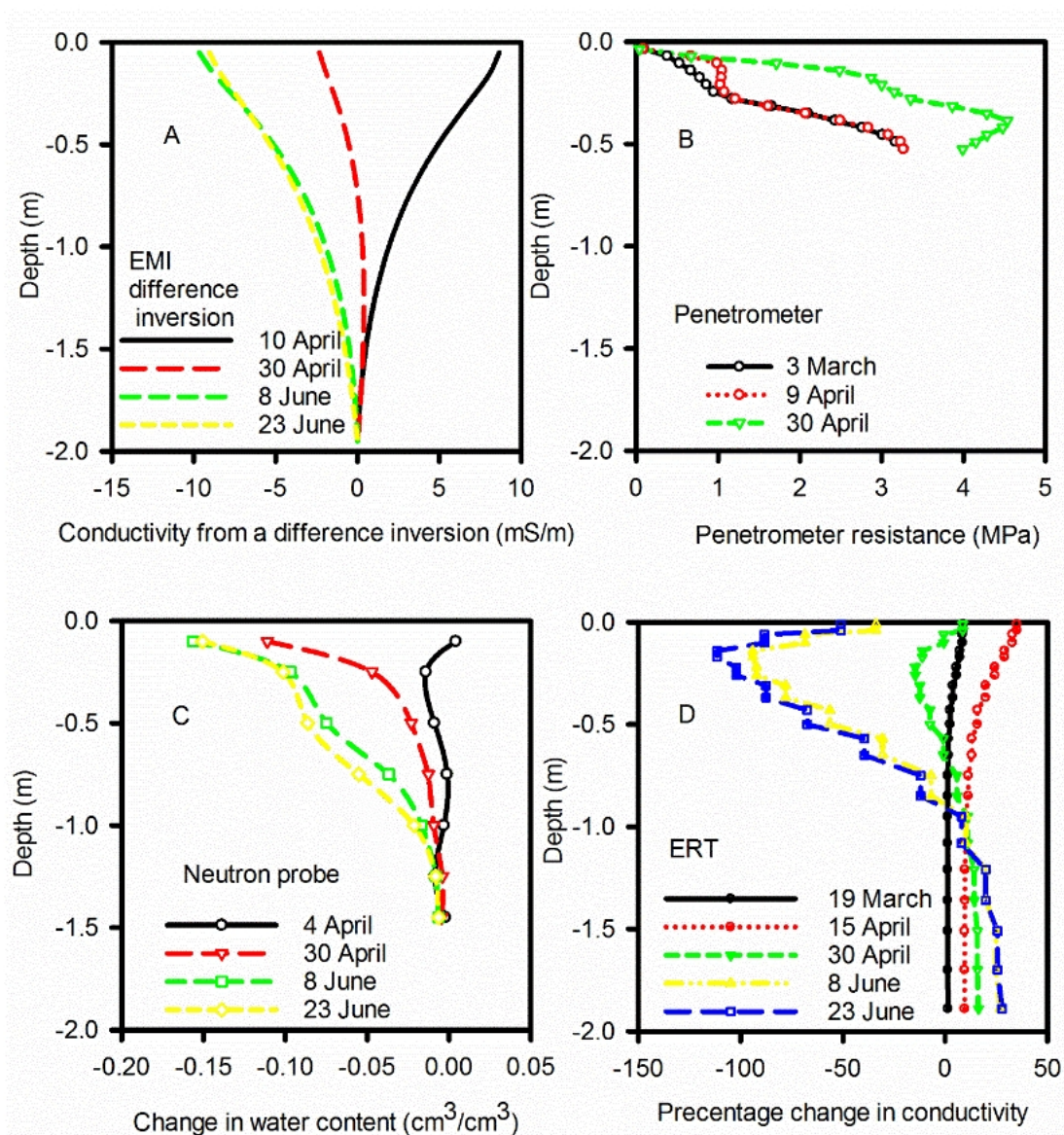
Figure D.3 – Comparison of EMI and other data from a 2015 survey of a wheat field. The effect of temporal patterns in soil drying with depth on data determined from the inversion of ERT (D) and EMI (A) data, penetrometer measurements (B) and neutron probe (C) measurements is shown. EMI and ERT data are obtained from the inversion routine that provides a continuous distribution over depth (From Whalley *et al.*, 2017).

Figure D.4 shows how changes in apparent electrical conductivity can be correlated with plant height and leaf area in wheat. This relationship is predicated on the assumption that a change in apparent conductivity is proportional to a change in water content (Whalley *et al.*, 2017), or root water uptake, and hence crop growth.
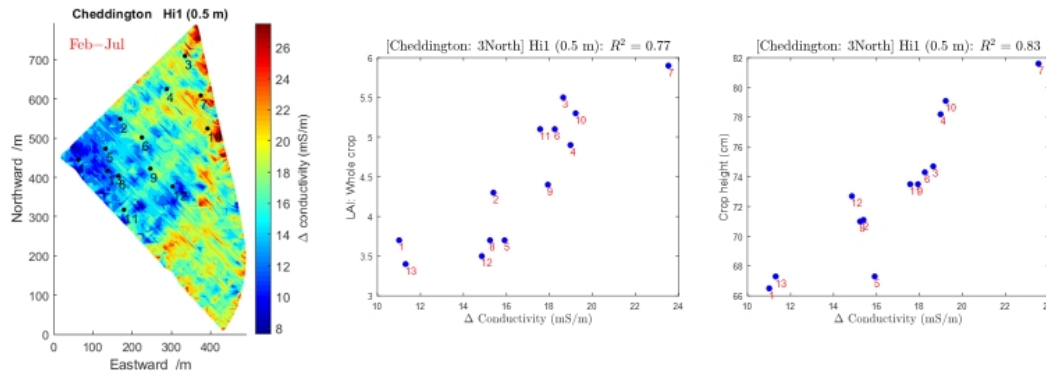
Figure D.4 – A map of the change in apparent conductivity between February and July 2018 obtained with a GF Instruments Mini-Explorer EMI instrument in vertical dipole mode (0.32m coil spacing) on a field near Cheddington, UK. At various locations in the field the height and leaf area index of wheat were measured and these are plotted against the change in apparent conductivity.

Information collected from EMI surveys can also be used to improve simulation of the crop productivity (Brogi *et al.*, 2019a, 2020). Zhu *et al.* (2013) used EMI maps to help explain variation in crop yield in terms of soil moisture and clay content. They developed an approach for using EMI data to help develop a functional map of soil variation in time and space to explain crop yield.

D.4   Electrical resistivity

The resistivity method requires galvanic contact with the soil (Binley & Kemna, 2005) and hence are more invasive than EMI. The method is based on injecting current between a pair of electrodes (A and B) and measuring the voltage difference between another electrode pair (M and N). Figure 4.1 illustrates three quadrupole configurations. The measurement provides an apparent resistivity (the equivalent electrical resistivity of the ground if it were homogenous). Increasing the electrode spacing results in a deeper depth of investigation. Measurements are typically made with an array of several tens of electrodes installed along a transect, providing a 2D vertical section of resistivity (3D images can be derived from data using multiple transects). For such applications the term electrical resistiv-

ity tomography (ERT) is commonly used. It requires the application of inverse methods (as discussed below) to determine the spatial distribution of resistivity. Mobile methods have also been developed in which the ground contact is achieved using heavy electrodes (e.g. Sørensen, 1996) or coulter-based electrodes (Panissod et al., 1998; Corwin & Lesch, 2005). Such approaches typically involve making measurements on a few voltage electrode pairs and thus can be used, like EMI, to provide estimate of resistivity at different depths. Mobile systems are limited to relatively flat sites with limited vegetation (due to the disturbance inevitable from the towing vehicle).

The spatial distribution of resistivity $\rho(x)$ is defined in Poisson's equation (Binley, 2015):

$$\nabla \cdot (\frac{1}{\rho(x)}\nabla V(x)) = -I\delta(x_0) \tag{D.10}$$

in which $V(x)$ represents the spatial distribution of the electric voltage or potential subject to a point current source with strength I located at x_0. The Dirac delta is denoted by $\delta()$, and ∇ is the gradient operator. For an idealised subsurface of uniform resistivity ρ with current electrodes on the flat surface of the soil, the half-space fundamental solution of Equation D.10 is

$$V(r) = \frac{I\rho}{2\pi r}, \tag{D.11}$$

where r is the distance from the current source when the current sink is located at infinity.

The voltage difference can be calculated by

$$\Delta V = \frac{I\rho}{2\pi}(\frac{1}{AM} - \frac{1}{BM} - \frac{1}{AN} + \frac{1}{BN}), \tag{D.12}$$

where AM is the distance between electrodes A and M, etc.

The most commonly used quadrupole configurations are the dipole-dipole, Schlumberger and Wenner configurations (Figure D.5). The receiver (voltage) electrodes of the Schlumberger and Wenner arrays are placed within their transmitter (current) pair, while the dipole-dipole array has its voltage pair outside and away from

the current electrodes.
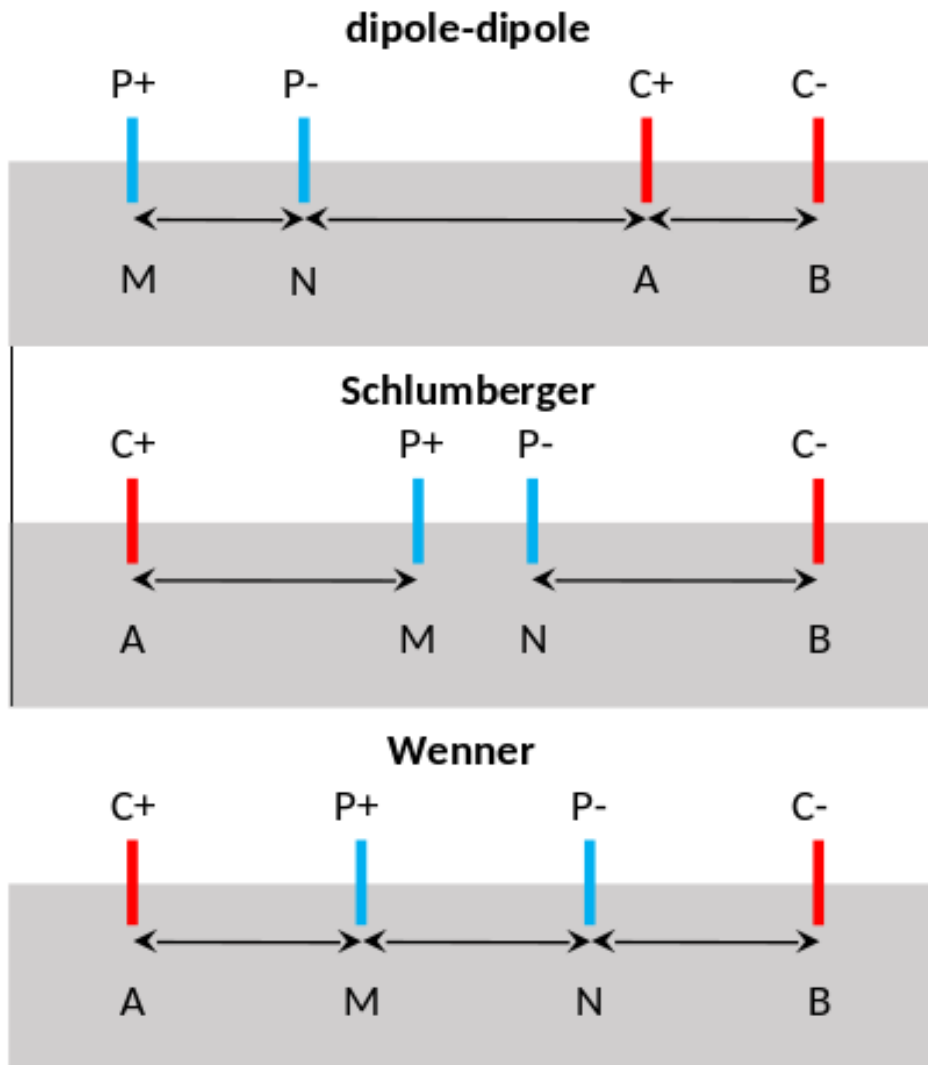
Figure D.5 – Schematic diagrams of dipole-dipole, Schumberger and Wenner arrays.

Among these arrays, the dipole-dipole configuration is realised by setting the same spacing for current and voltage dipoles ($AB = MN = a$) on the surface and the separation $n \times a$ between the nearest electrodes of these two dipole sets (with an integer n). Then, the apparent resistivity ρ_a of the dipole-dipole array may be calculated by (Binley, 2015)

$$\rho_a = \pi \times a \times n(n+1)(n+2)\frac{\Delta V}{I},\qquad(\text{D.13})$$

where I is the injected current and ΔV is the measured voltage difference.

The resistivity in Equation D.13 is an apparent resistivity from the measurement and can be a true resistivity of the subsurface only if the subsurface is

homogeneous and its surface is flat, which is an unlikely scenario in real applications. Therefore, inverse methods have to be applied to determine the resistivity structure of the subsurface (Binley, 2015). The depth of investigation, defined as a layer contributing the maximum amount to the total measured signal, of a dipole-dipole array is $0.18L$ for homogeneous subsurface (Roy & Apparao, 1971) which is deeper than the Schlumberger ($0.125L$) and Wenner ($0.11L$) arrays; here, being the distance between the two extreme active electrodes. The vertical resolution of a dipole-dipole array can be poorer than the other two array configurations, but its lateral resolution is better (Binley, 2015).

Due to advances in multi-channel switching systems in data acquisition, modern-day ERT measurement systems can measure on a number and configuration of electrodes. A resulting 2D image was traditionally presented in a pseudosection in which the apparent resistivities from individual four-electrode units are discretely marked in vertical and lateral positions according to the geometric configuration of the four electrodes. However, the pseudosection is merely a way of graphically presenting the apparent resistivity; hence, the subsurface structure of resistivity is not easily gleaned from the pseudosection. Nowadays, inverse methods are routinely used to determine an image of the subsurface resistivity that is consistent with the suite of apparent resistivity measurements.

Forward models are essentially to return a synthetic (or simulated) apparent resistivity (or equivalent parameters) for a given set of underground structure and distribution of true resistivity by solving Equation D.10. The problem is usually handled numerically for more general geometries of 2D and 3D by implementing the finite difference method or the finite element method (Binley, 2015). The spatial region of interest is first discretised to approximate the area by either structured or unstructured meshes; then, local resistivities are assigned to (or solved at) in cells (or elements) of the mesh which represent the degree of freedom for the problem.

The goal of inverse methods is to find a set of model parameters which reduces the difference between the measured data and the simulated data from forward models by means of numerical optimisation. Least-squares fitting is commonly used for this purpose by minimising the sum of the squares of the difference between

the observed data and the forward model outputs. The goodness of fit for this purpose may be expressed by (Binley & Kemna, 2005)

$$\Phi_d = ||W_d(f - F(m))||^2 = (d - F(m))^T W_d^T W_d(d - F(m)), \tag{D.14}$$

where d is the column vector composed of the observed data, $F(m)$ is the output of the forward model with model-parameter vector m. A matrix of data weighting is W_d; for the case of uncorrelated errors, it is a diagonal matrix with the inverse of data errors. The superscript T represents the transpose of a vector or matrix.

There are many numerical optimisation algorithms to minimise Equation D.14. In geophysical inversions, minimisation of Equation D.14 may lead to non-unique or unstable inversions. Therefore, some level of constraint is needed to guide the solution. One of the most successful and widely-adopted approaches in this regard is to introduce the smoothness constraint by spatial regularisation. Regularisation in this context can be implemented by considering a model penalty term:

$$\Phi_m = ||W_m m||^2 = m^T W_m^T W_m m = m^T R m. \tag{D.15}$$

Here, the spatial smoothness of the model parameters is constrained by a roughness matrix R which is usually a tridiagonal matrix and composed of a model-weighting matrix W_m.

The data and model misfit terms, Φ_d and Φ_m, respectively, can be combined by adding the two with an extra proportionality coefficient:

$$\Phi = \Phi_d + \alpha\Phi_m, \tag{D.16}$$

which is minimised instead of Φ_d alone. The scalar regularisation parameter α can be fixed throughout the optimisation or adjusted by iterative reduction starting from a large value. Minimisation of Equation D.16 can be carried out by using the Gauss-Newton approach (Binley & Kemna, 2005):

$$(J^T W_d^T W_d J + \alpha R)\Delta m = J^T W_d^T W_d(d - F(m_i)) - \alpha R m_i \tag{D.17}$$

$$m_{i+1} = m_i + \Delta m \tag{D.18}$$

where J is the Jacobian matrix; m_i is a set of model parameters at the ith iteration. Δm represents the amount of updates in model parameters.

The approach used above is commonly adopted for analysis of ERT data. (Binley, 2015) describes a range of modifications to the approach (including the analysis of time-lapse data) and more information on the inversion process.

D.4.1 Applications of electrical resistivity

ERT is commonly used to image variations in resistivity associated with soil texture. In a few cases it has been used, in time-lapse mode, to assess variations of spatial changes of resistivity due to soil water, e.g. the uptake by roots (Whalley et al., 2017). The photograph (Figure D.6) below shows an ERT array connected to an instrument capable of making the measurements shown schematically in Figure D.5.
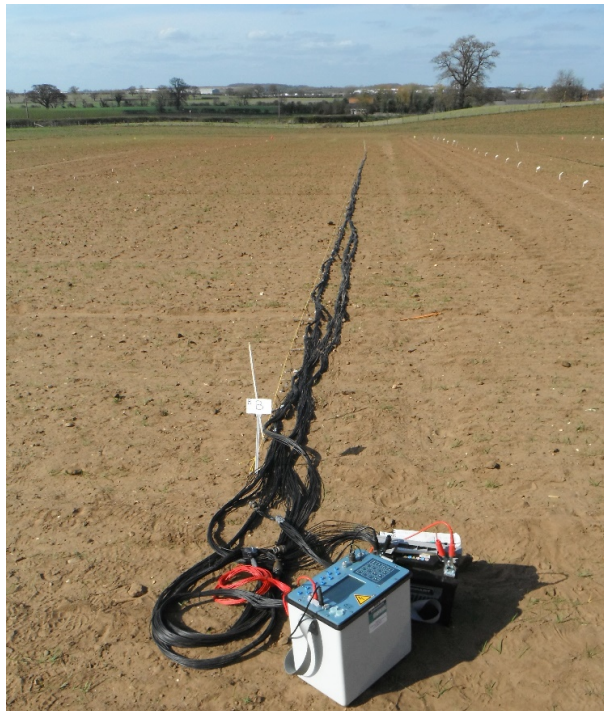
Figure D.6 – An ERT instrument connected to an ERT array set in Rothamsted's Experimental Farm at Woburn, Bedfordshire, UK.

In this application the ERT arrays were installed after experimental plots were sown, with the purpose of monitoring soil drying. The plots were approximately 2m wide and 10m long and the arrays were laid out to give a 2m ERT image of consecutive plots. Figure D.7 shows resistivity changes with time. It indicates

that by July resistivity increases can be observed at depth of nearly 1m and by inference soil dry to that depth. The names of the different lines are indicated on Figure D.7 along with a fallow plot with no wheat, and hence no drying, was used for the purpose of reference.
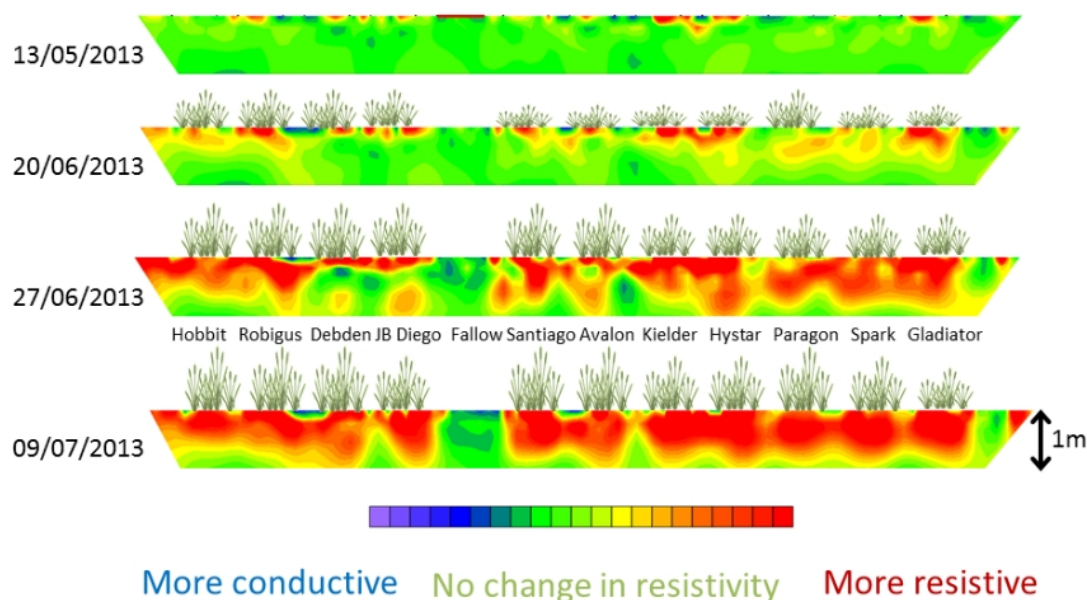
Figure D.7 – This shows a time-lapse ERT image showing changes in resistivity (from April 2013) because of soil drying by different winter wheat varieties (indicated). A fallow plot is also shown. The drier the soil the more resistive it becomes.

At the study site of Whalley *et al.* (2017) there are two types of soil: one sandy with a cemented hard layer at a depth of approximately 30cm and one with a deep clay rich profile. Figure D.8 compares spatial resistivity maps on these different soils in July following soil drying. It can be seen clearly that on the sandy soil (Butt Close) that only the very surface layers are dried by roots. In contrast, on the clay rich profile with no cemented layer (Warren Field) there is soil drying to depth.
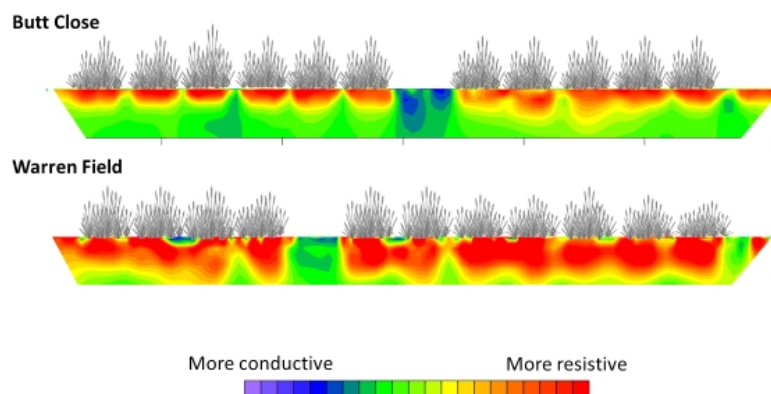
Figure D.8 – A comparison of ERT difference images (change from April to July 2013) following soil drying by wheat. The top image is from Butt Close near Woburn, UK which is a sandy site with a cemented layer at a depth of approximately 30cm. At this site soil drying is limited to the shallow layers (less than 30cm depth). The bottom image is from a neighbouring field with a deep clay rich profile. This site shows soil drying to depth.

While ERT methods may not give accurate soil water content data compared with a specialised soil water content sensor, they do give a wealth of spatial information. The spatial resolution depends on the electrode spacing and resolution, but in a field application the greatest resolution is likely to be in order of several centimetres.

ERT was also employed to monitor the three-dimensional distribution of soil water content in a maize field (Beff *et al.*, 2013), in which the effect of plants and rainfall event was investigated during the growing season. They deduced the water contents from the inversion of ERT data which were validated by TDR measurements. The high resolution of the ERT-based water content distribution allowed the identification of the drying pattern around maize root profiles.

A system of permanently installed ERT arrays was used to measure the temporal and spatial variation of the resistivities in an irrigation experiment over a three-year duration (Dahlin *et al.*, 2014). They also inverted the ERT data to construct the 2D and 3D images of resistivity patterns and observed the resistivity changes linked to the irrigation quantities and the growth of willow. Their result also confirmed the effectiveness of their groundwater sampling protocol carried

out in pipes installed in depth. Other examples of the use of ERT in crop studies include Michot *et al.* (2003) and Garré *et al.* (2011). Macleod *et al.* (2013) used ERT to help identify grass varieties that enhance soil structure and potentially minimise the risk of flooding.

ERT arrays have also been used in laboratory conditions. Rings of electrodes can be installed around the circumference of soil cores. Such configuration can be used to determine the 3D distribution of resistivity. Using this setup, Binley *et al.* (1996) demonstrated the effectiveness of ERT in solute tracing experiment in soils, using the ERT images to identify preferential flow pathways in the core. In a subsequent study, Koestel *et al.* (2008) used a combination of ERT and TDR measurements to develop solute transport properties of a soil core.

D.5   Acoustic-to-seismic coupling

When the soil is assumed as homogeneous and isotropic elastic solid without voids, then there are two waves which propagates separately: P-wave and S-wave. The phase velocity of P-wave is well established as

$$V_p = \sqrt{\frac{K + 4\mu/3}{\rho}}. \tag{D.19}$$

For S-wave, we have

$$V_s = \sqrt{\frac{\mu}{\rho}}, \tag{D.20}$$

where the mass density of the solid is ρ; two elastic moduli are K for bulk modulus and for shear modulus (also known as Lamé's second parameter).

For poroelastic media, models for two-phase poroelastic materials comprised of solid and a single fluid (either gas or liquid) have been widely studied since the seminal works by Biot (1956b,a) and have been contributed by many researchers since then. To some extent, the theory behind two-phase modelling can be judged almost matured while interesting applications are still being reported. By contrast, three-phase modelling is still being actively studied despite the first of the kind was reported some 55 years ago by Brutsaert (1964).

Just as simple as their phase velocities (Equation D.19 and Equation D.20), the

wave numbers of isotropic elastic solids are also succinctly expressed: $\omega\sqrt{\rho/(K + 4\mu/3)}$ for a compressional wave and $\omega\sqrt{\rho/\mu}$ for a shear wave. However, for fluid-saturated two-phase porous materials, the wavenumbers (l_1 and l_2) of two compressional waves and the wavenumber (l_3) for a shear wave can be obtained by solving the following equations (Shin *et al.*, 2013, 2017; Stoll, 1974):

$$(\rho_f\omega^2 - Cl_{1,2}^2)^2 = (\rho\omega^2 - Hl_{1,2}^2)(\rho_f q^2\omega^2/\Omega - Ml_{1,2}^2 + i\omega F\eta/k \tag{D.21}$$

$$(\rho_f\omega^2)^2 = (\rho\omega^2 - \mu l_3^2)(\rho_f q^2\omega^2/\Omega + i\omega F\eta/k \tag{D.22}$$

where f is the imaginary unit and the time-harmonic convention of $exp(-i\omega t)$ is used with t representing the time. The elastic constants H, C, M and D are further defined as (Stoll, 1974)

$$H = \frac{(K_r - K_b)^2}{D - K_b} + K_b + \frac{4}{3}\mu \tag{D.23}$$

$$C = \frac{K_r(K_r - K_b)}{D - K_b} \tag{D.24}$$

$$M = \frac{K_r^2}{D - K_b} \tag{D.25}$$

$$D = K_r(1 + \Omega(K_r/K_f - 1)) \tag{D.26}$$

Their constituent properties are fluid permeability (k), porosity (Ω), bulk density of soil (ρ), fluid density (ρ_f), fluid viscosity (θ), tortuosity (q^2), bulk modulus of the solid particle (K_r), bulk modulus of fluid (K_f), bulk modulus of the porous medium (K_b) and shear modulus of the porous medium (μ). In reality, the soil matrix is unlikely to be perfectly elastic. To this effect, the imaginary part accounting for damping can be introduced to the bulk moduli (K_b and μ) to incorporate the damping effect for elastic waves (Stoll, 1974). The symbol F represents the viscosity correction factor introduced by Biot (1956a) for higher frequencies to account

for the deviation from the Poiseuille flow within the pores. The details of the formula for depends on a model of a pore structure assumed for given soils Biot (1956a).

D.5.1   Model for acoustic-to-seismic coupling

When a propagating wave meets a boundary or a discontinuity in the medium composition, some of its energy is reflected and the rest is either transmitted or refracted except for total internal reflection. The amplitudes of these reflected and transmitted waves can be determined for a given source strength by solving a boundary value problem, as long as the complex wave numbers for the three types of waves have been calculated for each poroelastic layer.

To solve the boundary value problem, equations of motions for each layer must be established. Wave fields created by a point source have axial symmetry, and hence they can be represented by only two components of wave motions in the radial (r) and vertical (z) coordinates. When the height of an airborne acoustic source is z_s, the Green's function (Ψ_0) for an airborne layer and those ($\Psi_{1,n}$, $\Psi_{2,n}$, $\Psi_{3,n}$) for poroelastic waves in soils are (Shin et $al.$, 2013; Tooms et $al.$, 1993)

$$\Psi_0(\xi, z) = \frac{1}{\beta_0}e^{i|z-z_s|\beta_0} + A_0^\uparrow e^{-iz\beta_0} \tag{D.27}$$

$$\Psi_{1,n}(\xi, z) = A_{1,n}^\downarrow e^{i} \tag{D.28}$$

$$\Psi_{2,n}(\xi, z) = M_{1,n} \tag{D.29}$$

$$\Psi_{3,n}(\xi, z) = A_{3,n}^\downarrow e^{i} \tag{D.30}$$

where $M_{1,n}$ and $M_{2,n}$ indicate the ratio of the fluid-borne wave to the soil frame-borne wave; β with subscripts are the vertical wave numbers; ξ is the horizontal wave number. The vertical coordinates of upper and lower soil boundary of a layer n are denoted by d_n^+ and d_n^-. The upward ($A_{m,n}^\uparrow$) and downward ($A_{m,n}^\downarrow$) amplitudes of Green's functions can be calculated by applying appropriate boundary condi-

tions at layer interfaces. The systems of equations for the boundary conditions of each layer interface are then mapped together with those from others to form a linear system of a global matrix (Tooms *et al.*, 1993). Then, the amplitudes of propagating wave components in layers are calculated all together through standard methods for solving a system of linear equations. Once these amplitudes $(A_{m,n}^{\uparrow}$ and $A_{m,n}^{\downarrow})$ are determined for each layer and wave types, the acoustic pressure in the fluid(air) layer and particle velocities on the ground can be calculated; for detailed procedure, see Shin *et al.* (2013) and Tooms *et al.* (1993).
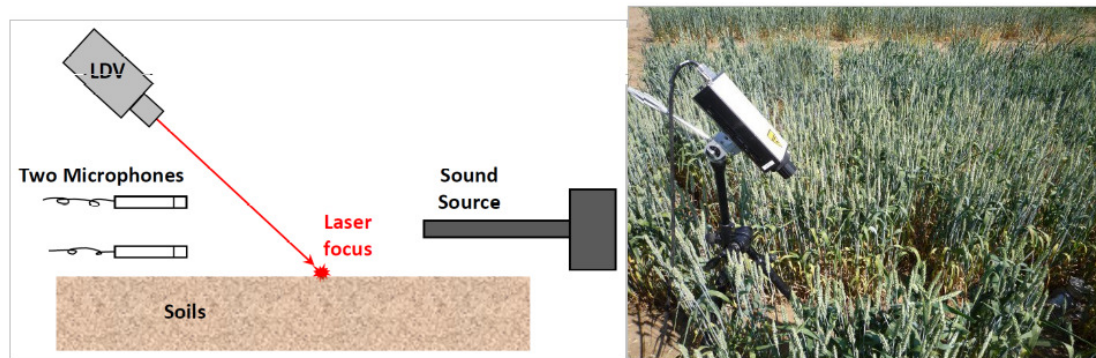
Figure D.9 – Schematic diagram and photograph of measurement configuration showing acoustic source, two microphones and an LDV. The left-hand side is adapted from Shin *et al.* (2013).

These simulated acoustic pressure and particle velocities on soil surface were compared to the measured counterparts. The acoustic pressure was measured by a pair of microphones; the soil particle velocity was recorded by a laser Doppler vibrometer (LDV). An acoustic-source system was composed of a compression driver extended by a metal pipe (Figure D.9). Instead of one-to-one comparisons, the measured and modelled signals were compared in terms of ratios: that is, transfer functions. Then, the numerical optimisation is carried out to minimise the differences between the transfer functions from the measurement and the simulation. For details about the optimisation procedure, see Shin *et al.* (2013).

The minimum set of properties required by a numerical optimization for this study comprises air permeability (k), porosity (Ω), complex shear modulus (μ), Poisson's ratio and the layer thickness for each of four layers: these are updated during the optimization. The rest of the aforementioned properties in the poroelasticity model are well documented and so are considered known. In place of μ,

we used the loss factor and S-wave speed which were first converted to the shear modulus, then to the penetration resistance.

D.5.2   Application of acoustic-to-seismic coupling model

Field measurements were carried out at Butt Furlong (52.012N; 0.597W) on the Woburn Experimental Farm operated by Rothamsted Research. The soil type belongs to the Cottenham series (WRB classification: Eutric Rubic Arenosols), which is a poorly structured Brown Sand over a Lower Greensand (Catt *et al.*, 1975). The soil texture is loamy sand, with typically around 80% sand, 10% silt and 10% clay. The non-invasive acoustic-to-seismic (A–S) coupling measurements were made within the crop on the selected plots of a much larger field experiment designed to investigate the performance of different winter wheat (*Triticum aestivum* L.) varieties. The plots chosen for A–S measurements included a fallow area and two contrasting wheat varieties: Paragon and Hystar hybrid.
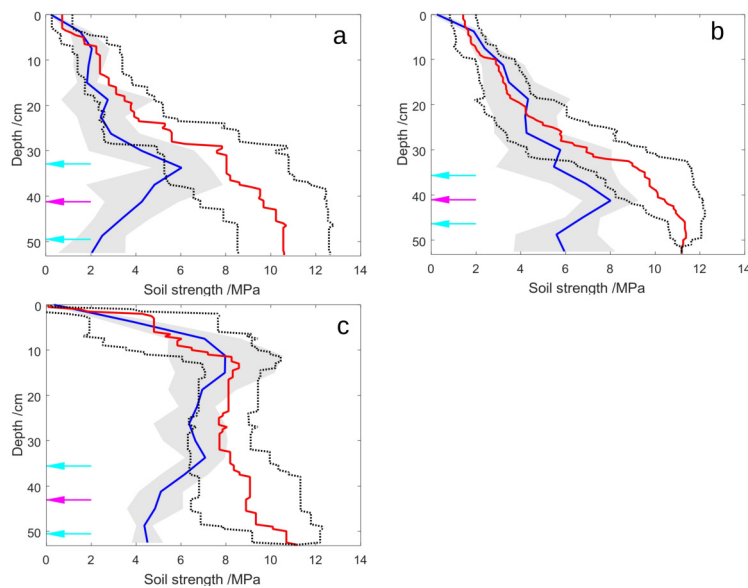
Figure D.10 – Plots of soil strength measured by a penetrometer (28 June) and deduced from measurements of the acoustic-to-seismic (A–S) coupling (a and b on 26 June; e on 27 June) for the experimental plots: (a) fallow (b) Paragon variety and (c) Hystar hybrid variety. Adapted from Shin *et al.* (2017).

Figure D.10 shows a comparison of the soil strength profile measured by a penetrometer (on 28 June) with that deduced from the measurements of A–S

coupling (on 26 and 27 June). These are the extracts from Shin *et al.* (2017); full results can be found therein. The blue line inside the grey strip shows the arithmetic mean of five penetrometer readings at a given depth and the boundaries of the grey region indicate one standard deviation. In some cases, the soil was too strong to enable penetrometer measurements to the desired depth; this will have led to an underestimate of the actual penetration resistance and an apparently smaller variability.

The red line in Figure D.10 indicates the average soil strength deduced from the measured A–S data. The two dotted black lines on either side of the red lines are the estimates of one standard deviation at a given depth. There are three arrows: the magenta one represents the average of the estimated depths of a hardpan and the two cyan arrows indicate the standard deviations of A–S-deduced hardpan depths. The deduced depths of hardpans are similar among three plots.

Figure D.10 shows the result for a fallow plot, Paragon variety of winter wheat and Hystar hybrid variety. The comparison of penetrometer soil strength between the fallow plot and the other experimental plots planted with wheat supports the fact that as the crop grows it tends to extract more water from the soil than supplied by rain, leading to increased soil strength.

Throughout the graphs in Figure D.10, the similarity between the penetrometer readings and deduced soil strength is good, especially for the upper layers. The agreement is less encouraging in the lower layers, partly because some of the penetrometer operations were not successful at those depths and partly because of lack of high-fidelity low-frequency signals for the A–S measurements.

The comparisons in Figure D.10 were made possible by the results of three independent efforts: the first involved A–S measurements and subsequent numerical optimization to deduce the shear modulus (μ), the second used a penetrometer to measure the penetration resistance (Q) and the third used an independently obtained relation between Q and μ to link the first two studies. The SI units of both μ and Q are Pascals; however, they do not represent the same quantity. In this paper, we have used the mean value of an empirical relation proposed by Gao *et al.* (2013):

$$Q \approx (0.0286 \pm 0.0013)\mu + (-53.0 \pm 12.9 kPa), \qquad \text{(D.31)}$$

for the type of soil in the area where the A–S measurements were carried out (see A_{SL} in their table 6). In other words, the shear modulus from the optimizer is also about 35 ($\approx 1/0.0286$) times larger than the penetration resistance. Therefore, it is encouraging that both A–S-deduced and penetrometer-based soil strengths match quite closely in the shallow layers in Figure D.10 through Equation D.31 from Gao *et al.* (2013).

D.5.3 Deducing the soil water contents by wave-speed measurements

Fluid-saturated two-phase models may describe the wave propagation in air-saturated sound absorbing materials or water-saturated sediments on sea floors. However, two-phase models can be too ideal to represent most of (arable) soils with partial water saturation, except low-level water contents as demonstrated in the previous section. In this regard, Brutsaert (1964) is widely credited to have initiated the theory of elastic wave propagation through unconsolidated unsaturated granular materials having three distinct phases of a solid and two immiscible fluids. Due to the introduction of the second fluid component, three compressional waves and one shear wave were predicted to propagate when the medium is unbounded. One noticeable shortcoming of his model was the lack of the inertial coupling between phase components as also pointed by others (Arora & Tomar, 2008; Lo & Sposito, 2013).

In his follow-up work (Brutsaert & Luthin, 1964), Brutsaert investigated the relationship between a wave speed and the soil moisture content. Among four waves, he focussed on the speed of the fastest wave which is the one closest to the P-wave in characteristics and hence often referred to as P1-wave (Lo & Sposito, 2013). Due perhaps to the lack of inertial coupling between different phases, Brutsaert contemplated the low-frequency application by proposing the "velocity of propagation of a low-frequency wave":

$$c = \sqrt{\frac{0.306 a p_e^{1/3} Z}{\rho_m \Omega b^{2/3}}} \qquad \text{(D.32)}$$

with $p_e = p_t - P_g - Sp_c$ where p_e, p_t, p_g and p_c are effective pressure, total pressure, equilibrium pressure in the gas, and capillary pressure in the liquid, respectively. The degree of saturation with liquid is S. The equation has the mass density $\rho_m = \rho_1 + \rho_2 + \rho_3$ with the masses of solid (ρ_1), gas (ρ_2) and liquid (ρ_3) per unit bulk volume. The porosity is denoted by Ω. The factors a and b are empirical. The remaining term Z was reported by Brutsaert & Luthin (1964) as

$$Z = (1 + 30.75bK_{eff}^{3/2}p_e^{-1/2})^{5/3}(1 + 46.12bK_{eff}^{3/2}p_e^{-1/2})^{-1} \qquad (D.33)$$

in which the effective bulk modulus was defined as $K_{eff} = (1 - S)K_q + SK_l$ with K_q and K_l for the bulk moduli of gas and liquid, respectively. Later, the choice of this specific formula of K_{eff} was considered as a typing error by others (Flammer *et al.*, 2001) who suggested a correct form might have been $K_{eff}^{-1} = (1-S)K_q^{-1} + SK_l^{-1}$. The former K_{eff} represents the weighted arithmetic mean (in short, K_{eff}^A) of component bulk moduli, while the latter is the weighted harmonic mean (K_{eff}^H). According to Domenico (1977) is applicable when gas and liquid are distributed equally throughout the pore space (i.e. uniform distribution); by contrast, K_{eff}^A is for a variable mixture of gas and liquid.

Despite this uncertainty on the use of K_{eff}^A or K_{eff}^H, Brutsaert's model has been revisited with the aim of establishing the relationship between the wave speeds and the soil water contents (Adamo *et al.*, 2009, 2010; Sharma & Gupta, 2010). Their works were essentially conducted and reported as forward approaches; however, the rationales behind some of these efforts were investigating the feasibility of inverse tools. Here, by the forward method, it studies "the velocity of sound in soils ... by function of the moisture content" which is actually part of the article title of Brutsaert & Luthin (1964). By contrast, the inverse model aims to solve "the moisture content ... by function of the velocity of sound in soils". Logically, the success of the former proposition (i.e. forward model) does not necessarily guarantee the success of the latter (i.e. inverse approach).

Another shortcoming from Brutsaert & Luthin (1964) is that the Poisson's ratio was fixed at the saturation-independent value of 0.2 (Shin *et al.*, 2016). The coefficient 0.306 in Equation D.31 was the result of assuming 0.2 for the Pois-

son's ratio. This assignment alone may not pose an issue, since the factor a in $0.306a$ is largely empirical; hence, a may incorporate some changes in Poisson's ratio. However, saturation-independent constant Poisson's ratio is not supported by modern-day experimental and theoretical investigations (Inci *et al.*, 2003; Kumar & Madhusudhan, 2012; Nakagawa *et al.*, 1997; Pereira & Fredlund, 2000). This has important implications for the deduction of moisture content from wave speeds when the Brutsaert model is addressed in the context of the inverse problem; for example, Adamo *et al.* (2009, 2010) incorporated the fixed Poisson's ratio of 0.2 and proposed incorrect models to identify the distributional status of pore water (Adamo *et al.*, 2009).

The effective pressure (p_e) in the Brutsaert's model essentially conforms to the effective stress (σ) for unsaturated soils (Bishop & Blight, 1963): $\sigma' = \sigma - u_a + \chi(u_a - u_w)$ where σ is the total stress; u_a, the pore air pressure; and u_w, the pore water pressure (Khalili & Khabbaz, 1998). The scaling factor (χ) to the matric potential ($\Psi = u_w - u_a$) or the matric suction ($u_a - u_w$) is called the effective stress parameter or Bishop's parameter.

There may arise two crucial questions. The first is about the nature of χ: how it is defined or determined (Bishop & Blight, 1963; Gray & Schrefler, 2001; Jennings & Burland, 1962; Nuth & Laloui, 2008). Secondly, the product of χ and ψ contributes to the effective stress and eventually the speed of elastic waves. The relationship between the two parameters is the soil moisture–suction relationship which is highly nonlinear. Then, which of χ or ψ can be a better parameter to measure when it comes to correlating the wave speed? Khalili & Khabbaz (1998) proposed the following empirical formula for χ by using the ratio of the matric suction to its air-entry value (with a subscript ae):

$$\chi = \left[\frac{u_a - u_w}{(u_a - u_w)_{ae}}\right]^{-0.55}$$

for $(u_a - u_w) > (u_a - u_w)_{ae}$; otherwise, $\chi = 1$. By using this estimation of χ, Whalley *et al.* (2012) were able to fit V_s to void ratio (e), net stress and matric potential with a set of four parameters common to all soils at various states of

saturation and consolidation:

$$V_s = A\frac{(2.97 - e)^2}{1 + e}[(\sigma_s - u_a)^r - (u_w - u_a)(\frac{u_w - u_a}{(u_w - u_a)_{ae}}^{-0.55}]^y$$

where 2.97 was recommended by Santamarina $et\ al.$ (2001) but can be also adjusted when a common A is used for different types of soils. With $u_w = u_a$, the equation conforms to the one for saturated soils proposed by Whalley $et\ al.$ (2011). It was envisaged, in a field application, the measurement of V_s could estimate the void ratio while the matric potential can be easily measured although it could also be estimated.

There is also a question whether the water content is a right parameter to investigate from the measurement of the elastic wave speeds in unsaturated soils. In theoretical aspects, it is related to the occurrence of the water content and potential as a product as shown in Sp_c or $\chi(u_w - u_a)$, but not separately.

Lu & Sabatier (2009) and Lu (2014) demonstrated that the sound speed in the unsaturated soils is closely related to the water potential rather than the moisture content and temperature. For example, when soil was dry, the sound speed changed rapidly even at constant moisture content (Lu & Sabatier, 2009); during the entire winter, the water content recorded little changes while the water potential and P-wave speed showed some degree of variations (Lu, 2014).

Similarly, in the case of shear waves, Whalley $et\ al.$ (2012) reported that, at matric potentials higher than the air entry potential, V_s in sands increased even at constant water content while the matric potential decreased. Therefore, in the context of possible inverse problems, the water potential could be the one to purse rather than the water content, although the matric potential could be easily measured (Whalley $et\ al.$, 2009).

Whether it is the water content or the water potential, its estimation based on the measurement of a single parameter, the elastic wave speed in this case, can be challenging even in the laboratory setting, let alone in the field of arable soils (Adamo $et\ al.$, 2009, 2010; Sharma & Gupta, 2010). Additional information is required, for example, the void ratio (or equivalently the porosity) when the water potential or the water content is deduced by measuring either V_p or V_s. The void

ratio requires a separately set of invasive measurements.

As briefed in a previous section, Shin *et al.* (2013, 2017) demonstrated the feasibility of using the acoustic-seismic coupling method to deduce various soil properties non-invasively. The acoustic-seismic coupling means that the method has the potential to investigate the pore-related and structure-related properties at the same time by a single set of related measurements. However, one of the theoretical bases behind the method is a fluid-saturated poroelastic model. Therefore, their method is currently limited to either dry or low-moisture soils. There is certainly room for improving the method by incorporating the three-phase poroelastic models to account for unsaturated soils with the moisture content whose amount invalidates the use of the two-phase poroelastic models. In this implementation, the hysteretic nature (Gallipoli *et al.*, 2003; Gregory *et al.*, 2010; Lu & Sabatier, 2009) of soil moisture-suction relationships may need to be known subject to specific soil conditions.

D.6   Summary

There are several geophysical methods which can deduce the characteristics of agricultural soils by measuring physical properties such as electric resistivity (or conductivity), elasticity constant, etc. These are electrical resistivity method, electromagnetic induction method, induced polarisation, ground penetrating radar, nuclear magnetic resonance, and acoustic-seismic method. Among these, we have focused on three: electromagnetic induction, electrical resistivity, and acoustic-seismic. For each method, a basic theoretical background has been briefly introduced, followed by agricultural applications: we have focused on the spatial and temporal mapping of soil water or drying by crops.

In the electromagnetic induction method, time-varying primary magnetic field induces very small eddy currents in the ground resulting in a secondary magnetic field. From the ratio of the primary to the secondary magnetic field, apparent electrical conductivity can be measured. Knowing the cumulative sensitivity pattern, inversion can be applied to deduce the depth-specific conductivity. The measurement itself can be done swiftly and non-invasively; hence it is widely used for

surveying large areas. For electromagnetic induction method, we presented the observation of the temporal pattern of soil drying by wheat, which was also accompanied by the measurement of electrical resistivity, penetration resistance and neutron probe. Another example was the correlation of apparent electrical conductivity with height and leaf area of wheat on the assumption that a change in soil conductivity is related to a change in soil water content associated with root water uptake.

The resistivity method requires galvanic contact with the measurand. Basic sensors are often arranged in a quadrupole configuration of a pair of current-injecting electrodes and another pair of voltage-measuring electrodes; nowadays, this configuration is extended in an array of numerous electrodes capable of 2D or 3D investigation due to advances in multi-channel switching systems. Measured apparent resistivity can be further processed with inverse methods to assess the spatial distribution of resistivity. By using the electrical resistivity tomography, we presented a time-lapse image showing considerable changes in resistivity because of soil drying by different winter wheat varieties; by contrast, a fallow plot experienced least change. In another example, the presence of a cemented hard layer was identifiable by the analysis of tomography images: only the very surface layers are dried by roots in presence of a hard layer; otherwise, soil drying was observed to depth.

The acoustic-to-seismic method exploits the coupling mechanism between airborne acoustic source and underground seismic activity. The soil is treated as poroelastic (i.e., porous and elastic) material; hence, the model is sensitive to the soil elastic characteristics and porosity. The poroelasticity theory is incorporated with wave propagation model in layered media. Several soil physical properties can be estimated through numerical optimisation against measured acoustic-to-seismic transfer functions. As applications, the penetration resistance of wheat-growing soils is compared between the measurement by a penetrometer and the estimation made from shear modulus deduced from the acoustic-to-seismic method. It was shown that as the wheat grew, the soil strength increased due to extraction of water.

Acknowledgments

References

Abdu, H., Robinson, D. A., & Jones, S. B. 2007. Comparing Bulk Soil Electrical Conductivity Determination Using the DUALEM-1S and EM38-DD Electromagnetic Induction Instruments. *Soil Science Society of America Journal*, **71**(1), 189–196. _eprint: https://acsess.onlinelibrary.wiley.com/doi/pdf/10.2136/sssaj2005.0394.

Abdu, H., Robinson, D. A., Seyfried, M., & Jones, S. B. 2008. Geophysical imaging of watershed subsurface patterns and prediction of soil texture and water holding capacity: GEOPHYSICAL IMAGING OF WATERSHED SUBSURFACE. *Water Resources Research*, **44**(4), n/a–n/a.

Adamo, F., Attivissimo, F., Fabbiano, L., Giaquinto, N., & Spadavecchia, M. 2010. Soil moisture assessment by means of compressional and shear wave velocities: Theoretical analysis and experimental setup. *Measurement*, **43**(3), 344–352. Publisher: Elsevier.

Adamo, Francesco, Attivissimo, Filippo, Fabbiano, Laura, & Giaquinto, Nicola. 2009. Velocity–moisture relationships for sandy soils: Experimental results and data analysis. *IEEE Transactions on Instrumentation and Measurement*, **58**(2), 311–317. Publisher: IEEE.

Akinsunmade, Akinniyi, Tomecka-Suchoń, Sylwia, & Pysz, Paweł. 2019. Correlation between agrotechnical properties of selected soil types and corresponding GPR response. *Acta Geophysica*, Sept.

Algeo, Jonathan, Van Dam, Remke L., & Slater, Lee. 2016. Early-Time GPR: A Method to Monitor Spatial Variations in Soil Water Content during Irrigation in Clay Soils. *Vadose Zone Journal*, **15**(11), 0.

Algeo, Jonathan, Slater, Lee, Binley, Andrew, Van Dam, Remke L., & Watts, Chris. 2018. A Comparison of Ground-Penetrating Radar Early-Time Signal Approaches for Mapping Changes in Shallow Soil Water Content. *Vadose Zone Journal*, **17**(1), 0.

Allred, Barry J., Daniels, Jeffrey J., & Ehsani, Mohammad Reza (eds). 2008. *Handbook of agricultural geophysics*. Books in soils, plants, and the environment. Boca Raton: CRC Press. OCLC: ocn181069227.

Altdorff, Daniel, Galagedara, Lakshman, Nadeem, Muhammad, Cheema, Mumtaz, & Unc, Adrian. 2018. Effect of agronomic treatments on the accuracy of soil moisture mapping by electromagnetic induction. *CATENA*, **164**(May), 96–106.

Amato, Mariana, Basso, Bruno, Celano, Giuseppe, Bitella, Giovanni, Morelli, Gianfranco, & Rossi, Roberta. 2008. In situ detection of tree root distribution and biomass by multi-electrode resistivity imaging. *Tree physiology*, **28**(10), 1441–1448.

Amato, Mariana, Bitella, Giovanni, Rossi, Roberta, Gómez, José A., Lovelli, Stella, & Gomes, João J. Ferreira. 2009. Multi-electrode 3D resistivity imaging of alfalfa root zone. *European Journal of Agronomy*, **31**(4), 213–222.

Amundson, Ronald, Berhe, Asmeret Asefaw, Hopmans, Jan W., Olson, Carolyn, Sztein, A. Ester, & Sparks, Donald L. 2015. Soil and human security in the 21st century. *Science*, **348**(6235). Publisher: American Association for the Advancement of Science Section: Review.

Anderson, Walter L. 1979. Numerical integration of related Hankel transforms of orders 0 and 1 by adaptive digital filtering. *Geophysics*, **44**(7), 1287–1305.

Andrade, F. C. M., Fischer, T., & Valenta, J. 2016. Study of errors in conductivity meters using the low induction number approximation and how to overcome them. *In: Near Surface Geoscience 2016-22nd European Meeting of Environmental and Engineering Geophysics*. Barcelona, Spain: EAGE.

Araus, José Luis, & Cairns, Jill E. 2014. Field high-throughput phenotyping: the new crop breeding frontier. *Trends in Plant Science*, **19**(1), 52–61.

Archie, Gustave E. 1942. The electrical resistivity log as an aid in determining some reservoir characteristics. *Transactions of the AIME*, **146**(01), 54–62.

Arora, Ashish, & Tomar, S. K. 2008. The effect of inertial coupling on seismic reflection amplitudes. *Geophysical prospecting*, **56**(5), 643–654. Publisher: European Association of Geoscientists & Engineers.

Atkinson, Jonathan A, Pound, Michael P, Bennett, Malcolm J, & Wells, Darren M. 2019. Uncovering the hidden half of plants using new advances in root phenotyping. *Current Opinion in Biotechnology*, **55**(Feb.), 1–8.

Attia al Hagrey, Said. 2007. Geophysical imaging of root-zone, trunk, and moisture heterogeneity. *Journal of Experimental Botany*, **58**(4), 839–854. Publisher: Oxford University Press.

Auken, Esben, Christiansen, Anders Vest, Kirkegaard, Casper, Fiandaca, Gianluca, Schamper, Cyril, Behroozmand, Ahmad Ali, Binley, Andrew, Nielsen, Emil, Effersø, Flemming, Christensen, Niels Bøie, Sørensen, Kurt, Foged, Nikolaj, & Vignoli, Giulio. 2015. An overview of a highly versatile forward and stable inverse algorithm for airborne, ground-based and borehole electromagnetic and electric data. *Exploration Geophysics*, **46**(3), 223–235.

Bai, C., Ge, Y., Ashton, R. W., Evans, J., Milne, A., Hawkesford, M. J., Whalley, W. R., Parry, M. A. J., Melichar, J., Feuerhelm, D., Basler, P. Bansept, & Bartsch, M. 2019. The relationships between seedling root screens, root growth in the field and grain yield for wheat. *Plant and Soil*, Apr.

Ball, Lyndsay B., Kress, Wade H., Steele, Gregory V., Cannia, James C., & Andersen, Michael J. 2006. *Determination of canal leakage potential using continuous resistivity profiling techniques, Interstate and Tri-State Canals, western Nebraska and eastern Wyoming, 2004*. USGS Numbered Series 2006-5032.

Bardossy, A, & Singh, S K. 2008. Robust estimation of hydrological model parameters. *Hydrol. Earth Syst. Sci.*, 11.

Batey, T. 2009. Soil compaction and soil management – a re-

view. *Soil Use and Management*, **25**(4), 335–345. _eprint: https://onlinelibrary.wiley.com/doi/pdf/10.1111/j.1475-2743.2009.00236.x.

Beamish, David. 2011. Low induction number, ground conductivity meters: A correction procedure in the absence of magnetic effects. *Journal of Applied Geophysics*, **75**(2), 244–253.

Beff, L., Günther, T., Vandoorne, B., Couvreur, V., & Javaux, M. 2013. Three-dimensional monitoring of soil water content in a maize field using Electrical Resistivity Tomography. *Hydrology and Earth System Sciences*, **17**(2), 595–609.

Befus, Kevin M. 2018. pyres : a Python wrapper for electrical resistivity modeling with R2. *Journal of Geophysics and Engineering*, **15**(2), 338–346.

Benech, Christophe, Lombard, Pierre, Rejiba, Fayçal, & Tabbagh, Alain. 2016. Demonstrating the contribution of dielectric permittivity to the in-phase EMI response of soils: example from an archaeological site in Bahrain. *Near Surface Geophysics*, **14**(4), 337–344. Publisher: European Association of Geoscientists & Engineers.

Benoit, Sien, Ghysels, Gert, Gommers, Kevin, Hermans, Thomas, Nguyen, Frederic, & Huysmans, Marijke. 2019. Characterization of spatially variable riverbed hydraulic conductivity using electrical resistivity tomography and induced polarization. *Hydrogeology Journal*, **27**(1), 395–407.

Besson, A., Cousin, I., Samouëlian, A., Boizard, H., & Richard, G. 2004. Structural heterogeneity of the soil tilled layer as characterized by 2D electrical resistivity surveying. *Soil and Tillage Research*, **79**(2), 239–249.

Besson, A., Séger, M., Giot, G., & Cousin, I. 2013. Identifying the characteristic scales of soil structural recovery after compaction from three in-field methods of monitoring. *Geoderma*, **204-205**(Aug.), 130–139.

Binley, Andrew. 2015. 11.08 - Tools and Techniques: Electrical Methods. *Pages 233–259 of:* Schubert, Gerald (ed), *Treatise on Geophysics (Second Edition)*. Oxford: Elsevier.

Binley, Andrew, & Kemna, Andreas. 2005. DC resistivity and induced polarization methods. *Pages 129–156 of: Hydrogeophysics.* Springer.

Binley, Andrew, Shaw, Ben, & Henry-Poulter, Siobhan. 1996. Flow pathways in porous media: electrical resistance tomography and dye staining image verification. *Measurement Science and Technology*, **7**(3), 384.

Binley, Andrew, Winship, Peter, Middleton, Roy, Pokar, Magdeline, & West, Jared. 2001. High-resolution characterization of vadose zone dynamics using cross-borehole radar. *Water Resources Research*, **37**(11), 2639–2652.

Binley, Andrew, Slater, Lee D., Fukes, Melanie, & Cassiani, Giorgio. 2005. Relationship between spectral induced polarization and hydraulic properties of saturated and unsaturated sandstone: SANDSTONE SIP-HYDRAULIC RELATIONSHIPS. *Water Resources Research*, **41**(12), n/a–n/a.

Binley, Andrew, Ullah, Sami, Heathwaite, A. Louise, Heppell, Catherine, Byrne, Patrick, Lansdown, Katrina, Trimmer, Mark, & Zhang, Hao. 2013. Revealing the spatial variability of water fluxes at the groundwater-surface water interface: Spatial Variability of Groundwater-Surface Water Fluxes. *Water Resources Research*, **49**(7), 3978–3992.

Binley, Andrew, Hubbard, Susan S., Huisman, Johan A., Revil, André, Robinson, David A., Singha, Kamini, & Slater, Lee D. 2015. The emergence of hydrogeophysics for improved understanding of subsurface processes over multiple scales: The Emergence of Hydrogeophysics. *Water Resources Research*, **51**(6), 3837–3866.

Biot, M. A. 1956a. Theory of Propagation of Elastic Waves in a Fluid-Saturated Porous Solid. I. Low-Frequency Range. *The Journal of the Acoustical Society of America*, **28**(2), 168–178.

Biot, Maurice A. 1956b. Theory of propagation of elastic waves in a fluid-saturated porous solid. II. Higher frequency range. *The Journal of the acoustical Society of america*, **28**(2), 179–191. Publisher: Acoustical Society of America.

Bishop, Alan W., & Blight, G. E. 1963. Some aspects of effective stress in saturated and partly saturated soils. *Geotechnique*, **13**(3), 177–197. Publisher: Thomas Telford Ltd.

Blanchy, Guillaume, Watts, Christopher W., Ashton, Rhys W., Webster, Colin P., Hawkesford, Malcolm J., Whalley, William R., & Binley, Andrew. 2020a. Accounting for heterogeneity in the ϑ–σ relationship: Application to wheat phenotyping using EMI. *Vadose Zone Journal*, **19**(1).

Blanchy, Guillaume, Saneiyan, Sina, Boyd, Jimmy, McLachlan, Paul, & Binley, Andrew. 2020b. ResIPy, an intuitive open source software for complex geoelectrical inversion/modeling. *Computers & Geosciences*, **137**(Apr.), 104423.

Borisjuk, Ljudmilla, Rolletschek, Hardy, & Neuberger, Thomas. 2012. Surveying the plant's world by magnetic resonance imaging: Surveying the plant's world by MRI. *The Plant Journal*, **70**(1), 129–146.

Boyd, James, Blanchy, Guillaume, Saneiyan, Sina, & Binley, Andrew. 2019. 3D geoelectrical problems with ResIPy, an open-source graphical user interface for geoeletrical data processing. *FastTIMES*, **24**(4).

Brevik, Eric C., Fenton, Thomas E., & Lazari, Andreas. 2006. Soil electrical conductivity as a function of soil water content and implications for soil mapping. *Precision Agriculture*, **7**(6), 393–404.

Brillante, L., Bois, B., Mathieu, O., & Lévêque, J. 2016a. Electrical imaging of soil water availability to grapevine: a benchmark experiment of several machine-learning techniques. *Precision Agriculture*, **17**(6), 637–658.

Brillante, Luca, Bois, Benjamin, Lévêque, Jean, & Mathieu, Olivier. 2016b. Variations in soil-water use by grapevine according to plant water status and soil physical-chemical characteristics—A 3D spatio-temporal analysis. *European Journal of Agronomy*, **77**(July), 122–135.

Brogi, C., Huisman, J.A., Pätzold, S., von Hebel, C., Weihermüller, L., Kaufmann, M.S., van der Kruk, J., & Vereecken, H. 2019a. Large-scale soil mapping

using multi-configuration EMI and supervised image classification. *Geoderma*, **335**(Feb.), 133–148.

Brogi, C., Huisman, J. A., Herbst, M., Weihermüller, L., Klosterhalfen, A., Montzka, C., Reichenau, T. G., & Vereecken, H. 2020. Simulation of spatial variability in crop leaf area index and yield using agroecosystem modeling and geophysics-based quantitative soil information. *Vadose Zone Journal*, **19**(1), e20009. _eprint: https://acsess.onlinelibrary.wiley.com/doi/pdf/10.1002/vzj2.20009.

Brogi, Cosimo, Huisman, Johan Alexander, Herbst, Michael, Klosterhalfen, Anne, & Weihermüller, Lutz. 2019b. Geophysics-based soil mapping improves the simulation of crop productivity at the field scale and beyond. 1.

Brosten, Troy R., Day-Lewis, Frederick D., Schultz, Gregory M., Curtis, Gary P., & Lane, John W. 2011. Inversion of multi-frequency electromagnetic induction data for 3D characterization of hydraulic conductivity. *Journal of Applied Geophysics*, **73**(4), 323–335.

Brutsaert, Wilfried. 1964. The propagation of elastic waves in unconsolidated unsaturated granular mediums. *Journal of Geophysical Research*, **69**(2), 243–257. Publisher: Wiley Online Library.

Brutsaert, Wilfried, & Luthin, James N. 1964. The velocity of sound in soils near the surface as a function of the moisture content. *Journal of Geophysical Research*, **69**(4), 643–652. Publisher: Wiley Online Library.

Butler, Karl E., Nadeau, Jean-Christophe, Parrott, Russell, & Daigle, Annie. 2004. Delineating recharge to a river valley aquifer by riverine seismic and EM methods. *Journal of Environmental & Engineering Geophysics*, **9**(2), 95–109. Publisher: Society of Exploration Geophysicists.

Byrd, Richard H., Lu, Peihuang, Nocedal, Jorge, & Zhu, Ciyou. 1995. A limited memory algorithm for bound constrained optimization. *SIAM Journal on scientific computing*, **16**(5), 1190–1208. Publisher: SIAM.

Cai, Jianchao, Wei, Wei, Hu, Xiangyun, & Wood, David A. 2017. Electrical conductivity models in saturated porous media: A review. *Earth-Science Reviews*, **171**(Aug.), 419–433.

Calamita, G., Brocca, L., Perrone, A., Piscitelli, S., Lapenna, V., Melone, F., & Moramarco, T. 2012. Electrical resistivity and TDR methods for soil moisture estimation in central Italy test-sites. *Journal of Hydrology*, **454-455**(Aug.), 101–112.

Calamita, G., Perrone, A., Brocca, L., Onorati, B., & Manfreda, S. 2015. Field test of a multi-frequency electromagnetic induction sensor for soil moisture monitoring in southern Italy test sites. *Journal of Hydrology*, **529**(Oct.), 316–329.

Callegary, James B., Ferré, Ty P. A., & Groom, R. W. 2007. Vertical Spatial Sensitivity and Exploration Depth of Low-Induction-Number Electromagnetic-Induction Instruments. *Vadose Zone Journal*, **6**(1), 158.

Callegary, James B., Ferré, Ty P. A., & Groom, R. W. 2012. Three-Dimensional Sensitivity Distribution and Sample Volume of Low-Induction-Number Electromagnetic-Induction Instruments. *Soil Science Society of America Journal*, **76**(1), 85.

Carminati, Andrea, & Javaux, Mathieu. 2020. Soil Rather Than Xylem Vulnerability Controls Stomatal Response to Drought. *Trends in Plant Science*, May.

Cassiani, G., Boaga, J., Vanella, D., Perri, M. T., & Consoli, S. 2015. Monitoring and modelling of soil–plant interactions: the joint use of ERT, sap flow and eddy covariance data to characterize the volume of an orange tree root zone. *Hydrology and Earth System Sciences*, **19**(5), 2213–2225.

Cassiani, Giorgio, Kemna, Andreas, Villa, Alberto, & Zimmermann, Egon. 2009. Spectral induced polarization for the characterization of free-phase hydrocarbon contamination of sediments with low clay content. *Near Surface Geophysics*, **7**(5-6), 547–562. _eprint: https://onlinelibrary.wiley.com/doi/pdf/10.3997/1873-0604.2009028.

Cassiani, Giorgio, Ursino, Nadia, Deiana, Rita, Vignoli, Giulio, Boaga, Jacopo, Rossi, Matteo, Perri, Maria Teresa, Blaschek, Michael, Duttmann, Rainer, Meyer, Swen, Ludwig, Ralf, Soddu, Antonino, Dietrich, Peter, & Werban, Ulrike. 2012. Noninvasive Monitoring of Soil Static Characteristics and Dynamic States: A Case Study Highlighting Vegetation Effects on Agricultural Land. *Vadose Zone Journal*, **11**(3), 0.

Castrignanò, A., Buttafuoco, G., Quarto, R., Parisi, D., Viscarra Rossel, R.A., Terribile, F., Langella, G., & Venezia, A. 2018. A geostatistical sensor data fusion approach for delineating homogeneous management zones in Precision Agriculture. *CATENA*, **167**(Aug.), 293–304.

Catt, J. A., King, D. W., & Weir, A. H. 1975. soils of Woburn Experimental Farm. I. Great Hill, Road Piece and Butt Close. *Rep Rothamsted Exp Stn*.

Celano, G., Palese, A.M., Ciucci, A., Martorella, E., Vignozzi, N., & Xiloyannis, C. 2011. Evaluation of soil water content in tilled and cover-cropped olive orchards by the geoelectrical technique. *Geoderma*, **163**(3-4), 163–170.

Chambers, J. E., Meldrum, P. I., Wilkinson, P. B., Ward, W., Jackson, C., Matthews, B., Joel, P., Kuras, O., Bai, L., Uhlemann, S., & Gunn, D. 2015. Spatial monitoring of groundwater drawdown and rebound associated with quarry dewatering using automated time-lapse electrical resistivity tomography and distribution guided clustering. *Engineering Geology*, **193**(July), 412–420.

Chambers, J.E., Gunn, D.A., Wilkinson, P.B., Meldrum, P.I., Haslam, E., Holyoake, S., Kirkham, M., Kuras, O., Merritt, A., & Wragg, J. 2014. 4D electrical resistivity tomography monitoring of soil moisture dynamics in an operational railway embankment. *Near Surface Geophysics*, **12**(1), 61–72.

Chloupek, Oldrich. 1977. Evaluation of the size of a plant's root system using its electrical capacitance. *Plant and Soil*, **48**(2), 525–532.

Christiansen, Anders, Pedersen, Jesper, Auken, Esben, Søe, Niels, Holst, Mads, & Kristiansen, Søren. 2016. Improved Geoarchaeological Mapping with Electromagnetic Induction Instruments from Dedicated Processing and Inversion. *Remote Sensing*, **8**(12), 1022.

Cimpoiaşu, Mihai Octavian, Kuras, Oliver, Pridmore, Tony, & Mooney, Sacha J. 2020. Potential of geoelectrical methods to monitor root zone processes and structure: A review. *Geoderma*, **365**(Apr.), 114232.

Cockett, Rowan, Kang, Seogi, Heagy, Lindsey J., Pidlisecky, Adam, & Oldenburg, Douglas W. 2015. SimPEG: An open source framework for simulation and gradient based parameter estimation in geophysical applications. *Computers & Geosciences*, **85**(Dec.), 142–154.

Consoli, S., Stagno, F., Vanella, D., Boaga, J., Cassiani, G., & Roccuzzo, G. 2017. Partial root-zone drying irrigation in orange orchards: Effects on water use and crop production characteristics. *European Journal of Agronomy*, **82**(Jan.), 190–202.

Constable, Steven C., Parker, Robert L., & Constable, Catherine G. 1987. Occam's inversion: A practical algorithm for generating smooth models from electromagnetic sounding data. *Geophysics*, **52**(3), 289–300.

Corneo, Paola E., Kertesz, Michael A., Bakhshandeh, Shiva, Tahaei, Hero, Barbour, Margaret M., & Dijkstra, Feike A. 2018. Studying root water uptake of wheat genotypes in different soils using water δ 18 O stable isotopes. *Agriculture, Ecosystems & Environment*, **264**(Sept.), 119–129.

Corwin, D. L. 2020. Climate change impacts on soil salinity in agricultural areas. *European Journal of Soil Science*, June.

Corwin, D L, & Lesch, S M. 2003. Application of Soil Electrical Conductivity to Precision Agriculture: Theory, Principles, and Guidelines. *AGRONOMY JOURNAL*, **95**, 17.

Corwin, D. L., & Rhoades, J. D. 1984. Measurement of inverted electrical conductivity profiles using electromagnetic induction. *Soil Science Society of America Journal*, **48**(2), 288–291. Publisher: Wiley Online Library.

Corwin, Dennis L. 2008. Past, present, and future trends in soil electrical conductivity measurements using geophysical methods. *Handbook of agricultural*

geophysics, 17–44. Publisher: CRC Press, Taylor & Francis Group: New York, NY, USA.

Corwin, D.L., & Lesch, S.M. 2005. Apparent soil electrical conductivity measurements in agriculture. *Computers and Electronics in Agriculture*, **46**(1-3), 11–43.

Corwin, D.L., Lesch, S.M., Oster, J.D., & Kaffka, S.R. 2006. Monitoring management-induced spatio–temporal changes in soil quality through soil sampling directed by apparent electrical conductivity. *Geoderma*, **131**(3-4), 369–387.

Costabel, Stephan, & Günther, Thomas. 2014. Noninvasive estimation of water retention parameters by observing the capillary fringe with magnetic resonance sounding. *Vadose Zone Journal*, **13**(6).

Coussement, Tom, Maloteau, Sophie, Pardon, Paul, Artru, Sidonie, Ridley, Simon, Javaux, Mathieu, & Garré, Sarah. 2018. A tree-bordered field as a surrogate for agroforestry in temperate regions: Where does the water go? *Agricultural Water Management*, **210**(Nov.), 198–207.

Crook, N., Binley, A., Knight, R., Robinson, D. A., Zarnetske, J., & Haggerty, R. 2008. Electrical resistivity imaging of the architecture of substream sediments. *Water Resources Research*, **44**(4).

Dahlin, Torleif, Aronsson, Pär, & Thörnelöf, Mats. 2014. Soil resistivity monitoring of an irrigation experiment. *Near Surface Geophysics*, **12**(1), 35–44. Publisher: European Association of Geoscientists & Engineers.

Dalton, F. N. 1995. In-situ root extent measurements by electrical capacitance methods. *Plant and soil*, **173**(1), 157–165.

Davies, Gareth, Huang, Jingyi, Monteiro Santos, Fernando Acacio, & Triantafilis, John. 2015. Modeling coastal salinity in quasi 2D and 3D using a DUALEM-421 and inversion software. *Groundwater*, **53**(3), 424–431. Publisher: Wiley Online Library.

de Oliveira, Luciano Alves, Woodbury, Bryan L., de Miranda, Jarbas Honorio, & Stromer, Bobbi S. 2020. Using electromagnetic induction technology to identify atrazine leaching potential at field scale. *Geoderma*, **375**(Oct.), 114525.

Delefortrie, Samuël, De Smedt, Philippe, Saey, Timothy, Van De Vijver, Ellen, & Van Meirvenne, Marc. 2014. An efficient calibration procedure for correction of drift in EMI survey data. **110**(Nov.), 115–125.

Dietrich, R. C., Bengough, A. G., Jones, H. G., & White, P. J. 2012. A new physical interpretation of plant root capacitance. *Journal of Experimental Botany*, **63**(17), 6149–6159.

Domenico, S. Norman. 1977. Elastic properties of unconsolidated porous sand reservoirs. *Geophysics*, **42**(7), 1339–1368. Publisher: Society of Exploration Geophysicists.

Doolittle, James A., & Brevik, Eric C. 2014. The use of electromagnetic induction techniques in soils studies. *Geoderma*, **223-225**(July), 33–45.

Duan, Qingyun, Sorooshian, Soroosh, & Gupta, Vijai K. 1994. Optimal use of the SCE-UA global optimization method for calibrating watershed models. *Journal of hydrology*, **158**(3-4), 265–284. Publisher: Elsevier.

Eigenberg, R. A, Doran, J. W, Nienaber, J. A, Ferguson, R. B, & Woodbury, B. L. 2002. Electrical conductivity monitoring of soil condition and available N with animal manure and a cover crop. *Agriculture, Ecosystems & Environment*, **88**(2), 183–193.

Ellis, Tim, Murray, Wayne, & Kavalieris, Laimonis. 2013. Electrical capacitance of bean (Vicia faba) root systems was related to tissue density—a test for the Dalton Model. *Plant and Soil*, **366**(1-2), 575–584.

Elwaseif, M., Robinson, J., Day-Lewis, F.D., Ntarlagiannis, D., Slater, L.D., Lane, J.W., Minsley, B.J., & Schultz, G. 2017. A matlab-based frequency-domain electromagnetic inversion code (FEMIC) with graphical user interface. *Computers & Geosciences*, **99**(Feb.), 61–71.

Fageria, N. K., Baligar, V. C., & Bailey, B. A. 2005. Role of Cover Crops in Improving Soil and Row Crop Productivity. *Communications in Soil Science and Plant Analysis*, **36**(19-20), 2733–2757. Publisher: Taylor & Francis _eprint: https://doi.org/10.1080/00103620500303939.

Farahani, H. J., Buchleiter, G. W., & Brodahl, M. K. 2005. Characterization of apparent soil electrical conductivity variability in irrigated sandy and non-saline fields in Colorado. *TRANSACTIONS-AMERICAN SOCIETY OF AGRICULTURAL ENGINEERS*, **48**(1), 155.

Farquharson, Colin G., Oldenburg, Douglas W., & Routh, Partha S. 2003. Simultaneous 1D inversion of loop–loop electromagnetic data for magnetic susceptibility and electrical conductivity. **68**(6), 1857–1869.

Farzamian, Mohammad, Paz, Maria Catarina, Paz, Ana Marta, Castanheira, Nádia Luísa, Gonçalves, Maria Conceição, Santos, Fernando A. Monteiro, & Triantafilis, John. 2019. Mapping soil salinity using electromagnetic conductivity imaging—A comparison of regional and location-specific calibrations. *Land Degradation & Development*, **30**(12), 1393–1406.

Flammer, I., Blum, A., Leiser, A., & Germann, P. 2001. Acoustic assessment of flow patterns in unsaturated soil. *Journal of Applied Geophysics*, **46**(2), 115–128. Publisher: Elsevier.

Fletcher, Reeves, & Reeves, Colin M. 1964. Function minimization by conjugate gradients. *The computer journal*, **7**(2), 149–154. Publisher: Oxford University Press.

Flores Orozco, Adrian Flores, Kemna, Andreas, Cassiani, Giorgio, & Binley, Andrew. 2016. Improved site contamination through time-lapse complex resistivity imaging.

Flores Orozco, Adrián, Williams, Kenneth H., & Kemna, Andreas. 2013. Time-lapse spectral induced polarization imaging of stimulated uranium bioremediation. *Near Surface Geophysics*, **11**(5), 531–544.

Flores Orozco, Adrián Flores, Kemna, Andreas, & Zimmermann, Egon. 2012. Data error quantification in spectral induced polarization imaging. **77**(3), E227–E237.

Fradgley, N., Evans, G., Biernaskie, J.M., Cockram, J., Marr, E.C., Oliver, A. G., Ober, E., & Jones, H. 2020 (Feb.). *Effects of breeding history and crop management on the root architecture of wheat.* preprint. Plant Biology.

Frederiksen, Rasmus Rumph, Christiansen, Anders Vest, Christensen, Steen, & Rasmussen, Keld Rømer. 2017. A direct comparison of EMI data and borehole data on a 1000ha data set. *Geoderma*, **303**(Oct.), 188–195.

Frischknecht, F. C. 1987. Electromagnetic physical scale modeling. *Electromagnetic methods in applied geophysics-theory*, 365–441.

Furbank, Robert T., & Tester, Mark. 2011. Phenomics – technologies to relieve the phenotyping bottleneck. *Trends in Plant Science*, **16**(12), 635–644.

Galambošová, Jana, Macák, Miroslav, Rataj, Vladimír, Barát, Marek, & Misiewicz, Paula. 2020. Determining Trafficked Areas Using Soil Electrical Conductivity – A Pilot Study. *Acta Technologica Agriculturae*, **23**(1), 1–6.

Gallipoli, D., Wheeler, S. J., & Karstunen, M. 2003. Modelling the variation of degree of saturation in a deformable unsaturated soil. *Géotechnique*, **53**(1), 105–112. Publisher: Thomas Telford Ltd.

Gao, W., Watts, C. W., Ren, T., Shin, H.-C., Taherzadeh, S., Attenborough, K., Jenkins, M., & Whalley, W. R. 2013. Estimating penetrometer resistance and matric potential from the velocities of shear and compression waves. *Soil Science Society of America Journal*, **77**(3), 721–728. Publisher: Wiley Online Library.

Garré, S., Javaux, M., Vanderborght, J., Pagès, L., & Vereecken, H. 2011. Three-Dimensional Electrical Resistivity Tomography to Monitor Root Zone Water Dynamics. *Vadose Zone Journal*, **10**(1), 412.

Garré, S., Günther, T., Diels, J., & Vanderborght, J. 2012. Evaluating Experimental Design of ERT for Soil Moisture Monitoring in Contour Hedgerow Intercropping Systems. *Vadose Zone Journal*, **11**(4), 0.

Garré, S., Coteur, I., Wongleecharoen, C., Kongkaew, T., Diels, J., & Vanderborght, J. 2013. Noninvasive Monitoring of Soil Water Dynamics in Mixed Cropping Systems: A Case Study in Ratchaburi Province, Thailand. *Vadose Zone Journal*, **12**(2), 0.

Ge, Y., Hawkesford, M.J., Rosolem, C.A., Mooney, S.J., Ashton, R.W., Evans,

J., & Whalley, W.R. 2019. Multiple abiotic stress, nitrate availability and the growth of wheat. *Soil and Tillage Research*, **191**(Aug.), 171–184.

Gebbers, Robin, Lück, Erika, Dabas, Michel, & Domsch, Horst. 2009. Comparison of instruments for geoelectrical soil mapping at the field scale. *Near Surface Geophysics*, **7**(3), 179–190. _eprint: https://onlinelibrary.wiley.com/doi/pdf/10.3997/1873-0604.2009011.

Geuzaine, Christophe, & Remacle, Jean-François. 2009. Gmsh: A 3-D finite element mesh generator with built-in pre- and post-processing facilities. *International Journal for Numerical Methods in Engineering*, **79**(11), 1309–1331.

Glover, P. W. J. 2015. 11.04–Geophysical Properties of the Near Surface Earth: Electrical Properties. *Treatise on geophysics*, 89–137. Publisher: Elsevier.

Godfray, H. C. J., Beddington, J. R., Crute, I. R., Haddad, L., Lawrence, D., Muir, J. F., Pretty, J., Robinson, S., Thomas, S. M., & Toulmin, C. 2010. Food Security: The Challenge of Feeding 9 Billion People. *Science*, **327**(5967), 812–818.

Gray, William G., & Schrefler, Bernhard A. 2001. Thermodynamic approach to effective stress in partially saturated porous media. *European Journal of Mechanics-A/Solids*, **20**(4), 521–538. Publisher: Elsevier.

Greenberg, Richard J., & Brace, W. F. 1969. Archie's law for rocks modeled by simple networks. *Journal of Geophysical Research*, **74**(8), 2099–2102.

Gregory, Andrew S., Bird, Nigel RA, Whalley, W. Richard, Matthews, G. Peter, & Young, Iain M. 2010. Deformation and shrinkage effects on the soil water release characteristic. *Soil Science Society of America Journal*, **74**(4), 1104–1112. Publisher: Wiley Online Library.

Guillemoteau, J., Simon, F.-X., Lück, E., & Tronicke, J. 2016. 1D sequential inversion of portable multi-configuration electromagnetic induction data. *Near Surface Geophysics*, **14**(2139).

Guillemoteau, Julien, Sailhac, Pascal, Boulanger, Charles, & Trules, Jérémie. 2015.

Inversion of ground constant offset loop-loop electromagnetic data for a large range of induction numbers. *GEOPHYSICS*, **80**(1), E11–E21.

Guillemoteau, Julien, Christensen, Niels Bøie, Jacobsen, Bo Holm, & Tronicke, Jens. 2017. Fast 3D multichannel deconvolution of electromagnetic induction loop-loop apparent conductivity data sets acquired at low induction numbers. *GEOPHYSICS*, **82**(6), E357–E369.

Guo, Li, Chen, Jin, Cui, Xihong, Fan, Bihang, & Lin, Henry. 2013. Application of ground penetrating radar for coarse root detection and quantification: a review. *Plant and Soil*, **362**(1-2), 1–23.

Guptasarma, D., & Singh, B. 1997. New digital linear filters for Hankel J0 and J1 transforms. *Geophysical prospecting*, **45**(5), 745–762.

Hamza, M. A., & Anderson, W. K. 2005. Soil compaction in cropping systems: A review of the nature, causes and possible solutions. *Soil and tillage research*, **82**(2), 121–145. Publisher: Elsevier.

Hanssens, D., Delefortrie, S., Pue, J. De, Meirvenne, M. Van, & Smedt, P. De. 2019. Frequency-Domain Electromagnetic Forward and Sensitivity Modeling: Practical Aspects of Modeling a Magnetic Dipole in a Multilayered Half-Space. *IEEE Geoscience and Remote Sensing Magazine*, **7**(1), 74–85.

Hassan, Asem, & Toll, David G. 2013. Electrical Resistivity Tomography for Characterizing Cracking of Soils. *Pages 818–827 of: Geo-Congress 2013@ Stability and Performance of Slopes and Embankments III*. ASCE.

Hayashi, Masaki. 2004. Temperature-electrical conductivity relation of water for environmental monitoring and geophysical data inversion. *Environmental Monitoring and Assessment*, **96**(1-3), 119–128.

Hayley, Kevin, Bentley, L. R., Gharibi, M., & Nightingale, M. 2007. Low temperature dependence of electrical resistivity: Implications for near surface geophysical monitoring. *Geophysical Research Letters*, **34**(18).

Heagy, Lindsey J., Cockett, Rowan, Kang, Seogi, Rosenkjaer, Gudni K., & Old-

enburg, Douglas W. 2017. A framework for simulation and inversion in electromagnetics. *Computers & Geosciences*, **107**(Oct.), 1–19.

Hedley, C. B., Yule, I. J., Eastwood, C. R., Shepherd, T. G., & Arnold, G. 2004. Rapid identification of soil textural and management zones using electromagnetic induction sensing of soils. *Soil Research*, **42**(4), 389.

Hinnell, A. C., Ferré, T. P. A., Vrugt, J. A., Huisman, J. A., Moysey, S., Rings, J., & Kowalsky, M. B. 2010. Improved extraction of hydrologic information from geophysical data through coupled hydrogeophysical inversion: COUPLED HYDROGEOPHYSICAL INVERSION. *Water Resources Research*, **46**(4).

Hobbs, Peter R, Sayre, Ken, & Gupta, Raj. 2008. The role of conservation agriculture in sustainable agriculture. *Philosophical Transactions of the Royal Society B: Biological Sciences*, **363**(1491), 543–555.

Hodgkinson, L., Dodd, I. C., Binley, A., Ashton, R. W., White, R. P., Watts, C. W., & Whalley, W. R. 2017. Root growth in field-grown winter wheat: Some effects of soil conditions, season and genotype. *European Journal of Agronomy*, **91**(Nov.), 74–83.

Horton, Jonathan L, & Hart, Stephen C. 1998. Hydraulic lift: a potentially important ecosystem process. *Trends in Ecology & Evolution*, **13**(6), 232–235.

Houska, Tobias, Kraft, Philipp, Chamorro-Chavez, Alejandro, & Breuer, Lutz. 2015. SPOTting model parameters using a ready-made python package. *PloS one*, **10**(12), e0145180.

Huang, H, & Won, I. 2000. Conductivity and Susceptibility Mapping Using Broadband Electromagnetic Sensors. *Journal of Environmental and Engineering Geophysics*, 12.

Huang, J., Monteiro Santos, F.A., & Triantafilis, J. 2016. Mapping soil water dynamics and a moving wetting front by spatiotemporal inversion of electromagnetic induction data. Nov.

Huang, J., Pedrera-Parrilla, A., Vanderlinden, K., Taguas, E.V., Gómez, J.A., & Triantafilis, J. 2017a. Potential to map depth-specific soil organic matter content

across an olive grove using quasi-2d and quasi-3d inversion of DUALEM-21 data. *CATENA*, **152**(May), 207–217.

Huang, J., Buchanan, S. M., Bishop, T. F. A., & Triantafilis, J. 2017b. *terra* GIS - a web GIS for delivery of digital soil maps in cotton-growing areas of Australia. *Soil Use and Management*, **33**(4), 568–582.

Huang, J., Scudiero, E., Clary, W., Corwin, D. L., & Triantafilis, J. 2017c. Time-lapse monitoring of soil water content using electromagnetic conductivity imaging. *Soil Use and Management*, **33**(2), 191–204.

Huang, Jingyi, McBratney, Alex B., Minasny, Budiman, & Triantafilis, John. 2017d. Monitoring and modelling soil water dynamics using electromagnetic conductivity imaging and the ensemble Kalman filter. *Geoderma*, **285**(Jan.), 76–93.

Huang, Jingyi, Purushothaman, Ramamoorthy, McBratney, Alex, & Bramley, Helen. 2018. Soil Water Extraction Monitored Per Plot Across a Field Experiment Using Repeated Electromagnetic Induction Surveys. *Soil Systems*, **2**(1), 11.

Huisman, J. A., Hubbard, S. S., Redman, J. D., & Annan, A. P. 2003. Measuring soil water content with ground penetrating radar. *Vadose zone journal*, **2**(4), 476–491.

Hunter, John D. 2007. Matplotlib: A 2D Graphics Environment. *Computing in Science & Engineering*, **9**(3), 90–95.

Inci, Gokhan, Yesiller, Nazli, & Kagawa, Takaaki. 2003. Experimental investigation of dynamic response of compacted clayey soils. *Geotechnical Testing Journal*, **26**(2), 125–141. Publisher: ASTM International.

Jadoon, Khan Zaib, Lambot, Sébastien, Scharnagl, Benedikt, Kruk, Jan van der, Slob, Evert, & Vereecken, Harry. 2010. Quantifying field-scale surface soil water content from proximal GPR signal inversion in the time domain. *Near Surface Geophysics*, **8**(6), 483–491. _eprint: https://onlinelibrary.wiley.com/doi/pdf/10.3997/1873-0604.2010036.

Jadoon, Khan Zaib, Moghadas, Davood, Jadoon, Aurangzeb, Missimer, Thomas M., Al-Mashharawi, Samir K., & McCabe, Matthew F. 2015. Estimation of soil salinity in a drip irrigation system by using joint inversion of multicoil electromagnetic induction measurements. *Water Resources Research*, **51**(5), 3490–3504.

JafarGandomi, Arash, & Binley, Andrew. 2013. A Bayesian trans-dimensional approach for the fusion of multiple geophysical datasets. *Journal of Applied Geophysics*, **96**(Sept.), 38–54.

Jayawickreme, Dushmantha H., Van Dam, Remke L., & Hyndman, David W. 2008. Subsurface imaging of vegetation, climate, and root-zone moisture interactions. *Geophysical Research Letters*, **35**(18).

Jayawickreme, Dushmantha H., Van Dam, Remke L., & Hyndman, David W. 2010. Hydrological consequences of land-cover change: Quantifying the influence of plants on soil moisture with time-lapse electrical resistivity. *GEOPHYSICS*, **75**(4), WA43–WA50.

Jayawickreme, Dushmantha H., Jobbágy, Esteban G., & Jackson, Robert B. 2014. Geophysical subsurface imaging for ecological applications. *New Phytologist*, **201**(4), 1170–1175.

Jennings, J. E. B., & Burland, J. B. 1962. Limitations to the use of effective stresses in partly saturated soils. *Géotechnique*, **12**(2), 125–144. Publisher: Thomas Telford Ltd.

Johnson, Timothy C., Hammond, Glenn E., & Chen, Xingyuan. 2017. PFLOTRAN-E4D: A parallel open source PFLOTRAN module for simulating time-lapse electrical resistivity data. *Computers & Geosciences*, **99**(Feb.), 72–80.

Kachanoski, R. G., Wesenbeeck, I. J. Van, & Gregorich, E. G. 1988. ESTIMATING SPATIAL VARIATIONS OF SOIL WATER CONTENT USING NON-CONTACTING ELECTROMAGNETIC INDUCTIVE METHODS. *Canadian Journal of Soil Science*, **68**(4), 715–722.

Karaoulis, M., Revil, A., Tsourlos, P., Werkema, D.D., & Minsley, B.J. 2013. IP4DI: A software for time-lapse 2D/3D DC-resistivity and induced polarization tomography. *Computers & Geosciences*, **54**(Apr.), 164–170.

Keller, G. V., & Frischknecht, F. C. 1966. Electrical methods in geophysical prospecting.

Keller, T., Lamand, M., Peth, S., Berli, M., Delenne, J.-Y., Baumgarten, W., Rabbel, W., Radja, F., Rajchenbach, J., Selvadurai, A.P.S., & Or, D. 2013. An interdisciplinary approach towards improved understanding of soil deformation during compaction. *Soil and Tillage Research*, **128**(Apr.), 61–80.

Keller, Thomas, Colombi, Tino, Ruiz, Siul, Manalili, Mervin Pogs, Rek, Jan, Stadelmann, Viktor, Wunderli, Hans, Breitenstein, Dani, Reiser, René, Oberholzer, Hansrudolf, Schymanski, Stanislaus, Romero-Ruiz, Alejandro, Linde, Niklas, Weisskopf, Peter, Walter, Achim, & Or, Dani. 2017. Long-Term Soil Structure Observatory for Monitoring Post-Compaction Evolution of Soil Structure. *Vadose Zone Journal*, **16**(4), vzj2016.11.0118.

Khalili, N., & Khabbaz, M. H. 1998. A unique relationship for χ for the determination of the shear strength of unsaturated soils. *Geotechnique*, **48**(5), 681–687. Publisher: Thomas Telford Ltd.

King, J. A., Dampney, P. M. R., Lark, R. M., Wheeler, H. C., Bradley, R. I., & Mayr, T. R. 2005. Mapping Potential Crop Management Zones within Fields: Use of Yield-map Series and Patterns of Soil Physical Properties Identified by Electromagnetic Induction Sensing. *Precision Agriculture*, **6**(2), 167–181.

Klenk, P., Jaumann, S., & Roth, K. 2015. Quantitative high-resolution observations of soil water dynamics in a complicated architecture using time-lapse ground-penetrating radar. *Hydrology and Earth System Sciences*, **19**(3), 1125–1139.

Klotzsche, A., Jonard, F., Looms, M.C., van der Kruk, J., & Huisman, J.A. 2018a. Measuring Soil Water Content with Ground Penetrating Radar: A Decade of Progress. *Vadose Zone Journal*, **17**(1), 0.

Klotzsche, Anja, Lärm, Lena, Weihermüller, Lutz, Vanderborght, Jan, & Vereecken, Harry. 2018b. Time-lapse horizontal borehole GPR measurements to investigate spatial and temporal soil-water content changes. *th Annual Meeting*, 5.

Klotzsche, Anja, Lärm, Lena, Vanderborght, Jan, Cai, Gaochao, Morandage, Shehan, Zörner, Miriam, Vereecken, Harry, & van der Kruk, Jan. 2019. Monitoring Soil Water Content Using Time-Lapse Horizontal Borehole GPR Data at the Field-Plot Scale. *Vadose Zone Journal*, **18**(1), 0.

Koestel, Johannes, Kemna, Andreas, Javaux, Mathieu, Binley, Andrew, & Vereecken, Harry. 2008. Quantitative imaging of solute transport in an unsaturated and undisturbed soil monolith with 3-D ERT and TDR. *Water Resources Research*, **44**(12), n/a–n/a.

Koganti, Triven, Narjary, Bhaskar, Zare, Ehsan, Pathan, Aslam Latif, Huang, Jingyi, & Triantafilis, John. 2018. Quantitative mapping of soil salinity using the DUALEM-21S instrument and EM inversion software. *Land Degradation & Development*, **29**(6), 1768–1781.

Korsaeth, A., Riley, H., Kværnø, S. H., & Vestgarden, L. S. 2008. Relations between a commercial soil survey map based on soil apparent electrical conductivity (ECa) and measured soil properties on a morainic soil in Southeast Norway. *Handbook of Agricultural Geophysics (Eds. Barry J. Allred, Jeffrey J. Daniels, and M. Reza Ehsani)*, 225–231.

Kumar, J., & Madhusudhan, B. N. 2012. Dynamic properties of sand from dry to fully saturated states. *Geotechnique*, **62**(1), 45–54. Publisher: Thomas Telford Ltd.

Kuzma, Tsukanov, & Schwartz, Nimrod. 2018. Spectral induced polarization of roots in hydroponic solution and soil. *th Annual Meeting*, 5.

LaBrecque, Douglas J., & Yang, Xianjin. 2001. Difference inversion of ERT data: A fast inversion method for 3-D in situ monitoring. *Journal of Environmental & Engineering Geophysics*, **6**(2), 83–89.

Laloy, E., Weynants, M., Bielders, C.L., Vanclooster, M., & Javaux, M. 2010. How efficient are one-dimensional models to reproduce the hydrodynamic behavior of structured soils subjected to multi-step outflow experiments? *Journal of Hydrology*, **393**(1-2), 37–52.

Laloy, E., Javaux, M., Vanclooster, M., Roisin, C., & Bielders, C. L. 2011. Electrical Resistivity in a Loamy Soil: Identification of the Appropriate Pedo-Electrical Model. *Vadose Zone Journal*, **10**(3), 1023.

Laloy, Eric, Linde, Niklas, & Jacques, Diederik. 2020. Approaching geoscientific inverse problems with adversarial vector-to-image domain transfer networks. *arXiv:1912.09954 [physics]*, May. arXiv: 1912.09954.

Lambot, Sébastien, Weihermüller, Lutz, Huisman, Johan A., Vereecken, Harry, Vanclooster, Marnik, & Slob, Evert C. 2006. Analysis of air-launched ground-penetrating radar techniques to measure the soil surface water content. *Water Resources Research*, **42**(11). _eprint: https://agupubs.onlinelibrary.wiley.com/doi/pdf/10.1029/2006WR005097.

Lambot, Sébastien, Slob, Evert, Chavarro, Diana, Lubczynski, Maciek, & Vereecken, Harry. 2008. Measuring soil surface water content in irrigated areas of southern Tunisia using full-waveform inversion of proximal GPR data. *Near Surface Geophysics*, **6**(6), 403–410. _eprint: https://onlinelibrary.wiley.com/doi/pdf/10.3997/1873-0604.2008028.

Lavoué, F., Van Der Kruk, J., Rings, J., André, F., Moghadas, D., Huisman, J. A., Lambot, S., Weihermüller, L., Vanderborght, Jan, & Vereecken, H. 2010. Electromagnetic induction calibration using apparent electrical conductivity modelling based on electrical resistivity tomography. *Near surface geophysics*, **8**(6), 553–561.

Lesparre, Nolwenn, Robert, Tanguy, Nguyen, Frédéric, Boyle, Alistair, & Hermans, Thomas. 2019. 4D electrical resistivity tomography (ERT) for aquifer thermal energy storage monitoring. *Geothermics*, **77**(Jan.), 368–382.

Liu, Xiuwei, Dong, Xuejun, & Leskovar, Daniel I. 2016. Ground penetrating radar

for underground sensing in agriculture: a review. *International Agrophysics*, **30**(4), 533–543.

Liu, Xiuwei, Dong, Xuejun, Xue, Qingwu, Leskovar, Daniel I., Jifon, John, Butnor, John R., & Marek, Thomas. 2018. Ground penetrating radar (GPR) detects fine roots of agricultural crops in the field. *Plant and Soil*, **423**(1-2), 517–531.

Lo, Wei-Cheng, & Sposito, Garrison. 2013. Acoustic waves in unsaturated soils. *Water Resources Research*, **49**(9), 5674–5684. Publisher: Wiley Online Library.

Lopes, Marta S., & Reynolds, Matthew P. 2010. Partitioning of assimilates to deeper roots is associated with cooler canopies and increased yield under drought in wheat. *Functional Plant Biology*, **37**(2), 147.

Lu, Z. 2014. Feasibility of Using a Seismic Surface Wave Method to Study Seasonal and Weather Effects on Shallow Surface Soils. *Journal of Environmental & Engineering Geophysics*, **19**(2), 71–85.

Lu, Zhiqu, & Sabatier, James M. 2009. Effects of soil water potential and moisture content on sound speed. *Soil Science Society of America Journal*, **73**(5), 1614–1625. Publisher: Wiley Online Library.

Lu, Zhiqu, Hickey, Craig J., & Sabatier, James M. 2004. Effects of compaction on the acoustic velocity in soils. *Soil Science Society of America Journal*, **68**(1), 7–16. Publisher: Wiley Online Library.

Ma, Ruijun, McBratney, Alex, Whelan, Brett, Minasny, Budiman, & Short, Michael. 2011. Comparing temperature correction models for soil electrical conductivity measurement. *Precision Agriculture*, **12**(1), 55–66.

Macleod, Christopher (Kit) J. A., Humphreys, Mike W., Whalley, W. Richard, Turner, Lesley, Binley, Andrew, Watts, Chris W., Skøt, Leif, Joynes, Adrian, Hawkins, Sarah, King, Ian P., O'Donovan, Sally, & Haygarth, Phil M. 2013. A novel grass hybrid to reduce flood generation in temperate regions. *Scientific Reports*, **3**(Apr.).

Mansoor, Nasser, Slater, Lee, Artigas, Francisco, & Auken, Esben. 2006.

High-resolution geophysical characterization of shallow-water wetlands. *GEO-PHYSICS*, **71**(4), B101–B109.

Mares, Rachel, Barnard, Holly R., Mao, Deqiang, Revil, André, & Singha, Kamini. 2016. Examining diel patterns of soil and xylem moisture using electrical resistivity imaging. *Journal of Hydrology*, **536**(May), 327–338.

Martinelli, Patricia, & Duplaá, María Celeste. 2008. Laterally filtered 1D inversions of small-loop, frequency-domain EMI data from a chemical waste site. *Geophysics*, **73**(4), F143–F149. Publisher: Society of Exploration Geophysicists.

Martinez, G., Huang, J., Vanderlinden, K., Giráldez, J. V., & Triantafilis, J. 2018. Potential to predict depth-specific soil-water content beneath an olive tree using electromagnetic conductivity imaging. *Soil Use and Management*, Apr.

Martini, Edoardo, Werban, Ulrike, Zacharias, Steffen, Pohle, Marco, Dietrich, Peter, & Wollschläger, Ute. 2017. Repeated electromagnetic induction measurements for mapping soil moisture at the field scale: validation with data from a wireless soil moisture monitoring network. *Hydrology and Earth System Sciences*, **21**(1), 495–513.

Mary, Benjamin, Abdulsamad, Feras, Saracco, Ginette, Peyras, Laurent, Vennetier, Michel, Mériaux, Patrice, & Camerlynck, Christian. 2017. Improvement of coarse root detection using time and frequency induced polarization: from laboratory to field experiments. *Plant and Soil*, **417**(1-2), 243–259.

Mary, Benjamin, Peruzzo, Luca, Boaga, Jacopo, Schmutz, Myriam, Wu, Yuxin, Hubbard, Susan S., & Cassiani, Giorgio. 2018. Small scale characterization of vine plant root water uptake via 3D electrical resistivity tomography and Mise-à-la-Masse method. *Hydrology and Earth System Sciences Discussions*, June, 1–30.

Mary, Benjamin, Peruzzo, Luca, Boaga, Jacopo, Cenni, Nicola, Schmutz, Myriam, Wu, Yuxin, Hubbard, Susan S., & Cassiani, Giorgio. 2020. Time-lapse monitoring of root water uptake using electrical resistivity tomography and mise-&#224;-la-masse: a vineyard infiltration experiment. *SOIL*, **6**(1), 95–114.

Maurya, P. K., Fiandaca, G., Christiansen, A. V., & Auken, E. 2018. Field-scale comparison of frequency- and time-domain spectral induced polarization. *Geophysical Journal International*, **214**(2), 1441–1466. Publisher: Oxford Academic.

McLachlan, P., Chambers, J., Uhlemann, S., & Binley, A. 2020a. Electrical resistivity and induced polarization imaging of riverbed sediments: Observations from laboratory, field and synthetic experiments. *Journal of Applied Geophysics*, Sept., 104173.

McLachlan, Paul, Blanchy, Guillaume, & Binley, Andrew. 2020b. EMagPy: open-source standalone software for processing, forward modeling and inversion of electromagnetic induction data. *Computers & Geosciences*, Aug., 104561.

McLachlan, P.J., Chambers, J.E., Uhlemann, S.S., & Binley, A. 2017. Geophysical characterisation of the groundwater–surface water interface. *Advances in Water Resources*, **109**(Nov.), 302–319.

McNeill, J. D. 1980. *Electromagnetic terrain conductivity measurement at low induction numbers*. Geonics Limited Ontario, Canada.

Mester, Achim, van der Kruk, Jan, Zimmermann, Egon, & Vereecken, Harry. 2011. Quantitative Two-Layer Conductivity Inversion of Multi-Configuration Electromagnetic Induction Measurements. *Vadose Zone Journal*, **10**(4), 1319.

Metzner, Ralf, Eggert, Anja, van Dusschoten, Dagmar, Pflugfelder, Daniel, Gerth, Stefan, Schurr, Ulrich, Uhlmann, Norman, & Jahnke, Siegfried. 2015. Direct comparison of MRI and X-ray CT technologies for 3D imaging of root systems in soil: potential and challenges for root trait quantification. *Plant Methods*, **11**(1), 17.

Mewes, Benjamin, Hilbich, Christin, Delaloye, Reynald, & Hauck, Christian. 2017. Resolution capacity of geophysical monitoring regarding permafrost degradation induced by hydrological processes. *The Cryosphere*, **11**(6), 2957–2974.

Michot, Didier, Dorigny, Abel, & Benderitter, Yves. 2001. Mise en evidence par resistivité electrique des ecoulements préférentiels et de l'assèchement par le maïs

d'un calcisol de Beauce irrigué. *Comptes Rendus de l'Académie des Sciences-Series IIA-Earth and Planetary Science*, **332**(1), 29–36.

Michot, Didier, Benderitter, Yves, Dorigny, Abel, Nicoullaud, Bernard, King, Dominique, & Tabbagh, Alain. 2003. Spatial and temporal monitoring of soil water content with an irrigated corn crop cover using surface electrical resistivity tomography: SOIL WATER STUDY USING ELECTRICAL RESISTIVITY. *Water Resources Research*, **39**(5), n/a–n/a.

Minsley, Burke J. 2011. A trans-dimensional Bayesian Markov chain Monte Carlo algorithm for model assessment using frequency-domain electromagnetic data: Bayesian MCMC algorithm for model assessment. *Geophysical Journal International*, **187**(1), 252–272.

Moghadas, Davood. 2020. One-dimensional deep learning inversion of electromagnetic induction data using convolutional neural network. *Geophysical Journal International*, Apr., ggaa161.

Moghadas, Davood, & Vrugt, Jasper A. 2019. The Influence of Geostatistical Prior Modeling on the Solution of DCT-Based Bayesian Inversion: A Case Study from Chicken Creek Catchment. *Remote Sensing*, **11**(13), 1549.

Moghadas, Davood, André, Frédéric, Bradford, John H., van der Kruk, Jan, Vereecken, Harry, & Lambot, Sébastien. 2012. Electromagnetic induction antenna modelling using a linear system of complex antenna transfer functions. *Near Surface Geophysics*, **10**(3), 237–247.

Moghadas, Davood, Jadoon, Khan Zaib, & McCabe, Matthew F. 2017. Spatiotemporal monitoring of soil water content profiles in an irrigated field using probabilistic inversion of time-lapse EMI data. *Advances in Water Resources*, **110**(Dec.), 238–248.

Monteiro Santos, Fernando A. 2004. 1-D laterally constrained inversion of EM34 profiling data. *Journal of Applied Geophysics*, **56**(2), 123–134.

Mooney, S. J., Pridmore, T. P., Helliwell, J., & Bennett, M. J. 2012. Developing

X-ray Computed Tomography to non-invasively image 3-D root systems architecture in soil. **352**(1), 1–22.

Moral, Francisco J., & Serrano, João M. 2019. Using low-cost geophysical survey to map soil properties and delineate management zones on grazed permanent pastures. *Precision Agriculture*, Jan.

Morelli, G., Zenone, T., Teobaldelli, M., Fischanger, F., Matteucci, M., & Seufert, G. 2007. Use of ground-penetrating radar (GPR) and electrical resistivity tomography (ERT) to study tree roots volume in pine forest and poplar plantation. *Napier, New Zealand*, **21**, 1–4.

Mulyono, A, Arisbaya, I, Sudrajat, Y, Djuwansah, M R, Suriadikusumah, A, & Harryanto, R. 2019. Determining of soil resistivity by electrical resistivity tomography in agroforestry land system. *IOP Conference Series: Earth and Environmental Science*, **393**(Dec.), 012063.

Mwakanyamale, Kisa, Slater, Lee, Binley, Andrew, & Ntarlagiannis, Dimitrios. 2012. Lithologic imaging using complex conductivity: Lessons learned from the Hanford 300 Area. *GEOPHYSICS*, **77**(6), E397–E409.

Nakagawa, K., Soga, K., & Mitchell, J. K. 1997. Observation of Biot compressional wave of the second kind in granular soils. *Geotechnique*, **47**(1), 133–147. Publisher: Thomas Telford Ltd.

Nath, Sankar Kumar, Shahid, Shamsuddin, & Dewangan, Pawan. 2000. SEIS-RES—a visual C++ program for the sequential inversion of seismic refraction and geoelectric data. *Computers & Geosciences*, **26**(2), 177–200.

Nelder, John A., & Mead, Roger. 1965. A simplex method for function minimization. *The computer journal*, **7**(4), 308–313. Publisher: Oxford University Press.

Nijland, Wiebe, van der Meijde, Mark, Addink, Elisabeth A., & de Jong, Steven M. 2010. Detection of soil moisture and vegetation water abstraction in a Mediterranean natural area using electrical resistivity tomography. *CATENA*, **81**(3), 209–216.

Ntarlagiannis, Dimitrios, Robinson, Judith, Soupios, Pantelis, & Slater, Lee. 2016. Field-scale electrical geophysics over an olive oil mill waste deposition site: Evaluating the information content of resistivity versus induced polarization (IP) images for delineating the spatial extent of organic contamination. **135**(Dec.), 418–426.

Nuth, Mathieu, & Laloui, Lyesse. 2008. Effective stress concept in unsaturated soils: Clarification and validation of a unified framework. *International journal for numerical and analytical methods in Geomechanics*, **32**(7), 771–801. Publisher: Wiley Online Library.

Nüsch, Anne-Kathrin, Dietrich, Peter, Werban, Ulrike, & Behrens, Thorsten. 2010. Acquisition and reliability of geophysical data in soil science. 4.

Ober, Eric S., Werner, Peter, Flatman, Edward, Angus, William J., Jack, Peter, Smith-Reeve, Lucy, & Tapsell, Chris. 2014. Genotypic differences in deep water extraction associated with drought tolerance in wheat. *Functional Plant Biology*, **41**(11), 1078.

Oelze, Michael L., O'Brien, William D., & Darmody, Robert G. 2002. Measurement of attenuation and speed of sound in soils. *Soil Science Society of America Journal*, **66**(3), 788–796. Publisher: Wiley Online Library.

Oldenburg, Douglas W., & Li, Yaoguo. 1999. Estimating depth of investigation in dc resistivity and IP surveys. *Geophysics*, **64**(2), 403–416.

Paetzold, R. F., Matzkanin, G. A., & Santos, A. De Los. 1985. Surface Soil Water Content Measurement Using Pulsed Nuclear Magnetic Resonance Techniques. *Soil Science Society of America Journal*, **49**(3), 537–540. _eprint: https://acsess.onlinelibrary.wiley.com/doi/pdf/10.2136/sssaj1985.03615995004900030001x.

Palacky, G. J. 1987. Clay mapping using electromagnetic methods. *First Break*, **5**(8), 295–306.

Panissod, C., Michot, D., Benderitter, Y., & Tabbagh, A. 2001. On the effectiveness of 2D electrical inversion results: an agricultural case study. *Geophysical Prospecting*, **49**(5), 570–576.

Panissod, Cedric, Dabas, Michel, Hesse, Albert, Jolivet, Alain, Tabbagh, Jeanne, & Tabbagh, Alain. 1998. Recent developments in shallow-depth electrical and electrostatic prospecting using mobile arrays. *Geophysics*, **63**(5), 1542–1550. Publisher: Society of Exploration Geophysicists.

Parasnis, Dattatray. 1988. Reciprocity theorems in geoelectric and geoelectromagnetic work. *Geoexploration*, **25**(3), 177–198.

Pereira, Jose HF, & Fredlund, Delwyn G. 2000. Volume change behavior of collapsible compacted gneiss soil. *Journal of geotechnical and geoenvironmental engineering*, **126**(10), 907–916. Publisher: American Society of Civil Engineers.

Pidlisecky, Adam, & Knight, Rosemary. 2008. FW2_5D: A MATLAB 2.5-D electrical resistivity modeling code. *Computers & Geosciences*, **34**(12), 1645–1654.

Prasanna, Boddupalli M., Araus, Jose L., Crossa, Jose, Cairns, Jill E., Palacios, Natalia, Das, Biswanath, & Magorokosho, Cosmos. 2013. High-Throughput and Precision Phenotyping for Cereal Breeding Programs. *Pages 341–374 of:* Gupta, Pushpendra K., & Varshney, Rajeev K. (eds), *Cereal Genomics II.* Dordrecht: Springer Netherlands.

Rao, Sathyanarayan, Meunier, Félicien, Ehosioke, Solomon, Lesparre, Nolwenn, Kemna, Andreas, Nguyen, Frédéric, Garré, Sarah, & Javaux, Mathieu. 2019. Impact of Maize Roots on Soil–Root Electrical Conductivity: A Simulation Study. *Vadose Zone Journal*, **18**(1), 0.

Rawls, W.J., Pachepsky, Y.A., Ritchie, J.C., Sobecki, T.M., & Bloodworth, H. 2003. Effect of soil organic carbon on soil water retention. *Geoderma*, **116**(1-2), 61–76.

Ren, Lidong, Nest, Thijs Vanden, Ruysschaert, Greet, D'Hose, Tommy, & Cornelis, Wim M. 2019. Short-term effects of cover crops and tillage methods on soil physical properties and maize growth in a sandy loam soil. *Soil and Tillage Research*, **192**(Sept.), 76–86.

Revil, A., Cathles, L. M., Losh, S., & Nunn, J. A. 1998. Electrical conductivity in shaly sands with geophysical applications. *J. geophys. Res*, **103**(23), 925–23.

Reyes, Javier, Wendroth, Ole, Matocha, Christopher, Zhu, Junfeng, Ren, Wei, & Karathanasis, A.D. 2018. Reliably Mapping Clay Content Coregionalized with Electrical Conductivity. *Soil Science Society of America Journal*, **0**(0), 0.

Rhoades, J. D., Raats, P. A. C., & Prather, R. J. 1976. Effects of liquid-phase electrical conductivity, water content, and surface conductivity on bulk soil electrical conductivity. *Soil Science Society of America Journal*, **40**(5), 651–655.

Rhoades, J. D., Manteghi, N. A., Shouse, P. J., & Alves, W. J. 1989. Soil Electrical Conductivity and Soil Salinity: New Formulations and Calibrations. *Soil Science Society of America Journal*, **53**(2), 433–439.

Robinson, D. A., Lebron, I., Lesch, S. M., & Shouse, P. 2004. Minimizing Drift in Electrical Conductivity Measurements in High Temperature Environments using the EM-38. *Soil Science Society of America Journal*, **68**(2), 339–345. _eprint: https://acsess.onlinelibrary.wiley.com/doi/pdf/10.2136/sssaj2004.3390.

Robinson, David A., Abdu, Hiruy, Lebron, Inma, & Jones, Scott B. 2012a. Imaging of hill-slope soil moisture wetting patterns in a semi-arid oak savanna catchment using time-lapse electromagnetic induction. *Journal of Hydrology*, **416-417**(Jan.), 39–49.

Robinson, Judith L., Slater, Lee D., & Schäfer, Karina V.R. 2012b. Evidence for spatial variability in hydraulic redistribution within an oak–pine forest from resistivity imaging. *Journal of Hydrology*, **430-431**(Apr.), 69–79.

Romero-Ruiz, Alejandro, Linde, Niklas, Keller, Thomas, & Or, Dani. 2018. A Review of Geophysical Methods for Soil Structure Characterization: GEOPHYSICS AND SOIL STRUCTURE. *Reviews of Geophysics*, Dec.

Rossi, R., Amato, M., Bitella, G., Bochicchio, R., Ferreira Gomes, J. J., Lovelli, S., Martorella, E., & Favale, P. 2011. Electrical resistivity tomography as a non-destructive method for mapping root biomass in an orchard. *European Journal of Soil Science*, **62**(2), 206–215.

Rossi, R., Pollice, A., Bitella, G., Labella, R., Bochicchio, R., & Amato, M. 2018. Modelling the non-linear relationship between soil resistivity and alfalfa

NDVI: A basis for management zone delineation. *Journal of Applied Geophysics*, **159**(Dec.), 146–156.

Roy, A., & Apparao, A. 1971. Depth of investigation in direct current methods. *Geophysics*, **36**(5), 943–959. Publisher: Society of Exploration Geophysicists.

Rudolph, S., van der Kruk, J., von Hebel, C., Ali, M., Herbst, M., Montzka, C., Pätzold, S., Robinson, D.A., Vereecken, H., & Weihermüller, L. 2015. Linking satellite derived LAI patterns with subsoil heterogeneity using large-scale ground-based electromagnetic induction measurements. *Geoderma*, **241-242**(Mar.), 262–271.

Rücker, Carsten, & Günther, Thomas. 2011. The simulation of finite ERT electrodes using the complete electrode model. *GEOPHYSICS*, **76**(4), F227–F238.

Rücker, Carsten, Günther, Thomas, & Wagner, Florian M. 2017. pyGIMLi: An open-source library for modelling and inversion in geophysics. *Computers & Geosciences*, **109**(Dec.), 106–123.

Sadeghi-Tehran, Pouria, & Hawkesford, Malcolm J. 2017. Automated Method to Determine Two Critical Growth Stages of Wheat: Heading and Flowering. *Frontiers in Plant Science*, **8**, 14.

Saey, Timothy, Verhegge, Jeroen, De Smedt, Philippe, Smetryns, Marthe, Note, Nicolas, Van De Vijver, Ellen, Laloo, Pieter, Van Meirvenne, Marc, & Delefortrie, Samuël. 2016. Integrating cone penetration testing into the 1D inversion of multi-receiver EMI data to reconstruct a complex stratigraphic landscape. *CATENA*, **147**(Dec.), 356–371.

Samouëlian, A., Richard, G., Cousin, I., Guerin, R., Bruand, A., & Tabbagh, A. 2004. Three-dimensional crack monitoring by electrical resistivity measurement. *European Journal of Soil Science*, **55**(4), 751–762.

Samouëlian, A., Cousin, I., Tabbagh, A., Bruand, A., & Richard, G. 2005. Electrical resistivity survey in soil science: a review. *Soil and Tillage Research*, **83**(2), 173–193.

Samouëlian, Anatja, Cousin, Isabelle, Richard, Guy, Tabbagh, Alain, & Bruand, Ary. 2003. Electrical Resistivity Imaging for Detecting Soil Cracking at the Centimetric Scale. *Soil Science Society of America Journal*, **67**(5), 1319.

Saneiyan, Sina, Ntarlagiannis, Dimitrios, Werkema, D. Dale, & Ustra, Andréa. 2018. Geophysical methods for monitoring soil stabilization processes. *Journal of Applied Geophysics*, **148**(Jan.), 234–244.

Saneiyan, Sina, Ntarlagiannis, Dimitrios, Ohan, Juliette, Lee, Junghwoon, Colwell, Frederick, & Burns, Susan. 2019. Induced polarization as a monitoring tool for in-situ microbial induced carbonate precipitation (MICP) processes. *Ecological Engineering*, **127**(Feb.), 36–47.

Santamarina, J. Carlos, Klein, K. A., & Fam, M. A. 2001. *Soils and Waves: Particulate Materials Behaviour, Characterisation and Process Monitoring*. Chichester: John Wiley & Sons.

Schlumberger, Conrad. 1920. *Etude sur la prospection electrique du sous-sol.* Gauthier-Villars.

Schwartz, N., & Furman, A. 2014. On the spectral induced polarization signature of soil organic matter. **200**(1), 589–595.

Seabold, Skipper, & Perktold, Josef. 2010. Statsmodels: Econometric and Statistical Modeling with Python. 5.

Senapati, N, Griffiths, S, Hawkesford, M, Shewry, Pr, & Semenov, Ma. 2020. Substantial increase in yield predicted by wheat ideotypes for Europe under future climate. *Climate Research*, **80**(3), 189–201.

Senapati, Nimai, & Semenov, Mikhail A. 2020. Large genetic yield potential and genetic yield gap estimated for wheat in Europe. *Global Food Security*, **24**(Mar.), 100340.

Shanahan, Peter W., Binley, Andrew, Whalley, W. Richard, & Watts, Christopher W. 2015. The Use of Electromagnetic Induction to Monitor Changes in Soil Moisture Profiles beneath Different Wheat Genotypes. *Soil Science Society of America Journal*, **79**(2), 459.

Sharma, R. K., & Gupta, A. K. 2010. Continuous wave acoustic method for determination of moisture content in agricultural soil. *Computers and electronics in agriculture*, **73**(2), 105–111. Publisher: Elsevier.

Sheets, Keith R., & Hendrickx, Jan M. H. 1995. Noninvasive Soil Water Content Measurement Using Electromagnetic Induction. *Water Resources Research*, **31**(10), 2401–2409.

Sherlock, Mark D., & McDonnell, Jeffrey J. 2003. A new tool for hillslope hydrologists: spatially distributed groundwater level and soilwater content measured using electromagnetic induction. *Hydrological Processes*, **17**(10), 1965–1977. Publisher: Wiley Online Library.

Shin, H.-C., Taherzadeh, S., Attenborough, K., Whalley, W. R., & Watts, C. W. 2013. Non-invasive characterization of pore-related and elastic properties of soils in linear Biot–Stoll theory using acoustic-to-seismic coupling. *European journal of soil science*, **64**(3), 308–323. Publisher: Wiley Online Library.

Shin, H.-C., Whalley, W. R., Attenborough, K., & Taherzadeh, S. 2016. On the theory of Brutsaert about elastic wave speeds in unsaturated soils. *Soil and Tillage Research*, **156**, 155–165. Publisher: Elsevier.

Shin, H.-C., Watts, C. W., Whalley, W. R., Attenborough, K., & Taherzadeh, S. 2017. Non-invasive estimation of the depth profile of soil strength with acoustic-to-seismic coupling measurement in the presence of crops. *European Journal of Soil Science*, **68**(5), 758–768. Publisher: Wiley Online Library.

Skibbe, Nico, Rochlitz, Raphael, Günther, Thomas, & Müller-Petke, Mike. 2020. Coupled magnetic resonance and electrical resistivity tomography: An open-source toolbox for surface nuclear-magnetic resonance. *GEOPHYSICS*, **85**(3), F53–F64.

Slater, Lee D., & Lesmes, David. 2002. IP interpretation in environmental investigations. *GEOPHYSICS*, **67**(1), 77–88.

Srayeddin, Iyad, & Doussan, Claude. 2009. Estimation of the spatial variability of

root water uptake of maize and sorghum at the field scale by electrical resistivity tomography. *Plant and Soil*, **319**(1-2), 185–207.

Stanley, John N., Lamb, David W., Falzon, Gregory, & Schneider, Derek A. 2014. Apparent electrical conductivity (ECa) as a surrogate for neutron probe counts to measure soil moisture content in heavy clay soils (Vertosols). *Soil Research*, **52**(4), 373.

Stoll, R. D. 1974. *Acoustic waves in saturated sediments: in Physics of Sound in Marine Sediments, edited by L. Hampton*. Plenum, New York.

Sudduth, K. A., Drummond, S. T., & Kitchen, N. R. 2001. Accuracy issues in electromagnetic induction sensing of soil electrical conductivity for precision agriculture. *Computers and electronics in agriculture*, **31**(3), 239–264.

Sudduth, K. A., Kitchen, N. R., Wiebold, W. J., Batchelor, W. D., Bollero, German A., Bullock, D. G., Clay, D. E., Palm, H. L., Pierce, F. J., & Schuler, R. T. 2005. Relating apparent electrical conductivity to soil properties across the north-central USA. *Computers and Electronics in Agriculture*, **46**(1-3), 263–283. Publisher: Elsevier.

Sørensen, K. 1996. Pulled Array Continuous Electrical Profiling. *First Break*, **14**(3). Publisher: European Association of Geoscientists & Engineers.

Sławiński, C., Cymerman, J., Witkowska-Walczak, B., & Lamorski, K. 2012. Impact of diverse tillage on soil moisture dynamics. *International Agrophysics*, **26**(3), 301–309.

Tan, Xihe, Mester, Achim, von Hebel, Christian, Zimmermann, Egon, Vereecken, Harry, van Waasen, Stefan, & van der Kruk, Jan. 2019. Simultaneous calibration and inversion algorithm for multiconfiguration electromagnetic induction data acquired at multiple elevations. *GEOPHYSICS*, **84**(1), EN1–EN14.

Tang, Skylar, Farooque, Aitazaz A., Bos, Melanie, & Abbas, Farhat. 2019. Modelling DUALEM-2 measured soil conductivity as a function of measuring depth to correlate with soil moisture content and potato tuber yield. *Precision Agriculture*, July.

Tooms, Stephen, Taherzadeh, Shahram, & Attenborough, Keith. 1993. Sound propagation in a refracting fluid above a layered fluid-saturated porous elastic material. *The Journal of the Acoustical Society of America*, **93**(1), 173–181. Publisher: Acoustical Society of America.

Topp, G. Clarke, Davis, J. L., & Annan, Aa P. 1980. Electromagnetic determination of soil water content: Measurements in coaxial transmission lines. *Water resources research*, **16**(3), 574–582.

Trachsel, Samuel, Kaeppler, Shawn M., Brown, Kathleen M., & Lynch, Jonathan P. 2011. Shovelomics: high throughput phenotyping of maize (Zea mays L.) root architecture in the field. **341**(1), 75–87.

Triantafilis, J., Laslett, G. M., & McBratney, A. B. 2000. Calibrating an electromagnetic induction instrument to measure salinity in soil under irrigated cotton. *Soil Science Society of America Journal*, **64**(3), 1009–1017. Publisher: Soil Science Society.

Triantafilis, John, & Lesch, S. M. 2005. Mapping clay content variation using electromagnetic induction techniques. *Computers and Electronics in Agriculture*, **46**(1-3), 203–237. Publisher: Elsevier.

Tso, Chak-Hau Michael, Kuras, Oliver, Wilkinson, Paul B., Uhlemann, Sebastian, Chambers, Jonathan E., Meldrum, Philip I., Graham, James, Sherlock, Emma F., & Binley, Andrew. 2017. Improved characterisation and modelling of measurement errors in electrical resistivity tomography (ERT) surveys. *Journal of Applied Geophysics*, **146**(Nov.), 103–119.

Tsukanov, Kuzma, & Schwartz, Nimrod. 2020. Relationship between wheat root properties and its electrical signature using the spectral induced polarization method. *Vadose Zone Journal*, **19**(1), e20014. _eprint: https://acsess.onlinelibrary.wiley.com/doi/pdf/10.1002/vzj2.20014.

Uhlemann, Sebastian, Wilkinson, Paul B, Maurer, Hansruedi, Wagner, Florian M, Johnson, Timothy C, & Chambers, Jonathan E. 2018. Optimized survey design for Electrical Resistivity Tomography: combined optimization of measurement configuration and electrode placement. 36.

Van Der Kruk, J., Meekes, J. A. C., Van Den Berg, P. M., & Fokkema, J. T. 2000. An apparent-resistivity concept for low-frequency electromagnetic sounding techniques. *Geophysical Prospecting*, **48**(6), 1033–1052.

Vanella, D., Cassiani, G., Busato, L., Boaga, J., Barbagallo, S., Binley, A., & Consoli, S. 2018. Use of small scale electrical resistivity tomography to identify soil-root interactions during deficit irrigation. *Journal of Hydrology*, **556**(Jan.), 310–324.

Vereecken, H., Huisman, J.A., Pachepsky, Y., Montzka, C., van der Kruk, J., Bogena, H., Weihermüller, L., Herbst, M., Martinez, G., & Vanderborght, J. 2014. On the spatio-temporal dynamics of soil moisture at the field scale. *Journal of Hydrology*, **516**(Aug.), 76–96.

Verhoef, A., Fernández-Gálvez, J., Diaz-Espejo, A., Main, B. E., & El-Bishti, M. 2006. The diurnal course of soil moisture as measured by various dielectric sensors: Effects of soil temperature and the implications for evaporation estimates. *Journal of Hydrology*, **321**(1), 147–162.

Vinegar, H. J., & Waxman, M. H. 1984. Induced polarization of shaly sands. *GEOPHYSICS*, **49**(8), 1267–1287.

Virlet, Nicolas, Sabermanesh, Kasra, Sadeghi-Tehran, Pouria, & Hawkesford, Malcolm J. 2017. Field Scanalyzer: An automated robotic field phenotyping platform for detailed crop monitoring. *Functional Plant Biology*, **44**(1), 143.

Virtanen, Pauli, Gommers, Ralf, Oliphant, Travis E., Haberland, Matt, Reddy, Tyler, Cournapeau, David, Burovski, Evgeni, Peterson, Pearu, Weckesser, Warren, Bright, Jonathan, Walt, Stéfan J. van der, Brett, Matthew, Wilson, Joshua, Millman, K. Jarrod, Mayorov, Nikolay, Nelson, Andrew R. J., Jones, Eric, Kern, Robert, Larson, Eric, Carey, C. J., Polat, İlhan, Feng, Yu, Moore, Eric W., VanderPlas, Jake, Laxalde, Denis, Perktold, Josef, Cimrman, Robert, Henriksen, Ian, Quintero, E. A., Harris, Charles R., Archibald, Anne M., Ribeiro, Antônio H., Pedregosa, Fabian, & Mulbregt, Paul van. 2020. SciPy 1.0: fundamental algorithms for scientific computing in Python. *Nature Methods*, **17**(3), 261–272. Number: 3 Publisher: Nature Publishing Group.

Viscarra Rossel, R. A., Adamchuk, V. I., Sudduth, K. A., McKenzie, N. J., & Lobsey, C. 2011. Chapter Five - Proximal Soil Sensing: An Effective Approach for Soil Measurements in Space and Time. *Pages 243–291 of:* Sparks, Donald L. (ed), *Advances in Agronomy*. Advances in Agronomy, vol. 113. Academic Press.

von Hebel, Christian, Rudolph, Sebastian, Mester, Achim, Huisman, Johan A., Kumbhar, Pramod, Vereecken, Harry, & van der Kruk, Jan. 2014. Three-dimensional imaging of subsurface structural patterns using quantitative large-scale multiconfiguration electromagnetic induction data. *Water Resources Research*, **50**(3), 2732–2748.

von Hebel, Christian, van der Kruk, Huisman, Johan A., Mester, Altdorff, Endres, Zimmermann, Garré, & Vereecken. 2019. Calibration, Conversion, and Quantitative Multi-Layer Inversion of Multi-Coil Rigid-Boom Electromagnetic Induction Data. *Sensors*, **19**(21), 4753.

Vrugt, J. A., & Ter Braak, C. J. F. 2011. DREAM(D): an adaptive Markov Chain Monte Carlo simulation algorithm to solve discrete, noncontinuous, and combinatorial posterior parameter estimation problems. *Hydrology and Earth System Sciences*, **15**(12), 3701–3713.

Wait, James R. 1955. Mutual electromagnetic coupling of loops over a homogeneous ground. *geophysics*, **20**(3), 630–637. Publisher: Society of Exploration Geophysicists.

Wait, James R. 1982. *Geo-electromagnetism*. Academic press edn.

Wang, Ping, Hu, Zhenqi, Zhao, Yanling, & Li, Xinju. 2016. Experimental study of soil compaction effects on GPR signals. **126**(Mar.), 128–137.

Wang, Yong-Qian, Zhao, Peng-Fei, Fan, Li-Feng, Zhou, Qiao, Wang, Zi-Yang, Song, Chao, Chai, Zhi-Qiang, Yue, Yang, Huang, Lan, & Wang, Zhong-Yi. 2019. Determination of water content and characteristic analysis in substrate root zone by electrical impedance spectroscopy. *Computers and Electronics in Agriculture*, **156**(Jan.), 243–253.

Ward, Adam S., Gooseff, Michael N., & Singha, Kamini. 2013. How Does Subsurface Characterization Affect Simulations of Hyporheic Exchange? *Groundwater*, **51**(1), 14–28.

Wasson, A. P., Richards, R. A., Chatrath, R., Misra, S. C., Prasad, S. V. S., Rebetzke, G. J., Kirkegaard, J. A., Christopher, J., & Watt, M. 2012. Traits and selection strategies to improve root systems and water uptake in water-limited wheat crops. *Journal of Experimental Botany*, **63**(9), 3485–3498.

Wasson, A. P., Rebetzke, G. J., Kirkegaard, J. A., Christopher, J., Richards, R. A., & Watt, M. 2014. Soil coring at multiple field environments can directly quantify variation in deep root traits to select wheat genotypes for breeding. **65**(21), 6231–6249.

Waxman, Monroe H., & Smits, L. J. M. 1968. Electrical conductivities in oil-bearing shaly sands. *Society of Petroleum Engineers Journal*, **8**(02), 107–122.

Weigand, M., Flores Orozco, A., & Kemna, A. 2017. Reconstruction quality of SIP parameters in multi-frequency complex resistivity imaging. *Near Surface Geophysics*, **1**(-9).

Weigand, Maximilian, & Kemna, Andreas. 2017. Multi-frequency electrical impedance tomography as a non-invasive tool to characterize and monitor crop root systems. *Biogeosciences*, **14**(4), 921–939.

Weigand, Maximilian, & Kemna, Andreas. 2018. Imaging and functional characterization of crop root systems using spectroscopic electrical impedance measurements. *Plant and Soil*, Nov.

Weller, A., & Slater, L.D. 2015. Induced polarization dependence on pore space geometry: Empirical observations and mechanistic predictions. **123**(Dec.), 310–315.

Werban, Ulrike, Attia al Hagrey, Said, & Rabbel, Wolfgang. 2008. Monitoring of root-zone water content in the laboratory by 2D geoelectrical tomography. *Journal of Plant Nutrition and Soil Science*, **171**(6), 927–935.

Whalley, W. R., Lock, G., Jenkins, M., Peloe, T., Burek, K., Balendonck, J., Take, W. A., Tuzel, I. H., & Tuzel, YÜKSEL. 2009. Measurement of Low Matric Potentials with Porous Matrix Sensors and Water-Filled Tensiometers. *Soil Science Society of America Journal*, **73**(6), 1796–1803. Publisher: Wiley Online Library.

Whalley, W. R., Jenkins, M., & Attenborough, K. 2011. The velocity of shear waves in saturated soil. *Soil Science Society of America Journal*, **75**(5), 1652–1657. Publisher: Wiley Online Library.

Whalley, W. R., Jenkins, M., & Attenborough, K. 2012. The velocity of shear waves in unsaturated soil. *Soil and Tillage research*, **125**, 30–37. Publisher: Elsevier.

Whalley, W.R., Binley, A., Watts, C.W., Shanahan, P., Dodd, I.C., Ober, E.S., Ashton, R.W., Webster, C.P., White, R.P., & Hawkesford, M. J. 2017. Methods to estimate changes in soil water for phenotyping root activity in the field. *Plant and Soil*, **415**(1-2), 407–422.

White, Charlotte A., Sylvester-Bradley, Roger, & Berry, Peter M. 2015. Root length densities of UK wheat and oilseed rape crops with implications for water capture and yield. *Journal of Experimental Botany*, **66**(8), 2293–2303.

Williams, B. G., & Baker, G. C. 1982. An electromagnetic induction technique for reconnaissance surveys of soil salinity hazards. *Soil Research*, **20**(2), 107–118. Publisher: CSIRO PUBLISHING.

Wu, Kaijun, Rodriguez, Gabriela Arambulo, Zajc, Marjana, Jacquemin, Elodie, Clément, Michiels, De Coster, Albéric, & Lambot, Sébastien. 2019. A new drone-borne GPR for soil moisture mapping. *Remote Sensing of Environment*, **235**(Dec.), 111456.

Wunderlich, Tina, Petersen, Hauke, Attia al Hagrey, Said, & Rabbel, Wolfgang. 2013. Pedophysical Models for Resistivity and Permittivity of Partially Water-Saturated Soils. *Vadose Zone Journal*, **12**(4), 0.

Zare, E., Huang, J., Santos, F. A., & Triantafilis, J. 2015. Mapping salinity in three dimensions using a DUALEM-421 and electromagnetic inversion software. *Soil Science Society of America Journal*, **79**(6), 1729–1740. Publisher: The Soil Science Society of America, Inc.

Zarif, Fardous, Kessouri, Pauline, & Slater, Lee. 2017. Recommendations for Field-Scale Induced Polarization (IP) Data Acquisition and Interpretation. *Journal of Environmental and Engineering Geophysics*, 16.

Zhang, X. X., Whalley, P. A., Ashton, R. W., Evans, J., Hawkesford, M. J., Griffiths, S., Huang, Z. D., Zhou, H., Mooney, S. J., & Whalley, W. R. 2020. A comparison between water uptake and root length density in winter wheat: effects of root density and rhizosphere properties. *Plant and Soil*, May.

Zhao, Peng-Fei, Wang, Yong-Qian, Yan, Shi-Xian, Fan, Li-Feng, Wang, Zi-Yang, Zhou, Qiao, Yao, Jie-Peng, Cheng, Qiang, Wang, Zhong-Yi, & Huang, Lan. 2019. Electrical imaging of plant root zone: A review. *Computers and Electronics in Agriculture*, **167**(Dec.), 105058.

Zhu, Q., Lin, H.S., & Doolittle, J.A. 2013. Functional soil mapping for site-specific soil moisture and crop yield management. *Geoderma*, **200-201**(June), 45–54.